Analysing the impact of detector properties on pulse shape discrimination in plastic scintillation detectors using Monte Carlo simulations

Caroline Julie Holroyd, MPhys

School of Engineering

Lancaster University

A thesis submitted for the degree of

Doctor of Philosophy

December, 2025

Analysing the impact of detector properties on pulse shape discrimination in plastic scintillation detectors using Monte Carlo simulations

Caroline Julie Holroyd, MPhys.

School of Engineering, Lancaster University

A thesis submitted for the degree of *Doctor of Philosophy*. December, 2025.

Abstract

This thesis investigates how key detector parameters influence the pulse shape characteristics and pulse shape discrimination (PSD) performance of the commercially available plastic scintillator EJ-276. Plastic scintillators provide a cost-effective and physically robust alternative to conventional neutron detection technologies, such as ^{3}He detectors, liquid scintillators, and crystal scintillators. However, previous studies have shown that PSD performance in plastic scintillators deteriorates as the scintillator length increases, posing a significant limitation for large-area applications, such as radiation portal monitors (RPMs) used in homeland security.

To address this, a systematic study was conducted using the Monte Carlo simulation toolkit Geant4. This research evaluates how variations in scintillator geometry and length, optical surface treatment, and photodetector noise impact light collection efficiency (LCE), pulse shape formation, and PSD performance. The simulations incorporate recent updates to Geant4 which enable more accurate modelling of scintillation decay components and their particle-dependent intensities, building on prior work in the field.

Results show that increasing the scintillator length reduces light collection efficiency (LCE) and introduces pulse shape artefacts. These distortions deviate from the Gaussian-like appearance observed in smaller scintillators and increase susceptibility to noise, leading to degraded PSD performance in elongated detectors. While highly reflective and specular surface treatments enhance LCE, diffuse reflectors better preserve pulse shape fidelity.

These findings provide new insights into the causes of PSD degradation in elongated plastic scintillators.

For Mum.

Acknowledgements

"You're on your own kid, you always have been" **— Dr. Taylor Alison Swift**

This PhD would not have been possible without the support and encouragement of the many wonderful people who helped me cultivate the resilience necessary to complete this thesis.

I would like to extend my heartfelt gratitude, first and foremost, to my supervisor, Dr. Michael Aspinall. There were countless moments during these past 7 years when I felt I might never reach the end of this journey and struggled to believe I was cut out for a PhD. Throughout all of this, Michael was consistently there with a helpful, pragmatic approach, seemingly able to find a solution to every problem I encountered during my research. I am deeply grateful for his steadfast support, guidance, and encouragement.

I would also like to thank one of the most important people in my life — my mum — who believed in me even when I didn't believe in myself and fostered my love of learning. She always encouraged me to keep going and not give up, and indulged my passion for scintillators despite having no idea what I was talking about most of the time. I dedicate this thesis to you, but don't worry, you don't have to read it all. Thank you, Mothership, I got there in the end.

My sincere thanks go to my industrial supervisor, Dr. Tom Deakin from LabLogic Systems Ltd., for all the help and support he offered during my PhD journey, particularly during the more difficult times when I was progressing at tortoise speed. Thank you, too, for our chats in Café Nero — they were always appreciated.

This research was funded by the Engineering and Physical Sciences Research Council (EPSRC) via the Centre for Doctoral Training (CDT) in Nuclear Fission — Next Generation Nuclear (NGN), and through a grant provided by the Nuclear Data Network.

I would like to thank Laurie Gracie in the School of Engineering at Lancaster University for her help and reassurance, my friends and family for their constant encouragement, the National Physical Laboratory for all their assistance and advice during the planning of experimental work, Saed Alrawash for his help with experimental work when I could not be on campus, Dr. Andrew Parker for his help with Geant4, Professor Graeme Burt for his mentorship, and Colin from Randstad for his encouragement and understanding.

Lastly, but very importantly, I would like to thank a regrettably since closed charity in my home city of Leeds, called The Market Place. I was involved with this organisation as a service user, volunteer, and later trustee for many years, and was deeply saddened by its closure after 36 years this past September. The Market Place was an incredible organisation that carried out vital work supporting young people struggling with their mental health. I don't know if I would ever have had the self-belief to go to university in the first place were it not for their compassionate support, encouragement, and belief in me and my abilities when I was younger. The legacy of their work lives on in all of us who were helped by The Market Place.

Declaration

I, Caroline Julie Holroyd, hereby certify that this thesis and the research described in it is all my own work unless otherwise indicated and has not been submitted in any previous application for a higher degree. The work presented here was carried out between October 2018 and May 2025.

Assistance from an AI language model were used to improve MATLAB scripts and Geant4 code, and refine the drafting of certain sections of this thesis. This support contributed to enhancing clarity and presentation; however, all original ideas and substantive content are the sole work of the author.

Date: 03/06/2025 Signature of candidate: Caroline Julie Holroyd

I, Dr Michael Douglas Aspinall, hereby certify that the candidate has fulfilled the conditions of the resolution and regulations appropriate for the degree of Doctor of Philosophy at Lancaster University and that the candidate is qualified to submit this thesis in application for that degree.

Date: 03/06/2025 Signature of supervisor: Michael Douglas Aspinall

Publications

The following peer-reviewed publications have resulted from the research presented in this thesis:

1. C. Holroyd, M. Aspinall, T. Deakin, Pulse shape simulations for organic scintillation detectors using Geant4, in: EPJ Web Conf., 2021: p. 11002. https://doi.org/10.1051/epjconf/202125311002.

2. C. Holroyd, M. Aspinall, T. Deakin, Improving neutron/gamma pulse shape discrimination (PSD) of EJ-276 plastic scintillation detectors for nuclear security applications using Monte Carlo simulations, Int. J. Mod. Phys. E 34 (2025). https://doi.org/10.1142/S0218301325450089.

This work was also presented at the following conferences:

- Virtual IEEE Nuclear Science Symposium and Medical Imaging Conference (NSS), 2021.
- 6th International Conference on Advancements in Nuclear Instrumentation Measurement Methods and their Applications (ANIMMA), 2021.
- The International Conference on Applications of Nuclear Techniques (CRETE23), 2023.
- 8th International Conference on Advancements in Nuclear Instrumentation Measurement Methods and their Applications (ANIMMA), 2023.

Contents

List of Tables

List of Figures

Chapter 1

Introduction

The rapid and reliable detection of Special Nuclear Material (SNM), primarily enriched uranium and plutonium, is fundamental to global nuclear non-proliferation efforts (UNODA, 2023). Amid escalating geopolitical tensions, especially in Europe and the Middle East, the threat of illicit SNM trafficking and its potential acquisition by non-nuclear weapon states poses a critical challenge to international security.

Radiation Portal Monitors (RPM) are installed at international border crossings, ports, and secure facilities to prevent the illicit transport of SNM. These stationary detection systems offer passive, continuous radiation monitoring. Each RPM consists of two vertical monitoring panels positioned on either side of the vehicle path. Typical dimensions of RPMs are approximately 4–6 metres in height, 3–4 metres in width, and less than 1 metre in depth. These dimensions ensure that the system can accommodate large vehicles while maintaining the sensitivity required for detecting SNM, which is vital for accurate monitoring without compromising the effectiveness of the system.

Traditionally, neutron detection in RPMs has relied on ^{3}He gas-filled proportional counters, which detect thermal neutrons via the ^{3}He(n,p)^{3}H reaction (Tomanin, Peerani, and Janssens-Maenhout, 2013). These detectors are highly efficient for thermal neutrons, inherently less sensitive to gamma radiation, and non-hazardous. This insensitivity is due to their detection mechanism and the low probability of

gamma-ray interactions with low atomic number (Z) materials such as ^{3}He. The near insensitivity to gamma rays, or the ability to differentiate effectively between neutron and gamma radiation, is crucial for neutron detectors because neutrons are typically emitted alongside gamma rays, creating a mixed radiation field.

However, there are certain disadvantages to the use of ^{3}He-based technology for neutron detection. The probability of neutron capture by ^{3}He decreases with increasing neutron energy, which means that these detectors are less efficient for the direct detection of fast neutrons. Consequently, neutrons must first undergo thermalisation to slow them down to thermal energies before they can effectively be detected by ^{3}He. Thermalisation is typically achieved using a moderator material, such as polyethylene, where successive collisions with hydrogen atoms reduce the neutron's energy.

During thermalisation, information about the original neutron energy, its direction of travel, and the time of emission is generally lost. This loss of information can limit the effectiveness of ^{3}He detectors in applications that require detailed analysis of the characteristics of neutrons (Stromswold et al., 1998). Additionally, concerns over potential shortages of ^{3}He have motivated the development of alternative detector technologies for large-area neutron detectors and RPMs used in nuclear security (Kouzes, Ely, et al., 2010; Kouzes, Lintereur, and Siciliano, 2015).

1.1 Motivation

Given these limitations, there has been significant interest in the development of alternative neutron detection technologies. Organic scintillators, in particular, offer the potential for efficient fast neutron detection without the need for thermalisation.

Fast neutrons can be detected using organic scintillators (Kouzes, Lintereur, and Siciliano, 2015). Organic scintillators are primarily composed of low-Z elements, such as hydrogen and carbon. Hydrogen, in particular, has a high scattering cross-section for fast neutrons, making organic scintillators effective candidates for neutron

detection. The detection mechanism of such scintillators is primarily based on the elastic scattering of neutrons by hydrogen atoms. When a neutron elastically scatters off a hydrogen nucleus (proton), it transfers a portion of its kinetic energy to the recoil proton. This proton then deposits its energy in the scintillator, producing scintillation light. The light emission in organic scintillators is independent of the physical state of the molecule; therefore, organic scintillators can exist in various forms, including crystals, liquids, glasses, and plastics (Knoll, 2000).

Organic scintillators offer several advantages, including hydrogen-rich composition, fast timing, high light output (LO), and the ability to discriminate between neutrons and gamma rays via pulse shape discrimination (PSD) (J.B. Birks, 1964). PSD exploits subtle differences in the shapes of neutron- and gamma-induced pulses, which originate from the scintillation light emitted in prompt (fast) and delayed (slow) components. The prompt component is emitted within nanoseconds of particle interaction, whereas the delayed component is emitted a few hundred nanoseconds later. Neutrons, losing energy more efficiently through elastic scattering, produce a relatively larger delayed component compared to gamma rays, enabling effective particle discrimination.

Over the years, various PSD methods have been developed to exploit these pulse shape differences and maximise the separation between neutron- and gamma-induced pulses. One of the most widely used methods is the Charge Comparison Method (CCM). This method compares the integrals under the pulse over two distinct time intervals, typically referred to as the long and short integrals. The long integral represents the area under the entire pulse, whereas the short integral captures only a portion of the pulse, including part of the decay tail, starting at a defined reference point after the pulse peak. Because neutron pulses decay more slowly than gamma pulses, they produce a larger short integral, enabling discrimination between neutrons and gamma-rays based on this difference (Brooks, 1959; Adams and White, 1978).

The PSD performance of neutron detectors can be quantified using a metric

called the Figure of Merit (FoM). This is given by: $FoM = S/(\delta_{gamma} + \delta_{neutron})$, where S is the separation between the neutron and gamma pulse peaks, and δ_{gamma} and $\delta_{neutron}$ are the full widths at half maximum (FWHM) of the corresponding peaks. Typically, a FoM value greater than 1.27 corresponds to well separated Gaussian distributions considered indicative of effective PSD performance (N. Zaitseva, Rupert, et al., 2012).

Historically, trans-stilbene crystals have been the scintillator of choice for neutron detection due to their superior light output (LO), high hydrogen content, and excellent PSD performance (J.B. Birks, 1964). However, despite advancements in solution growth methods (N. Zaitseva, A. Glenn, et al., 2015), stilbene crystals remain expensive and difficult to grow in large dimensions. They are rarely produced in sizes exceeding 10 cm, with typical sizes ranging from 6 to 8 cm (Budakovsky et al., 2006). Additionally, the material's fragility, attributed to its monoclinic crystal structure (Reddy, Padmanabhan, and Desiraju, 2006), and the anisotropy of its scintillator response (Weldon et al., 2019) pose challenges for its application in large-scale neutron detectors.

Organic liquid scintillators have been used for several decades to detect both fast and thermal neutrons (Brooks, 1979). They provide high LO, fast timing response, and effective PSD, offering performance comparable to organic crystals but without the constraints of crystal growth. Because they lack a crystalline structure, they are less susceptible to radiation damage. They can be manufactured in large quantities, for a range of geometries, and at relatively low cost (Knoll, 2000).

Historically, the industrial use of liquid scintillators was limited by their flammability, as a result of low flash points and material toxicity. However, the development of high flash point, non-toxic liquid scintillators, such as EJ-309, has allowed their use outside of laboratory environments (Lavietes et al., 2012).

Despite these advancements, a common issue with large scintillator cells is the potential for liquid leakage through micro-gaps at joints. This can lead to the formation of undesired bubbles inside the detector cells, which may degrade the

quality of the pulses (Roy et al., 2018). While liquid scintillators can be constructed in large volumes, concerns about handling and field applications — primarily due to leakage risks — remain. These challenges have driven the search for alternative, solid-state scintillators that can be used in large-area field applications as viable replacements for liquid and crystal scintillators without compromising detection performance.

Plastic scintillators with pulse shape discrimination (PSD) capabilities provide a solid-state alternative to traditional organic liquid and crystal detectors for neutron detection. They are cost-effective, physically robust, easy to transport, and can be fabricated in a wide range of geometries — including rods, bars, sheets, and large-area panels. Non-PSD plastic scintillators, such as EJ-200, are already used in RPMs as an alternative to ^{3}He detectors (Corre et al., 2015), while PSD-capable plastics are being explored as a practical, cost-effective option for the detection of Special Nuclear Material (SNM) (Bertrand et al., 2015) and for future use in RPMs (Ellis, Duroe, and Kendall, 2016).

Early efforts to develop efficient PSD in plastics resulted in either unstable materials (Brooks, Pringle, and Funt, 1960) or an inability to achieve effective discrimination between neutron- and gamma-induced signals (Vance et al., 2010). Consequently, the prevailing view was that plastics inherently lacked PSD capabilities, a conclusion attributed to their, "low proportion of delayed component in their scintillation decays" (Brooks, 1979). However, this perspective shifted in 2012 when Lawrence Livermore National Laboratory (LLNL) in the United States successfully developed the first plastic scintillators with efficient PSD.

One key factor contributing to the earlier view that plastics were incapable of PSD was the low concentration of scintillating dyes typically used in their preparation. To address this, LLNL researchers increased the concentration of a highly soluble scintillation dye, 2,5-diphenyloxazole (PPO), leading to the successful development of PSD-capable plastics. Studies demonstrated that the PSD mechanisms were remarkably similar to those observed in liquid and crystal

scintillators. Small-scale tests by LLNL showed that the light output (LO) and PSD performance of these plastics were comparable to liquid scintillators of the same size and shape (N. Zaitseva, Rupert, et al., 2012).

Despite significant progress, when the first commercially produced PSD plastics became available at larger sizes in February 2012 through Eljen Technologies, under the trade name EJ-299, studies reported generally poorer PSD performance of plastics compared to liquids and crystals (Pozzi, Bourne, and Clarke, 2013; Cester et al., 2014; Lawrence et al., 2014; Iwanowska-Hanke et al., 2014).

A key limitation of the first PSD plastics was the deterioration of PSD performance with an increase in the dimensions of the scintillator, primarily due to significant self-absorption of scintillation light. Early testing of 3×3 inch cylindrical EJ-299-33 plastic scintillators demonstrated very poor PSD performance, mainly attributed to low light output (LO). A FoM of 0.86 was reported at an energy window of 300 keV_{ee} (electron equivalent energy) (Nishada, 2014). This value was much poorer than that reported for a 2×2 inch plastic cylindrical scintillator, which gave a FoM of 1.2 for a 300 keV_{ee} window (Iwanowska-Hanke et al., 2014).

In 2018, all versions of EJ-299 were replaced by EJ-276 and EJ-276G, following developments by the Zaitseva group at LLNL (N. P. Zaitseva, A. M. Glenn, Mabe, et al., 2018). These new plastics offered improved physical robustness and long-term optical and scintillation stability over previous versions through compositional modifications (Eljen-Technology, 2017). Although studies have shown that EJ-276 provides better PSD performance than EJ-299-33 (Ngo et al., 2023), organic liquid and crystalline scintillators were found to still exhibit superior PSD capabilities overall (Grodzicka-Kobylka et al., 2020).

For remote radiation detection, large-volume plastic scintillators ($\geq$ 1 m in any direction) offer improved sensitivity due to their increased interaction probability with ionising radiation. Additionally, when implemented in segmented configurations, such detectors can also be useful for localised detection and to support multiplicity analysis for particle identification. However, scaling up to larger

sizes introduces several challenges not typically encountered in smaller scintillators. Structural defects such as cracks, bubbles, and inclusions, as well as optical degradation, such as discolouration and increased opacity, become significantly more detrimental at larger volumes. This is due to enhanced light attenuation, which reduces the amount of light detected by the photodetector (Ford et al., 2021).

1.2 Current Deficiencies

The underlying causes of reduced pulse shape discrimination (PSD) performance in plastic scintillators — compared to liquid and crystalline scintillators — are not yet fully understood. However, several contributing factors have been identified that influence the neutron- and gamma-induced pulse shapes used in PSD analysis to compute the Figure of Merit (FoM). These include scintillator geometry, reflector wrapping, and the location of scintillation photon emission (Hubbard, Paul J Sellin, and Lotay, 2020).

As scintillator volume increases, variations in photon path length lead to inconsistencies in the arrival time distribution of photons at the photodetector. According to Hubbard, these variations introduce additional time constants into the pulse shape, which obscure the intrinsic decay time differences between neutron- and gamma-induced pulses. The cumulative effect is a degradation in PSD performance.

This performance deterioration poses a major challenge for nuclear security applications, where large-area plastic scintillators are being explored as cost-effective alternatives to ^{3}He-based neutron detectors (Ellis, Duroe, and Kendall, 2016). However, the scalability of PSD-capable plastics remains a significant constraint, as changes in geometry have been shown to adversely affect their discrimination capability.

For example, the impact of geometry on PSD performance has been investigated using EJ-299-34 scintillators over a range of sizes, from small cubic samples to larger flat panels with high aspect ratios. These studies showed that as one dimension of

the scintillator increases, while the other dimensions remain fixed, PSD performance degrades. Representative samples included a small cubic piece $(25 \times 25 \times 15)$ mm and a larger flat panel $(120 \times 25 \times 15)$ mm. The results demonstrated a measurable reduction in the Figure of Merit (FoM) as the scintillator transitioned from cubic to flat-panel geometry. At an energy threshold of 1 $\mathrm{MeV_{ee}}$ (electron-equivalent energy), the larger sample exhibited a FoM approximately 20% lower than that of the smaller cubic sample (Payne et al., 2016).

In addition to geometry, several other factors have been found to influence the shape of neutron- and gamma-induced pulses in plastic scintillators, which can in turn affect pulse shape discrimination (PSD) performance in some cases. These factors include multiple dye interactions within the scintillator material (N. P. Zaitseva, A. M. Glenn, Carman, et al., 2020), photodetector positioning, reflector material and surface finish (M. Ebrahimi Shohani et al., 2017), reflector wrapping techniques (Taheri and Peyvandi, 2017; Ghorbani et al., 2018), and digitisation of the scintillation signal using readout electronics (Hellesen et al., 2013).

1.3 Research Aims and Approach

The aims of this research are to use the Monte Carlo toolkit Geant4 to generate neutron- and gamma-induced temporal pulse shapes of EJ-276, a plastic scintillator with pulse shape discrimination (PSD) capabilities, and to investigate how key detector parameters affect pulse shape and PSD performance.

Specifically, this work addresses the following research questions:

1. How do variations in scintillator geometry and length affect pulse shapes and PSD performance?

2. How do variations in the optical surface properties of the scintillator influence pulse shapes and PSD performance?

3. How do different levels and types of photodetector noise affect pulse shapes

and PSD performance?

4. How accurately can Geant4 simulate the temporal pulse shapes of EJ-276 scintillation detectors?

Geant4 was chosen because of its widespread use in radiation detector simulations and its demonstrable capability to model the generation, transport, and collection of optical photons in both organic and inorganic scintillation detectors. These features make Geant4 particularly well-suited for characterising and optimising scintillator performance. Furthermore, its continuous development, open-source availability, and comprehensive validation record enhance its suitability for this research.

EJ-276 was selected due to its commercial availability and its status as a PSD-capable plastic scintillator that has been proposed as a viable alternative to liquid scintillators for homeland security applications (Ellis, Duroe, and Kendall, 2016).

Monte Carlo simulations provide a robust and efficient framework for systematically investigating how various detector parameters — such as scintillator geometry, dimensions, and surface finish — affect the shapes of neutron- and gamma-induced pulses. Compared to experimental approaches, which are often resource-intensive and time-consuming, simulations offer a rapid, cost-effective means of evaluating potential detector design modifications prior to physical fabrication. By exploring the parameters that most significantly affect pulse shape characteristics — and, by extension, PSD performance — this study aims to provide insight into the underlying factors contributing to reduced PSD performance. Such insights are essential for guiding the design and optimisation of next-generation plastic scintillators with enhanced PSD capabilities for advanced neutron detection applications.

Furthermore, simulations enable the isolation of the effects of individual detector parameters by allowing each to be systematically varied and decoupled from external influences known to affect pulse shapes, such as photodetector response and data acquisition electronics. This makes it possible to examine light pulse formation in detail and to assess the specific contributions of individual factors to overall pulse shape discrimination (PSD) performance. In experimental

setups, meaningful comparisons of PSD performance between detectors are often complicated by variations in detector geometry, photodetector type, readout electronics, and the specific PSD algorithms employed. Simulations therefore offer a controlled, reproducible environment for investigating the fundamental mechanisms that influence PSD capability.

1.4 Novelties of this Research

Geant4 has long been used for simulating the generation, transport, and collection of optical photons for applications involving the characterisation and optimisation of many types of radiation detectors (Khodaei et al., 2023), including plastic scintillation detectors (Archambault et al., 2003; Li-Ming et al., 2004; Riggi et al., 2010; Ghadiri and Khorsandi, 2015). However, prior studies often omitted key aspects of scintillator behaviour — specifically, the full set of known decay time constants, their particle-type dependencies, and the relative intensities of each component. This omission was identified as a limitation of Geant4 when simulating the pulse shapes of scintillation detectors with more than two decay time components (Comrie et al., 2014).

This limitation stemmed largely from constraints in earlier versions of Geant4. Before version 10.7, users could specify at most two decay time constants for particle-independent yields, and only a single constant for particle-dependent yields — restricting the accuracy of pulse shape simulations for scintillators with more complex decay profiles.

With the introduction of enhanced decay time modelling in Geant4 version 10.7 and later, it is now possible to define multiple decay time constants and their corresponding relative intensities. This improvement allows for the possibility of more accurate simulations of PSD-capable plastic scintillators, such as EJ-276, which typically exhibit two or more decay components that vary depending on whether the interacting particle is a neutron or a gamma-ray.

The pulse shapes produced by plastic scintillators result from the convolution of scintillation emission, light transport within the scintillator, and the response of the photodetector and readout electronics. The simulations presented in this thesis uniquely investigate the pulse shapes *prior* to conversion and amplification by the photodetector and electronics — a stage that is difficult to isolate experimentally due to numerous uncontrollable factors. By capturing the pulse at this intermediate stage, the simulations enable detailed analysis of how specific processes influence the intrinsic scintillation pulse shape before photodetector and electronic effects are introduced.

This work extends the simulation-based research initiated in (Hubbard, Paul J Sellin, and Lotay, 2020), which combined experiments and simulations to study the impact of light transport on the PSD performance of plastic scintillators. This work identified factors which impact the pulse shapes output from plastic scintillators. In contrast, the present study is entirely simulation-based, allowing for isolation and systematic investigation of specific parameters to evaluate their direct influence on pulse shape — critical for understanding and optimising PSD performance.

Leveraging the new capabilities of Geant4, this research systematically explores how variations in key detector parameters affect pulse shapes and PSD performance by performing simulated PSD on the generated light pulses. Additionally, this study examines the impact of noise — an important factor neglected in previous work — and investigates specific surface types and geometries that can produce artefacts distorting the light pulse shapes. The case in which no explicit optical surface is applied to the scintillator is also considered, a scenario likely encountered by new Geant4 users due to the steep learning curve associated with modelling optical materials in Geant4. Beyond improving simulation accuracy, this work further evaluates the broader capabilities and limitations of Geant4 in simulating PSD-capable plastic scintillators.

Several previous studies have made progress in related areas. Hartwig and Gumplinger, for example, simulated pulse shapes and PSD performance from EJ-309

— a liquid scintillator with three known decay time components — but included only the first two in their model. While the simulated pulse decay tails agreed well with experimental data, rise times were poorly reproduced, partly due to the exclusion of photodetector timing effects (Hartwig and Gumplinger, 2014). To better match experimental pulse shapes, Liao and Yang convolved Geant4 generated pulses from liquid scintillators with the single-electron time response of a photomultiplier tube (PMT), achieving good agreement between experiment and simulation (Liao and Yang, 2014).

Similarly, Ogawara and Ishikawa modelled pulse shapes from inorganic scintillators by convolving Geant4-derived photon arrival times with experimentally measured PMT response functions. Their results reproduced experimental data across various scintillator geometries, although the PMT response function was obtained using a plastic scintillator, complicating efforts to isolate the PMT's intrinsic behaviour. Nevertheless, their work demonstrated that Geant4 can reliably reproduce experimental pulse shapes for a range of scintillator types and configurations (Ogawara and Ishikawa, 2016).

Most previous simulation studies have focused primarily on detector characterisation and optimisation. Few studies, however, have first simulated neutron- and gamma-induced pulse shapes and then used these pulses to perform PSD, in order to examine how variations in key detector parameters affect both the pulse shapes and PSD performance in plastic scintillation detectors.

In summary, this research builds upon and addresses limitations in prior studies by:

- Utilising the enhanced decay time modelling available in recent versions of Geant4.

- Systematically analysing the impact of key detector parameters on the pulse shapes and PSD performance of EJ-276, a commercially available, PSD-capable plastic scintillator.

- Investigating the impact of photodetector noise on the pulse shapes and subsequent PSD performance of EJ-276.

Chapter 2

Background

2.1 Radiation Types and Sources

Radiation is defined as the emission or transmission of energy in the form of waves or particles through a medium. It can be broadly categorised as either ionising or non-ionising, depending on its energy. Generally, radiation with an energy above 10 eV is classified as ionising because this is the minimum amount of energy required to produce ionisation in typical materials (Knoll, 2000). Types of ionising radiation include: alpha particles, beta particles, neutrons, gamma rays, and X-rays. In contrast, non-ionising radiation includes examples such as visible light, infrared, microwave, and radio waves.

2.1.1 Radioactive Decay

Radioactivity was first discovered in 1896 by French physicist Henri Becquerel. During his experiments with uranium salts, Becquerel observed that these materials could fog photographic plates, even in the absence of light, revealing a previously unknown form of radiation. This discovery was made almost entirely by accident while Becquerel was investigating phosphorescence. Following Becquerel's findings, Marie and Pierre Curie conducted further research into radioactivity. This led to the discovery of additional radioactive elements such as polonium and radium (Jönsson,

2021).

Unstable atomic nuclei are described as radioactive. Radioactive decay is the process whereby these unstable nuclei emit radiation to reach an energetically stable state. The forms of radiation emitted during radioactive decay include: alpha particles, beta particles, gamma rays, and other secondary radiation. Radioactive decay is a stochastic process, which means it is not possible to predict when any one particular atom will decay. The activity of a radioactive sample is defined as its rate of decay and is given by the differential equation:

$$\frac{dN}{dt} = \lambda N \tag{2.1}$$

Here, N is the number of radioactive nuclei at a given time t, and λ is the decay constant. Equation 2.1 is the law of radioactive decay.

The time dependence of radioactive decay is expressed in terms of its half-life ($t^{\frac{1}{2}}$). This represents the time required for atoms in a given radioactive sample to decay to half of their initial value. The half-life varies greatly between different radioisotopes and can range from fractions of a second to millions of years (Choppin et al., 2013). On integrating Equation 2.1 we get:

$$N = N_0 e^{-\lambda t} \tag{2.2}$$

Here, N_0 is the initial number of radioactive atoms in a given sample at $t = 0$. The half-life can then be given by:

$$t^{1/2} = ln(2/\lambda) \tag{2.3}$$

where $1/\lambda$ is equal to τ, the mean lifetime. This is defined as the average time that a radioactive nucleus remains intact before decaying.

Beta Decay

Beta decay is a radioactive decay process which occurs when the ratio of protons and neutrons in an atomic nucleus is unbalanced. This process is mediated by the weak nuclear force, which makes it a relatively slow process.

There are two types of beta decay: negative beta decay and positive beta decay. Negative beta decay results in the emission of a beta particle (β) in the form of a fast-moving electron, while positive beta decay results in the emission of a β-particle in the form of a fast-moving positron. In both types of beta decay, the mass number of the atom remains the same, but the atomic number changes. The equations for negative and positive beta decay are given by Equations 2.4 and 2.5 for negative and positive beta decay, respectively.

$$ {}^{A}_{Z}\mathrm{X} \rightarrow {}^{A}_{Z+1}\mathrm{Y} + \beta^{-} + \bar{\nu} \tag{2.4} $$

$$ {}^{A}_{Z}\mathrm{X} \rightarrow {}^{A}_{Z-1}\mathrm{Y} + \beta^{+} + \nu \tag{2.5} $$

where A is the mass number and Z is the atomic number. X represents the parent nucleus, and Y is the daughter nucleus following nuclide conversion. β^{-} is a fast electron and β^{+} is a positron. ν is a neutrino, and $\bar{\nu}$ is an anti-neutrino.

Negative beta decay (β^{-}) occurs in nuclei that have an excess of neutrons. In this process, a neutron is converted into a proton, accompanied by the emission of a fast electron (β-particle) and an antineutrino.

Conversely, positive beta decay (β^{+}) occurs in nuclei that have an excess of protons. In this process, a proton is converted into a neutron, accompanied by the emission of a positron (β-particle) and a neutrino (Nagy and N.M., 2018).

Alpha Decay

Alpha decay is a form of radioactive decay in which an atomic nucleus spontaneously emits an alpha particle, which is the nucleus of a ${}^{4}He$ atom. This process causes

the original nucleus to lose two protons and two neutrons, transforming it into a different atomic nucleus with an atomic number reduced by two and a mass number reduced by four. The formula for alpha decay is given by Equation 2.6.

$$ {}^{A}_{Z}\mathrm{X} \rightarrow {}^{A-4}_{Z-2}\mathrm{Y} + {}^{4}\mathrm{He} \tag{2.6} $$

where A is the mass number, Z is the atomic number, X represents the parent nucleus, and Y is the daughter nucleus formed after the emission of the alpha particle.

Alpha decay primarily occurs in heavy nuclei such as uranium, thorium, and radium, which undergo this process to increase nuclear stability by reducing both their mass number and atomic number. The nuclear strong force, which binds protons and neutrons together within the nucleus, is typically much stronger than the repulsive Coulomb force between the positive charged protons. However, the strong nuclear force has a very short range, whereas the Coulomb force, which is proportional to the square of the charge (Z^2), acts over an infinite range.

As nuclei grow larger, the strong force, which is proportional to the number of nucleons (protons and neutrons) are unable to counterbalance the increasing Coulomb repulsion between protons. In nuclei with around 210 or more nucleons, the balance between forces becomes unstable. The emission of an alpha particle allows the nucleus to reduce the Coulomb repulsion to achieve a more energetically stable state.

Electron Capture

Electron capture is a process whereby a proton-rich nucleus of an electrically neutral atom absorbs an inner atomic electron, usually from the K or L electron shells. This process serves the same purpose as positive beta decay since it converts a proton to a neutron and also causes the emission of an electron neutrino.

2.1.2 Sources of Gamma Radiation

Unlike X-rays, which originate from interactions involving electrons outside the atomic nucleus, gamma rays are produced by processes within the atomic nucleus. X-rays are emitted by electron transitions or high-energy electron interactions, while gamma rays result from nuclear reactions, radioactive decay, or particle interactions such as annihilation events.

Gamma radiation is a highly penetrating form of ionising radiation that can be harmful to biological tissues. It has frequencies above 3×10^{19} Hz and the shortest wavelengths in the electromagnetic spectrum, typically less than 10^{-10} m.

Natural sources of gamma rays include radioactive decay processes, secondary radiation resulting from cosmic rays interacting with Earth's atmosphere, and the spontaneous emission of gamma rays from certain isotopes. Artificial sources of gamma radiation arise from nuclear fission in reactors and high-energy physics experiments.

Extremely high-energy gamma rays have also been detected from astronomical objects, such as supernovae, neutron stars, and black holes. On Earth, natural sources of gamma radiation include isotopes such as Potassium-40 and Uranium-238, which are present in the Earth's crust.

Gamma Decay

Gamma decay occurs after other forms of radioactive decay, such as alpha and beta decay. When a radioactive nucleus decays by emitting an alpha or beta particle, the resulting daughter nucleus is often left in an excited state. To transition to a lower energy state, the nucleus emits a gamma-ray photon. In gamma decay, unlike alpha and beta decay, both the atomic number and the mass number of the nucleus remain unchanged.

The energy of the gamma radiation emitted corresponds to the difference in energy between the excited nuclear state and the ground state. Gamma decay can also occur after nuclear processes such as neutron capture, nuclear fission, or nuclear

fusion.

For gamma radiation with energies below approximately 2.8 MeV, commonly used laboratory sources can be employed. These sources are often used for the calibration of gamma detectors due to their well-defined and stable energy emissions. A common method to produce such gamma radiation is through beta decay, where the parent radionuclide decays, leaving the daughter nuclei in an excited state. As these nuclei de-excite, gamma radiation is emitted.

Some of the most commonly used laboratory gamma-ray sources for calibration purposes include ^{22}Na, ^{60}Co, and ^{137}Cs.

While the emitted gamma rays have a half-life characteristic of the parent ^{60}Co nucleus, the energy of the gamma radiation is due entirely to the difference in energy between the nuclear states of the daughter ^{60}Ni nucleus.

If gamma rays with energies above approximately 2.8 MeV are required, these can be created through various nuclear reactions that produce nuclei in higher energy states. One such reaction is shown in Equation 2.7.

$$^{4}_{2}\alpha + ^{13}_{6}\mathrm{C} \rightarrow ^{16}_{8}\mathrm{O}^{*} + ^{1}_{0}\mathrm{n} \tag{2.7}$$

In this reaction, the $^{16}_{8}\mathrm{O}^{*}$ is in an excited state with an energy of 6.130 MeV above its ground state. This reaction can be exploited by combining a radioisotope that decays by alpha emission with an appropriate target material, such as carbon or beryllium.

Gamma rays are also commonly emitted after the absorption of thermal neutrons by nuclei. Sources of thermal neutrons used to produce gamma rays include intense beams from nuclear reactors or accelerators, as well as weaker fluxes from moderated radioisotope neutron sources.

2.1.3 Sources of Neutron Radiation

Typically, sources of neutrons are either from spontaneous fission or from nuclear reactions in which the incident particle is produced by conventional radioactive decay processes. Neutrons can also be generated in large-scale devices such as nuclear fission and fusion reactors, as well as high-energy particle accelerators, including spallation sources.

Spontaneous Fission

Spontaneous fission is a form of radioactive decay that only occurs in certain transuranic isotopes with very large mass number. In spontaneous fission, the atomic nucleus splits into two or more smaller nuclei. In addition to the emission of gamma rays, fission fragments, and decay products, spontaneous fission emits neutrons. For each fission event, several fast neutrons may be emitted; hence, samples of isotopes known to undergo spontaneous fission can be used as a neutron source. Isotopes used as neutron sources are usually encapsulated in a thick casing to ensure only fast neutrons and gamma rays are emitted, excluding other products of fission.

One of the most commonly used neutron sources which undergoes spontaneous fission is Cf−252. This has a half-life of approximately 2.638 years. The dominant decay mechanism for Cf−252 is α-decay, with neutrons emitted by spontaneous decay in approximately 3% of decays. α-decay is the dominant form of radioactive decay for Cf−252, with α-emission around 32 times that of spontaneous fission. The neutron yield from Cf−252 is approximately 0.116 neutrons per second per Becquerel (Bq), which translates to 2.30×10^6 neutrons per microgram of sample. On average, 3.8 neutrons are emitted in each fission from Cf−252, and it produces an average of 0.8 gamma-ray photons per fission. Neutrons emitted from this isotope span a range of energies from thermal to a few hundred keV. The neutron energy spectrum is similar to that of a fission reactor, and the most probable energy is 0.7 MeV, with an average energy of 2.1 MeV (Martin, Knauer, and Balo, 2000).

Nuclear Reactions

Neutrons can be produced when alpha particles produced through radioactive decay strike certain light isotopes. These include the isotope beryllium and oxygen, which are described as the "target" in such reactions. Hence, small, self-contained neutron sources can be produced through the mixing of an alpha-emitter, such as radium, polonium, or americium, with a low-atomic weight isotope. This is often achieved by blending two elements together as powders. A common example of these sources is that of Americium-Beryllium (AmBe).

2.2 Interactions with Matter

Understanding how different types of radiation interact with matter is fundamental to the operation of radiation detectors. Radiation can be categorised as either ionising or non-ionising, and further divided into charged or uncharged types. Examples of charged radiation include: protons, electrons, and alpha particles. Examples of uncharged radiation include: gamma rays, neutrons, and X-rays.

2.2.1 Interactions of Charged Particles

When charged particles penetrate matter, they primarily interact with the electrons and nuclei in the material through the electromagnetic force. For charged particles with energies of 1 MeV or higher, this energy is significantly greater than the binding energy of the electrons in the atom. Therefore, as a first approximation, matter can be modelled as a collection of free electrons and stationary nuclei (Tavernier, 2010).

In this context, the penetrating particle experiences an electromagnetic force due to the electromagnetic fields of the electrons and nuclei, undergoing both elastic and inelastic collisions. During these interactions, the particle can lose energy and change direction.

For a proton interacting with an atomic nucleus, the proton can transfer a portion of its energy to the nucleus and change direction; in some instances, the proton can

even bounce backwards. Since the proton is much lighter than most nuclei, the amount of energy transferred during these collisions is typically small. Using non-relativistic kinematics and energy-momentum conservation, it can be shown that the maximum amount of energy transferred ($\Delta Emax$) during the elastic collision of a proton with mass m with a nucleus of mass M is given by:

$$\Delta E_{\max} = \frac{1}{2}mv^2 \left(\frac{4mM}{(m+M)^2} \right) \tag{2.8}$$

If the mass of the proton, m, is much smaller than the mass of the nuclei, M, we get:

$$\Delta E_{\max} \simeq \frac{1}{2}mv^2 \left(4\frac{m}{M} \right) \quad \text{for } m \ll M \tag{2.9}$$

In the limit where the mass of the nucleus approaches infinity, the energy transfer becomes negligible.

The elastic scattering of α-particles off nuclei was first demonstrated by Ernest Rutherford in 1911, through his observations of how a beam of α-particles was scattered after striking a thin piece of gold foil (Rutherford, 2012). This experiment led to the discovery of the atomic nucleus and the development of scattering techniques in particle physics. However, for radiation detection purposes, interactions with nuclei are relatively rare compared to interactions with electrons. Therefore, charged particle detectors primarily rely on interactions with electrons to produce a detectable response.

For an interaction between a proton and an electron, the proton can transfer a considerable amount of energy to the electron. However, because the proton has a much greater mass than the electron, the direction of the proton can only be slightly altered during this interaction. Therefore, most of the energy loss experienced by the proton is a result of collisions with electrons, while significant changes in direction are due to collisions with atomic nuclei.

Heavily charged particles, such as α-particles, interact with matter primarily

through Coulomb forces between the positively charged α-particles and the negatively charged orbital electrons of the atoms in the material. When the α-particle penetrates the material, it interacts simultaneously with many electrons. In any one interaction, an electron experiences an impulse from the α-particle passing close by. Depending on how close the two particles get, this force may be sufficient to raise the electron to a higher energy level within the atom of the material, a process known as excitation. Alternatively, if the α-particle transfers enough energy, it may completely liberate the electron from the atom to create an ion, a process known as ionisation.

When a charged particle transfers its energy to an electron during an encounter, the energy loss results in a decrease in the kinetic energy of the charged particle. Since kinetic energy is proportional to the square of the particle's velocity, this energy loss results in a decrease in the charged particle's velocity. With each encounter, the charged particle loses a portion of its energy to the electron, causing the particle to slow down in the material.

Since at any given time the charged particle is interacting with many electrons through multiple scatterings, its velocity will continuously decrease until the particle is stopped in the material. While most of the electrons only receive a small amount of energy, some acquire enough energy to travel larger distances in the material. These high-energy electrons can have sufficient energy to excite or ionise atoms in the medium.

Stopping Power

The amount of energy lost by a charged particle as it penetrates matter is quantified by the linear stopping power. The linear stopping power, S, for charged particles traversing a material is given by:

$$S = -\frac{dE}{dx} \tag{2.10}$$

Here, dE is the differential energy loss of the particle and dx is the corresponding

differential path length. The quantity $-\frac{dE}{dx}$ is also known as the specific energy loss of the particle along its track. For charged particles, S, increases as the velocity of the particle is decreased.

The classical expression describing the mean rate of energy loss (stopping power) of charged particles travelling through a medium, due to their interactions with the electrons of the material, is given by the Bethe-Bloch equation. This equation is used to calculate the stopping power of moderately relativistic charged particles with intermediate and high energies. At lower energies, the accuracy of the Bethe-Bloch equation decreases, and various corrections must be applied due to the impact of other effects, including nuclear stopping power and electron capture. The Bethe-Bloch equation is given by:

$$-\frac{dE}{dx} = \frac{4\pi e^4 z^2}{m_0 v^2} NB \tag{2.11}$$

$$B = Z\left[\ln\left(\frac{2m_0v^2}{I}\right) - \ln\left(1 - \frac{v^2}{c^2}\right) - \frac{v^2}{c^2}\right] \tag{2.12}$$

Here, v denotes the particle velocity, z the charge number, e the elementary charge, m_0 the electron rest mass, c the speed of light in vacuum, N the number density of atoms, and Z the atomic number of the material. The quantity I represents the mean excitation and ionisation potential of the material, treated as an experimentally determined parameter for each element. For non-relativistic charged particles $v \ll c$, the equation simplifies, and the term $\frac{v^2}{c^2}$ becomes less significant. This equation is generally valid for a wide range of charged particles provided their velocity remains much larger compared to the velocities of the orbital electrons in the atoms of the material.

2.2.2 Interactions of Uncharged Particles

In the previous section, the interaction of charged radiation with matter was described. It was noted that when an incoming charged particle interacts with

a material, it simultaneously interacts with all the electrons and nuclei along its path. Although the energy transferred in any single interaction is typically small, the cumulative effect of multiple interactions causes the charged particle to gradually lose energy and slow down as it collides with electrons and nuclei in the material. These collisions lead to excitation and ionisation. It is the cumulative effect of many interactions that significantly impacts the particle's energy loss.

Conversely, uncharged radiation interacts very differently with matter, which impacts how this form of radiation is detected. Uncharged radiation includes gamma rays, neutrons, and X-rays. The following section will focus on how gamma rays and neutrons interact with matter. Since this radiation is uncharged, it is unaffected by the Coulomb force and can travel large distances in matter before any significant interaction takes place. For example, gamma rays and X-rays are capable of travelling through many centimetres of lead or concrete before an interaction occurs. Neutrons can penetrate even deeper since they primarily interact with atomic nuclei, however their penetration depth depends on their energy and the type of material they are passing through. Uncharged radiation is often referred to as indirectly ionising because radiation detection methods rely on the detection of secondary radiation, such as charged particles.

The primary distinction in detection methods arises from the different interaction mechanisms of charged versus uncharged radiation with matter. Charged particles cause direct ionisation and excitation, leading to measurable energy loss, while uncharged radiation requires secondary processes to produce detectable signals.

2.2.2.1 Gamma Radiation

Gamma rays and X-rays are both forms of high-energy, ionising radiation with correspondingly short wavelengths. There is some overlap in the energies of gamma rays and X-rays, but a key distinction between the two forms of radiation lies in their origin. X-rays are emitted by excited atoms, while gamma radiation is emitted by excited nuclei. Their higher photon energies mean they can penetrate more deeply

into materials, enabling their use in gamma-ray tomography applications, among other uses. Gamma rays originate from the radioactive decay of atomic nuclei due to transitions in nuclear energy levels. The difference in energy between these levels is emitted as gamma rays.

Gamma rays are uncharged and therefore are unaffected by the electromagnetic force that governs the energy loss of charged particles. Unlike charged particles such as alpha particles, gamma rays are indirectly ionising. This means they must first be converted to secondary, charged particles for ionisation to occur, and these secondary particles are detected through radiation detection methods. When this form of radiation interacts with matter, it primarily interacts with the electrons of the material rather than the atomic nuclei. In these interactions, the gamma ray either disappears completely or is scattered at a significant angle. What we detect are the secondary particles created in these processes.

A beam of gamma rays will be attenuated in intensity but not in energy. The probability of absorption of a gamma ray when it passes through matter is proportional to the thickness of the layer, the density of the material, and the absorption cross-section of the material. The total absorption shows an exponential decrease of intensity with distance travelled in the material. This is given by the equation:

$$I(x) = I_0 e^{-\mu x} \tag{2.13}$$

Here, x is the thickness of the material from the incident surface, $\mu = \eta\sigma$ is the absorption coefficient (measured in cm^{-1}), η is the number of atoms per cm^3 of the material (atomic density), and σ is the absorption cross section in cm^2. While gamma rays can interact with matter in many different ways, three key processes are important for radiation detection.

Gamma rays interact with matter through three primary processes: photoelectric absorption, Compton scattering, and pair production. These interactions result in

either the full or partial transfer of gamma-ray energy to the electrons in the detector medium. As a consequence of these interactions, the gamma ray photon will either be completely absorbed or scattered at a significant angle. This outcome contrasts with that of charged particle interactions with matter, where the particle continuously slows down due to multiple interactions. The relative probability of each process depends on the energy of the gamma ray and the atomic number of the material. These three processes will be described in more detail in the next subsection.

Photoelectric Absorption

In photoelectric absorption, a gamma ray photon interacts with an electron bound within an atom and transfers all its energy to this electron. As a result, the electron is ejected from one of the atom's electron shells, becoming what is known as a photoelectron. The photoelectric effect involves the atom as a whole because the energy of the photon must overcome the binding energy holding the electron in its shell. Consequently, this process cannot occur with free electrons, as the interaction requires the presence of an atomic electron bound within the atom's electron shells. For gamma rays with significant energy, the electron is most likely to be ejected from the most tightly bound shell, typically the K-shell, although electrons from other shells can also be ejected depending on the photon's energy and the atomic number of the material.

The energy of the photoelectron is given by:

$$E_e = E_\gamma - E_b \tag{2.14}$$

- E_e: The kinetic energy of the photoelectron.
- E_b: The binding energy of the electron in its original shell.
- E_γ: The energy of the incident gamma ray photon. In terms of photon frequency, this is given by $E_\gamma = hv$, where h is Plank's Constant and v is the frequency of the photon.

Equation 2.14 shows that the kinetic energy of the photoelectron is equal to the energy of the incident gamma ray photon minus the original binding energy of the electron in its shell. In this interaction, most of the energy of the gamma ray photon is transferred to the photoelectron.

The photoelectric absorption process is the predominant interaction mechanism for gamma rays of relatively low energy. The process is enhanced for materials of high atomic number, Z. This dependence on the atomic number of the material is the reason why materials of high-Z are used for gamma radiation shielding in radiation protection.

Compton Scattering

Compton scattering involves an interaction between an incident gamma ray photon and an electron in a material, such as that of a detector medium. During this interaction, the gamma ray transfers a portion of its energy to a stationary electron, which is then referred to as the recoil electron. This interaction results in the deflection of the gamma ray through an angle, θ, relative to its original direction. In this process, all scattering angles are possible; therefore, the energy transferred to the recoil electron can vary between zero and a significant fraction of the original gamma ray energy. Compton scattering is the predominant interaction mechanism for gamma rays with energies typical of those from standard laboratory radioisotopes.

For small scattering angles, very little energy is transferred. Since the probability of Compton scattering per atom depends on the number of electrons available as scattering targets, the probability of this process increases linearly with atomic number, Z. The probability additionally decreases with increasing energy. The dependence on energy can be described by the Klein-Nishina formula. Compton scattering is the dominant process for intermediate gamma-ray energies.

Pair Production

Pair production is the predominant interaction mechanism for highly energetic gamma rays and involves the creation of an electron-positron pair. The probability of this process increases significantly for photon energies above several MeV. While it competes with the photoelectric effect and Compton scattering at lower energies, pair production dominates at higher photon energies. Consequently, pair production is only observed for gamma rays with sufficient energy.

This interaction cannot occur in empty space; it would be impossible due to lack of conservation of energy and momentum. The reaction must take place in the strong electric field of the nucleus so the nucleus can take up momentum, and in this way energy and momentum can be conserved and the reaction becomes energetically possible.

The process of pair production becomes energetically possible only when the incoming energy of the gamma ray photon exceeds a threshold of 1.022 MeV. This corresponds to the combined rest-mass energy of the electron-positron pair created in the process. Pair production can only occur in the vicinity of an atomic nucleus, as the nucleus is required to conserve momentum during the interaction. In this process, the gamma ray photon disappears and is replaced by an electron-positron pair. Any excess energy carried in by the incident gamma ray above the 1.022 MeV threshold required for creation of the pair, is converted to kinetic energy, which is shared between the electron-positron pair.

The positron will annihilate after slowing down in matter due to interactions with charged particles. This annihilation results in the production of two annihilation photons, which are secondary particles generated from the original pair production interaction.

There is no straightforward equation describing the probability of pair production per nucleus, but the probability of pair production increases with the energy of the gamma ray and also the magnitude varies as approximately the square of the atomic number, Z, of the nearby atom.

2.2.2.2 Neutrons

Neutrons were first discovered in 1932 by James Chadwick (Chadwick, 1932). They are subatomic particles similar in size to protons but have a rest mass of approximately 1.675×10^{-27} kg. Unlike protons, neutrons carry no electric charge, meaning they do not interact with matter via the Coulomb force — the dominant energy loss mechanism for charged particles. Their lack of charge allows neutrons to easily penetrate even dense materials such as lead, without significant attenuation, making them difficult to detect. This property has enabled the use of neutrons in imaging applications, such as neutron tomography (Brenizer, 2013), where traditional radiations like gamma rays and X-rays cannot adequately penetrate the material.

When neutrons do interact, it is with the atomic nucleus as a consequence of the strong force. Neutrons interact via scattering and absorption reactions. This results in the neutron either disappearing completely and been replaced by one or more secondary radiations, or in scattering reactions where the direction or energy of the neutron is significantly altered. In contrast with gamma ray reactions, the secondary radiations produced as a result of neutron interactions are almost always heavily charged particles. These particles may be produced as either a result of neutron-induced nuclear reactions or they may be the nuclei of the absorbing material itself, which have gained energy as a result of neutron collisions.

Neutrons may be categorised as either fast or thermal, depending on their energy, and this categorisation is important when it comes to both how the neutrons will interact with matter and the methods employed for neutron detection. The type of reaction depends crucially on a variety of factors, as detailed below. This includes the energy of the neutrons and the density of the material through which they pass.

Fast Neutrons

Neutrons produced from fission and neutron sources typically have energies from keV to MeV and are referred to as fast neutrons. The principal nuclear interaction

for fast neutron detection is elastic scattering from light nuclei. In elastic scattering, the neutron transfers a portion of its kinetic energy to the atomic nucleus, resulting in a recoil nucleus that can then be detected. Since neutrons and protons are of comparable mass, the largest energy transfer for this reaction occurs between a neutron and a hydrogen nucleus. It is this proton recoil reaction which forms the basis of the majority of fast neutron detectors (Michael F. L'Annunziata, 2016).

Thermal Neutrons

Elastic scattering from nuclei results in fast neutrons slowing down to thermal energies; that is, the energy at which they are in thermal equilibrium with their surroundings. At room temperature, thermal neutrons have an average energy of 0.025 eV (Geist, Santi, and Swinhoe, 2024). The reduced speed of thermal neutrons results in very little energy being imparted to recoil nuclei during further elastic scatterings. For this reason, the scattering reaction cannot be used as the basis of thermal neutron detection. Instead, the nuclear reaction of importance for the detection of thermal neutrons is neutron capture. This involves the absorption of a neutron by an atomic nucleus to create an unstable compound nucleus. This then de-excites, emitting secondary charged particles which can be directly detected.

Neutron capture cross sections provide us with information about the probability that a neutron will interact with a given isotope via neutron capture. This probability decreases with increasing neutron energy and is highest for neutrons in the thermal energy range. Certain isotopes, including ^{6}Li and ^{10}B have large neutron capture cross sections for thermal neutrons. These isotopes are often incorporated into scintillators to enable thermal neutron detection, and are referred to as loaded scintillators.

Detection Challenges

While advantageous for neutron imaging purposes, the charge neutrality of neutrons poses a challenge for their detection because, unlike charged particles such as protons and electrons, neutrons are indirectly ionising. Their detection therefore relies on

the creation of secondary charged particles.

Gamma rays are often emitted concurrently with neutrons in many nuclear processes, resulting in a mixed field of neutrons and high-energy photons. This complicates the unambiguous detection of neutrons, particularly when using organic scintillation detectors that are sensitive to both radiation types. Since gamma rays and neutrons can produce overlapping pulse height spectra in these detectors, relying solely on pulse height spectra for particle identification can lead to misclassification (Tobergte and Curtis, 1991).

An effective neutron detector must convert incident neutrons into a detectable signal in the form of charged particles. It must also either be insensitive to gamma radiation or capable of differentiating between the two types of radiation, and the detection method depends critically on the energy of the incoming neutron (Knoll, 2000).

2.2.2.3 Optical Photons

Optical photons are a form of non-ionising radiation, belonging to the visible part of the electromagnetic spectrum. These photons have energies in the range of a few electronvolts (eV). Specifically, visible light spans from approximately 1.65 eV (for red light) to about 3.1 eV (for violet light). In contrast, ionising radiation such as gamma rays and X-rays typically has energies greater than about 100 eV, often exceeding 1 keV (1000 eV). The higher energy of ionising radiation allows it to remove tightly bound electrons from atoms and molecules, whereas the lower energy of optical photons is insufficient for ionisation.

The lower energy and corresponding longer wavelengths of optical photons, compared to ionising radiation, determine the types of interactions these photons have with matter. Optical photon interactions are therefore generally limited to processes such as absorption, reflection, refraction, and scattering.

The wavelength of optical photons is typically on the order of nanometres (nm), which is much larger than the atomic spacing between nuclei, usually on the order of

picometres (pm). This difference in scale is a key reason why optical photons interact differently with matter compared to ionising radiation. Since their wavelengths exceed atomic spacing, optical photons do not strongly interact with individual nuclei or core electrons. Instead, they primarily interact with outermost electrons, resulting in non-ionising effects.

There are several mechanisms through which optical photons interact with matter, and these are governed by both the wavelength of the light and the material properties. These interaction processes will be described in more detail below.

Absorption and Scattering

Optical photons can be absorbed by electrons in atoms or molecules within a material. Absorption occurs when the energy of the photon matches the energy difference between the current energy state and a higher energy state within the atom of molecule. When a photon is absorbed, its energy is transferred to an electron, promoting it to that higher energy state.

Several types of scattering can occur when optical photons interact with matter. Scattering arises from interactions with particles or inhomogeneities within a material. In the optical regime, the most relevant types are Rayleigh scattering and Mie scattering. These processes are typically elastic, meaning that the photon's energy and momentum are conserved, and its wavelength remains unchanged. Instead, scattering primarily alters the photon's direction. Whether Mie scattering or Rayleigh scattering occurs depends on the size of the scattering target relative to the photon's wavelength.

Mie Scattering

Mie scattering is the scattering of light by particles whose size is comparable to or larger than the wavelength of the incident light. This form of scattering typically occurs when the target particles, such as water droplets, dust, or aerosols, have sizes similar to or greater than the wavelength of the light interacting with them. This characteristic distinguishes Mie scattering from Rayleigh scattering, which occurs

when the size of the target particles is much smaller than the wavelength of the incident light.

Unlike Rayleigh scattering, Mie scattering is not strongly wavelength-dependent, meaning it tends to scatter light more uniformly across different wavelengths. As a result, Mie scattering does not preferentially scatter shorter wavelengths over longer ones. This phenomenon is visible in nature through the white appearance of clouds, which contain water droplets large enough to scatter all visible wavelengths uniformly.

Mie scattering predominantly directs light in the forward direction, along the path of the incident light. However, it is also capable of significant side and back scattering, depending on the relative size of the scattering particles, and the wavelength of the incident light. This forward scattering contributes to the hazy appearance of foggy or smoky environments, as light is scattered in multiple directions.

Rayleigh Scattering

Rayleigh scattering is the scattering of light by particles much smaller than the wavelength of the incident light. Unlike Mie scattering, Rayleigh scattering is strongly dependent on wavelength. According to Equation 2.15, the intensity of Rayleigh scattering is inversely proportional to the fourth power of the wavelength. This mathematical relationship means that shorter wavelengths of light are scattered much more strongly than longer wavelengths.

$$I(\lambda) = I_0 \frac{1 + \cos^2 \theta}{2R^2} \left(\frac{2\pi}{\lambda}\right)^4 \left(\frac{n^2 - 1}{n^2 + 2}\right)^2 \left(\frac{6 + 3\rho}{6 - 7\rho}\right) \tag{2.15}$$

where,

- I_0 is the incident light intensity
- θ is the scattering angle
- R is the distance to the observer

- n is the refractive index of the scattering medium
- ρ is the depolarization ratio.

The intensity of Rayleigh scattering decreases rapidly with increasing wavelength. This type of scattering applies only when particle sizes are much smaller than the wavelength of light; for larger particles, Mie scattering or geometrical scattering dominates. Rayleigh scattering is nearly isotropic, though there is a slight preference for forward and backward scattering.

A familiar example of Rayleigh scattering in nature is the blue colour of the sky during the daytime. Although sunlight is composed of many different wavelengths of light, shorter wavelengths are scattered much more effectively by the small gas molecules in the Earth's atmosphere. Although violet light is scattered even more than blue, it is mostly absorbed by the upper atmosphere, and human eyes are more sensitive to blue light, making the sky appear predominantly blue.

At sunset, the sky appears red and orange because sunlight travels through a greater thickness of atmosphere. This scatters the shorter blue and violet wavelengths out of the direct path to the observer, leaving the longer red and orange wavelengths to dominate the sky's appearance.

When optical photons encounter boundaries between different materials, processes such as transmission, reflection, and refraction can occur. These optical effects are commonly explained using the wave description of light. As light propagates through a medium, its phase velocity, v, may differ from its speed of light in a vacuum, given by $c = 3.0 \times 10^8$ m/s. The material's refractive index, n, determines the phase velocity, causing light to travel more slowly in the medium than in a vacuum.

The index of refraction is given by Equation 2.16:

$$N(\lambda) = \frac{c}{v(\lambda)} \tag{2.16}$$

where,

- $N(\lambda)$ is the refractive index as a function of wavelength λ
- c is the speed of light in vacuum, approximately 3.0×10^8 m/s,
- $v(\lambda)$ is the phase velocity of light in the medium at wavelength λ.

The refractive index is wavelength-dependent and may also be temperature-dependent, although this mechanism is not fully understood (Waxler and Cleek, 1973). Snell's Law can be used to determine the direction of light when light is crossing an interface between two media with different indices of refraction.

Refraction of light is when light bends or changes direction as it passes from one medium to another with a different refractive index. This occurs because light changes speed when it moves between materials with different optical densities.

For instance, light goes slower in water than in air, and slower, slightly, in air than in a vacuum. This effect is described by the index of refraction, n.

Refraction is the change in direction of a wavefront when it passes from one medium to another. This is due to the light changing speed when passing from one medium into another.

Refraction follows Snell's Law, which is given by Equation 2.17:

$$n_1 \sin\theta_1 = n_2 \sin\theta_2 \tag{2.17}$$

where,

- n_1 is the refractive index of the first medium.
- θ_1 is the angle of incidence, measured between the incoming light ray and the normal to the boundary surface in medium 1.
- n_2 is the refractive index of the second medium.
- θ_2 is the angle of refraction, measured between the refracted ray and the normal in medium 2.

For scintillators, there are various types of reflection which may occur and these are listed below:

Total Internal Reflection: This is when scintillation light strikes the internal surface of the scintillator at an angle which is greater than the critical angle. The light is therefore reflected back into the scintillator, rather than escaping. This type of reflection can aid in guiding the light towards the photodetector; hence, improving light collection efficiency.

Specular Reflection: When the internal surfaces of the scintillator are smooth, light can be reflected in a way where the angle of incidence equals the angle of reflection; this is 'mirror-like' reflection.

Diffuse Reflection: In the case where the internal surfaces of the scintillator are rough, light can scatter in a variety of directions upon reflection; this is in contrast to specular reflection, where the directions are more predictable. This form of reflection can lead to the loss of light as light is absorbed or scattered prior to detection.

Reflection at Boundaries: Light can be reflected at the boundary between volumes – such as between a scintillator and the surrounding materials, such as air or an optical coupling agent. When the refractive index of the scintillator is higher than that of the surrounding material, some light will be reflected back into the scintillator, while some may refract out, resulting in light loss.

2.3 Scintillation Detectors

When ionising radiation interacts with a material, it can excite or ionise molecules within it. In certain materials, when these excited molecules return to their ground state, they may emit photons in the visible or near-visible range of the electromagnetic spectrum, through a process known as scintillation. Materials that exhibit this property are called scintillators. Broadly speaking, scintillating

materials are categorised as either organic or inorganic. Commonly used scintillators include inorganic crystals, such as sodium iodide, as well as organic crystals, liquids, and plastics. Organic and inorganic scintillators differ in their chemical structures, the mechanisms by which they produce scintillation, and their applications.

Detecting scintillation light is one of the most effective methods for measuring various types of radiation. Scintillation detectors typically consist of a scintillator coupled to a photosensor, such as a photomultiplier tube (PMT) or a photodiode. When the scintillator absorbs energy from the incident radiation, it emits light, with the intensity directly proportional to the energy deposited. The photosensor then detects this scintillation light and converts it into an electrical pulse.

For a scintillator to be effective in detecting ionising radiation, it should ideally possess the following properties (Knoll, 2000):

1. It should efficiently convert the kinetic energy of charged particles into detectable light, with high scintillation efficiency.

2. The light yield should be proportional to the energy deposited by ionising particles over a wide range of energies.

3. The scintillator material should be transparent to the wavelength of its own emitted light to optimise light collection and reduce photon loss due to self-absorption.

4. The light pulses should be as short as possible, with minimal delayed emission, to enable fast pulse generation.

5. The scintillator material should have good optical quality and be manufactured in sizes large enough for practical detector applications.

6. The refractive index of the material should be close to that of glass (≈ 1.5) to ensure efficient coupling of the scintillation light to the photodetector.

Other desirable properties for scintillator materials include chemical and mechanical stability, ease of production, cost-effectiveness, and radiation tolerance. However, no single material satisfies all these criteria and therefore the choice of scintillator is usually a compromise between various factors.

Inorganic crystals generally offer higher light output (LO) and better linearity but tend to have slower response times. In contrast, organic scintillators provide faster response times but produce lower light output. The selection of a scintillator is crucially determined by its intended application. For example, the high atomic number (Z) and density of inorganic scintillators make them ideal for gamma-ray spectroscopy, while organic scintillators, with their high hydrogen content, are preferred for beta spectroscopy and fast neutron detection applications (Knoll, 2000).

2.3.1 Organic Scintillators

The fundamental principle behind all scintillators is fluorescence, which is the prompt emission of visible light from molecules within a substance following excitation by ionising radiation. In organic scintillators, fluorescence occurs due to transitions in the energy level structure of individual molecules. Unlike crystalline inorganic scintillators, such as sodium iodide, fluorescence in organic scintillators is observed regardless of the physical state of the molecular species. For example, anthracene fluoresces whether it is in solid form, a vapour, or as part of a multi-component solution.

Organic molecules commonly used for scintillation typically have a π-electron structure, such as aromatic molecules. The energy levels of such a molecule are illustrated in Figure 2.1. Excitation by ionising radiation results in a series of excited singlet and triplet states, labelled as $S_1, S_2, S_3, ...$ and $T_1, T_2, T_3, ...$, respectively. Each energy level is further divided into a set of finer vibrational sub-levels, with typical spacings on the order of 0.15 eV, corresponding to various vibrational states of the molecule. A second subscript is commonly used to indicate these vibrational

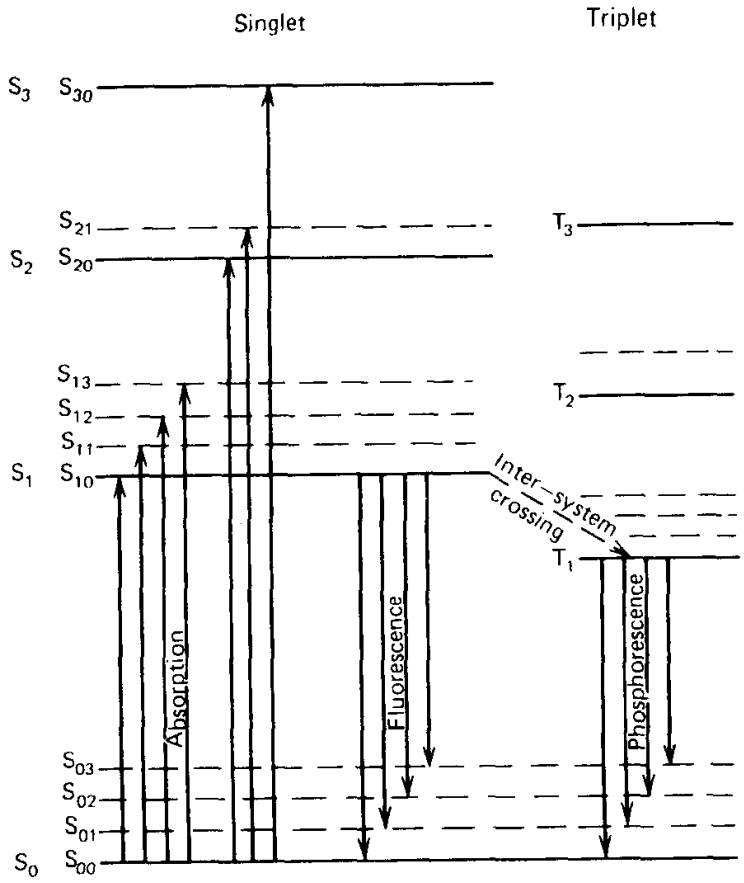

Figure 2.1: Energy level diagram of an organic molecule with a π-electron structure, showing singlet and triplet excited states, vibrational sub-levels, and fluorescence transitions following excitation by ionising radiation. Adapted from J.B. Birks, 1964, as cited in Knoll, 2000.

states. In Figure 2.1, S_{00} represents the lowest vibrational state of the molecule's ground state.

Fluorescence in organic molecules consists of two components: prompt and delayed. The prompt fluorescence is emitted within a few nanoseconds after excitation, arising from transitions between the first singlet excited state (S_1), specifically S_{10}, and one of the vibrational states of the ground state (S_0). When higher singlet states are excited, they undergo rapid radiationless de-excitation to S_1 via internal conversion, typically within picoseconds.

The delayed fluorescence component is emitted typically a few hundred nanoseconds following excitation and results from a process known as inter-system crossing. This is where molecules in the excited singlet state (S_1) non-radiatively transition to the triplet state (T_1). While in the T_1 state, some molecules can non-radiatively return to S_1 and subsequently decay via normal fluorescence to the ground state (S_0), though this emission is delayed relative to the prompt component. This is the origin of delayed fluorescence in organic scintillators.

The intensity of prompt fluorescence, I, at time t, following excitation by ionising radiation, is given by:

$$I = I_0 e^{-t/\tau} \tag{2.18}$$

where I_0 is the intensity of the prompt fluorescence at $t = 0$ and τ is the decay time constant.

An additional component can be included in this expression to account for delayed fluorescence. The resulting equation becomes:

$$L(t) = Ae^{(-t/\tau_p)} + Be^{(-t/\tau_d)} \tag{2.19}$$

Here:

- $L(t)$ is the scintillation light intensity as a function of time.

- A and B are constants that determine the relative contributions of the fast (prompt) and slow (delayed) components to the overall light output, and they depend on the scintillator material.

- τ_p and τ_d are the decay time constants of the prompt and delayed fluorescence components, respectively, and represent intrinsic properties of the scintillator.

The scintillation efficiency of a scintillator is defined as the fraction of all incident particle energy that is ultimately converted into visible light. In organic molecules, not all the energy deposited produces light because of quenching: rather than undergoing radiative de-excitation, some excited molecules lose their energy through non-radiative processes, in which the excitation energy is converted primarily into heat.

In organic scintillators — whether crystal, liquid, or plastic — the process of scintillation follows a similar pattern. An incident particle first excites the molecules of the bulk solvent or base material. This excitation energy is subsequently transferred to the fluor molecules, which emit visible scintillation light. Secondary fluors (wavelength shifters) are often added to shift the emission spectrum to better match the spectral response of common photodetectors.

Pure Organic Crystals

Scintillation has been demonstrated in organic crystals such as anthracene, trans-stilbene, and p-terphenyl organic crystals. Stilbene is commonly used for fast neutron detection due to its excellent efficiency, high light output (LO), and superior pulse shape discrimination (PSD) performance. Stilbene generally outperforms that of both liquid and plastic scintillators; however, its fragility and high manufacturing costs limit its use in large-area detectors and make transportation for field applications challenging. Additionally, the scintillation efficiency is known to depend on the orientation of the ionising particle with respect to the crystal axis (Weldon et al., 2019).

Crystals like anthracene and stilbene offer high scintillation efficiency but are

expensive to produce in large sizes, which restricts their application in nuclear security.

Organic Liquid Scintillators

Organic liquid scintillators, such as EJ-301 and EJ-309, have been used for decades in both fast and thermal neutron detection due to their high hydrogen content, good light output, and excellent pulse shape discrimination (PSD) capabilities. These scintillators are produced by dissolving highly efficient fluor compounds in an appropriate solvent. Liquid scintillators can consist of two components or three components if a wavelength shifter is added to the solution. Wavelength shifters are materials that absorb higher-frequency photons and re-emit them at a lower frequency to better match the spectral response of the photodetector.

Liquid scintillators are often the preferred choice when large-volume detectors are required. Since they lack a crystal structure, they are resistant to radiation damage and can be manufactured in large quantities with various geometries.

Plastic Scintillators

Plastic scintillators were first developed in the 1950s (Schorr and Torney, 1950) as a solid-state alternative to liquid scintillators for fast neutron detection. Although they are inexpensive, well suited for large-volume applications due to their ease of fabrication, and have relatively long attenuation lengths to minimise self-absorption, their light output (LO) and pulse shape discrimination (PSD) performance are generally lower than those of crystal and liquid scintillators.

Plastic scintillators are produced by dissolving organic fluors in an appropriate solvent, followed by bulk polymerisation. Their composition closely resembles that of liquid scintillator, except that the liquid solvent is replaced by aromatic polymers such as polyvinyltolene (PVT) or polystyrene (PS). Common fluors include 2,5-diphenyloxazole (PPO) and n-terphenyl (PTP).

Plastic scintillators are organic materials and therefore primarily composed of hydrogen and carbon atoms. Gamma-ray interactions occur mainly through

Compton scattering, as expected for low-Z materials and as detailed in Section 2.2.2. Fast neutrons predominantly interact via elastic scattering on hydrogen nuclei, producing recoil protons:

$$n + H^1 \rightarrow n + p \tag{2.20}$$

A smaller contribution comes from elastic scattering on carbon nuclei because carbon is heavier than hydrogen, producing carbon recoils:

$$n + {}^{12}\mathrm{C} \rightarrow n + {}^{12}\mathrm{C} \tag{2.21}$$

Carbon recoils produce far less scintillation light than protons due to both limited energy transfer and quenching, and therefore contribute little to the overall light output of the scintillator.

Inelastic scattering on carbon can also occur, but this requires energies above 4.44 MeV, making the process negligible for lower-energy fast neutrons.

After multiple elastic scatterings, neutrons may reach thermal energies, at which point capture reactions on hydrogen and carbon nuclei becomes possible. However, the capture cross sections are so small that in typically sized plastic scintillators neutron capture remains a rare interaction. In very large detectors, or in systems with neutron moderators, the probability of capture increases significantly.

2.3.2 Inorganic Scintillators

The scintillation mechanism in inorganic scintillators depends on the energy levels of the material, which are determined by its crystalline lattice structure. This differs from the mechanism governing scintillation in organic scintillators, which is molecular in nature. In inorganic materials, electrons occupy discrete energy levels within two main bands: the lower energy valence band, where electrons are bound to atoms in the lattice, and the higher energy conduction band, where electrons are

free to move through the material. These bands are separated by an energy gap known as the band gap, or forbidden band, where electrons cannot normally exist.

When an incoming high-energy particle interacts with the material, it can excite an electron from the valence band into the conduction band, leaving behind a positively charged hole in the valence band. The excited electron and the hole can move through the lattice, and their movement is influenced by the crystalline structure, as well as by any impurities or activator ions present in the material. As the free electrons recombine with the holes, energy is released, which can result in the emission of photons in the near-visible to visible range. This light emission is responsible for the prompt fluorescence observed in inorganic scintillators.

In many inorganic scintillators, activator ions, such as thallium in Nal(TI), are introduced into the crystal to enhance light emission by creating specific energy levels within the band gap. These activators modify the electronic structure of the material, providing intermediate energy states within the forbidden band that electrons can temporarily occupy.

Recombination of electron-hole pairs often occurs at activator sites. The activator plays a crucial role by offering energy levels that enable efficient and controlled recombination, leading to the emission of light at a specific wavelength. For example, in Nal(TI) the thallium activator induces light emission at around 410 nm, in the blue-violet region of the electromagnetic spectrum.

2.4 Photodetector Technology

Photodetectors play a critical role in radiation detection and measurement by converting the weak light output from scintillators into measurable electrical signals. The most commonly used photodetectors in this context are photomultiplier tubes (PMTs) and silicon photomultipliers (SiPMs).

2.4.1 Photomultiplier Tubes (PMTs)

A photomultiplier tube (PMT) is a vacuum phototube used to detect low-energy photons. Typically, PMTs are constructed with their components housed in an outer glass vessel, which serves as a pressure boundary to maintain the vacuum conditions necessary for electron acceleration. Internal electric fields within the tube facilitate the movement of electrons through the PMT.

The structure of a typical PMT is shown in Figure 2.2. The window of the PMT allows incident light to pass through within a specific wavelength range, determined by the window material. For example, borosilicate glass is commonly used for detecting near ultra-violet and blue light.

A PMT consists of three main components: (1) a semi-transparent photocathode, (2) an electron multiplier, and (3) an anode. The photocathode is a thin layer of photoemissive material deposited on the inner surface of the window. When incident photons are absorbed by the photocathode, low-energy electrons (called photoelectrons) are emitted via the photoelectric effect. The efficiency of the photocathode is crucial, as it should convert as many incident photons as possible into photoelectrons. Thus, selecting the optimal material for the photocathode is essential for maximising high conversion efficiency.

The process of detecting light and generating an output signal in a PMT occurs through the following sequential steps (Polyakov, 2013):

1. Incident light enters the PMT through the input window.

2. The photocathode absorbs the incident light, transferring energy to electrons within the photocathode material. This energy excites the electrons, allowing them to migrate to the surface and escape into the vacuum as photoelectrons.

3. The photoelectrons are accelerated and focused by a focusing electrode toward the first dynode. Upon striking the dynode, secondary electrons are emitted due to secondary emission. This process is repeated at each subsequent dynode, with each stage amplifying the number of electrons.

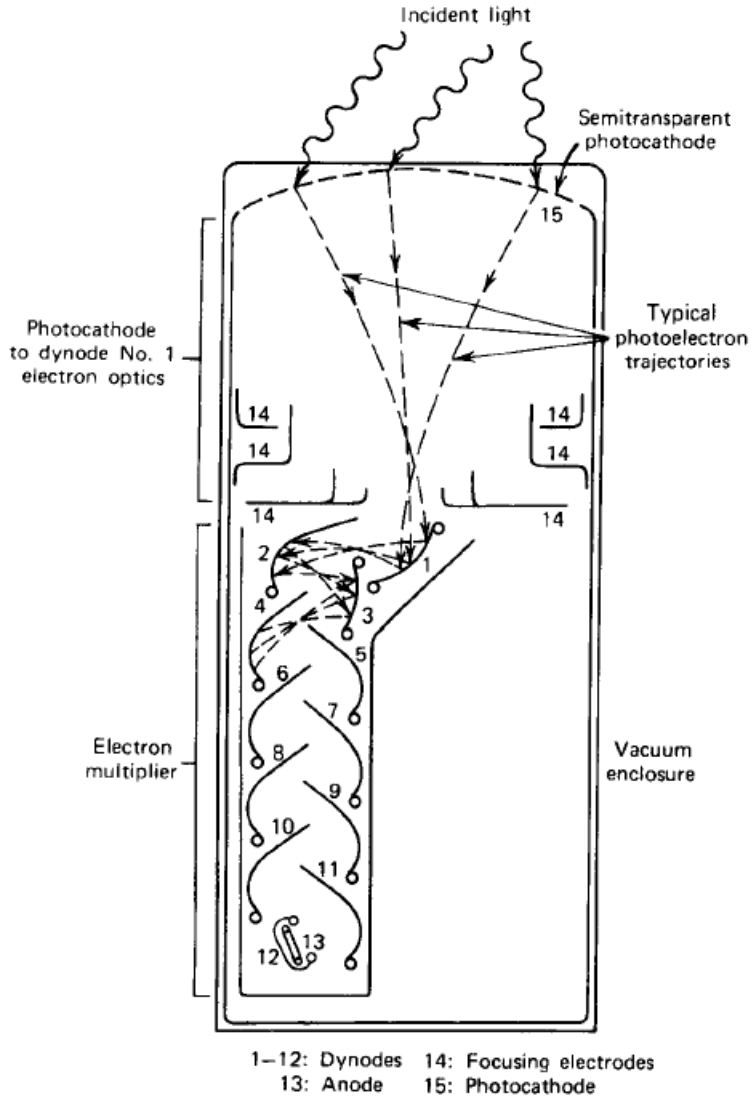

Figure 2.2: Schematic of components of a typical photomultiplier tube (PMT). Image reproduced from Knoll, 2000

.

4. Signal collection occurs at the anode, where the multiplied electrons from the last dynode are collected, generating an electrical signal which can be measured.

The energy transferred from the photon to the electron in the second step is determined by the photon's energy, given by hv, where h is Planck's Constant and v is the photon frequency. For blue light — typical of the light emitted by many commonly used scintillators — the photon energy is approximately 3 eV. During this step, some energy is lost due to electron-electron collisions. By the time the electron reaches the third step, it must retain sufficient energy to overcome the potential barrier at the interface between the material and the vacuum. This potential barrier, known as the work function, imposes a minimum energy threshold on the incident photons. To maximise the number of escaping electrons, the photocathode material must have a low work function (typically less than 4 eV). A low work function allows more electrons to escape, thereby enhancing the overall efficiency of the PMT.

2.4.2 Photomultiplier Tube (PMT) Noise

This section discusses the sources of noise that affect photomultiplier tubes (PMTs). Noise refers to any fluctuation — random or otherwise — that interferes with the current or voltage being measured. This limits the accuracy of measurements, particularly in low-light applications. In radiation detection systems using a PMT, such as scintillation detectors, noise can be broadly categorised based on whether it occurs in the absence of a signal or when a signal is present.

Dark Current and Dark Noise

Even in complete darkness, a measurable current can still be detected at the anode of a photomultiplier tube (PMT). This current is known as dark current, and the fluctuations in current due to this effect are referred to as dark noise. Like the photoelectric current, the dark current primarily consists of discrete pulses, typically of the same duration as the photoelectric pulses. When observed on an

oscilloscope with wide bandwidth, the dark current appears as pulses with widely varying amplitudes. The rate at which these pulses occur is commonly referred to as dark noise.

Both dark current and dark noise limit the detectivity of a PMT. Dark noise establishes a baseline level of noise in PMTs, producing spurious signals in the absence of light. This spurious noise reduces detection accuracy, especially for low-intensity or low-energy radiation. Minimising dark noise is essential for improving the signal-to-noise ratio (SNR) of PMTs and optimising their performance in various scientific and technical applications, such as radiation detection and measurement.

Dark current has two components:

- A continuous component due to current leakage on glass and insulation surfaces.
- An intermittent component, consisting of pulses lasting a few nanoseconds.

There are both temporary and permanent causes of dark current. The impact of these causes varies depending on operating and environmental conditions, such as applied voltage, gain, temperature, and humidity. Some causes may lead to temporary effects, resulting in a settling of dark current to a stable level, while others are permanent and independent of the tube's history.

Permanent causes of dark current include:

- Ohmic leakage.
- Thermionic emission.
- Field emission.

Ohmic Leakage

This component of dark noise arises from the flow of electrical current between electrodes on glass and insulating surfaces, such as plastic bases and sockets. This

type of dark noise is influenced by the gain and temperature of the photomultiplier tube (PMT), and it is most significant when the PMT operates at low gain ($< 10^4$) or at low temperatures.

Factors such as dirt and humidity can contribute to Ohmic leakage, while soldering flux can be particularly detrimental, producing large pulses that resemble those from a scintillator across all gain values. These effects can be minimised through proper maintenance and cleanliness (Photonis, 2002).

Thermionic Emission

The most significant source of random noise in a photomultiplier tube (PMT) arises from thermionic emission, which is the process by which electrons with sufficient thermal energy are spontaneously emitted by the photocathode. At non-zero temperatures, electrons within the photocathode possess thermal kinetic energy, averaging around 0.025 eV at room temperature. Although there is a distribution of energies among these electrons, some can gain enough energy from thermal fluctuations to exceed the work function of the material. If such an electron is close enough to the surface, it may escape, resulting in a spontaneous, thermally induced signal. These electrons are known as thermionic electrons, and thermionic noise is a key characteristic of photocathodes.

The dark pulses generated from thermionic emission correspond to single photoelectrons, which limits the amplitude of the observed signal to the lower end of the pulse height spectrum. In scintillation counting, each detected pulse typically corresponds to multiple photoelectrons, so this form of noise less significant. Pulse height discrimination techniques can be used to eliminate contributions from thermal noise. However, when measuring very low-energy radiation or single electrons, thermionic noise can become indistinguishable from the true signal. In such cases, minimising this noise contribution is vital (Knoll, 2000).

Thermionic emission is temperature-dependent and follows Richardson's Law, which predicts an approximate tenfold increase in emission for every 15 °C rise in

temperature. At higher temperatures, more electrons can gain sufficient energy to overcome the work function of the photocathode. Therefore, lowering the temperature of a PMT can effectively reduce thermionic emission, provided other sources of dark current do not become dominant (Photonis, 2002). Additionally, the rate of dark pulses is proportional to the area of the photocathode, so choosing a small diameter photocathode can help reduce dark pulses. The emission rate of thermionic electrons per unit area also varies significantly depending on the material used for the photocathode. For example, bialkali photocathodes are among the quietest, with typical emission rates at room temperature ranging from $10^2 - 10^4$ electrons $\mathrm{cm}^{-2}\ \mathrm{s}^{-1}$ (Knoll, 2000). Both dark current and dark noise rate increases exponentially with temperature.

Field Emission

Field emission, also known as cold emission, is the process by which electrons are emitted from a surface, such as a photocathode, under the influence of a strong electric field. In this process, the intense electric field lowers the potential barrier at the surface, allowing electrons to tunnel through the barrier via quantum mechanical effects, even in the absence of thermal energy.

In photomultiplier tubes (PMTs), local electric fields can be extremely high, especially near high-voltage regions or due to surface imperfections. Small irregularities, such as surface blemishes or loose particles on the electrode, can locally enhance the electric field, making these regions potential sources of field emission. Once emitted, the electrons are accelerated toward other surfaces within the PMT, such as dynodes. Electrons with energies as low as 1 keV may be capable of extracting additional photoelectrons from the cathode or dynodes, contributing to the dark current (Photonis, 2002).

Field emission is a significant source of dark current and dark noise in PMTs, especially in designs that require high sensitivity and those operated at high voltages. The magnitude of this noise is largely determined by the strength of the electric field,

with stronger fields leading to greater field emission.

While both thermionic and field emission contribute to dark current and noise, field emission typically produces more discrete, sharp pulses, due to the influence of strong electric fields. This contrasts with thermionic emission, which generally produces more continuous noise because it depends on thermal energy. Minimising dark current due to field emission can typically be achieved by operating PMTs well below their maximum voltage rating and ensuring the cleanliness of the tube.

Shot Noise

Shot noise is a fundamental type of noise present in all electronic systems where current flows, arising from the discrete nature of electric charge. In photomultiplier tubes (PMTs), shot noise results from statistical fluctuations in the number of photoelectrons generated by incoming photons and subsequently detected at the anode. Shot noise is proportional to the square root of the average current flowing through the tube, meaning that higher overall current (including dark current) leads to greater shot noise.

Additionally, the process of electron multiplication within the PMT is subject to its own statistical fluctuations. As a result, the number of electrons reaching the anode can also fluctuate, further contributing to shot noise. Shot noise follows a Poisson distribution because it arises from the discrete and random arrival of charge carrier (photons and electrons). However, for practical applications such as PMTs, where a high number of photoelectrons are involved, shot noise is often approximated by a Gaussian (normal) distribution. In this approximation, the variance is proportional to the mean current or the number of photoelectrons. Since shot noise is an intrinsic property of electrical charge, it does not depend on temperature and occurs in any device where there is a flow of current.

The impact of shot noise is most prominent at low-light levels where it can limit detection accuracy. When the photon flux is high or in systems with sufficient signal-to-noise ratio (SNR), other types of noise, such as dark current or thermal noise,

may become more relevant.

Johnson-Nyquist Noise

Johnson-Nyquist noise, also known as thermal noise, is a type of noise originating from the random thermal fluctuations of stationary charge carriers (typically electrons) inside a conductor. This form of noise occurs even in the absence of any applied voltage and is an inherent property of all materials at temperatures above absolute zero. This is because at any non-zero temperatures, free electrons in a conductor move at random due to having thermal energy. It is these random movements which cause small fluctuations in the voltage across the conductor, which manifests as noise. The magnitude of this noise is dependent on the temperature of the conductor and the resistance of the material.

This form of noise is important for PMTs because they operate at room temperature or higher, therefore thermal noise will be present in the components of the tube. Johnson-Nyquist noise contributes a baseline level of noise which is independent of the photon flux or light intensity. It can therefore occur even in the absence of light due to the dark current. This noise is temperature dependent and hence any variation in the operating temperature of the PMT can affect the level of noise. An increase in temperature naturally leads to an increase in the thermal energy of the electrons, leading to more random motion, resulting in higher thermal noise in the system. Lowering the operating temperature of the PMT can therefore reduce the impact of this form of noise on measurements.

Afterpulses

Afterpulses are spurious pulses that can occur following a true signal pulse, after a short delay. One mechanism responsible for afterpulsing is the emission of light from the latter stages of the PMT's multiplier structure, which may then be reflected or scattered back to the photocathode. These afterpulses are delayed by a time characteristic of the electron transit time through the tube, typically around 20 ns to 50 ns. Because these pulses often correspond to a single photon, their amplitude

is usually quite small. Another source of afterpulsing can arise from an imperfect vacuum within the tube. Residual gas molecules can be ionized by the passage of electrons through the multiplier structure. The resulting positive ions drift in the reverse direction and may find a path back to the photocathode. When these ions strike the photocathode, they can liberate tens or even hundreds of photoelectrons, resulting in a much larger pulse. Since the velocity of positive ions is relatively slow, the time it takes for them to drift back to the photocathode can range from hundreds of nanoseconds to microseconds or more. As a result, the time spacing between the primary pulse and the afterpulse in this case is much larger.

2.5 Pulse Shape Analysis

First demonstrated in 1959 by F.D. Brooks using trans-stilbene crystals, pulse shape discrimination (PSD) is a valuable technique in neutron detection. PSD relies on analysing subtle differences in the temporal pulse shapes generated by neutron and gamma-ray interactions in organic scintillators (Brooks, 1959). Gamma rays interact primarily through recoil electrons, while neutrons produce recoil protons — each depositing energy at different rates in the scintillator, which gives rise to scintillation light with characteristic time profiles. Even for the same deposited energy, protons have a higher specific energy loss (dE/dx) than electrons, which enhances triplet-triplet interactions and results in a greater proportion of delayed fluorescence, as detailed in Section 2.3.1. This fundamental difference underpins the separation of neutron- and gamma-induced signals by PSD.

Neutron radiation fields are almost always accompanied by background gamma radiation, typically produced through neutron activation of surrounding materials. Since scintillator-based neutron detectors are sensitive to both gamma and neutron radiation, PSD is essential for distinguishing between the two and suppressing the gamma-ray signal component (Knoll, 2000).

Heavier particles, such as protons, lose energy more rapidly in scintillator

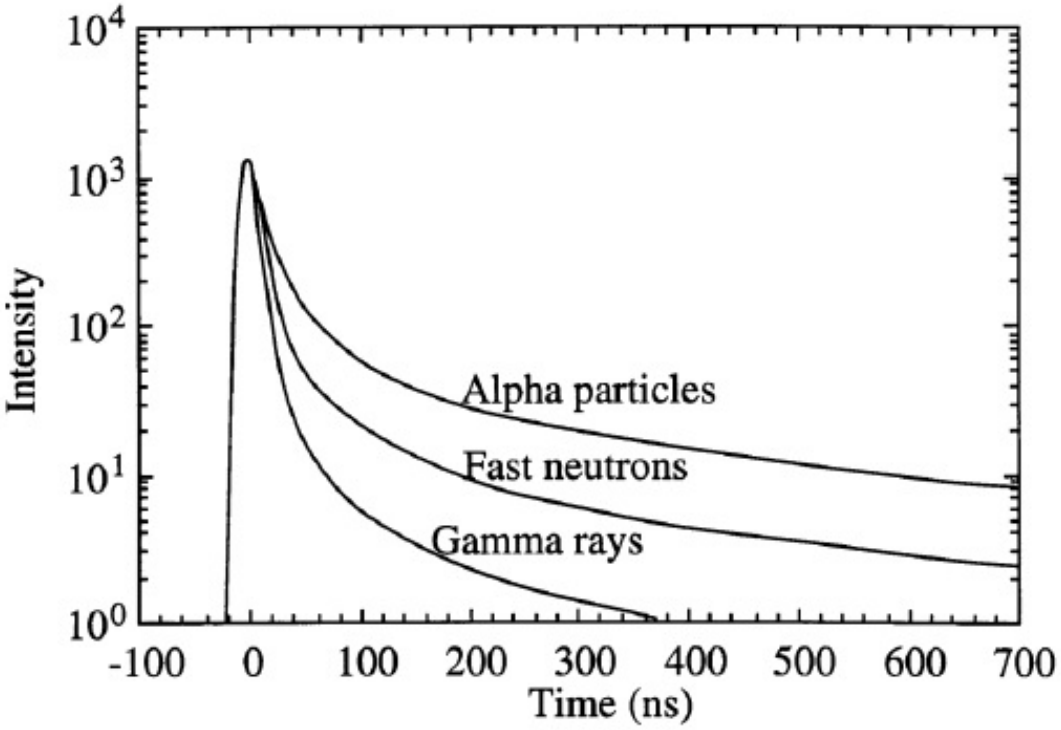

Figure 2.3: Illustration of pulse shapes generated by three different particle types in a scintillator. The variation in decay characteristics, particularly in the pulse decay tail, forms the basis for pulse shape discrimination (PSD). Image reproduced from Knoll, 2000.

materials than lighter particles, such as electrons. As a result, protons generate a higher proportion of delayed fluorescence, leading to neutron-induced pulses that decay more slowly compared to those produced by gamma rays. These differences between particle types are most apparent in the decay tail of the pulse, as illustrated in Figure 2.3 for three different particle types. The variation in the proportion of delayed fluorescence among different particles forms the physical basis of PSD, enabling particle identification based on pulse shape characteristics.

Over the years, a variety of techniques have been developed to implement PSD, with the overall goal of achieving optimal separation between neutron- and gamma-ray induced signals. The main techniques are described below.

2.5.1 Charge Comparison Method (CCM)

The Charge Comparison Method (CCM) is one of the most widely employed techniques for pulse shape discrimination (PSD) and is extensively used in both the analogue (Brooks, 1959) and digital domains (Bell, 1981; Zecher et al., 2003; Jastaniah and P. J. Sellin, 2004). Due to its simplicity, ease of implementation, and robust performance, CCM is suitable for a wide range of applications — most notably for distinguishing neutron and gamma-ray interactions in scintillation detectors — and maintains stable, reliable discrimination across a broad energy range (Comrie et al., 2015).

The CCM works by comparing the integrals of the charge under a pulse over two distinct time intervals: the long integral and the short integral. The long integral represents the total charge accumulated over the entire pulse, hence capturing the the full energy deposited by the radiation. In contrast, the short integral captures only a portion of the pulse, typically associated with the decay tail.

The decay tail is particularly informative for pulse shape discrimination purposes, as the pulse shape characteristics in this region exhibit significant differences between gamma ray and neutron radiation. The long integral starts at the start of the pulse, while the short integral begins at a reference point after the pulse peak.

This reference point is strategically chosen to maximise the separation between the gamma- and neutron-induced pulses. The endpoint of both the long and short integrals is the end of the pulse.

Neutron pulses typically exhibit slower decay rates compared to gamma ray pulses, leading to a larger short integral for neutron-induced pulses. This difference in decay rates forms the basis for pulse shape discrimination (PSD) in CRM. Specifically, the relative proportions of the long and short integrals are used to calculate a value known as the PSD parameter.

The PSD parameter is computed by dividing the short integral by the long integral. When plotted on a two-dimensional histogram against energy, the data typically form two distinct bands: one for neutron interactions and another for gamma ray interactions. This separation is a direct result of the differing decay characteristics of the pulses from each radiation type.

Alternatively, the PSD parameter can also be plotted against the long integral, yielding a similar separation between the two radiation types. In these plots, the upper plume of the histogram corresponds to neutron interactions, which exhibit larger short integrals due to the slower decay, whereas the lower plume corresponds to gamma ray interactions, characterised by smaller short integrals due to their faster decay rates.

These histograms are used to quantify the separation between the two types of pulses, providing a measure of how effectively the detector discriminates between neutron and gamma ray interactions.

The overall PSD performance of a detector can be quantified using a metric called the Figure of Merit (FoM). This is defined as the distance between the two plumes (S) in a specific energy range when fitted with a Gaussian function, divided by the sum of the full-widths at half-maximum (FWHM) of the PSD plumes (Winyard, Lutkin, and McBeth, 1971). The formula for the FoM is given by Equation 2.22.

$$FoM = \frac{S}{FWHM_{\gamma} + FWHM_{\text{neutron}}} \tag{2.22}$$

Typically, a high FoM is considered a good indicator of how well a scintillator distinguishes between neutrons and gamma rays, suggesting improved PSD performance. A FoM value of 1.27 is considered to correspond to a good level of signal separation (N. Zaitseva, Rupert, et al., 2012). However, the FoM can sometimes be misleading because it assumes that the two bands have a Gaussian shape along the PSD axis, which is not always the case. This assumption becomes particularly problematic in the presence of pulse pile-up, where two pulses arrive nearly simultaneously. In such cases, the FoM may not fully reflect the gamma-rejection capability of the detector, defined as the fraction of gamma rays mistakenly classified as neutrons when only gamma rays are present (Langeveld et al., 2017). Parameters can be optimised to improve performance. In the case of the CCM, the short integral can be changed for optimisation.

Although signals from organic scintillators are typically very fast, there are circumstances where a detector must operate in a high-flux environment. The random nature of radiation means that pulses can arrive simultaneously, leading to an overestimation of the energy of the second event. Furthermore, in such cases, the discrimination technique may fail to identify either pulse, leading to discarded data.

The CCM can be susceptible to pulse pile-up, a phenomenon where two or more pulses overlap or "pile up" within a short time interval. This results in reduced detection rates and spurious pulse assignments. Pile-up recovery is possible but often requires extension processing and can be time-consuming. Pulse pile-up leads to signal overlap, where the detector cannot distinguish between pulses, resulting in inaccurate or missing data. This can distort measurements, reduce resolution, and even lead to the loss of data.

2.5.2 Pulse Gradient Analysis (PGA)

Pulse Gradient Analysis (PGA) involves sampling the peak amplitude of a pulse and comparing it to the amplitude of a sample taken at a defined time interval

after the peak, referred to as the discrimination amplitude. The selection of this discrimination amplitude depends on the characteristics of the scintillator and the photomultiplier tube (PMT) used (D'Mellow et al., 2007; Aspinall, D'Mellow, Mackin, M. J. Joyce, Hawkes, et al., 2007). Signal separation is achieved by recognising that neutron pulses exhibit a shallower gradient compared to gamma ray pulses.

PGA is computationally simple, enabling early discrimination between neutrons and gamma rays, and providing some immunity to pulse pile-up. It is a fast discrimination method since it responds to features early in the pulse's lifetime, making it less prone to the effects of pulse pile-up. This method requires experimentation to determine the optimal time interval between the peak and the discrimination amplitude. Using a discrimination amplitude closer to the peak has the potential to improve pile-up rejection, as all the necessary information for PSD is typically captured by this point in the pulse.

2.5.3 Neutron/Gamma Model Analysis

Until relatively recently, detailed studies of the fast pulses arising from neutron and gamma-ray interactions in liquid and plastic scintillators were not feasible. The development of high-speed digital electronics has since enabled the acquisition of large numbers of pulses with nanosecond-level timing precision (Hawkes and Taylor, 2013). The resulting pulse shapes, as a function of time, depend on both the type of interacting particle and the location of the interaction within the scintillator.

Scintillation light pulses can be characterised by their rising edge and multiple decay time constants, which are related to the scintillation mechanism following the initial particle interaction. Additional time constants may be convolved with the light pulse to model the complex processes that distort the signal as it travels from the scintillator to the digital processing electronics.

The fitting of theoretical functions to measured pulse shapes provides quantitative insight into the processes occurring within the scintillator, allowing the

extraction of key parameters such as decay time constants. Traditionally, pulse shapes have been modelled using exponential functions, with the widely accepted two-lifetime description for pulse shape formation in organic scintillators (Knoll, 2000). Exponential-based pulse shape functions have been used by Marrone et al. (Marrone et al., 2002) and Aspinall et al. (Aspinall, D'Mellow, Mackin, M. J. Joyce, Jarrah, et al., 2007) to model measured pulse shapes from neutron and gamma-ray interactions in liquid scintillators, using Marrone's six-parameter model. While this approach provides a reasonable overall description of the measured pulses, it does not accurately reproduce the rising edge.

Theoretical fits based on a combination of exponential and Gaussian functions have been used to model measured pulses collected from an EJ-299-33 plastic scintillator. Unlike previous studies, the signal transmission function — which accounts for the effects of photodetector and read-out electronics — was described using a Gaussian function. Convolution of this with the exponential function representing the light pulse produced by an ExGaussian function, which was then applied to average neutron and gamma-ray pulse shapes.

While this approach accurately reproduced the rising edge, it failed to match the measured pulse shape at longer times. The authors speculated that this discrepancy could be due to the plastic scintillator containing multiple chemical components and the energy transfer between them, suggesting that a third time constant may be required to account for this (Hawkes and Taylor, 2013). Today, many PSD-capable plastic scintillators, including EJ-276, are typically characterised using three-decay time constants to account for the key fluorescent components (Eljen-Technology, 2017), with some studies including a fourth component (Grodzicka-Kobylka et al., 2020; Boxer et al., 2023) to describe an additional, long-lived slow component.

2.5.4 Frequency Gradient Analysis (FGA)

Frequency Gradient Analysis (FGA) exploits the difference in neutron and gamma-ray pulse shapes in the frequency domain. This approach uses a Fourier Transform

to analyse the frequencies that contribute to the waveform. The Fourier transform decomposes the time-based signal into a Fourier series, revealing the frequencies responsible for the waveform. These frequencies can then be used to characterise the signal. Since pulses are continuous signals rather than periodic, a Discrete Fourier Transform (DFT) is required.

FGA focuses on analysing the frequency content of pulse signals and how their spectral characteristics change over time. The idea behind this method is that the frequency content of the scintillation pulse varies depending on the type of radiation.

In FGA, a scintillation output pulse is obtained, and the temporal pulse is converted into the frequency domain using a Fourier Transform, often a Fast Fourier Transform (FFT). This process converts the time-domain pulse into its frequency components, providing insight into how the signal's power is distributed across different frequencies.

To transform the pulse into the frequency domain, a frequency transform such as the Discrete Fourier Transform (DFT) is used. The DFT is often preferred due to its lower computational overhead. Pulse Shape Discrimination (PSD) in FGA is achieved by analysing the difference between the zero frequency and the first frequency component of the Fourier Transform, allowing the separation of neutron and gamma-ray pulses based on their spectral characteristics.

2.6 Monte Carlo Simulations

Monte Carlo (MC) simulation packages are computational tools that apply Monte Carlo methods to model and simulate complex systems characterised by randomness, uncertainty, or probabilistic behaviour. These packages implement algorithms that rely on repeated random sampling to approximate solutions to mathematical problems that are otherwise intractable, or too complex to solve analytically. MC simulations have broad applications across diverse fields, including numerical integration, modelling thermodynamic processes, simulating the behaviour of

radiation detectors, and analysing the performance of complex optical systems. MC simulation packages also play a crucial role in system design and performance evaluation, especially when conducting physical experiments is impractical or prohibitively expensive.

In optical modelling, MC simulations are widely used to analyse the behaviour of light, including its reflection, refraction, scattering, and transmission through various media. Most optical simulation software, however, is primarily tailored for lens design rather than for modelling scintillation light. Tools such as Zemax OpticStudio typically employ ray-tracing techniques to simulate the transportation of light within optical systems but often treat the light as a point source, neglecting the physical processes involved in its generation. This simplification makes such software unsuitable for applications requiring a detailed understanding of scintillation light production, which results from particle interactions in a scintillator.

For more comprehensive simulations that account for both the generation and transportation of scintillation light, physics-based MC packages are often required. These packages simulate the underlying physical interactions that result in the production of scintillation light, enabling accurate modelling of light transport. These capabilities are essential for applications in radiation detection, medical imaging, and other fields where light modelling is crucial.

Some widely recognised packages for such purposes include MCNP, FLUKA, PENELOPE, SRIM, CompHEP, EGS, and Geant4. However, many of these packages are primarily tailored for high-energy particle physics applications, which can make them less suitable for low-energy simulations. At high energies, certain processes such as molecular interactions, may be negligible, but these interactions become significant at lower energies. Among these, Geant4 and MCNP have been shown to be capable of modelling both the generation and transportation of scintillation light, and their specific features and applications are discussed in the following sections.

2.6.1 Monte Carlo N-Particle Transport

Monte Carlo N-Particle Transport (MCNP) is a radiation transport code developed by Los Alamos National Laboratory (LANL) and written in the Fortran 90 programming language. MCNP is capable of simulating the transport of various particle types over a wide energy range. Its applications span diverse fields, including medical physics, nuclear reactor design, nuclear decommissioning, high-energy physics experiments, radiation safety and dosimetry, and radiation shielding.

Historically, MCNP has been paired with other Fortran-based tools, such as PoliMi, to simulate optical processes. Extensions like MCNP-PoliMi and MCNP-PHOTRACK have broadened the range and complexity of detector systems that can be modelled. However, these extensions require significant post-processing and code coupling. For example, MCNP-PHOTRACK can evaluate the effects of optical parameters on pulse shape discrimination (PSD). However, neither MCNP-PoliMi nor MCNP-PHOTRACK can directly simulate PSD through time-resolved production, transport, and detection of optical photons (Hartwig and Gumplinger, 2014).

The current version, MCNP6, integrates the capabilities of its predecessors, MCNP5 and Monte Carlo N-Particle eXtended (MCNPX). MCNPX was developed specifically for simulating particle interactions. By incorporating MCNPX features, MCNP6 now supports optical photon interactions and transport, enabling more comprehensive optical modelling. Validation studies have shown that MCNP6 produces results that align closely with experimental data, demonstrating its reliability and versatility.

2.6.2 Geant4 (GEometry ANd Tracking)

Geant4 is an object-oriented C++ Monte Carlo toolkit designed to simulate the passage of particles through matter, including detailed modelling of how various types of radiation interact with different materials (Allison, Amako, Apostolakis, Araujo, et al., 2006).

Developed by an international collaboration of scientists and organisations, including the European Organisation for Nuclear Research (CERN), Geant4 serves as the simulation framework of choice for high-energy physics experiments at the Large Hadron Collider (LHC). Geant4 covers a wide variety of physics processes for electromagnetic and hadronic physics, covering a large energy range from the eV to the TeV scale.

Beyond high-energy physics, Geant4 has been widely adopted in fields such as nuclear physics, astrophysics, space engineering, and accelerator science. It has also been used extensively by the medical physics community for radiation beam therapy, microdosimetry, and radiation protection applications (Allison, Amako, Apostolakis, Arce, et al., 2016).

In Geant4, particle transport is modelled as a series of discrete steps through defined geometrical volumes, during which particles may undergo various physical interactions. The interaction probabilities and path lengths are determined using cross-sectional data derived from experimental measurements. These cross-sections are sampled to compute both the distance a particle travels between interactions and the likelihood of each interaction type. This approach allows Geant4 to provide highly detailed and accurate simulations of particle-matter interactions.

2.6.2.1 Structure of Geant4

The construction of a simulation in Geant4 is performed by the user and is highly flexible. The object-oriented design and modular structure of the C++ code enables the creation of a wide variety of physics libraries in the form of classes. To customise a simulation, the user must select and extend specific classes based on the requirements of the simulation. Customisation involves defining several key classes, including three mandatory ones that are essential for any working Geant4 simulation.

The three mandatory classes are:

1. `DetectorConstruction:` Specifies the geometric shape, material, and position

of constructed volumes.

2. `PhysicsList:` Defines the physics processes and particle interactions required for the simulation.

3. `PrimaryGeneratorAction:` Sets up the initial particles and conditions for the simulation.

Each of these classes will be detailed below. These classes represent the minimum amount of information required to build a working simulation.

DetectorConstruction Class

The `DetectorConstruction` class is implemented by inheriting from the abstract base class `G4VUserDetectorConstruction`. This class allows users to define the physical volumes and materials required for the simulation.

Defining Geometry:

The geometry of the simulation is built using predefined shapes, such as boxes, cylinders, and spheres, or more complex forms, including polygons and rotational solids. These shapes can be combined to build more realistic geometries. One key volume, often referred to as the 'World' volume, is a unique physical volume that fully contains all other volumes. The world volume defines the global coordinate system, with its origin placed at the centre of the world volume. In this sense, the world volume can be thought of as representing the entire experimental setup or laboratory.

Assigning Materials:

Once the geometry is defined, users must assign materials to each solid. This can be done in two ways:

1. **Using the NIST Database:** Geant4 includes a material database from the National Institute of Standards and Technology (NIST) (National Institute

of Standard and Technology (NIST), 2017). This database contains a broad collection of predefined material properties, including elements, isotopes, and chemical compounds.

2. **Defining Custom Materials:** For maximum flexibility, users have the option of defining custom materials by specifying the precise composition of elements or isotopes, along with their density, state (solid, liquid, or gas), pressure, and temperature.

Sensitive Detectors:

Users can designate specific volumes as 'sensitive detectors' by associating them with a custom class derived from the `G4VSensitiveDetector` class. Sensitive detectors process information about particle interactions and `Hits` within these designated volumes, enabling detailed tracking of simulation data. The information that can be collected using sensitive detectors includes energy deposited, the position of interaction, and timing information, among others.

For every sensitive detector, a `Hit` class is required, which is derived from the `G4VHit` class. A `Hit` is an object in which any `Step` relevant information is stored. For every `Hit` created it is added to a vector of hits called the `HitsCollection`.

DetectorMessenger Class

The `DetectorMessenger` class is a messenger class which links to the `DetectorConstruction` class and allows users to define commands that are executed at runtime to modify various aspects of the simulation, such as detector geometries, material properties, surface properties, and other key parameters based on the simulation requirements. These commands can be issued via macro files in batch mode or through the Geant4 interactive command interface, enabling real-time modifications and fast visualisation of the impact of parameter changes. This class provides the flexibility to test different detector configurations without the need to recompile the entire simulation, which can be time-consuming.

PhysicsList Class

The `PhysicsList` class is implemented by inheriting from the abstract base class `G4VPhysicsList`. This class allows users to select and configure the physics list, which is critical for defining how particles interact with the simulated geometries. The physics list includes particle definitions and the various physics processes that govern their interactions, such as electromagnetic, hadronic, optical, and decay processes. Choosing the appropriate physics list is essential for ensuring the accuracy of the simulation, as it directly influences how particles behave within the simulated environment. Therefore, when choosing a physics list, it is important that the user has a good general understanding of the physics required for the simulation as the omission of relevant particles and/or physics interactions may lead to inaccurate simulation results.

There is no default Physics List available in Geant4, however there are predefined physics lists available.

PrimaryGeneratorAction Class

The `PrimaryGeneratorAction` class is implemented by inheriting from the abstract base class `G4VUserPrimaryGeneratorAction`. This class is responsible for generating the primary particles used in the Geant4 simulation. Users can specify the initial conditions, including parameters such as particle type, initial position, kinetic energy or momentum, and momentum direction. This class allows the definition of particle sources, which can range from a simple point source to more complex spatial and energy distributions. Additionally, this is where polarisation can be set for optical photons. There are two main particle generators used for generating primary particles in Geant4. These are:

1. `G4ParticleGun:` A simple and straightforward method for defining and shooting particles with basic configurations. Users can specify input parameters such as particle type, energy, position, and momentum direction. This method is suitable for scenarios requiring a single particle source with fixed properties.

2. `G4GeneralParticleSource` **(GPS):** A more flexible and versatile method designed for complex particle source configurations. GPS allows users to define the spectral, spatial, and angular distributions of primary particles. It also supports the definition of multiple independent sources, enabling the simulation of complex particle environments in a single run.

In addition to the mandatory classes required to construct a working simulation in Geant4, an executable main program must be created. This program links the necessary libraries and serves as the entry point for the simulation, similar to the main function in a standard C++ program. In Geant4 examples, the main program is typically named after the simulation. For instance, the main executable for the OpNovice2 example is named OpNovice2.cc.

In Geant4, each simulation run begins with an instance of the `G4Run` class. During a run, critical elements such as detector geometry, external electromagnetic fields, and other simulation parameters are locked in to ensure consistency. A `G4Run` consists of one or more `G4Event` objects, each representing an individual event in the simulation.

Each event starts with the `GeneratePrimaries()` method, implemented in the `PrimaryGeneratorAction` class, which initialises primary particles with a vertex position. These particles propagate through the simulation volumes based on the defined geometries and fields. During propagation, interactions with the medium may produce secondary particles, which are subsequently tracked.

Particle tracking is managed by `G4Track` objects, which encapsulates a particle's properties (e.g.: position, momentum, and energy). Each track is divided into `G4Step` objects, representing the particle's motion between two points. These steps record detailed information, including energy loss and position changes. Tracking stops when the particle exits a volume, loses all its kinetic energy, decays, or meets a user-defined condition for termination. While `G4Track` objects are transient, `G4Trajectory` objects store track data for visualisation and analysis.

When a particle crosses boundaries between materials, steps are defined at the

interface. Otherwise, step lengths are determined by the constraints from physics processes, with the shortest allowable step dictating the size. If a process terminates a particle or the step is below a threshold, the track is killed and the particle is no longer tracked.

Geant4 provides action classes, which gives users control over various aspects of the simulation. These include:

- `RunAction`: Controls the start and end of the simulation.
- `EventAction`: Operates on an event basis, often used to populate output data files.
- `SteppingAction`: Manages processes at the smallest increments, enabling detailed particle analysis.

The collection of output data is essential for extracting meaningful information from the simulation. Geant4 defines scoring regions, which gather data from particles or interactions. Data, referred to as 'hits', can be collected through the following methods:

- **Primitive Scorers:** These record a single quantity per event, such as energy deposition.
- **Sensitive Detectors:** These use user-defined scorers and hit classes for multi-quantity recording and in-simulation analysis. A `G4SensitiveDetector`, for example, can represent a photomultiplier tube (PMT) and record data from a specific volume.

2.6.3 Optical Physics Processes in Geant4

In Geant4, optical photons are treated as a distinct particle class, separate from gamma photons. A photon is classified as optical if its wavelength is significantly greater than the typical atomic spacing. Notably, there is no overlap or smooth

transition between gamma and optical photons in Geant4; a gamma photon cannot convert into an optical photon (Geant4 Collaboration, 2023).

When a charged particle loses energy in a scintillator, Geant4 generates the mean number of scintillation photons $\langle N_{\text{scint}} \rangle$, which is typically sampled from a statistical distribution. The mean number of photons is given by:

$$\langle N_{\text{scint}} \rangle = Y_{\text{scint}} \times E_{\text{dep}} \tag{2.23}$$

Here:

- Y_{scint} is the scintillation yield, representing the number of photons produced per unit of energy deposited.
- E_{dep} is the energy deposited in the scintillator during the particle's interaction.

The actual number of scintillation photons N_{scint} is then sampled from a statistical distribution. In Geant4, the distribution used to sample the actual number of photons can be either Gaussian or Poisson. When $\langle N_{\text{scint}} \rangle$ is smaller than 10, the emitted photons are typically sampled from a Poisson distribution with a mean of $\langle N_{\text{scint}} \rangle$. For larger values of $\langle N_{\text{scint}} \rangle$, a Gaussian distribution is often used as an approximation (Riggi et al., 2010).

Optical photons undergo various interactions, including reflection and refraction at medium boundaries, bulk absorption, Mie and Rayleigh scattering. These interactions are essential for accurately simulating the behaviour of optical photons in different materials and at medium boundaries. In Geant4, optical photons are generated through several processes, including scintillation, Cerenkov radiation, and wavelength shifting (WLS).

When optical physics processes are included in a Geant4 simulation, it is necessary to define the optical properties of the materials. For each material, a refractive index spectrum and an absorption length spectrum must be specified, where absorption length is defined as the characteristic distance in a material over

which light intensity decreases to $1/e$ (approximately 37%) of its original value, purely due to absorption processes.

For special optical materials, such as scintillators and wavelength-shifting materials, additional parameters for full characterisation are required, including emission spectra, rise times, and decay times. These parameters are typically not needed for other materials. Additionally, surface properties such as reflectivity can be assigned to optical interfaces between volumes to accurately model boundary interactions.

There are several important steps involved in simulating optical photons in Geant4. These are outlined below (Geant4 Collaboration, 2023):

1. Optical photons and their interaction processes must be specified and configured:

This is achieved by including the `G4OpticalPhysics` class in a custom physics list or directly in the `main()` application. The `G4OpticalPhysics` class provides predefined optical processes, including Cerenkov radiation, scintillation, bulk absorption, and boundary processes (such as reflection and refraction). By default, it includes all necessary optical physics processes and offers a standard configuration suitable for most applications involving optical photons.

Users can customise simulations by activating or deactivating specific processes. The configuration is managed through the `G4OpticalParameters` class and can be accessed or modified using the `G4OpticalParametersMessenger` class. For example, individual processes such as Cerenkov radiation or scintillation can be enabled or disabled via process-specific commands, which can be incorporated into macro files or invoked via C++ methods. By default, all the processes are activated.

2. Optical properties need to be assigned to the relevant materials and surfaces:

To implement optical physics processes in Geant4, optical properties must be assigned to the appropriate materials and surfaces. These properties are stored in a

`G4MaterialPropertiesTable`, which is linked to the corresponding `G4Material` or `G4OpticalSurface`. Optical properties can either be constant across photon energies or vary as a function of photon energy, depending on the simulation requirements.

3. If an optical photon is a primary particle, its polarisation must be set:

When an optical photon is used as a primary particle in Geant4, its polarisation must be explicitly set by the user to ensure accurate simulation. Specifically, the linear polarisation of primary optical photons must be defined by the user. This can be done in various ways: within the user's `PrimaryGeneratorAction` class, through user interface commands, or by using macro commands with the `G4ParticleGun` or `G4GeneralParticleSource` (GPS) methods.

For non-primary optical photons, polarisation is handled automatically. This includes optical photons generated as secondaries through processes such as scintillation and Cerenkov radiation.

2.6.4 Interactions at Medium Boundaries

In Geant4, volumes can be assigned optical surfaces to define the behaviour of optical photons at their boundaries. When an optical photon interacts with such a surface, it can undergo refraction, reflection, and absorption. The specific interaction depends on the optical properties assigned to the surface.

Optical boundaries can occur between two dielectric materials or between a dielectric material and a metal. The behaviour of a photon at a medium boundary depends on the nature of the materials that form the boundary. At a dielectric-metal interface, such as that between a scintillator and a photocathode, the photon can either be reflected back into the dielectric or absorbed by the metal. If absorbed, the photon may be detected, depending on the photoelectron efficiency of the metal. Conversely, at a dielectric-dielectric interface, such as between a scintillator and the surrounding air, the photon can be absorbed, reflected, or refracted.

In Geant4, there are three primary methods for defining an optical surface. The method chosen by the user is dependent on the requirements of the simulation. These methods can be categorised as follows: simple case, skin surface, and border surface. Each is summarised below (Geant4 Collaboration, 2023).

1. Simple Case: For a perfectly smooth interface between two dielectric materials, the optical surface can be defined using the refractive indices of the two materials. These refractive indices are stored in the corresponding `G4MaterialPropertiesTable` of the materials. This approach is straightforward and suitable for simulations where a smooth boundary with minimal complexity is required.

2. Skin Surface: A skin surface applies to all external faces of a single logical volume, effectively creating a virtual wrapping around it. This method is particularly useful for simulating scenarios where a scintillator is wrapped in materials such as Teflon, aluminium foil, or other reflective materials. It is especially advantageous when the entire outer surface of the volume requires uniform treatment, as it simplifies the implementation. However, a limitation of this approach is that the skin surface must exhibit the same optical properties across all sides of the enclosed volume, which may restrict its applicability in cases where non-uniform surface properties are required.

3. Border Surface: A border surface is defined specifically at the interface between two physically adjacent volumes, each with its own refractive index. It is specified by defining an ordered pair of physical volumes that share the boundary. The ordering allows different optical properties to be assigned for photons approaching the interface from opposite directions. This method enables precise modelling of optical properties specific to the boundary between volumes. For instance, a border surface can be used to simulate a scintillator enclosed within a reflective housing.

2.6.4.1 Surface Models

Geant4 provides several models to simulate the interaction of optical photons with surfaces, determining how photons are reflected, refracted, or scattered. As of Geant4 version 11.3, the available models are: GLISUR, UNIFIED, LUT, and LUT-DAVIS.

The GLISUR Model

The GLISUR model, inherited from Geant3, is the original optical surface model in Geant4. While it shares some features with the more advanced UNIFIED model, it offers fewer options for surface finishes and reflection mechanisms. If no optical surface model is specified by the user, Geant4 defaults to the GLISUR model with a polished surface finish, unless a different surface model or finish is explicitly defined.

For dielectric-metal interfaces, or when the GLISUR model is explicitly chosen, only two surface finish options are available: `polished` and `ground`. The surface finish determines the reflection characteristics and is related to surface roughness. A polished surface corresponds to a smooth, mirror-like finish, resulting in specular-dominated reflection, whereas a ground surface represents a rougher surface, leading to a mixture of specular and diffuse reflections.

The GLISUR model also includes a *polish* parameter that quantifies surface roughness. This parameter ranges from 0 to 1, with 1 indicating a perfectly polished surface, and lower values corresponding to increasing roughness.

In the GLISUR model, the surface is represented as a collection of microfacets. These are small, microscopic features that describe surface roughness. Even surfaces that appear smooth on a macroscopic scale typically have microscopic roughness. Therefore, the surface can be thought of as consisting of microfacets oriented at different angles. These microfacets contribute to complex scattering and reflection behaviour.

When a photon undergoes reflection, a microfacet is randomly selected from a distribution of these microfacets. The roughness is described by these microfacets,

which influence the direction of the reflected or refracted photons. The microfacet normal is calculated as the sum of two vectors: the average surface normal and a second vector that is randomly selected from a sphere of radius (1- `polish`), where the value of `polish` is less than 1. This second vector is added to the first, resulting in the orientation of the microfacet.

The UNIFIED Model

The UNIFIED model was initially developed for simulating reflectors and surface finishes for scintillators (Levin and Moisan, 1996).

It is a more detailed and versatile model compared to the GLISUR model, supporting a broader range of reflection types and offering additional options for surface finishes. This model provides greater control over the optical behaviour of a surface by incorporating parameters such as surface roughness and reflection probabilities. Users can specify the type of surface interface, surface finish, and associated reflection probabilities. Like the GLISUR model, the UNIFIED model is based on a distribution of microfacet orientations. The standard deviation of the microfacet orientation distribution that defines the macro-surface is represented by a surface roughness parameter, σ_α, for ground surface types. Depending on the selected finish type, the model uses either a global normal or an average microfacet normal for reflection calculations.

The model allows for the definition of the interface between two dielectric materials using the following surface finish options:

- `polished`
- `ground`
- `polishedbackpainted`
- `groundbackpainted`
- `polishedfrontpainted`

- `groundfrontpainted`

For the interface between a dielectric and a metal, the available finish types are `polished` and `ground`. The physical processes occurring at the surface depend on the chosen surface finish.

The UNIFIED model also supports the modelling of wrapped surfaces that include an air gap between the wrapping material and the scintillator. These surfaces are referred to as `backpainted`.

The UNIFIED model offers four types of surface reflections, with the individual probabilities of each reflection type able to be set by the user. These probabilities must sum to 100% of the reflected light. If the user selects a specular lobe reflection type, the surface distribution parameter, σ_α, must be specified. The four reflection types are:

1. Specular Spike: This type describes the probability of reflection around the average surface normal. The reflected photon behaves similarly to one reflected from a perfect mirror, being reflected symmetrically around the average surface normal. This results in a sharp reflection 'spike' with little to no scattering, with most light being reflected in a very narrow cone around the normal.

2. Specular Lobe: This reflection type models the probability of reflection based on the orientation of the surface microfacets. The microfacets are distributed according to a Gaussian distribution centred around the average surface normal. This results in a broader reflection peak compared to the specular spike, with light scattered around the microfacet normal rather than around the average surface normal.

3. Diffuse Lobe: This reflection type models diffuse reflection according to the Lambertian law. In this model, the probability of a photon being reflected is proportional to the cosine of the angle θ, between the surface normal and the direction of the incoming photon. This type of reflection is isotropic within the

hemisphere above the surface, meaning light is scattering uniformly in all directions.

4. Backscatter: This describes a scenario where a photon undergoes multiple reflections within deep microfacet grooves, ultimately being reflected back in the direction from which it came.

Each surface finish type corresponds to a specific set of reflection mechanisms, as outlined below:

- `polished`: Fresnel reflection, total internal reflection, and refraction.
- `polishedbackpainted`: Specular lobe reflection, specular spike reflection, backscatter, diffuse reflection, refraction, and absorption.
- `polishedfrontpainted`: Specular lobe reflection, spike reflection, backscatter, diffuse reflection, and absorption.
- `ground`: Specular lobe reflection, specular spike reflection, backscatter, diffuse reflection, and refraction.
- `groundbackpainted`: Specular lobe, specular spike, backscatter, diffuse reflection, refraction, and absorption.
- `groundfrontpainted`: Diffuse lobe and absorption.

Further details on the reflection mechanisms available for different combinations of surface and finish types for the UNIFIED model is shown in Figure 2.4.

LUT and LUT-DAVIS Models

One key issue with the models previously described, particularly the UNIFIED model, is their heavy reliance on the estimation of several parameters, which can be challenging to even experienced Geant4 users. Notably, the UNIFIED model assumes that the four reflection-type probabilities are constant, irrespective of the incidence angle of the light. However, this assumption does not fully agree with

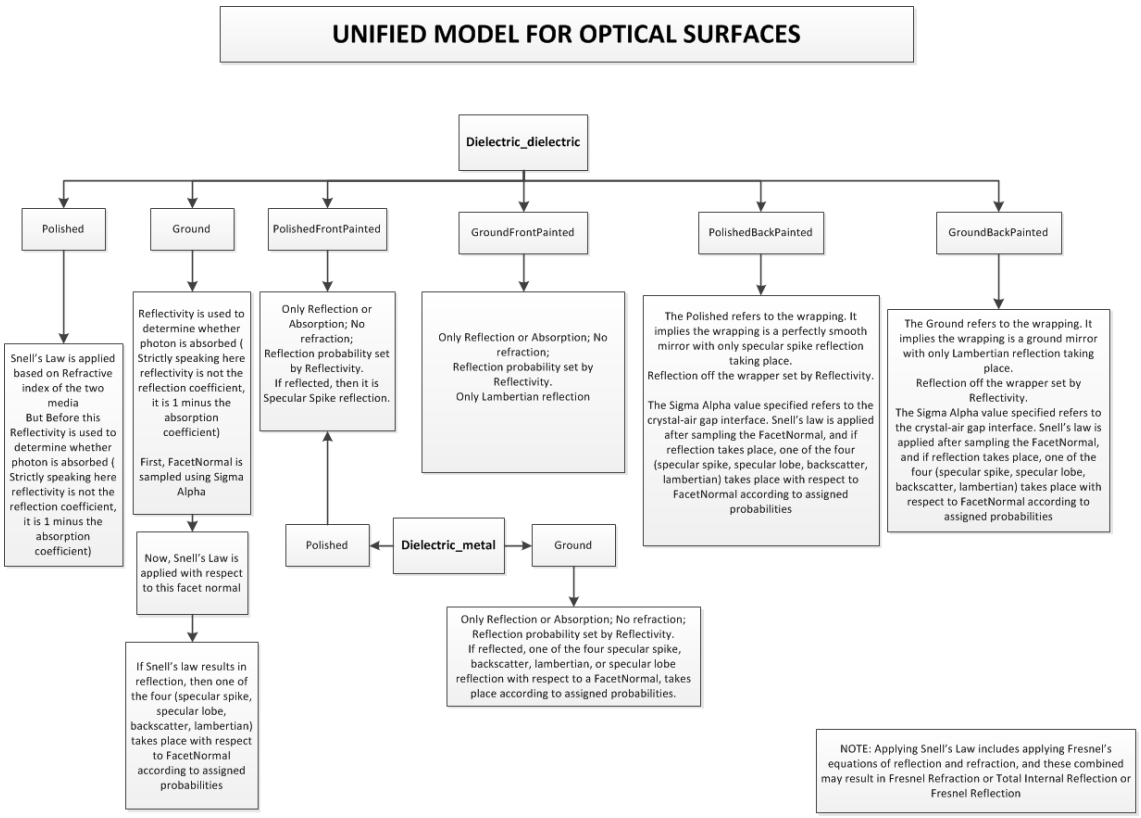

Figure 2.4: UNIFIED Model. Reproduced from Geant4 Collaboration, 2023

experimental data. Additionally, the value of the sigma alpha parameter, which is important for the UNIFIED model, is difficult for most users to estimate, even when they have a method to measure it (Janecek and Moses, 2010).

Look-Up Tables (LUTs) offer a potentially more accurate approach to modelling a variety of optical surfaces in Geant4, as they utilise experimentally measured data. Janecek and Moses (Janecek and Moses, 2010) incorporated experimental measurements of angular reflectivity distributions within BGO scintillator crystals, considering various surface treatments and reflector materials. By combining different surface conditions (e.g.: rough-cut or chemically etched surfaces) and reflector materials (e.g.: Teflon or ESR film), LUTs allow for the modelling of more complex surfaces and has been integrated into the Geant4 framework.

An alternative approach that also incorporates experimental data for surface modelling in Geant4 is the LUT-DAVIS model. This model is based on 3D surface reflectance measurements using atomic force microscopy (AFM) (Roncali and Simon R Cherry, 2013; Roncali, Stockhoff, and Simon R. Cherry, 2017; Stockhoff et al., 2017). The team scanned both polished and unpolished crystal surfaces and calculated the angular distributions of reflected photons for various incidence angles. The model accommodates different surface finishes — rough and polished — while the degree of roughness is determined experimentally. Additionally, coupling agents, such as air and optical grease, can be modelled.

Chapter 3

Methodology

This chapter outlines the simulation tools and analytical methods employed in this research. First, a detailed overview of the Geant4 simulation setup is provided, highlighting the key components that remain consistent across all simulation studies presented in this thesis, including the input parameters used for modelling the EJ-276 plastic scintillator. Next, the specific configurations for each simulation study are described, along with the methods and techniques used for data collection and analysis.

3.1 Simulation Setup

The Monte Carlo toolkit Geant4 (version 11.2) was used for all simulations presented in this thesis. The physics list employed in these simulations consisted of the QGSP_BIC_HP_EMZ reference list (Geant4 Collaboration, n.d.), along with with the `G4OpticalPhysics` class, which is essential for modelling the production and transport of scintillation photons. The default production cut of 1 mm was applied.

The QGSP_BIC_HP_EMZ list is a predefined, validated physics list distributed with Geant4. It is based on the QGSP_BIC list for hadronic interactions but includes High Precision (HP) neutron models for neutron energies below 20 MeV, the energy range relevant for this work. These HP models use evaluated cross-section data from

the G4NDL library, which is based on nuclear data from JEFF-3.3, to accurately simulate neutron elastic scattering, inelastic scattering, and capture reactions (NEA Nuclear Data Services, 2022). Additionally, the EMZ component incorporates `G4EmStandardPhysics_option4`, providing the most precise electromagnetic physics models currently available in Geant4.

Geant4 simulations were conducted to investigate the influence of key detector parameters on the neutron- and gamma-induced pulse shapes generated in an EJ-276 pulse shape discrimination (PSD)-capable plastic scintillator. The simulation geometry was implemented in the `DetectorConstruction` class, in which three distinct volumes were defined.

1. The World volume.
2. The EJ-276 plastic scintillator.
3. The photodetector.

The scintillator and photodetector were constructed and positioned within the World volume. For modularity and clarity, material properties — including optical properties and associated material property tables — were managed in a separate, custom `Materials` class, rather than being directly defined within `DetectorConstruction`. This approach separates material definitions from the construction and placement of the detector volumes, enhancing modularity and clarity in the simulation setup.

The three constructed volumes in Geant4 are shown in Figure 3.1, while a redrawn version focusing on the EJ-276 scintillator and photodetector is shown in Figure 3.2, highlighting the volumes and axes.

The World volume was defined with air as the constituent material. This material was sourced from the NIST database, which provides accurate material properties, including density and refractive index, without requiring the user to explicitly specify them (Geant4 Collaboration, 2023). The use of air for the World volume is typical

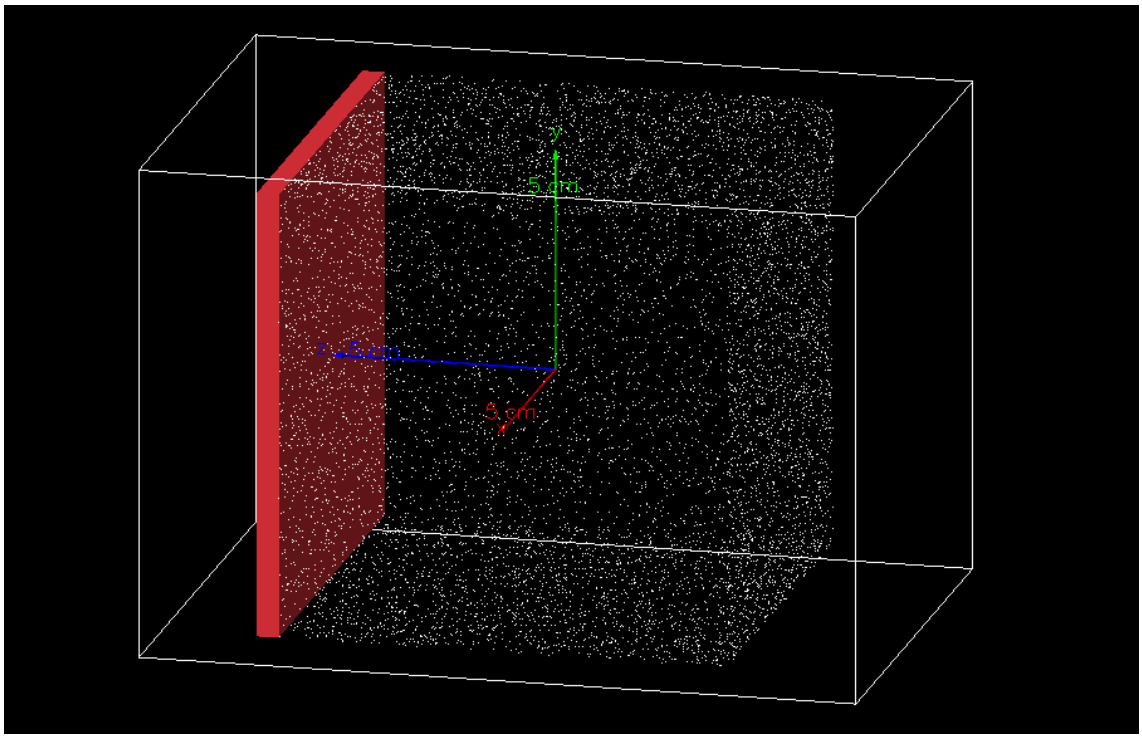

Figure 3.1: A cuboid volume of a 10 cm^3 EJ-276 plastic scintillator, with the photodetector shown in solid red and coupled by air to one side of the scintillator volume. Both the scintillator and the photodetector are placed inside the world volume, often referred to as the 'mother' volume.

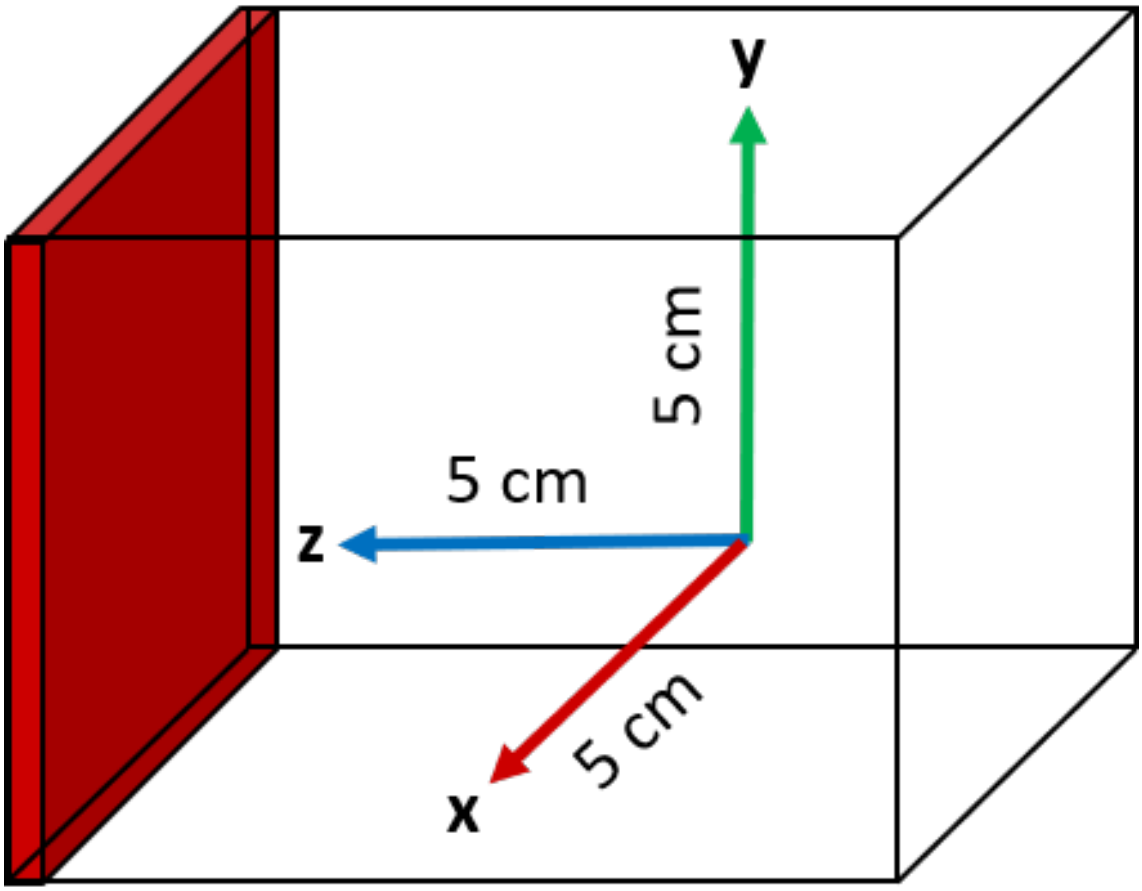

Figure 3.2: Redrawn cuboid volume of a 10 cm^3 EJ-276 plastic scintillator, showing the photodetector in solid red. This figure highlights the axes and dimensions of the scintillator and photodetector volumes and is redrawn from Figure 3.1

.

in simulations where the surrounding environment is assumed to be empty or non-interacting.

Table 3.1: Material properties of EJ-276 plastic scintillator used as input to the EJ-276 `G4MaterialPropertiesTable`.

Material Property	**EJ-276**
Scintillation Yield	8600/MeV
H atoms per cm^3 ($\times 10^{22}$)	4.53
C atoms per cm^3 ($\times 10^{22}$)	4.89
Density	1.096 g/cm^3

3.1.1 EJ-276 Plastic Scintillator

EJ-276 is a PSD-capable plastic scintillator developed by Eljen Technologies, composed primarily of hydrogen and carbon.

Figure 3.3 shows experimentally measured time-dependent EJ-276 pulses, illustrating the characteristic pulse shapes resulting from neutron and gamma interactions in the detector using an Americium-Beryllium (AmBe) source. The figure presents the average neutron- and gamma-induced pulses after photodetection with a silicon photomultiplier (SiPM) and subsequent signal processing. These pulses therefore reflect the combined effects of scintillation light emission, the photodetector response, electronic noise, and serve as an example of the typical experimental pulse shapes produced by EJ-276.

As stated in Section 2.5.1, when PSD is performed using the Charge Comparison Method (CCM), the result is a two-dimensional histogram in which the PSD parameter (Q_{long}/Q_{short}) is plotted against energy. An example of such a histogram for experimental measurements with EJ-276 is shown in Figure 3.4 (Boxer et al., 2023).

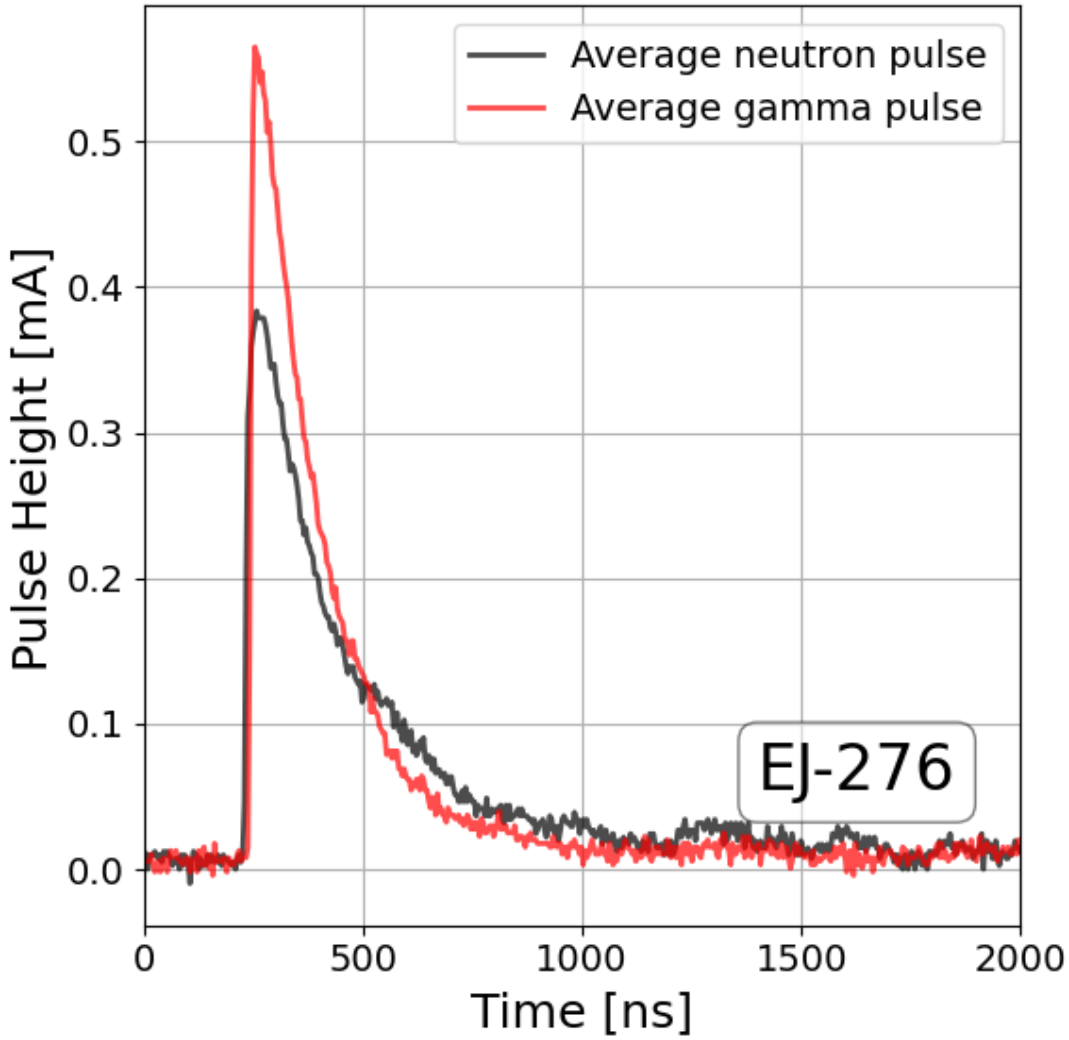

Figure 3.3: Average measured neutron and gamma pulse shapes in EJ-276 corresponding to a 100 keV_{ee} interaction, obtained using an AmBe source. Image reproduced from (Boxer et al., 2023).

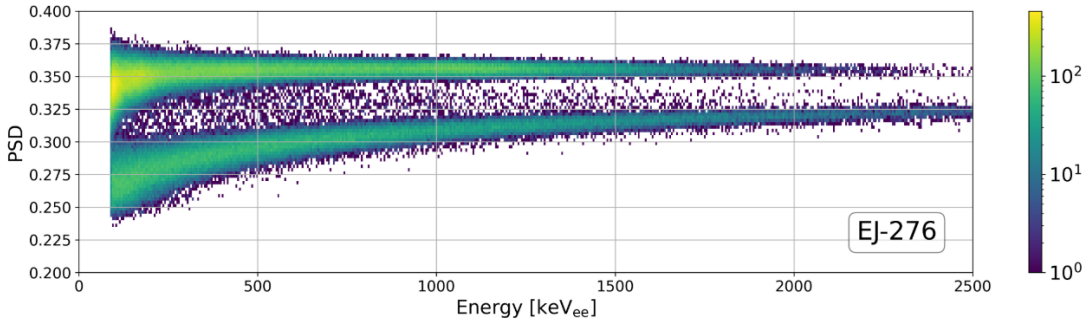

Figure 3.4: Pulse shape discrimination (PSD) values as a function of electron-equivalent energy for events above 90 keV$_{ee}$ in EJ-276 using an AmBe mixed source. Image reproduced from (Boxer et al., 2023).

The EJ-276 scintillator material was constructed in a custom Materials class, based on the constituent elements and properties provided in the Eljen Technologies data sheet (Eljen-Technology, 2017), reproduced in Appendix 9.1. Portions of the implementation were adapted from (Hubbard, Paul J Sellin, and Lotay, 2020) to construct both the EJ-276 material and its optical properties. The resulting parameters are summarised in Table 3.1, with the full EJ-276 material definition given in Appendix 9.2.

The optical properties used for all Geant4 simulations with EJ-276 are listed in Table 3.2. Instead of adopting the gamma and neutron decay time constants provided by the manufacturer, the simulations employed experimentally determined values reported by Iwanowska-Hanke et al., 2014 for EJ-299-34 — the predecessor to EJ-276. These values include relative intensity data for each decay component, enabling more accurate pulse shape modelling within the simulation framework.

The EJ-276 emission spectrum is shown in Figure 3.5. Wavelengths were converted to photon energy (eV) as required by Geant4 (Erik Dietz-Laursonn, 2016), and tabulated along with along with corresponding light outputs in the `G4MaterialPropertiesTable`.

Table 3.2: Optical properties of EJ-276 plastic scintillator used in the EJ-276 `G4MaterialPropertiesTable`.

Optical Property	**EJ-276**
Scintillation Yield	8600/MeV
Refractive Index	1.58
Absorption Length	3.8 m
Rise Time	0.9 ns
Birk's Constant	0.126 mm/MeV
Decay Time Constants (gamma excitation)	4.3 ns, 18 ns, 140 ns
Relative Intensity (gamma)	74%, 14%, 12%
Decay Time Constants (neutron excitation)	4.5 ns, 20 ns, 170 ns
Relative Intensity (neutron)	58%, 18%, 24%

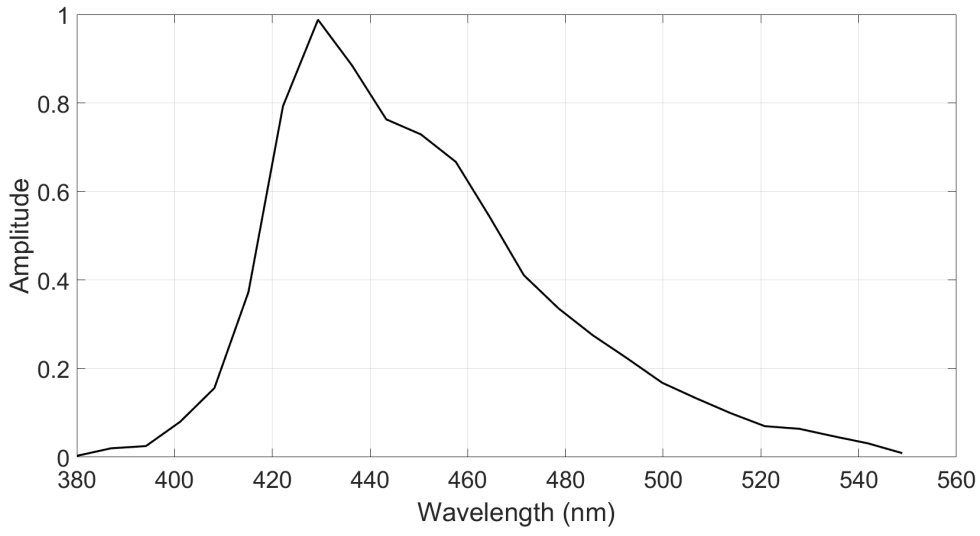

Figure 3.5: Emission spectrum for EJ-276 plastic scintillator.

Certain optical properties — specifically the refractive index, bulk absorption length, and rise time — were unavailable from the Eljen Technologies data sheet or published literature and rise time is deactivated by default in Geant4. Consequently, values were sourced from the EJ-200 plastic scintillator data sheet (Eljen Technology, 2023), owing to its compositional similarity to EJ-276. It should be noted that, while EJ-200 does not exhibit PSD capabilities, its bulk absorption properties were considered sufficiently comparable for this purpose. To account for quenching effects, Birk's Constant was set to 0.127 mm/MeV a standard value used for plastic scintillators (Torrisi, 2000).

The absorption length is the mean free path for absorption: the average distance an optical photon will travel before being absorbed in the material. Absorption length is wavelength dependent and therefore in Geant4 it is defined as dependent on the emission spectrum of the scintillator.

Both the EJ-276 scintillator and the photodetector volumes were designated as `G4SensitiveDetector`'s within the `DetectorConstruction` class to record hits and collect relevant data. Sensitive detectors were preferred over primitive scorers as they allow multiple quantities — such as time and energy — to be recorded for each event. The photodetector was modelled as a simple detecting region composed of borosilicate glass, a material commonly used in photomultiplier tube (PMT) windows (Knoll, 2000).

For all simulations, the `G4GeneralParticleSource` (GPS) was employed as the primary particle generator. GPS was chosen over `G4ParticleGun` because it enables the modelling of complex particle sources, providing greater flexibility over parameters such as particle type, energy, and position. The particle source (1 MeV neutrons or gamma-rays) was located at co-ordinates $X = 0$ mm, $Y = 25$ mm, and $Z = 0$ mm for all Geant4 simulations.

A Random Number Generator (RNG) was implemented in the simulation's `main()` program and seeded with a unique value each time the simulation was run. The RanecuEngine, a pseudo-random number generator, was selected for this

purpose. Seeding was based on the system time, ensuring the random number sequence differed between simulation runs. This variability was essential, as it prevented simulations from producing identical results in different runs, thereby avoiding determinism and enabling a more accurate statistical representation of the stochastic processes involved in photon production and transport.

Detector hits were handled by custom sensitive detector classes. Data collected were stored in histograms for immediate visualisation and analysis using the built-in ROOT interface via the `G4AnalysisManager` class (Brun and Rademakers, 1997). In parallel, data were saved as ASCII files to ensure maximum flexibility in subsequent data analysis using MATLAB. A custom `Analysis` class managed data collection and processing, with the `G4AnalysisManager` used for histogramming and file output at the end of each event.

Throughout this thesis, the term "Gaussian-like" is used to describe the shapes of certain simulated neutron- and gamma-induced pulses. For clarity, this refers to the overall shape of the pulses, which visually resemble a Gaussian distribution, without implying a strict analytical or mathematical Gaussian fit.

3.2 Scintillator Geometry and Length

Geant4 simulations were performed to investigate how variations in the geometrical shape and length of an EJ-276 plastic scintillation detector affect the neutron- and gamma-induced pulse shapes. Three geometries were considered — cuboid, cylinder, and slab — as these are commonly employed in plastic scintillator designs. These simulated geometries are shown in Figure 3.6.

In all simulations, two dimensions were held constant while the length along the Z-axis was systematically varied. For each geometry, the photodetector face was matched to the corresponding scintillator face to ensure consistent optical coupling. Scintillator lengths of 50 mm, 100 mm, 200 mm, 400 mm, 1000 mm, and 2000 mm were simulated, with 1000 events generated for each particle type.

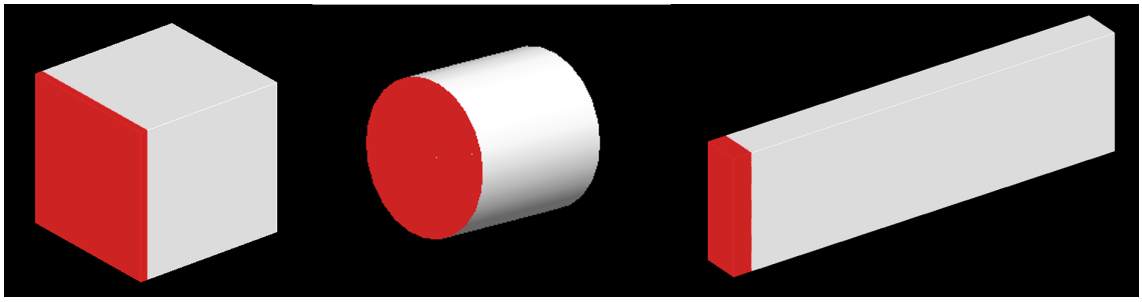

Figure 3.6: From left to right, cuboid, cylinder, and slab geometries, with the photodetector highlighted in red.

Photon arrival times at the photodetector surface were recorded using the `GlobalTime()` method of the photodetector's sensitive detector class, which registers the time at which each photon reaches the photodetector relative to the start of the event. This distribution represents the resulting light pulses after scintillation and optical photon transport through the detector volume.

Simulations were executed in batch mode using a custom macro file, enabling systematic variation of scintillator length while collecting data in both histogram and ASCII formats. The recorded times incorporate the intrinsic scintillation emission time, governed by the scintillator's decay time constants, as well as the optical photon transit time through the scintillator. No additional timing corrections were applied.

To simplify the simulations and ensure that only a single variable was altered per run, an isotropic 1 MeV point source of either neutrons or gamma rays was used. This energy was selected because it is characteristic of emissions from radioactive sources and nuclear reactions involving gamma and neutron radiation. Separate simulation runs were conducted for each particle type. A binning resolution of 0.5 nanoseconds (ns) was employed to capture subtle differences in pulse shapes between gamma rays and neutrons, as well as variations arising from changes in scintillator geometry.

No explicit optical surfaces were defined in these simulations to isolate the effects

of geometrical shape and length on neutron- and gamma-induced pulse shapes. Reflective coatings and wrapping, which are known to influence scintillation pulse characteristics, were deliberately excluded at this stage. In the absence of explicitly defined optical surfaces, Geant4 defaults to a perfectly polished surface with a dielectric_dielectric interface. Under this configuration, optical photon interactions — such as reflection and refraction — are governed solely by Snell's Law and the Fresnel equations, which depend on the refractive indices of the adjacent materials. Surface roughness, boundary absorption, and diffuse scattering are not considered unless explicitly modelled (Khodaei et al., 2023).

Consequently, absorption at medium boundaries does not occur, and photons propagate through materials until they are absorbed in the bulk (as defined by the material's attenuation length via the `ABSLENGTH` property in the `G4MaterialPropertiesTable`) or reach a `G4SensitiveDetector`. Only specular (mirror-like) reflection is possible under the default model. The Fresnel equations determine the probability of reflection versus transmission at an interface, based on the angle of incidence and the refractive indices of the two materials. Without the explicit specification of an optical surface in Geant4, phenomena such as diffuse reflection, boundary absorption, or micro-facet scattering, cannot occur.

To perform pulse shape discrimination (PSD) on the simulated data, a large number of pulses needed to be generated for each particle type. Due to the computationally intensive nature of optical photon generation and transport in Geant4, the High-End Computing Cluster (HEC) at Lancaster University was utilised (Mike Pacey, 2023). A total of 1000 pulses were generated for each particle type, balancing the need for statistical robustness with the computational resources available.

The simulated data were collected in ASCII format and subsequently combined and analysed using a bespoke MATLAB script to produce gamma/neutron pulse shape plots. In these plots, the X-axis represents the photon arrival time in nanoseconds, while the Y-axis shows the amplitude, corresponding to the photon

count per time bin.

For each geometry and scintillator length, the gamma and neutron pulse data were first summed to average out random fluctuations and then normalised using MATLAB's `normalize(..., 'range')` function. This process linearly scaled each pulse shape to the range [0,1], ensuring that all pulses shared a common amplitude scale and could be directly compared in shape. The normalisation preserved key temporal characteristics — such as the rise time, decay times, and peak position — that are crucial for effective pulse shape discrimination (PSD). Consequently, this approach allowed for a shape-based comparison independent of amplitude, which naturally varies between neutron and gamma-ray interactions due to their differing interaction mechanisms within the scintillator material. Additionally, all pulses were aligned by their respective peak positions to facilitate direct temporal comparison.

The bespoke MATLAB script was used to sum individual pulses, but also to apply the Charge Comparison Method (CCM) for pulse shape discrimination (PSD) using the simulated pulses. Numerical integration was performed using MATLAB's trapz function, which calculates integrals based on the trapezoid rule. This method approximates the area under a curve by dividing it into trapezoidal segments and summing their areas.

The long integral was defined as the total area under the normalised pulse, representing the full integral of the summed simulated pulse.

The short integral value was selected based on the time point at which the difference between the normalised neutron and gamma pulses was greatest — that is, where the separation between the two pulse shapes was largest, with the neutron pulse exceeding the gamma pulse. This was determined using the summed, noise-free, normalised pulses obtained from the HEC.

To identify the optimal short integral point, a point-by-point difference was computed between the normalised summed gamma and neutron pulses. A negative value in this difference indicates that the neutron pulse is larger than the gamma at that moment in time. The first minimum of this difference curve — where the

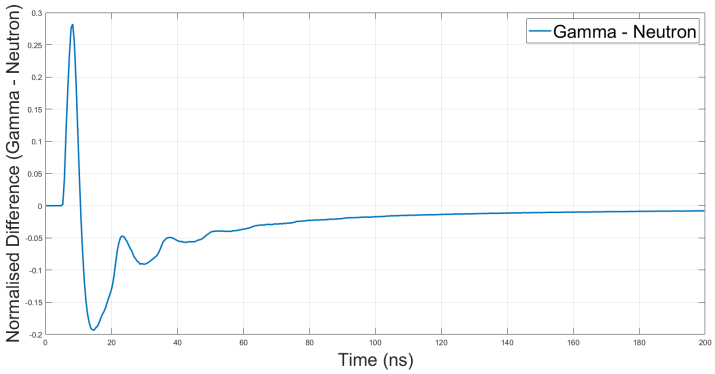

Figure 3.7: Difference curve used to determine optimal short integral values. In this case, for the 50 mm slab scintillator.

neutron pulse is most dominant relative to the gamma — was selected as the short integral for pulse shape discrimination (PSD) calculations. An example of this difference curve is shown in Figure 3.7.

3.3 Optical Surfaces

To evaluate the impact of different optical surface types , wrappings, and finishes on the neutron- and gamma-induced light pulse shapes from an EJ-276 plastic scintillation detector, and to assess the subsequent pulse shape discrimination (PSD) performance, a series of simulations were performed using Geant4. In these simulations, various `G4OpticalSurface` properties were applied to the scintillator volume, while all other parameters were held constant. The surfaces modelled were chosen to replicate reflectors and surface finishes commonly used in scintillation detectors.

The reflector materials simulated were: Teflon, EJ-510 reflective paint, Aluminium foil, and Enhanced Specular Reflector (ESR) film. The UNIFIED surface model was employed for all surfaces, with the surface type set as `G4SkinSurface`, which is typically used to model volumes coated or wrapped with a reflector material. For Teflon, two different surface finishes were explored: `groundbackpainted` and

`polishedbackpainted`. In the `groundbackpainted` configuration, the scintillator surface is rough, resulting in predominantly diffuse reflections, while the `polishedbackpainted`configuration assumes a smooth surface, leading to more specular reflections.

The specific simulation parameters applied to each reflector type are summarised in Table 3.3. When `backpainted` surfaces are defined using the UNIFIED model in Geant4, the simulation implicitly assumes the presence of a thin air gap between the scintillator surface and the reflective wrapping. This virtual gap represents the physical separation that occurs when no optical coupling (e.g.: optical grease) is used. Consequently, for reflector configurations that involve wrapping around the scintillator, the refractive index of the air gap must be explicitly defined to accurately model photon interactions at the interface.

The photocathode was modelled with a `G4OpticalSurface` with 100% efficiency for photon detection. This is an idealised assumption in order to investigate the effects of varying different detector parameters in the simulations undertaken. The optical surface defined for the photodetector is shown in Appendix 9.2

3.4 Simulating Photodetector Noise

In experimental scintillation detector systems, output signals are affected by several sources of photodetector noise, which can degrade signal quality and consequently impact the pulse shape discrimination (PSD) performance of the detector. To assess the influence of these noise sources on PSD performance, photodetector noise was modelled using MATLAB (version 2023b).

Two primary types of noise were modelled: shot noise, which is signal-dependent and scales with the pulse amplitude, and Gaussian noise, which is signal-independent and represents a fixed background contribution. These noise types reflect the dominant noise sources in photomultiplier tubes (PMTs): Gaussian noise represents noise sources such as dark noise, while shot noise arises from the discrete, statistical

Table 3.3: Optical surface parameters simulated for various reflector materials in Geant4.

Material	**Model**	**Finish**	**Rindex**	**Reflectivity**	**Material Type**	σ_α	**Specular Lobe**	**Specular Spike**
Teflon	UNIFIED	GBP	1.0 (air gap)	0.98	dielectric_dielectric	0.2	0	0
Aluminium Foil	UNIFIED	PBP	1.0 (air gap)	0.95	dielectric_dielectric	0	0	1.0
EJ-510	UNIFIED	GFP	N/A	0.97	dielectric_metal	0.2	0	0
Teflon	UNIFIED	PBP	1.0 (air gap)	0.98	dielectric_dielectric	0	0.5	0.2
ESR Film	UNIFIED	PBP	1.0 (air gap)	0.98	dielectric_dielectric	0	0	1

nature of electric charge; it is present in any system in which current flows and is characterised by a Poisson distribution, as detailed in Section 2.4.2. These noise components were implemented using a custom MATLAB script, provided in Appendix 9.4.

The simulated noise was applied to previously collected neutron and gamma pulse shape data collected from the geometrical and optical surface simulations. Shot noise was added to each sample of a pulse, with amplitude proportional to the square root of the signal, to model its signal dependent nature. Gaussian noise was added by drawing a random value for each sample from a normal distribution with mean zero and a fixed standard deviation, representing signal-independent background fluctuations such as PMT noise. Although the noise values differ for each sample, the typical magnitude of fluctuations is determined by the chosen standard deviation

The Gaussian noise levels investigated, defined as the standard deviation of the Gaussian distribution, were: 2×10^2, 4×10^2, 8×10^2, 1×10^3, and 2×10^3. For each Gaussian noise level, shot noise was also included, resulting in a combined contribution of Gaussian noise and shot noise. Shot noise was included in all cases because it represents a fundamental, unavoidable component of electronic systems and therefore reflects the realistic operating conditions of a photomultiplier.

Figure 3.8 shows how this combination of two noise types (shot noise plus Gaussian noise with a noise level of 1×10^3) affects the average Geant4-simulated pulse shapes for neutron- and gamma-induced pulses in a slab scintillator with dimensions 20 mm $\times$ 50 mm $\times$ 400 mm.

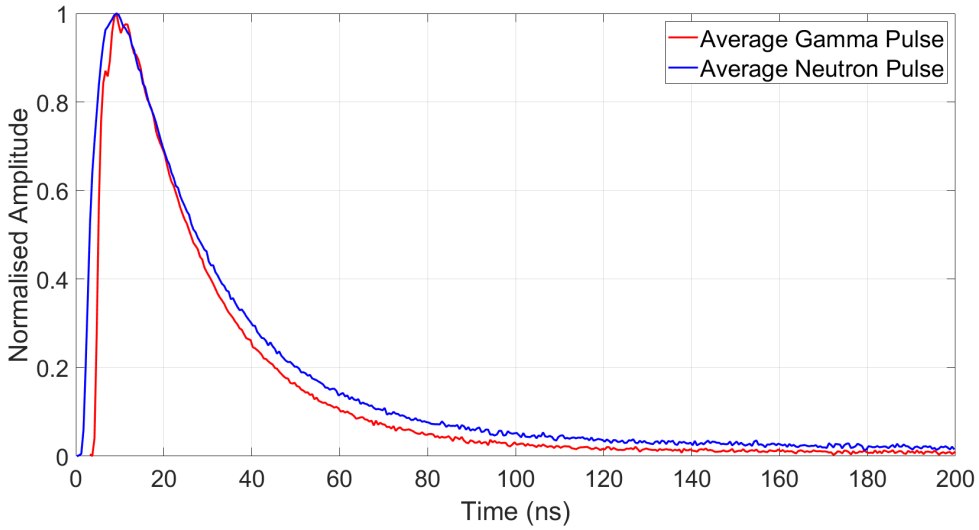

Figure 3.8: Average neutron and gamma pulse shapes affected by combined shot and Gaussian noise, with a Gaussian noise level of 1×10^3, for a slab scintillator geometry.

Chapter 4

Scintillator Geometry and Length

This chapter presents results from Geant4 simulations evaluating how variations in the geometry and length of an EJ-276 plastic scintillator affect the shapes of light pulses generated by 1 MeV neutron and gamma-ray interactions, and how these changes influence pulse shape discrimination (PSD) performance across the geometries studied. To isolate geometrical effects, only one dimension of the scintillator — along the Z-axis — was varied at a time, while the photodetector size (`G4SensitiveDetector`) was kept constant across all configurations.

No explicit optical surface was defined in these simulations. Consequently, Geant4 applied its default boundary handling at the interfaces, treating them as perfectly polished dielectric-dielectric boundaries, with photon reflection and transmission governed by the Fresnel equations.

The simulated light pulses represent the arrival time distributions of scintillation photons at the photodetector surface. These distributions characterise the pulse shapes following scintillation emission and photon transport through the scintillator, but prior to conversion and signal amplification by a photodetector, and before the influence of readout electronics. Each pulse shape shown is the sum of 1000 independent simulation runs, with 1000 primary particles (either neutrons or gamma rays) simulated per run.

In each case, the peak amplitude corresponds to the maximum number of

scintillation photons detected per time bin at the photodetector surface. To enable comparison, the pulses were normalised so that their peak amplitude was 1, allowing analysis of their temporal shapes independent of amplitude. Furthermore, the pulses were temporally aligned at their respective peak positions to facilitate direct comparison of their shapes.

The particle source (1 MeV neutrons or gamma rays emitted isotropically) was located at co-ordinates $X = 0$ mm, $Y = 25$ mm, and $Z = 0$ mm for all Geant4 simulations, placing it on the top surface of the scintillator.

4.1 Slab Geometry

This section presents simulation results evaluating the impact of increasing the scintillator length along the Z-axis for an EJ-276 plastic scintillator with a slab geometry. The dimensions along the X- and Y-axes were fixed at 20 mm and 50 mm, respectively, while the photodetector volume was held constant at 20 mm $\times$ 50 mm $\times$ 5 mm. The study investigates how changes in Z-axis length influence the shape of scintillation light pulses generated by neutron and gamma-ray interactions and explores the resulting implications for pulse shape discrimination (PSD) performance.

Figure 4.1 shows the summed light pulses obtained for varying Z-axis lengths ranging from 50 mm to 200 mm, prior to normalisation and temporal alignment. As the scintillator length increases, notable changes in pulse shape are observed. Neutron-induced pulses consistently exhibit lower peak amplitudes — a result of quenching effects — and show a delayed onset compared to gamma-ray-induced pulses. This delay arises from the differing interaction mechanisms: gamma rays primarily interact via prompt Compton scattering, whereas neutrons undergo slower nuclear recoil interactions, as discussed in Section 2.2.2.

The highest peak amplitude occurs for the 50 mm slab, while the lowest peak amplitude occurs for the 200 mm slab.

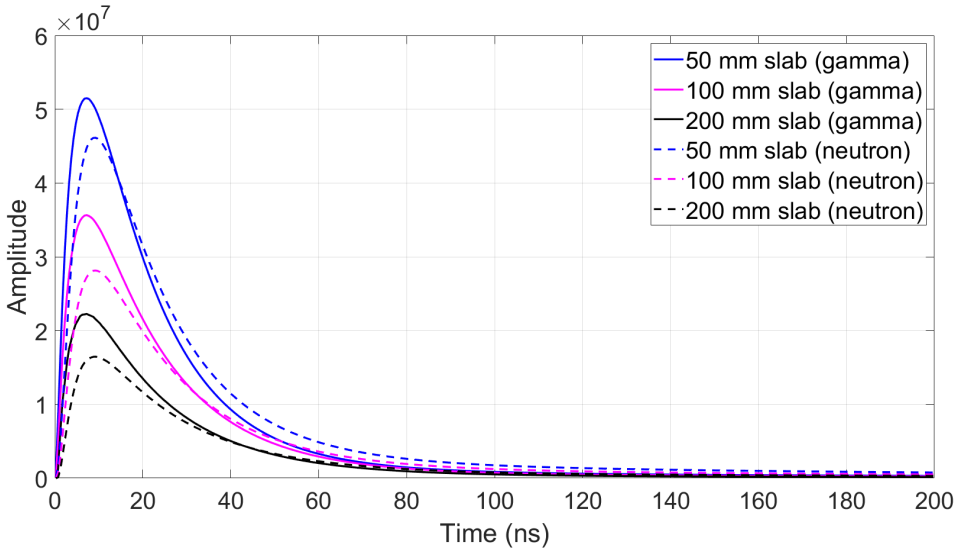

Figure 4.1: Summed simulated light pulses from neutron (dotted) and gamma-ray (solid) interactions in an EJ-276 plastic scintillator with slab geometry. Scintillator lengths along the Z-axis range from 50 mm to 200 mm. Each pulse shape represents the sum of 1000 pulses before normalisation and temporal alignment. The Y-axis shows amplitude, corresponding to photon counts per time bin, while the X-axis represents photon arrival time.

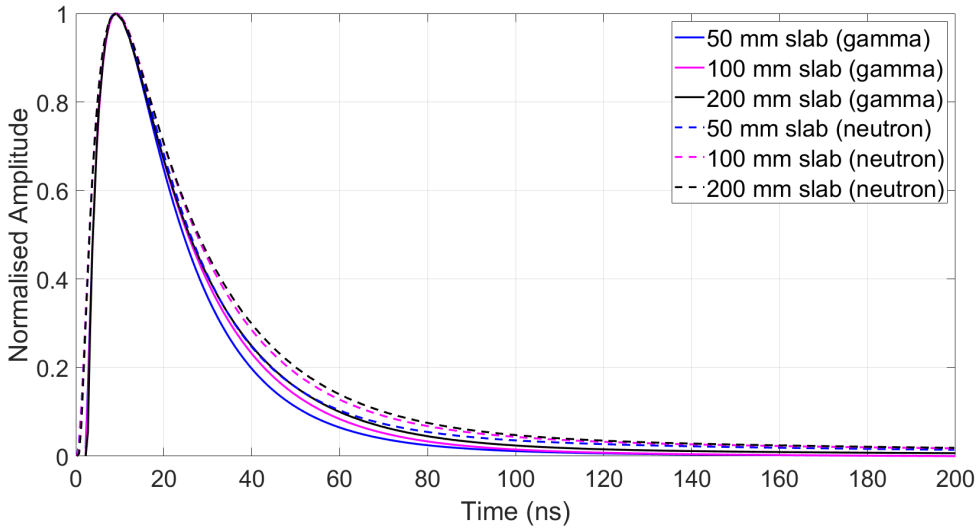

Figure 4.2: Summed simulated light pulses from neutron (dotted) and gamma-ray (solid) interactions in an EJ-276 plastic scintillator with slab geometry. Scintillator lengths along the Z-axis range from 50 mm to 200 mm. Each pulse shape represents the sum of 1000 pulses, normalised to a peak amplitude of 1 and aligned at their peaks.

For the 50 mm slab, the gamma-induced pulse reaches a peak amplitude of 5.15×10^7 photons at 7.25 ns, while the corresponding neutron-induced pulse peaks at 4.61×10^7 photons at 9.25 ns. In contrast, for the 200 mm slab, the gamma-induced pulse peaks at a reduced amplitude of 2.23×10^7 photons at 7.25 ns, and the neutron-induced pulse at 1.65×10^7 photons at 9.25 ns.

The total number of detected scintillation photons (i.e., the integral of each pulse) also decreases with increasing scintillator length. For gamma-induced pulses, the total photon count drops from 1.37×10^9 at 50 mm, to 6.48×10^8 at 200 mm. For neutron-induced pulses, it decreases from 1.47×10^9 to 5.74×10^8 over the same length range.

Figure 4.2 shows the same light pulses, following temporal alignment and normalisation. For all slab lengths, both neutron- and gamma-induced pulses have a

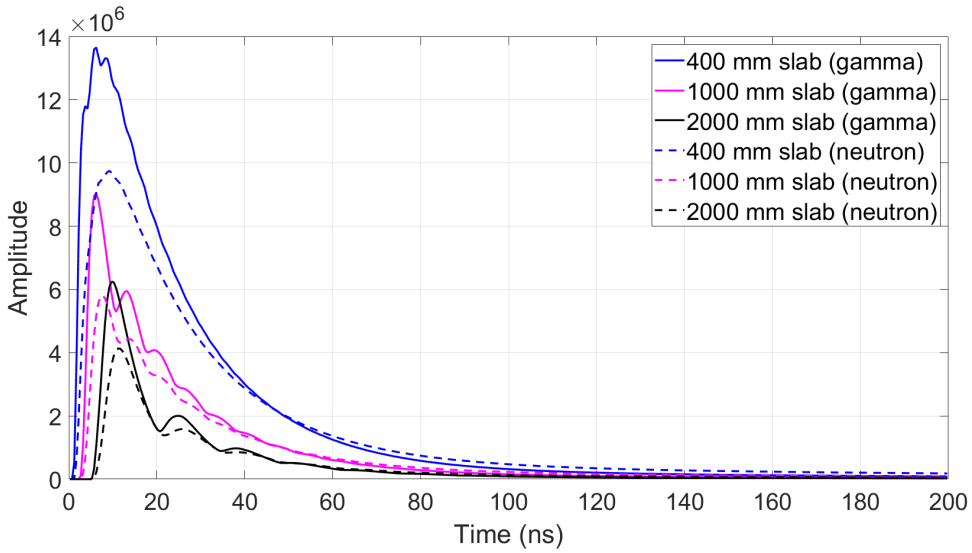

Figure 4.3: Summed simulated light pulses from neutron (dotted) and gamma-ray (solid) interactions in an EJ-276 plastic scintillator with slab geometry. Scintillator lengths along the Z-axis range from 400 mm to 2000 mm. Each pulse shape represents the sum of 1000 individual pulses, prior to normalisation and temporal alignment.

smooth, Gaussian-like shape, with clear temporal separation — particularly evident in the decay tails, the crucial feature for pulse shape discrimination (PSD) using the Charge Comparison Method (CCM).

Figure 4.3 presents the summed light pulses obtained for varying Z-axis lengths, ranging from 400 mm to 2000 mm, prior to temporal alignment and normalisation. At these larger dimensions, clear distinctions between neutron- and gamma-induced pulses remain visible in both timing and amplitude. Specifically, neutron-induced pulses continue to exhibit lower peak amplitudes and a delayed onset relative to the gamma-induced pulses. The trend of decreasing maximum photon counts at the photodetector with increasing scintillator length — first observed in Figure 4.1 — continues at these larger slab lengths: the highest peak amplitude is observed for the 400 mm slab, while the 2000 mm slab exhibits the lowest.

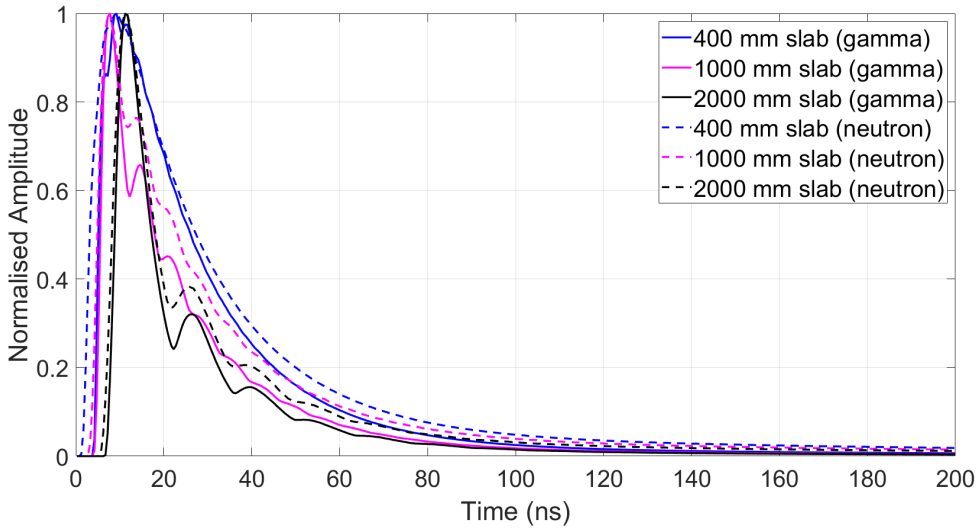

Figure 4.4: Summed simulated light pulses from neutron (dotted) and gamma-ray (solid) interactions in an EJ-276 plastic scintillator with slab geometry. Scintillator lengths along the Z-axis range from 400 mm to 2000 mm. Each pulse shape represents the sum of 1000 pulses, following normalisation and temporal alignment.

For the 400 mm slab, the gamma-induced pulse peaks at 1.36×10^7 photons at 6.25 ns, while the neutron-induced pulse peaks at 9.75×10^6 photons at 9.25 ns. In comparison, for the 2000 mm slab, the gamma-induced pulse peaks at 6.25×10^6 photons at 9.75 ns, and the neutron-induced pulse at 4.13×10^6 photons at 11.25 ns.

The total number of detected scintillation photons continues to decline with increasing scintillator length. For gamma-induced pulses, the total photon count drops from 3.86×10^8 at 400 mm to 1.04×10^8 at 2000 mm. For neutron-induced pulses, it decreases from 3.35×10^8 to 9.00×10^7 over the same length range.

Figure 4.4 shows the normalised and temporally aligned simulated light pulses for scintillator lengths ranging from 400 mm to 2000 mm. Beginning at 400 mm, deviations from the smooth, Gaussian-like pulse shapes observed at shorter lengths become apparent. At this length, artefacts are most noticeable in the rising edge and peak of the gamma-induced pulse.

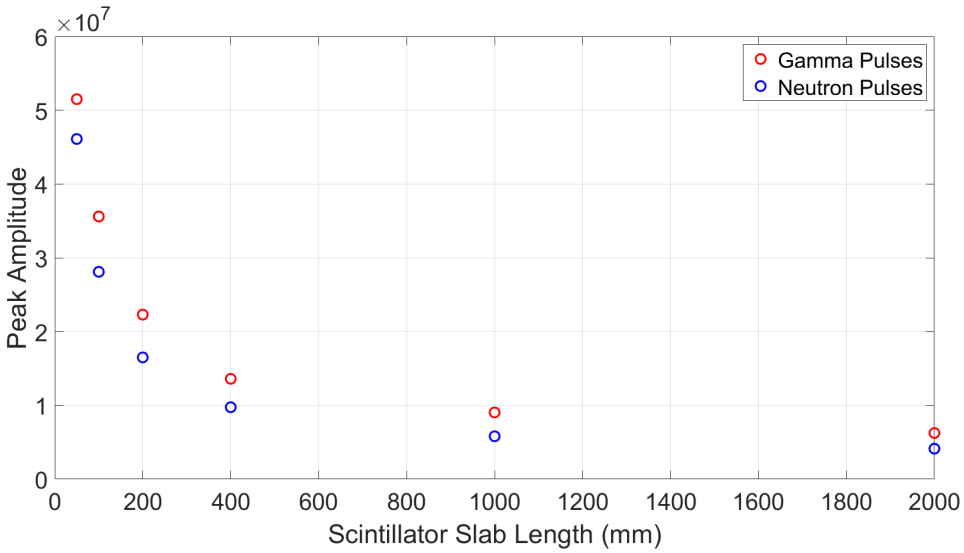

Figure 4.5: Peak amplitude (maximum number of photons detected per time bin) of simulated light pulses as a function of scintillator slab length, for lengths ranging from 50 mm to 2000 mm. Results are shown for neutron (blue)– and gamma-ray (red)–induced pulses.

As the scintillator length increases, the distortion becomes more pronounced. By 1000 mm, significant shape changes are evident, including the emergence of secondary peaks — at 14.75 ns for the gamma-induced pulse and 13.75 ns for the neutron-induced pulse. Despite these distortions, temporal separation between neutron- and gamma-induced pulses remains distinct.

At 2000 mm, these effects intensify: clearly defined secondary peaks emerge at 26.25 ns (gamma) and 25.75 ns (neutron). Although the pulse shapes are significantly altered, temporal separation is still maintained. Additionally, for both the 1000 mm and 2000 mm slabs, the pulses exhibit narrower widths and steeper rising edges, resulting in sharper and faster initial peaks. The Gaussian-like appearance is completely lost at these longer slab lengths.

Figure 4.5 illustrates the variation in peak amplitude as a function of scintillator length along the Z-axis for slab geometries ranging from 50 mm to 2000 mm.

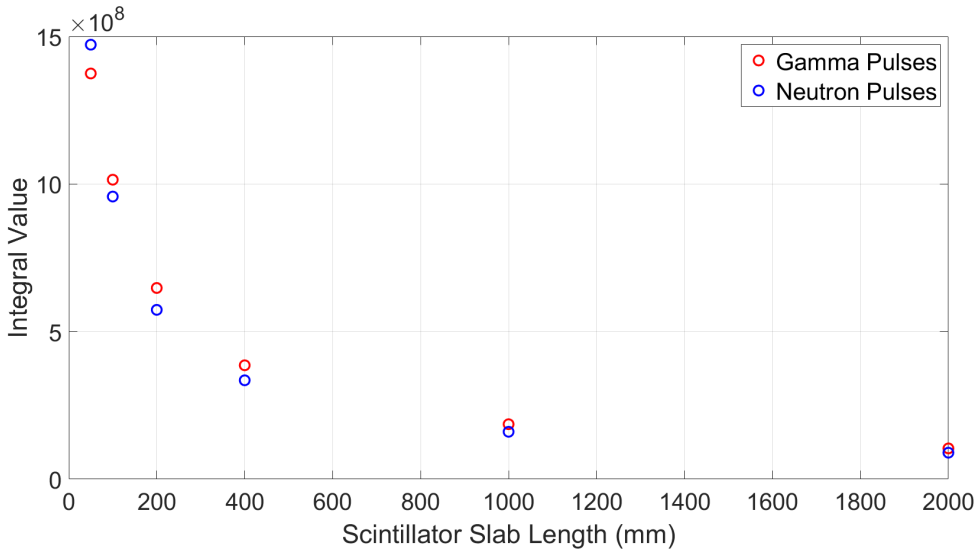

Figure 4.6: Integral (total number of detected photons) versus length for simulated light pulses in a slab geometry, for lengths ranging from 50 mm to 2000 mm. Results are shown for neutron (blue)– and gamma-ray (red)–induced pulses.

Correspondingly, Figure 4.6 depicts the variation in the integral value as a function of scintillator length.

Table 4.1 presents the integrals, peak amplitudes, and neutron-to-gamma ratios for these slab lengths.

Figure 4.7 presents the pulse shape discrimination (PSD) performance of an EJ-276 plastic scintillation detector with slab geometry, for varying Z-axis lengths from 50 mm to 2000 mm. Each subplot shows the PSD parameter — defined as the ratio of the long integral to the short integral — as a function of the long integral for simulated neutron and gamma-ray pulses. These results correspond to simulations performed without noise and thus represent idealised PSD plots.

Neutron-induced pulses consistently exhibit higher PSD values than those induced by gamma rays, reflecting a more pronounced decay tail component. This behaviour is expected, given the distinct interaction mechanisms of neutrons within the scintillator, which result in a greater proportion of delayed fluorescence compared

Table 4.1: Peak amplitudes, integrated photon counts, and neutron-to-gamma integral ratios for gamma- and neutron-induced pulses as a function of scintillator slab length.

Length (mm)	**Peak Amplitude (gamma)**	**Peak Amplitude (neutron)**	**Integral (gamma)**	**Integral (neutron)**	**Ratio (neutron/gamma)**
50	5.15×10^7	4.61×10^7	1.37×10^9	1.47×10^9	1.071
100	3.56×10^7	2.81×10^7	1.01×10^9	9.57×10^8	0.944
200	2.23×10^7	1.65×10^7	6.48×10^8	5.74×10^8	0.886
400	1.36×10^7	9.75×10^6	3.86×10^8	3.35×10^8	0.868
1000	9.04×10^6	5.81×10^6	1.86×10^8	1.61×10^8	0.862
2000	6.25×10^6	4.13×10^6	1.04×10^8	8.97×10^7	0.861

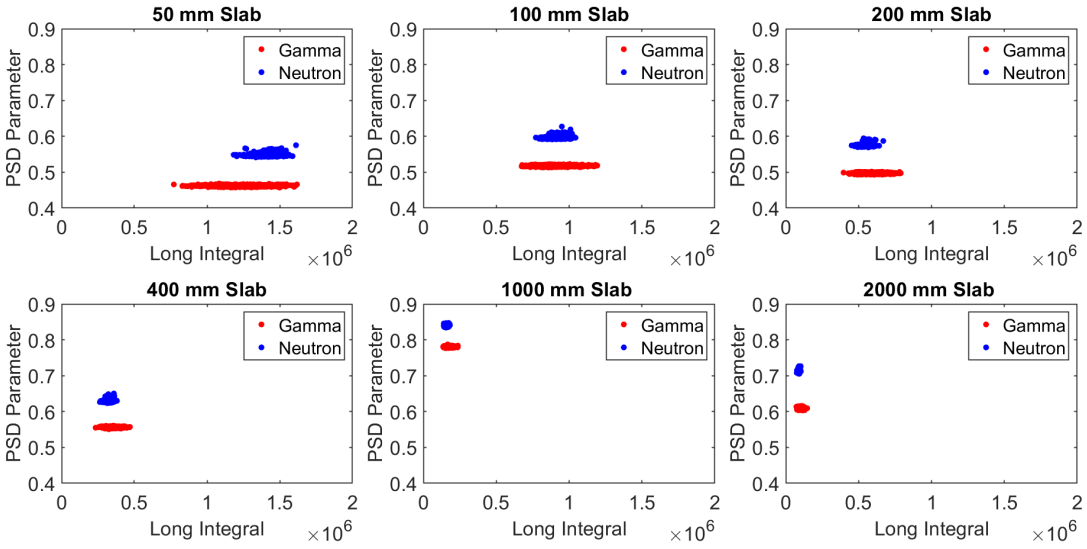

Figure 4.7: PSD parameter distributions for neutron and gamma-ray pulses in an EJ-276 slab scintillator for various Z-axis lengths (50 mm to 2000 mm), simulated without noise. The PSD parameter is defined as the ratio of long to short integrals.

to gamma-ray interactions. The range of the long integrals for both distributions decreases with increasing slab length, attributable to the reduced light collection efficiency (LCE) summarised in Table 4.1.

Clear separation between the neutron and gamma-ray PSD distributions is observed across all scintillator slab lengths. For slabs shorter than 400 mm, both distributions exhibit limited variability in their PSD parameters. At a slab length of 1000 mm, the PSD values increase to ≈ 0.84 for neutrons and ≈ 0.78 for gamma rays. At 2000 mm, these values decrease to ≈ 0.71 and ≈ 0.61, respectively. Nevertheless, the distributions remain fully separated at all lengths, with no visible overlap.

4.2 Cylindrical Geometry

This section presents simulation results investigating the effect of increasing the scintillator length along the Z-axis for an EJ-276 plastic scintillator with cylindrical

geometry. In all simulations, the diameter of the cylinder was fixed at 50 mm, and the photodetector volume was held constant with a diameter of 400 mm and a thickness of 5 mm.

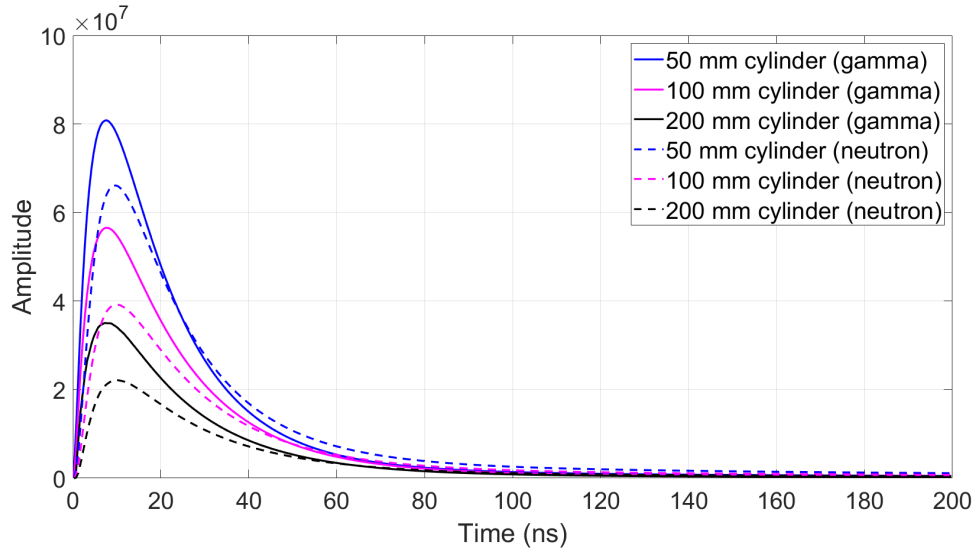

Figure 4.8: Summed simulated light pulses from neutron (dotted) and gamma-ray (solid) interactions in an EJ-276 plastic scintillator with cylinder geometry. Scintillator lengths along the Z-axis range from 50 mm to 200 mm. Each pulse shape represents the sum of 1000 individual pulses, prior to normalisation and temporal alignment.

Figure 4.8 shows the summed light pulses obtained for Z-axis lengths ranging from 50 mm to 200 mm, prior to normalisation and temporal alignment. Similar trends to the slab geometry are observed, with neutron-induced pulses showing reduced peak amplitudes and delayed onsets. The peak amplitude decreases as the cylinder length increases, with the 50 mm cylinder producing the highest and the 200 mm cylinder the lowest.

For the 50 mm cylinder, the gamma-induced pulse reaches a peak amplitude of 8.08×10^7 photons at 7.75 ns, while the neutron-induced pulse peaks at an amplitude of 6.61×10^7 photons at 9.75 ns. For the 200 mm cylinder, the gamma-ray-induced

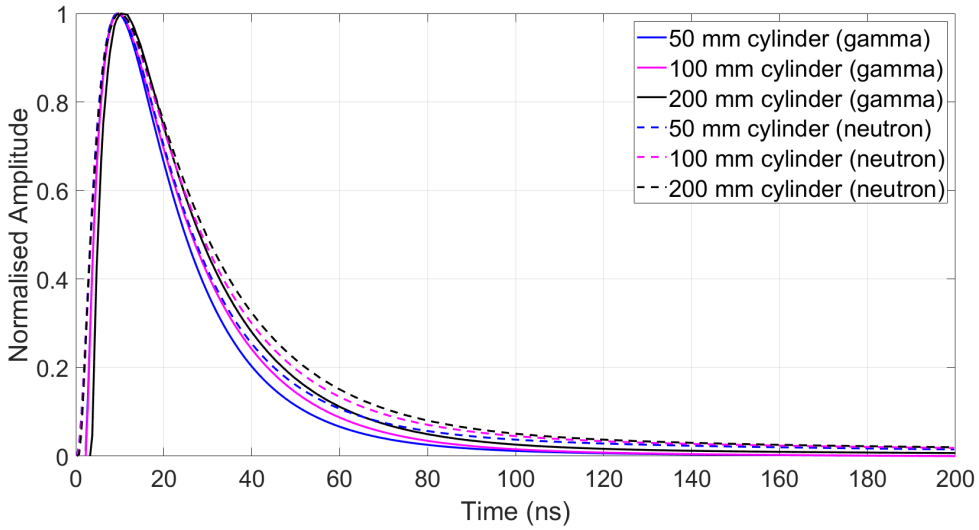

Figure 4.9: Summed simulated light pulses from neutron (dotted) and gamma-ray (solid) interactions in an EJ-276 plastic scintillator with cylinder geometry. Scintillator lengths along the Z-axis range from 50 mm to 200 mm. Each pulse shape represents the sum of 1000 individual pulses, following normalisation and temporal alignment.

pulse reaches a peak amplitude of 3.50×10^7 photons at 7.25 ns, while the neutron-induced pulse peaks at an amplitude of 2.21×10^7 photons at 10.25 ns.

The total number of detected scintillation photons also shows a decline. For gamma-induced pulses, the total photon count drops from 2.18×10^9 at 50 mm to 1.06×10^9 at 200 mm. For neutron-induced pulses, it decreases from 2.13×10^9 to 8.04×10^8 over the same length range.

Figure 4.9 shows the same pulse shapes following temporal alignment and normalisation. Across all scintillator lengths, clear distinctions remain between neutron- and gamma-induced pulses. In all cases, the pulse shapes are smooth and exhibit an approximately Gaussian-like appearance, consistent with the trend observed for the slab geometry. A broadening of the pulse width is again evident as the scintillator length increases along the Z-axis.

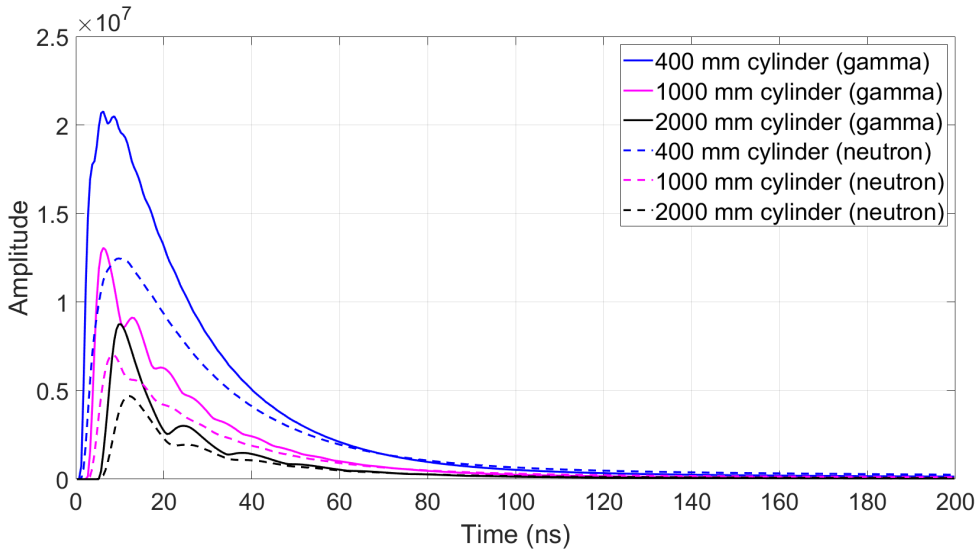

Figure 4.10: Summed simulated light pulses from neutron (dotted) and gamma-ray (solid) interactions in an EJ-276 plastic scintillator with cylinder geometry. Scintillator lengths along the Z-axis range from 400 mm to 2000 mm. Each pulse shape represents the sum of 1000 individual pulses, prior to normalisation and temporal alignment.

Figure 4.10 presents the summed light pulses obtained for Z-axis lengths ranging from 400 mm to 2000 mm, prior to temporal alignment and normalisation. As with shorter scintillator lengths, neutron-induced pulses exhibit lower peak amplitudes and delayed onset relative to the gamma-induced pulses. The highest peak amplitude is observed for the 400 mm cylinder, and the lowest for the 2000 mm cylinder.

For the 400 mm, the gamma-ray-induced pulse reaches a peak amplitude of 2.80×10^7 photons at a time of 6.25 ns, while the neutron-induced pulse peaks at an amplitude of 1.25×10^7 photons at 9.75 ns. For the 2000 mm scintillator, the gamma-induced pulse reaches a peak amplitude of 8.75×10^6 photons at 10.25 ns, while the neutron-induced pulse peaks at an amplitude of 4.70×10^6 photons at 12.25 ns.

For gamma-induced pulses, the total photon count drops from 6.22×10^8 at 400 mm to 1.58×10^8 at 2000 mm. For neutron-induced pulses, it decreases from 2.13×10^9 to 8.04×10^8 over the same length range.

Figure 4.11 presents the temporally aligned and normalised pulses for the cylindrical geometry. For the 400 mm cylinder, some distortion remains at the peak of the gamma-induced pulse, though it is less severe than that observed for the slab geometry. The neutron-induced pulse for this length retains a smooth shape with minimal peak distortion.

At scintillator lengths of 1000 mm and 2000 mm, more significant changes in pulse shape are observed. Secondary peaks emerge in the gamma-induced pulses at 14.75 ns for 1000 mm and 26.25 ns for 2000 mm. For the neutron-induced pulses, a secondary peak is observed at 25.25 ns for the 2000 mm cylinder, although it is less distinct. These features are consistent with changes in pulse shape also observed in the slab geometry at equivalent lengths.

Figure 4.12 illustrates the variation in peak amplitude as a function of scintillator length along the Z-axis for cylindrical geometries ranging from 50 to 2000 mm. Correspondingly, Figure 4.13 depicts the variation in the integral value as a function

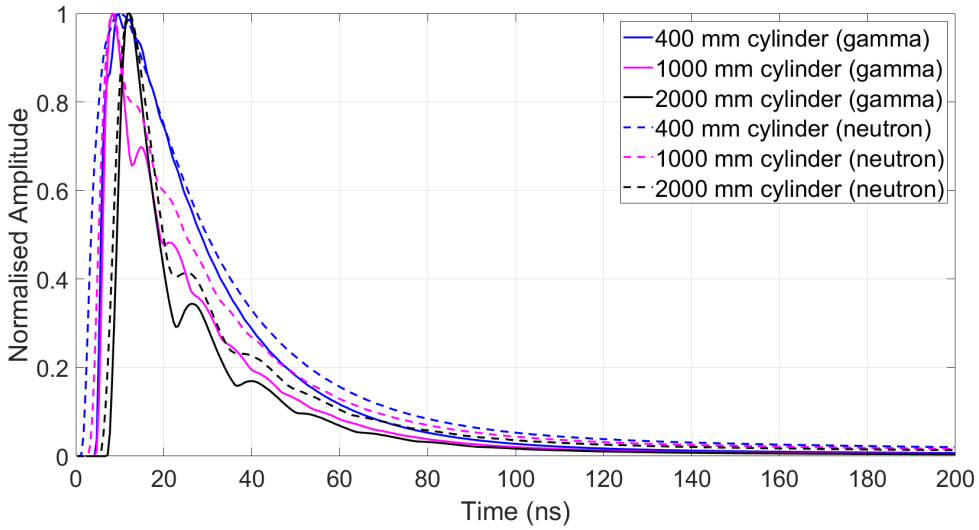

Figure 4.11: Summed simulated light pulses from neutron (dotted lines) and gamma-ray (solid lines) interactions in an EJ-276 plastic scintillator with cylindrical geometry, for Z-axis lengths ranging from 400 mm to 2000 mm. Each pulse shape represents the sum of 1000 individual pulses, following temporal alignment and normalisation.

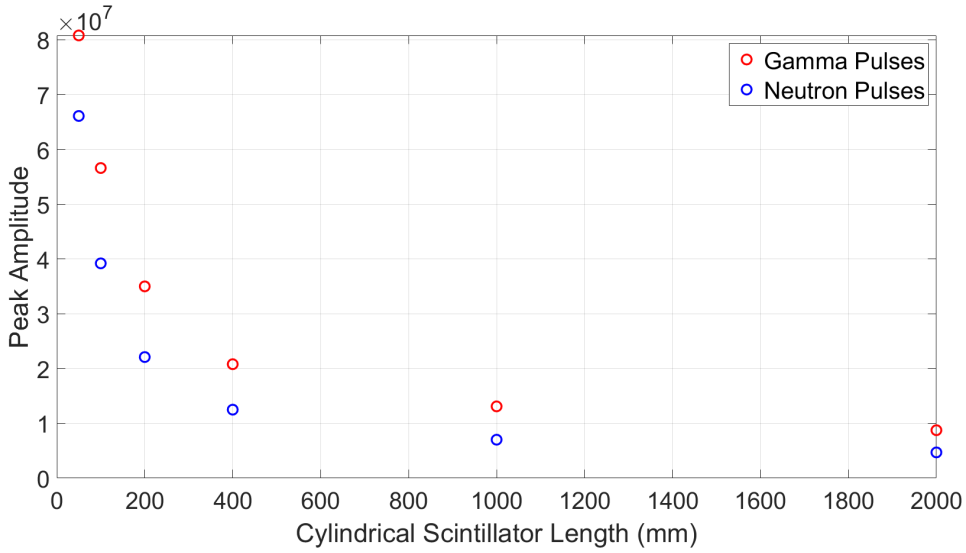

Figure 4.12: Peak amplitude of simulated light pulses as a function of cylindrical length, for lengths ranging from 50 mm to 2000 mm. Results are shown for neutron (blue)- and gamma-ray (red)-induced pulses.

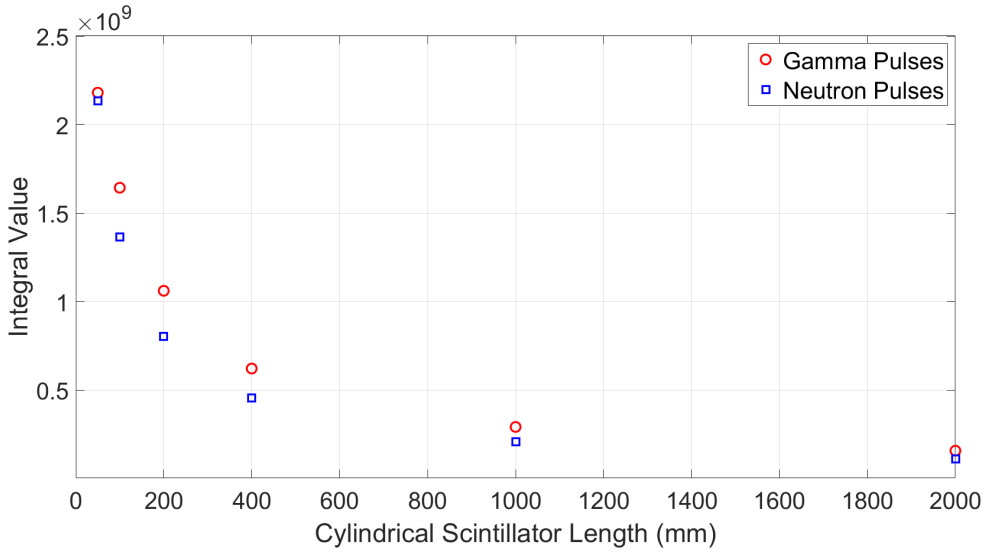

Figure 4.13: Integral versus length for simulated light pulses in a cylindrical geometry, for lengths ranging from 50 to 2000 mm. Results are shown for neutron (blue)– and gamma-ray (red)–induced pulses.

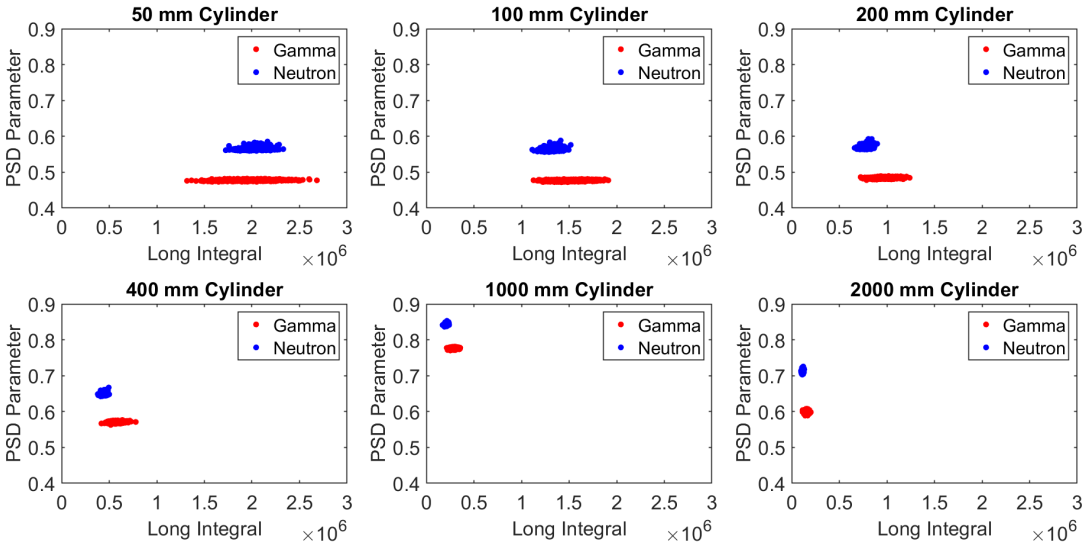

Figure 4.14: PSD parameter distributions for neutron (blue) and gamma-ray (red) pulses in an EJ-276 cylindrical scintillator for various Z-axis lengths (50–2000 mm), simulated without noise. The PSD parameter is defined as the ratio of long to short integrals.

of scintillator length.

Table 4.2 shows that as the length of the cylindrical geometry increases from 50 mm to 2000 mm, both the peak amplitudes and integrated photon counts of gamma- and neutron-induced pulses decrease.

Figure 4.14 presents the pulse shape discrimination (PSD) performance of an EJ-276 plastic scintillation detector with cylindrical geometry for varying Z-axis lengths ranging from 50 mm to 2000 mm. Each subplot shows the PSD parameter (long integral/short integral) as a function of the long integral for simulated neutron (blue) and gamma-ray (red) pulses, shown in the absence of simulated noise.

As with Figure 4.7, neutron-induced pulses exhibit higher PSD parameter values than gamma-ray-induced pulses, with clear separation between the two distributions, observed across all cylinder lengths. For cylinders shorter than 400 mm, the PSD values for both neutrons and gamma-rays show limited variability. As the scintillator

Table 4.2: Peak amplitudes, integral values, and neutron-to-gamma integral ratios for cylindrical scintillators of varying length along the Z-axis.

Length (mm)	**Peak Amplitude (gamma)**	**Peak Amplitude (neutron)**	**Integral (gamma)**	**Integral (neutron)**	**Ratio (neutron/gamma)**
50	8.08×10^7	6.61×10^7	2.18×10^9	2.13×10^9	0.978
100	5.66×10^7	3.92×10^7	1.64×10^9	1.37×10^9	0.831
200	3.50×10^7	2.21×10^7	1.06×10^9	8.04×10^8	0.757
400	2.08×10^7	1.25×10^7	6.22×10^8	4.56×10^8	0.733
1000	1.31×10^7	7.02×10^6	2.92×10^8	2.09×10^8	0.715
2000	8.75×10^6	4.70×10^6	1.58×10^8	1.13×10^8	0.713

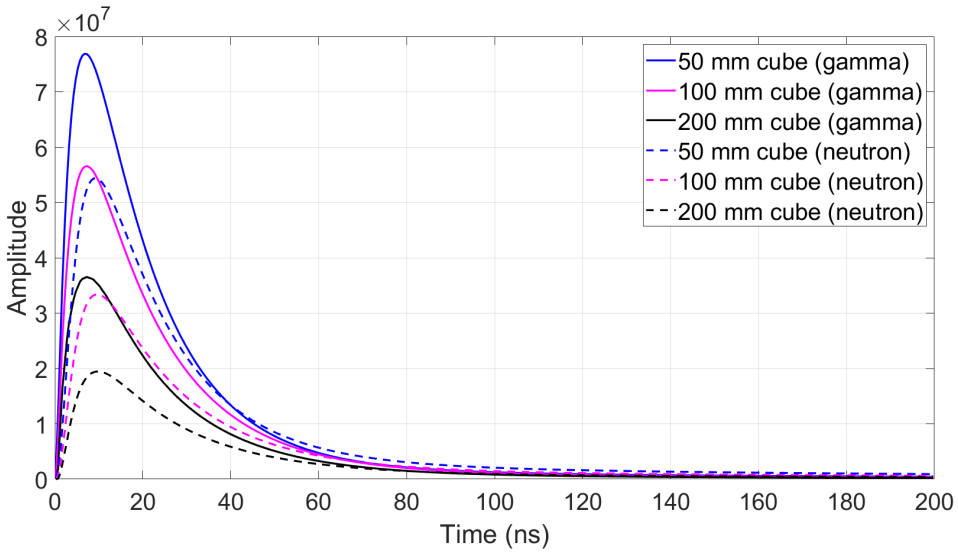

Figure 4.15: Summed simulated light pulses from neutron (dotted) and gamma-ray (solid) interactions in an EJ-276 plastic scintillator with cuboid geometry. Scintillator lengths along the Z-axis range from 50 mm to 200 mm. Each pulse shape represents the sum of 1000 pulses, prior to normalisation and temporal alignment.

length increases to 400 mm and 1000 mm, the PSD values for both particle types increases. However, at 2000 mm, the PSD values decrease slightly for both neutrons and gamma-rays, following a similar trend to that observed for the slab geometry. This geometry also shares with the slab the trend of decreasing range in the long integral as scintillator length increases, consistent with the data summarised in Table 4.2 for the integrals and peak amplitudes.

4.3 Cuboid Geometry

This section presents simulation results investigating the effect of increasing the scintillator length along the Z-axis for an EJ-276 plastic scintillator with cuboid geometry. In all simulations, the dimensions along the X- and Y-axes were fixed at 50 mm, and the photodetector volume was maintained at 50 mm $\times$ 50 mm $\times$ 5 mm.

Figure 4.15 displays the summed light pulses for cuboid scintillators with Z-axis lengths ranging from 50 mm to 200 mm, prior to normalisation and temporal alignment. Consistent with the trends observed for the slab and cylindrical geometries, neutron-induced pulses exhibit lower peak amplitudes and a delayed onset compared to gamma-induced pulses. The highest peak amplitude is observed for the 50 mm cuboid, while the 200 mm cuboid yields the lowest, indicating a reduction in early-arriving photons with increasing scintillator length, which was also observed for the slab and cylindrical geometries.

For the 50 mm cuboid, the gamma-induced pulse reaches a peak amplitude of 7.69×10^7 photons at time 6.75 ns, while the neutron-induced pulse peaks at an amplitude of 5.44×10^7 photons at time 9.25 ns.

For gamma-induced pulses, the total photon count drops from 2.01×10^9 at 50 mm to 1.06×10^9 at 200 mm. For neutron-induced pulses, it decreases from 1.72×10^9 to 6.08×10^8 over the same length range.

Figure 4.16 presents the temporally aligned and normalised pulse shapes for cuboid scintillators with Z-axis lengths from 50 mm to 200 mm. Across all lengths, clear differences are observed between neutron- and gamma-induced pulses. The pulse shapes exhibit smooth, approximately Gaussian-like profiles, consistent with the behaviour noted for the slab and cylindrical geometries. A broadening of the pulse width is also evident with increasing length along the Z-axis.

Figure 4.17 presents the summed light pulses obtained for Z-axis lengths ranging from 400 mm to 2000 mm, prior to temporal alignment and normalisation. Neutron pulses continue to exhibit lower peak amplitudes than gamma pulses, along with a delayed onset. The highest peak amplitude is observed for the 400 mm cuboid and the lowest for the 2000 mm cuboid.

For the 400 mm cuboid, the gamma-induced pulse reaches a peak amplitude of 2.23×10^7 photons at time 6.25 ns, while the neutron-induced pulse peaks at an amplitude of 1.13×10^7 photons at time 9.75 ns. For the 2000 mm cuboid, the gamma-induced pulse reaches a peak amplitude of 1.03×10^7 photons at time 9.75 ns,

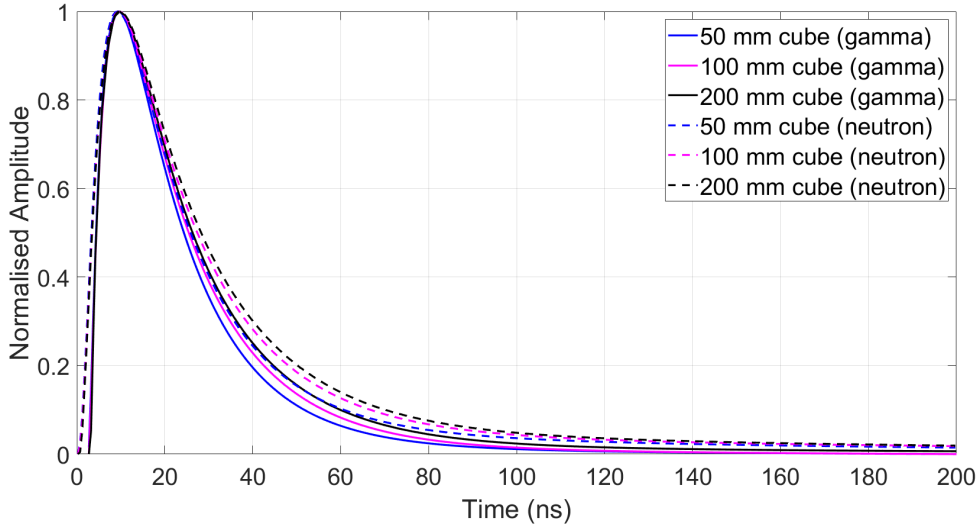

Figure 4.16: Summed simulated light pulses from neutron (dotted) and gamma-ray (solid) interactions in an EJ-276 plastic scintillator with cuboid geometry. Scintillator lengths along the Z-axis range from 50 mm to 200 mm. Each pulse shape represents the sum of 1000 pulses, following normalisation and temporal alignment.

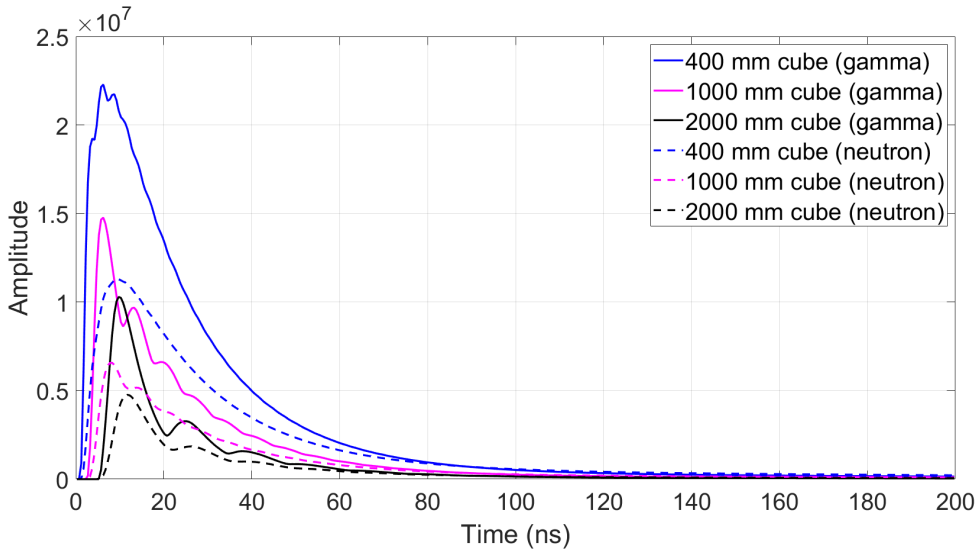

Figure 4.17: Summed simulated light pulses from neutron (dotted) and gamma-ray (solid) interactions in an EJ-276 plastic scintillator with cuboid geometry. Scintillator lengths along the Z-axis range from 400 mm to 2000 mm. Each pulse shape represents the sum of 1000 pulses, prior to normalisation and temporal alignment.

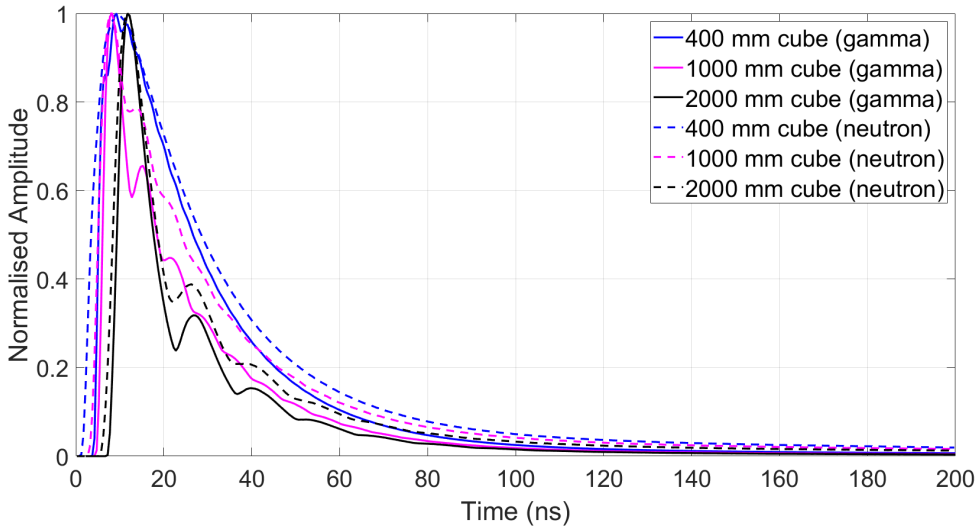

Figure 4.18: Summed simulated light pulses from neutron (dotted) and gamma-ray (solid) interactions in an EJ-276 plastic scintillator with cuboid geometry. Scintillator lengths along the Z-axis range from 400 mm to 2000 mm. Each pulse shape represents the sum of 1000 pulses, following normalisation and temporal alignment.

while the neutron-induced pulse peaks at an amplitude of 4.76×10^6 photons at time 11.75 ns.

For gamma-induced pulses, the total photon count drops from 6.38×10^8 at 400 mm to 1.71×10^8 at 2000 mm. For neutron-induced pulses, it decreases from 4.00×10^8 to 1.10×10^8 over the same length range.

Figure 4.18 presents the temporally aligned and normalised pulses for the cuboid geometry For the 400 mm there is distortion in the peaks of the neutron- and gamma-induced pulses.

At lengths of 1000 mm and 2000 mm, significant changes in pulse shape are evident, consistent with the trends observed in the slab and cylindrical geometries. Secondary peaks appear in the gamma-induced pulses at 13.25 ns for the 1000 mm cuboid and 24.75 ns for the 2000 mm cuboid. For the neutron-induced pulses, the

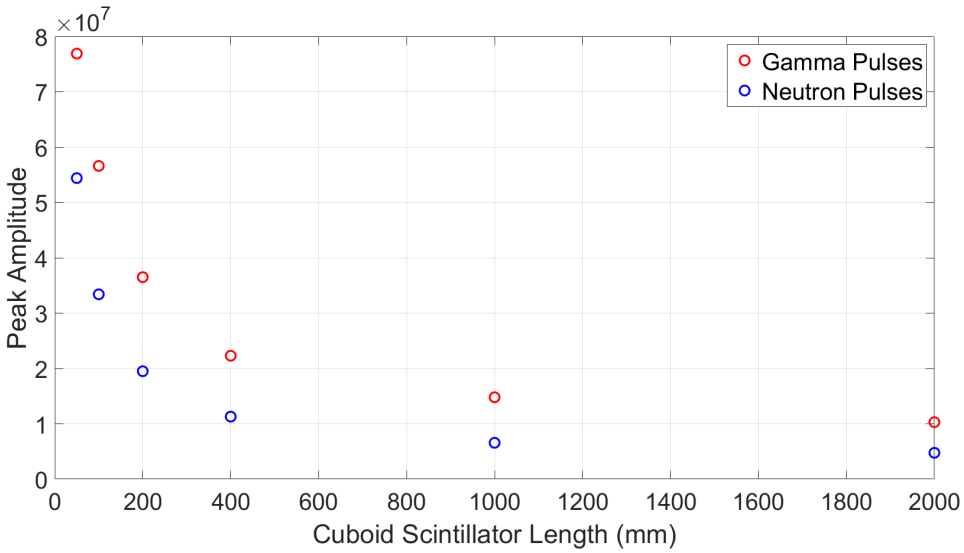

Figure 4.19: Peak amplitude of simulated light pulses as a function of cuboid length, for lengths ranging from 50 mm to 2000 mm. Results are shown for neutron (blue)- and gamma-ray (red)-induced pulses.

distortion manifests as a broad shoulder rather than a distinct secondary peak.

Figure 4.19 illustrates the variation in peak amplitude as a function of scintillator length along the Z-axis for cuboid geometries ranging from 50 mm to 2000 mm. Correspondingly, Figure 4.20 depicts the variation in the integral value as a function of scintillator length.

Table 4.3 presents the integrals, peak amplitudes, and neutron-to-gamma ratios for these cuboid lengths.

Figure 4.21 shows the pulse shape discrimination (PSD) performance of an EJ-276 plastic scintillation detector with cuboid geometry for varying Z-axis lengths ranging from 50 mm to 2000 mm. Each subplot shows the PSD parameter (long integral/short integral) as a function of the long integral for simulated neutron (blue) and gamma-ray (red) pulses, shown in the absence of simulated noise.

As with Figures 4.7 and 4.14, neutron-induced pulses exhibit consistently higher PSD parameter values than gamma-ray-induced pulses, with clear separation

Table 4.3: Peak amplitudes, integral values, and neutron-to-gamma integral ratios for cuboid scintillators of varying length along the Z-axis.

Length (mm)	**Peak Amplitude (gamma)**	**Peak Amplitude (neutron)**	**Integral (gamma)**	**Integral (neutron)**	**Ratio (neutron/gamma)**
50	7.69×10^7	5.44×10^7	2.01×10^9	1.72×10^9	0.855
100	5.66×10^7	3.34×10^7	1.58×10^9	1.12×10^9	0.713
200	3.65×10^7	1.95×10^7	1.06×10^9	6.80×10^8	0.642
400	2.23×10^7	1.13×10^7	6.38×10^8	3.98×10^8	0.623
1000	1.48×10^7	6.57×10^6	3.06×10^8	1.90×10^8	0.620
2000	1.03×10^7	4.76×10^6	1.71×10^8	1.06×10^8	0.620

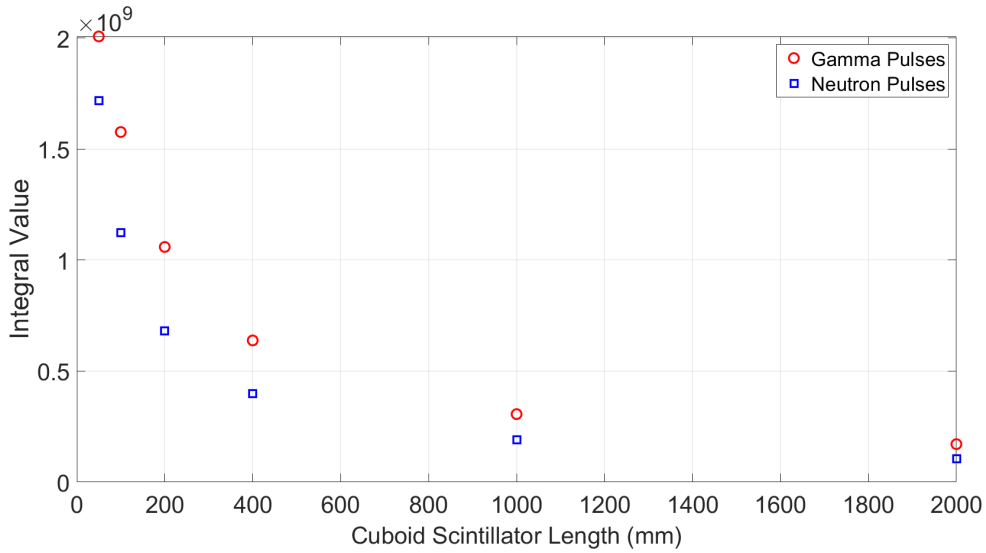

Figure 4.20: Integral versus length for simulated light pulses in a cuboid geometry, for lengths ranging from 50 to 2000 mm. Results are shown for neutron (blue)– and gamma-ray (red)–induced pulses.

between the two distributions observed across all cuboid lengths. The trend of increasing PSD parameter values with scintillator length — followed by a drop at 2000 mm — is also present in this geometry. Additionally, the decreasing range in the long integral with increasing scintillator length persists, consistent with the pulse integral values summarised in Table 4.3.

Work by Hubbard, Paul J Sellin, and Lotay, 2020 showed that the artefacts — described as 'bumps' — in the pulse shapes for large-sized scintillators of different geometries was due to the initial emission direction of scintillation photons. To further examine this effect in the Geant4 simulations presented in the previous sections, heat maps were generated showing the initial emission direction of scintillation photons in both a 50 mm × 50 mm × 50 mm and a 50 mm × 50 mm × 2000 mm cuboid, respectively. These are shown in Figures 4.22 and 4.24, respectively. The gamma-induced pulse shapes corresponding to these heat maps are shown in Figures 4.23 and 4.25 for the two cuboids.

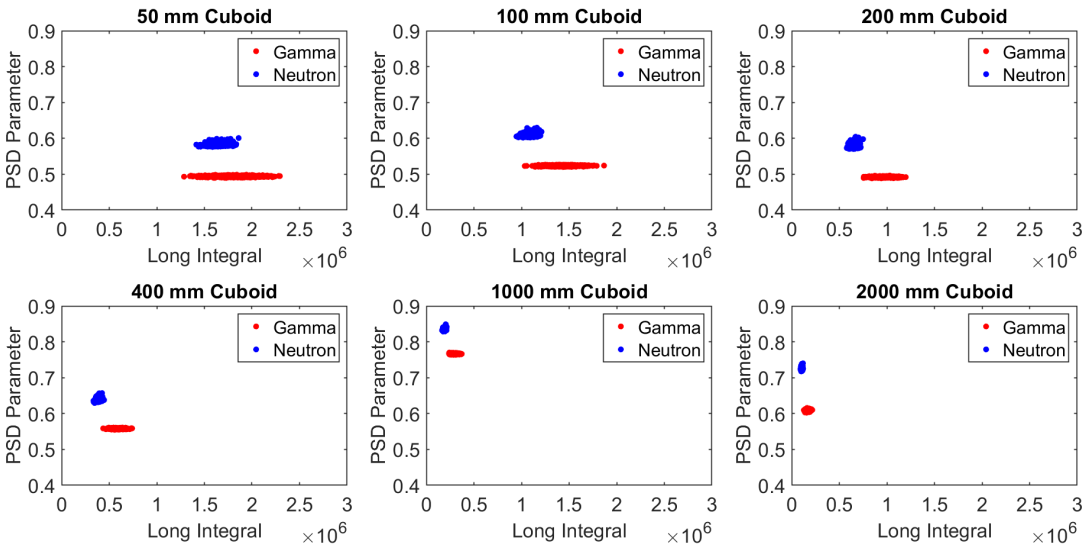

Figure 4.21: PSD parameter distributions for neutron (blue) and gamma-ray (red) pulses in an EJ-276 cuboid scintillator for various Z-axis lengths (50 mm to 2000 mm), simulated without noise. The PSD parameter is defined as the ratio of long to short integrals.

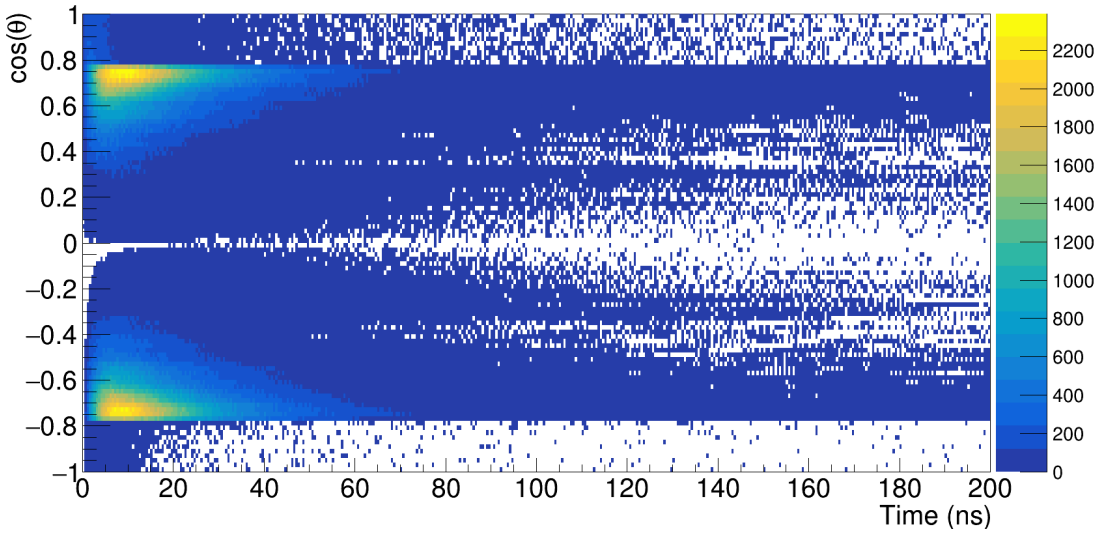

Figure 4.22: Heat map showing initial photon emission angle, θ, as a function of arrival time at the photodetector for a 50 mm cuboid scintillator, with scintillation photons generated from incident 1 MeV gamma-rays.

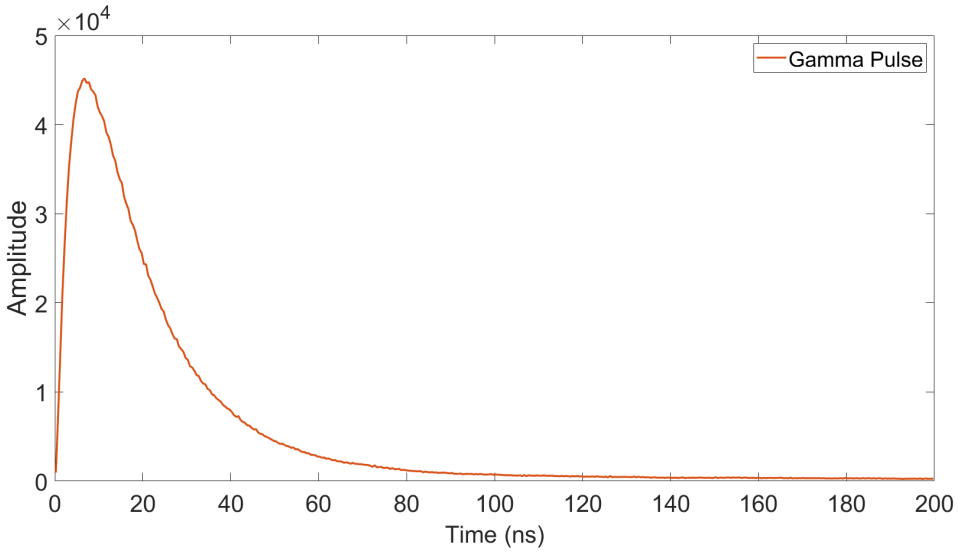

Figure 4.23: Gamma-induced pulse shape for 50 mm × 50 mm × 50 mm EJ-276 cuboid scintillator.

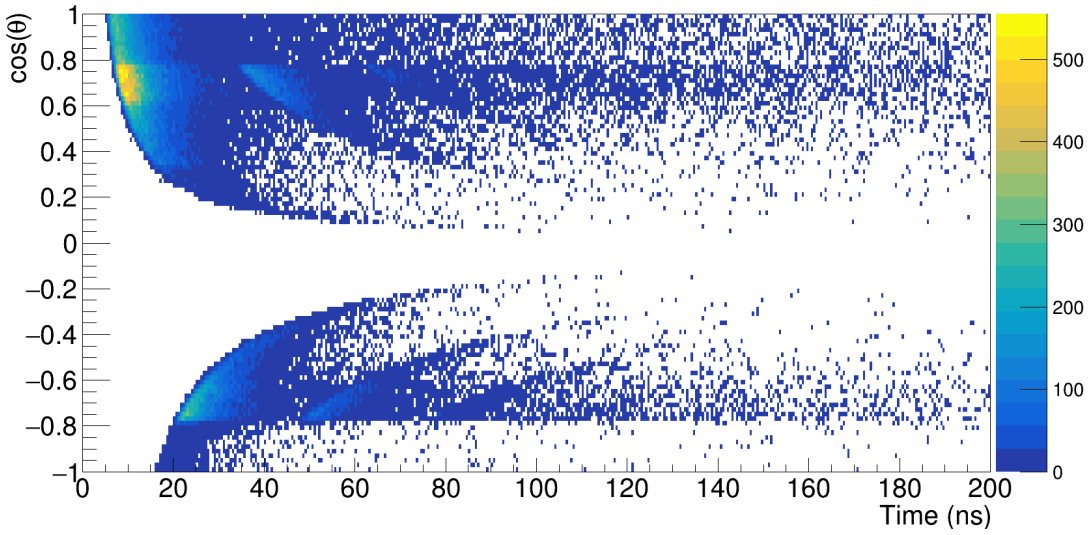

Figure 4.24: Heat map showing initial photon emission angle, θ, as a function of arrival time at the photodetector for a 2000 mm cuboid scintillator, with scintillation photons generated from incident 1 MeV gamma-rays.

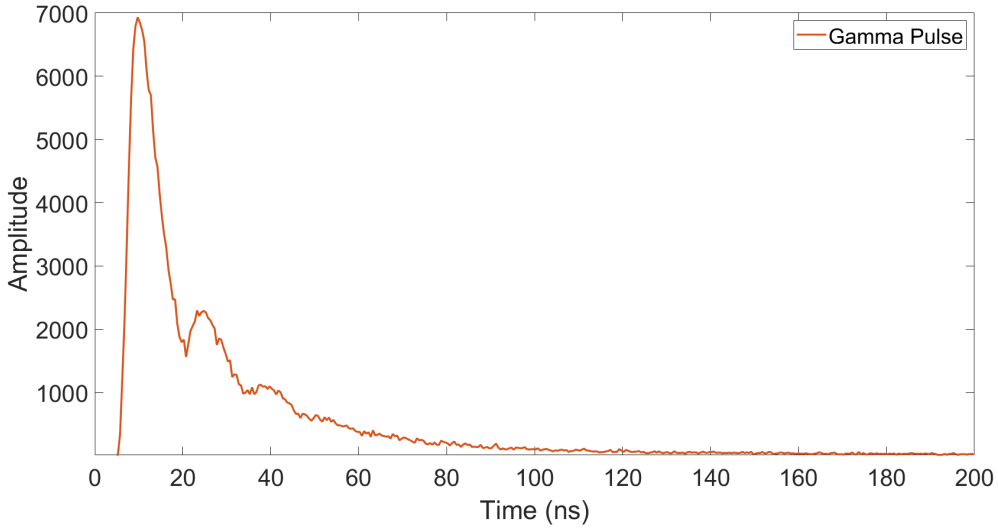

Figure 4.25: Gamma-induced pulse shape for 50 $mm \times 50\ mm \times 2000\ mm$ EJ-276 cuboid scintillator.

The X-axis is the arrival time of scintillation photons at the photodetector, while the Y-axis shows $\cos(\theta)$, where θ is the emission direction angle of the scintillation photons relative to the detector axis. Thus, where $\cos(\theta) = +1$ corresponds to photons initially emitted toward the photodetector surface and $\cos(\theta) = -1$ corresponds to photons initially emitted away from the photodetector surface.

Figure 4.24 helps explain both the secondary peak artefact observed in Figure 4.25 and the results presented in this chapter. The secondary peak appears at approximately 20–30 ns, which coincides with the arrival time of scintillation photons that were initially emitted away from the photodetector (i.e. those with an initial emission angle near $\cos(\theta) \approx -1$). These photons traverse a longer optical path through the scintillator — often involving one or more reflections — before eventually reaching the photodetector. The corresponding increase in path length delays their arrival, giving rise to the secondary peak in the simulated pulse shape.

In contrast, the heat map shows that photons initially emitted toward the photodetector (i.e. those with $\cos(\theta) \approx -1$ arrive at approximately 5 ns. This early-arriving component corresponds to the rising edge in Figure 4.25. The rising edge is comparatively slower than that of the 50 mm $\times$ 50 mm $\times$ 50 mm cuboid, because photons in the elongated 2000 mm geometry must on average travel a significantly longer distance before detection. In the smaller, shown in Figure 4.23, the photon transit times are short, resulting in an almost instantaneous rising edge.

Chapter 5

Optical Surfaces

This chapter presents the results of simulations investigating how variations in the optical surface of an EJ-276 plastic scintillator affect the generated pulse shapes resulting from neutron- and gamma-ray interactions within the scintillator volume. Unless otherwise specified, the scintillator was a cuboid with fixed dimensions of 50 mm $\times$ 50 mm $\times$ 50 mm cuboid, and the photodetector dimensions were also held constant at 50 mm $\times$ 50 mm $\times$ 5 mm.

Except in cases where no explicit optical surface was defined — referred to as the "Default Surface" in this work — the UNIFIED optical model was used. In each simulation, the defined optical surface was applied exclusively to the EJ-276 scintillator volume.

In contrast to the previous geometrical simulations, an additional optical surface (defined using `G4OpticalSurface`) was applied to the photodetector volume to simulate the photocathode surface. This surface was assigned fixed optical parameters and remained unchanged throughout the simulations presented in this chapter. Furthermore, no absorption was assumed at the interface between the scintillator and the photodetector; this was implemented by setting the optical surface efficiency of the photodetector to zero in its surface definition.

As in the geometrical simulations, the gamma-ray or neutron source was positioned at co-ordinates $X = 0$ mm, $Y = 25$ mm, and $Z = 0$ mm, placing it

on the top surface of the scintillator. The source emitted particles isotropically, with an energy of 1 MeV for both neutrons and gamma-rays.

5.1 Teflon Wrapping

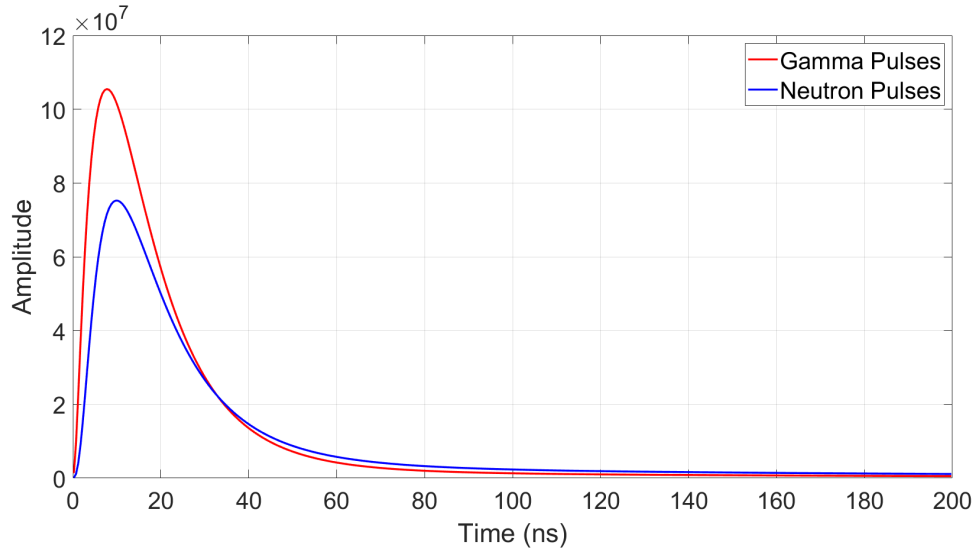

Figure 5.1: Summed simulated light pulses from neutron and gamma-ray interactions in an EJ-276 plastic scintillator with a simulated Teflon `groundbackpainted` (GBP) optical surface. Each pulse shape represents the sum of 1000 individual pulses, prior to normalisation and temporal alignment.

Figure 5.1 shows the summed simulated light pulses obtained using a Teflon-defined optical surface with a `groundbackpainted` (GBP) finish. In this simulation, the surface reflectivity was set to 98%, and the surface roughness parameter (σ_α) was 0.2°, representing a Teflon-wrapped scintillator with a moderately rough surface. The material type was dielectric-dielectric. The gamma-induced pulse reaches a peak amplitude of 1.05×10^8 photons at 7.75 ns, while the neutron-induced pulse peaks at 7.52×10^7 photons at 9.75 ns.

The total number of detected photons is 2.49×10^9 for gamma-ray events and

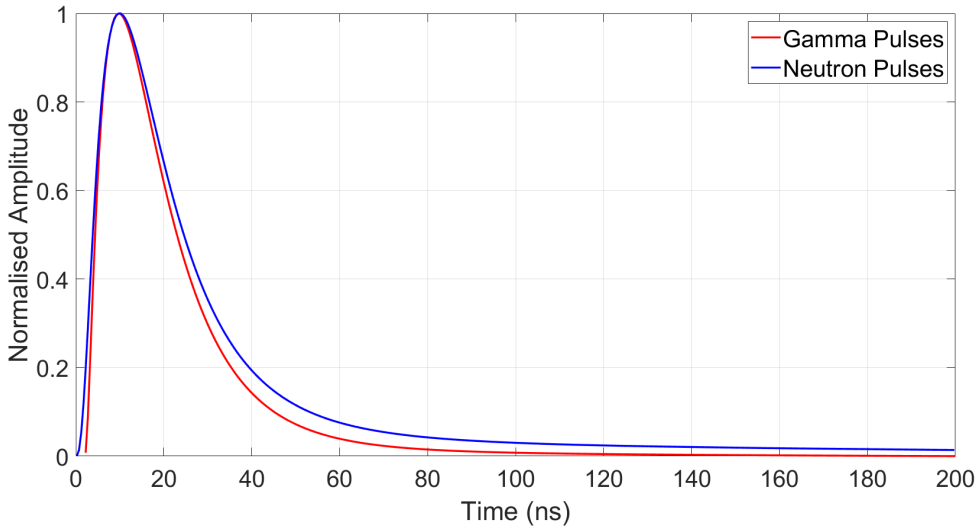

Figure 5.2: Summed simulated light pulses from neutron and gamma-ray interactions in an EJ-276 plastic scintillator with a simulated Teflon `groundbackpainted` optical surface. Each pulse shape represents the sum of 1000 individual pulses, following normalisation and temporal alignment.

2.15×10^9 for neutron events.

Figure 5.2 shows the same pulses after normalisation and temporal alignment. A clear temporal separation between the neutron- and gamma-induced pulses is observed. Both pulse shapes exhibit smooth, Gaussian-like shapes, free from distortions or artefacts.

Figure 5.3 compares the Teflon `groundbackpainted` (GBP) optical surface with Geant4's Default Surface The Teflon configuration produces higher peak amplitudes for both gamma- and neutron-induced interactions. However, the gamma pulse reaches its peak at 7.75 ns and the neutron pulse at 9.75 ns whereas for the Default Surface, these occur slightly earlier — at 6.75 ns for the gamma and 9.25 ns for the neutron.

Figure 5.4 shows the same pulses after normalisation and temporal alignment. For the same scintillator geometry, the Teflon `groundbackpainted` surface results

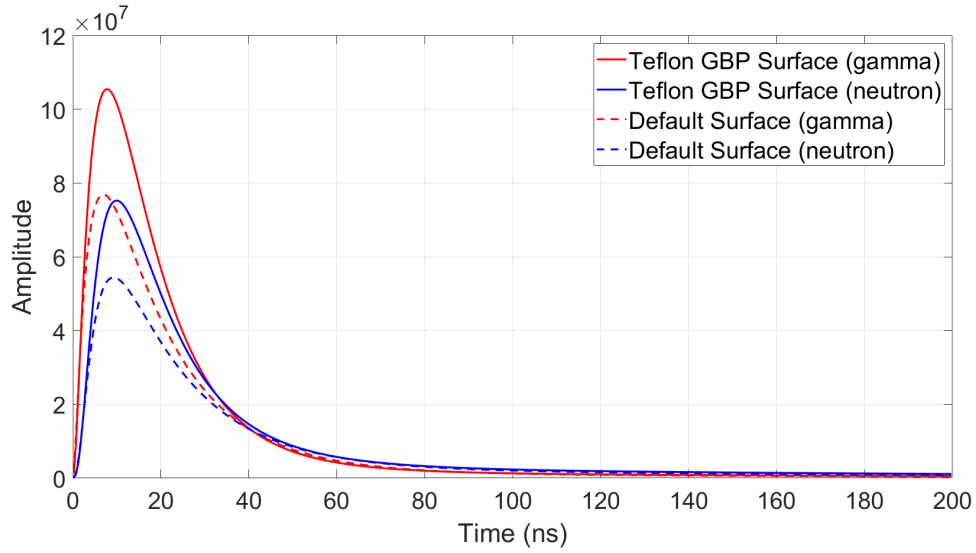

Figure 5.3: Comparison of summed light pulses generated using the simulated Teflon `groundbackpainted` (GBP) optical surface and Geant4's Default Surface (without an explicitly defined surface), prior to normalisation and temporal alignment.

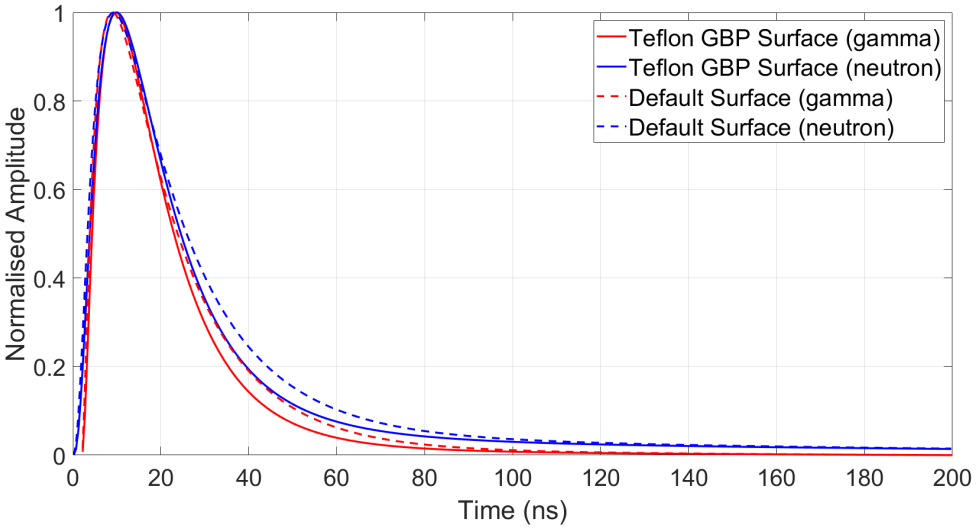

Figure 5.4: Comparison of summed light pulses generated using the simulated Teflon `groundbackpainted` (GBP) optical surface and Geant4's Default Surface (without an explicitly defined surface), after normalisation and temporal alignment.

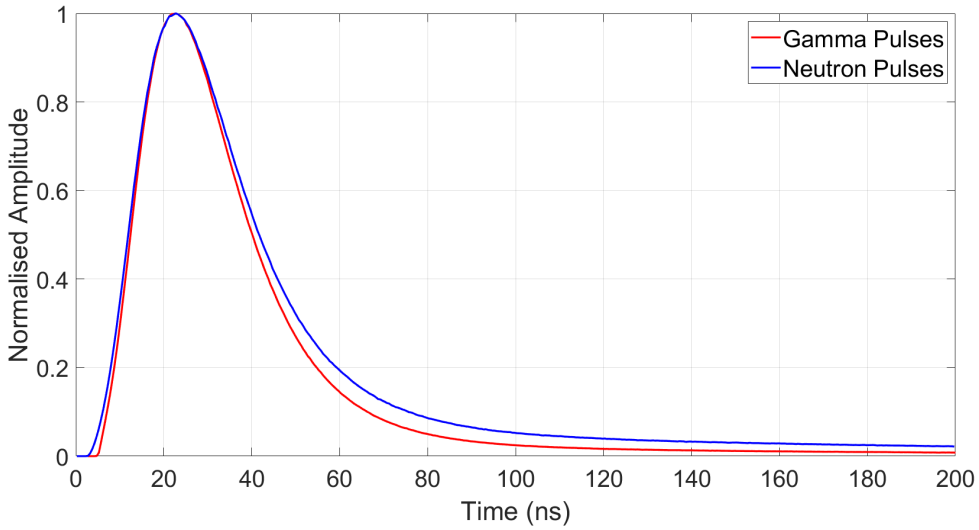

Figure 5.5: Summed simulated light pulses from neutron and gamma-ray interactions in a 50 mm × 50 mm × 1000 mm EJ-276 plastic scintillator with a simulated Teflon `groundbackpainted` (GBP) optical surface. Each pulse shape represents the sum of 1000 individual pulses, following normalisation and temporal alignment.

in faster pulse decay for both gamma- and neutron-induced interactions.

Figure 5.5 shows the normalised and temporally aligned pulse shapes for a cuboid with a Z-axis length of 1000 mm. Unlike the 1000 mm cuboid used in the geometrical simulations, these neutron and gamma-induced pulse shapes do not exhibit the secondary peaks in the decay tail observed for the cuboid geometry with Default Surface, for the same scintillator length. Although broadened due to the increased length, the pulses remain smooth, Gaussian-like, and free of artefacts or distortions.

Figure 5.6 shows the pulse shape discrimination (PSD) performance of an EJ-276 plastic scintillation detector with a Teflon `groundbackpainted` (GBP) surface. Each subplot shows the PSD parameter (long integral/short integral) as a function of the long integral for simulated neutron (blue) and gamma-ray (red) pulses, shown in the absence of simulated noise.

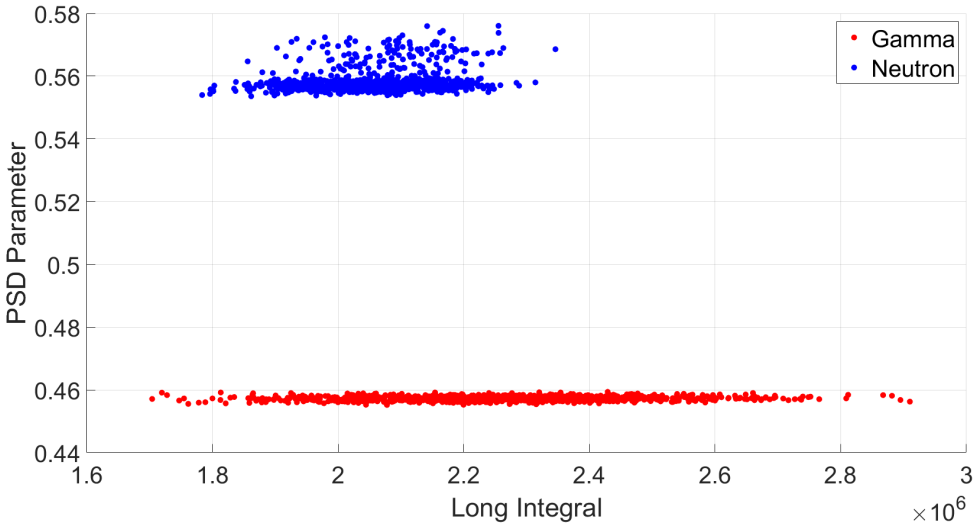

Figure 5.6: PSD parameter distributions for neutron and gamma-ray pulses in an EJ-276 cuboid scintillator with a Teflon `groundbackpainted` optical surface. The PSD parameter is defined as the ratio of long to short integrals.

As observed in Figure 4.21, there is clear separation between the neutron and gamma-ray PSD parameter distributions. This separation is also evident for the same cuboid length when a Teflon `groundbackpainted` (GBP) surface is applied to the scintillator. In this case, the distributions are narrower, and the long integral values are shifted to higher ranges for both particle types, attributable to the improved light collection efficiency provided by the Teflon GBP surface. Gamma-ray events cluster around a PSD parameter of approximately 0.45, while neutron events cluster near 0.56. The neutron distribution exhibits slightly greater vertical spread in PSD parameter values compared to the gamma distribution.

Figure 5.7 shows the summed light pulses obtained from simulations using a Teflon optical surface with a `polishedbackpainted` (PBP) finish. As with the Teflon `groundbackpainted` (GBP) surface, the surface reflectivity was set to 98%, however, in this case no surface roughness parameter was specified. The material type was dielectric-dielectric. Instead, the optical surface was defined using a

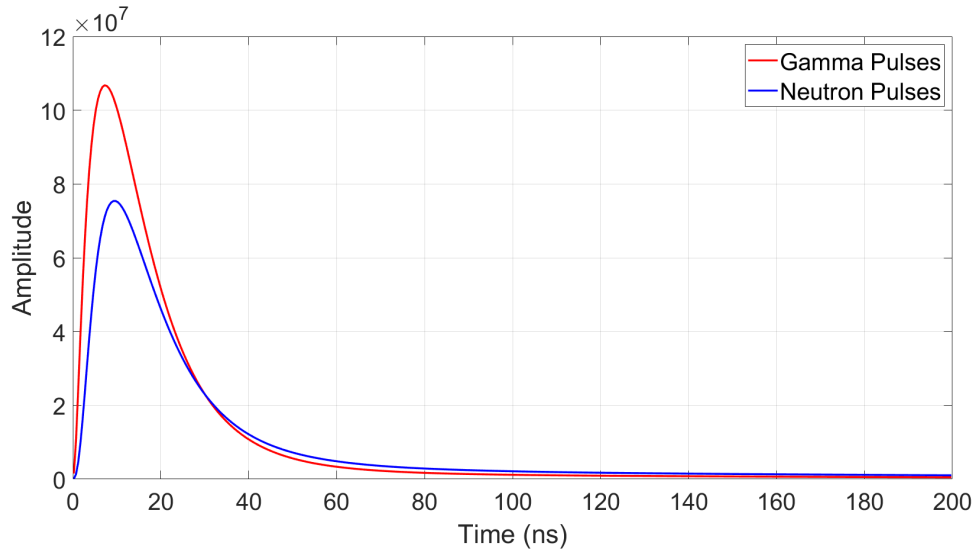

Figure 5.7: Summed simulated light pulses from neutron and gamma-ray interactions in an EJ-276 plastic scintillator with a simulated Teflon `polishedbackpainted` optical surface. Each pulse shape represents the sum of 1000 individual pulses, prior to normalisation and temporal alignment.

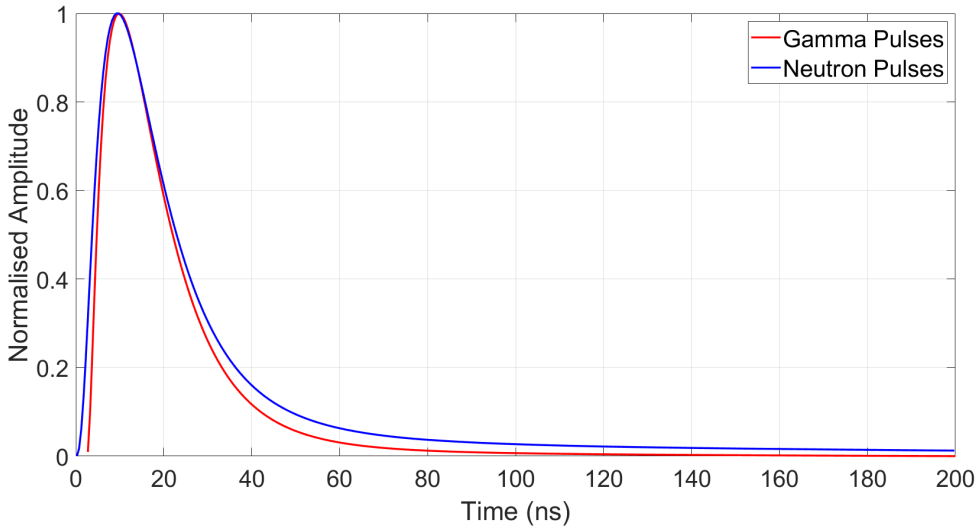

Figure 5.8: Summed simulated light pulses from neutron and gamma-ray interactions in an EJ-276 plastic scintillator with a simulated Teflon `polishedbackpainted` (PBP) optical surface. Each pulse shape represents the sum of 1000 individual pulses, following normalisation and temporal alignment.

specular lobe component of 0.5 and a specular spike component of 0.2, representing a semi-specular polished Teflon-wrapped scintillator.

Under these conditions, both the gamma- and neutron-induced pulses exhibit smooth, Gaussian-like shapes, free from noticeable distortions or artefacts. The gamma-induced pulse reaches a peak amplitude of 1.07×10^8 photons at 7.25 ns, while the neutron-induced pulse peaks at 7.54×10^8 photons at 9.75 ns.

The total number of detected photons is 2.34×10^9 for gamma-ray events and 2.01×10^9 for neutron events.

Figure 5.8 shows the same pulses following normalisation and temporal alignment. The neutron- and gamma-induced pulses show clear temporal separation, particularly in the decay tails.

Figure 5.9 compares the response of the polished Teflon-wrapped surface, with Geant4's Default Surface. As observed in Figure 5.1, the polished Teflon surface

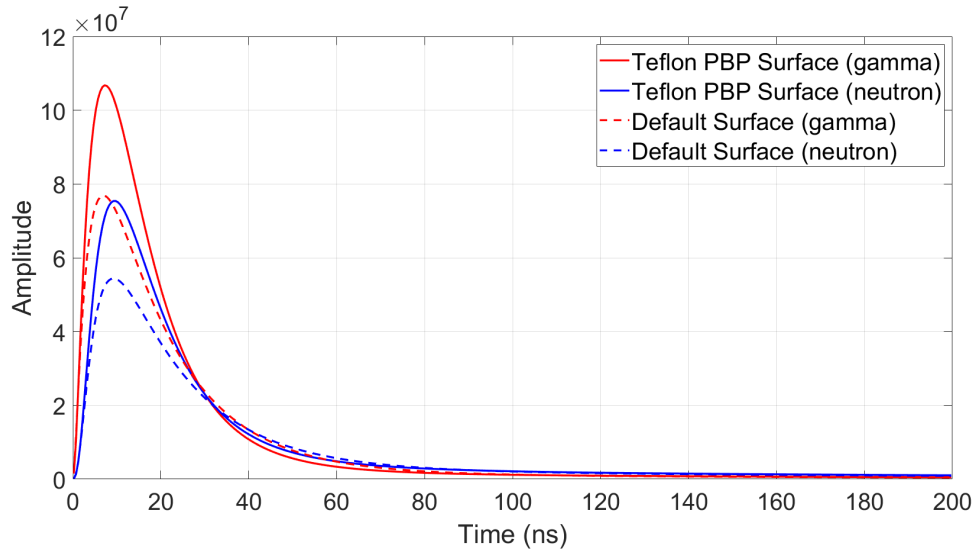

Figure 5.9: Comparison of summed light pulses generated using the Teflon `polishedbackpainted` (PBP) optical surface and Geant4's Default Surface (without an explicitly defined surface), prior to normalisation and temporal alignment.

exhibits improved light collection efficiency (LCE) compared to the Default Surface.

Figure 5.10 presents the pulses after normalisation and temporal alignment. It can be observed that the pulse shapes associated with the Default Surface are broader than those associated with the Teflon PBP surface, indicating slower photon collection at the photodetector.

Figure 5.11 presents normalised and temporally aligned simulated light pulses obtained from simulations of a cuboid scintillator 50 mm × 50 mm × 1000 mm with a Teflon `polishedbackpainted` (PBP) surface. Similar to the pulses shown in Figure 5.5, these neutron- and gamma-induced pulse shapes do not exhibit the secondary peaks in the decay tail observed in Figure 4.18 for the same scintillator length. Although the pulses are broadened due to the increased scintillator length, they remain smooth, Gaussian-like, and free of distortions or artefacts.

Figure 5.12 illustrates the pulse shape discrimination (PSD) performance of an EJ-276 plastic scintillation detector with a simulated Teflon wrapping having

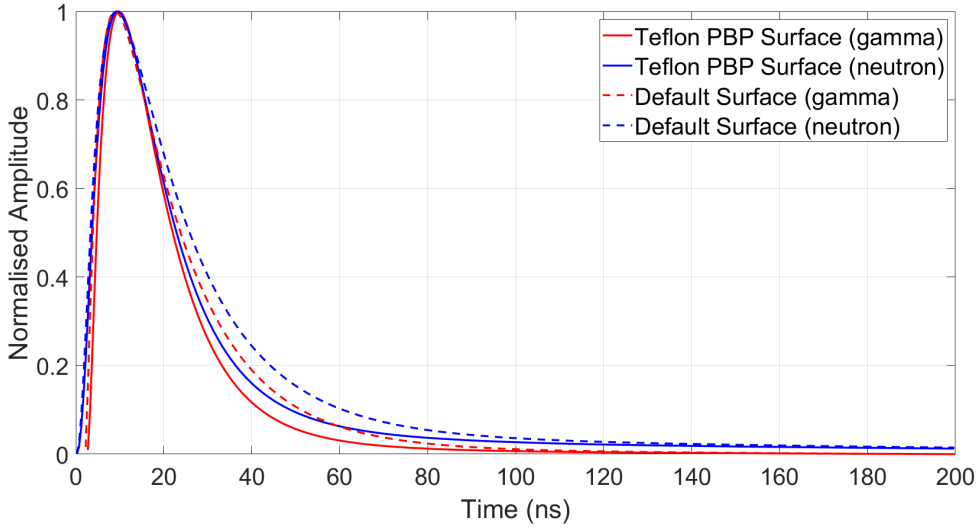

Figure 5.10: Comparison of summed light pulses generated using the simulated Teflon `polishedbackpainted` (PBP) optical surface and Geant4's Default Surface (without an explicitly defined surface), following normalisation and temporal alignment.

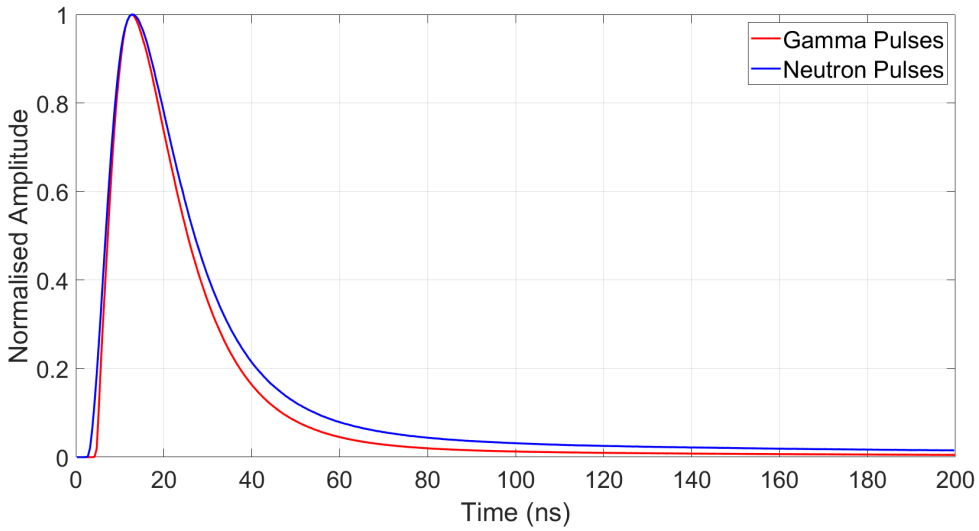

Figure 5.11: Summed simulated light pulses from neutron and gamma-ray interactions in a 50 mm × 50 mm × 1000 mm EJ-276 plastic scintillator with a simulated Teflon `polishedbackpainted` (PBP) optical surface. Each pulse shape represents the sum of 1000 individual pulses, following normalisation and temporal alignment.

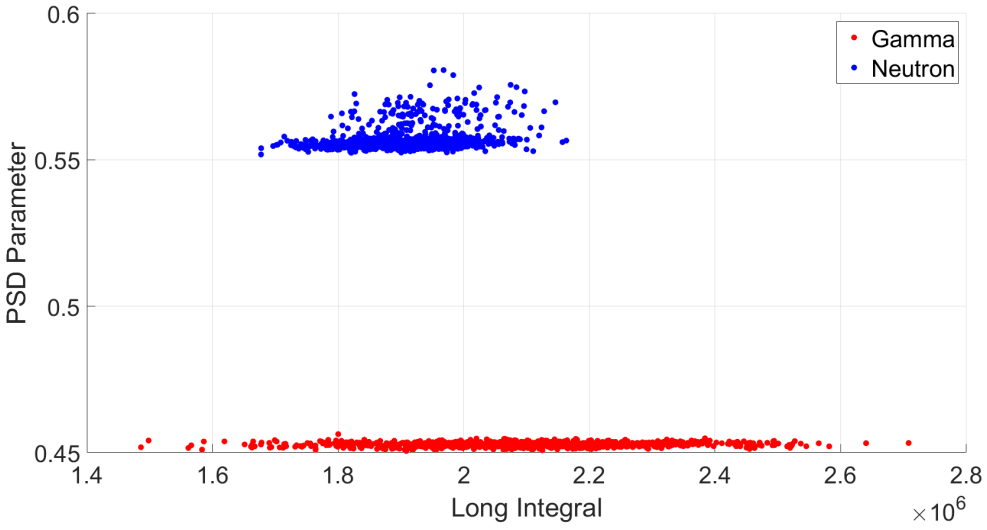

Figure 5.12: PSD parameter distributions for neutron and gamma-ray pulses in an EJ-276 cuboid scintillator with a Teflon `polishedbackpainted` optical surface. The PSD parameter is defined as the ratio of long to short integrals.

a `polishedbackpainted` (PBP) finish. Each subplot depicts the PSD parameter (long integral/short integral) plotted against the long integral for simulated neutron (blue) and gamma-ray (red) pulses, in the absence of any simulated noise.

For this idealised, noise-free case, the neutron and gamma plumes are distinctly well separated with limited variability in PSD parameter for both distributions. The gamma plume is centred around a PSD parameter of ≈0.45 and the neutron plume near ≈0.55.

5.2 EJ-510 Reflective Paint

Figure 5.13 presents the summed simulated light pulses obtained using an optical surface designed to emulate the optical properties of EJ-510 reflective paint. In this configuration, the surface was assigned a reflectivity of 97%, a roughness parameter of 0.2°, and a material type of dielectric-metal. No values were specified for the

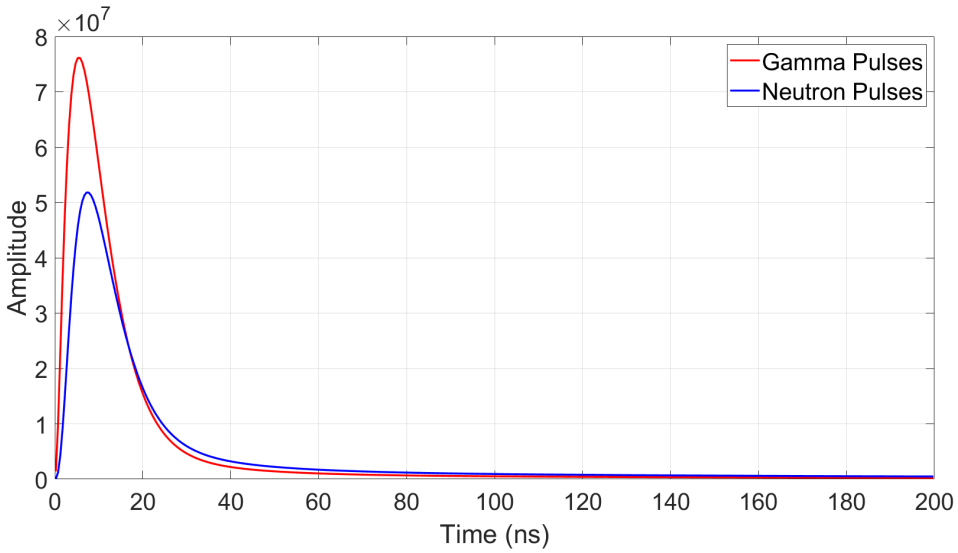

Figure 5.13: Summed simulated light pulses from neutron and gamma-ray interactions in an EJ-276 plastic scintillator with a simulated EJ-510 `groundfrontpainted` (GFP) optical surface. Each pulse shape represents the sum of 1000 individual pulses, prior to normalisation and temporal alignment.

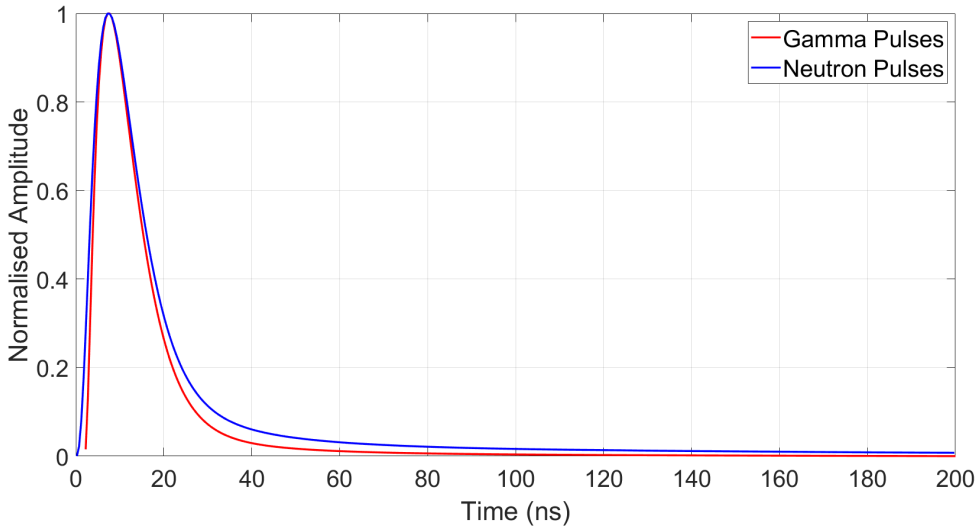

Figure 5.14: Summed simulated light pulses from neutron and gamma-ray interactions in an EJ-276 plastic scintillator with a simulated EJ-510 `groundfrontpainted` optical surface. Each pulse shape represents the sum of 1000 individual pulses, following normalisation and temporal alignment.

specular lobe or specular spike components, as the surface was intended to represent a fully diffuse reflector. The optical surface finish applied was `groundfrontpainted` (GFP).

Under these conditions, the gamma-induced pulse reaches a peak amplitude 7.61×10^7 photons at 5.25 ns, while the neutron-induced pulse peaks at 5.81×10^7 photons at 7.25 ns.

Figure 5.14 shows the same pulses when normalised and temporally aligned. The neutron- and gamma-induced pulses show clear temporal separation, particularly in the decay tail.

Figure 5.15 presents a comparison of the summed light pulses obtained using the EJ-510 `groundfrontpainted` (GFP) optical surface and those generated with Geant4's Default Surface.

Figure 5.16 shows the normalised and temporally aligned pulses obtained from

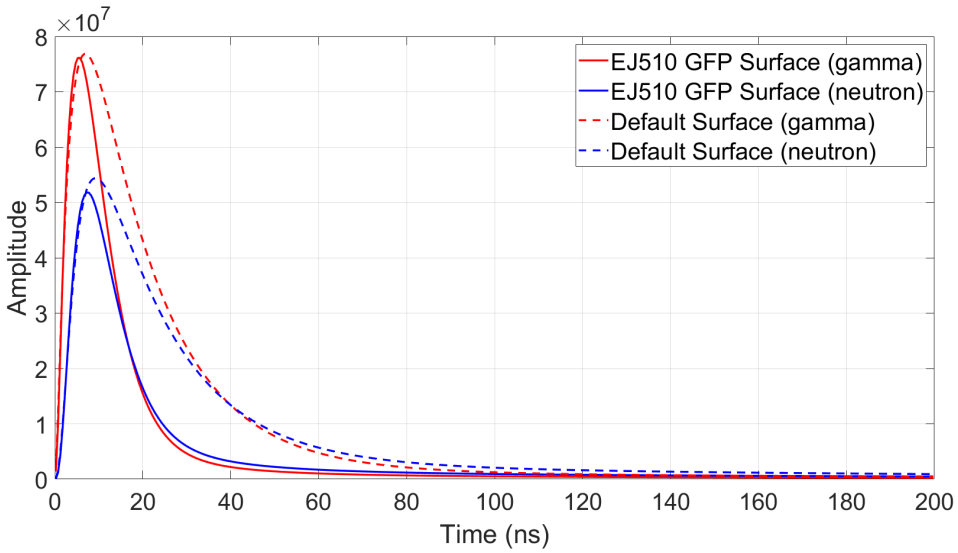

Figure 5.15: Comparison of summed light pulses generated using the simulated EJ-510 `groundfrontpainted` (GBP) optical surface and Geant4's Default Surface (without an explicitly defined surface), prior to normalisation and temporal alignment.

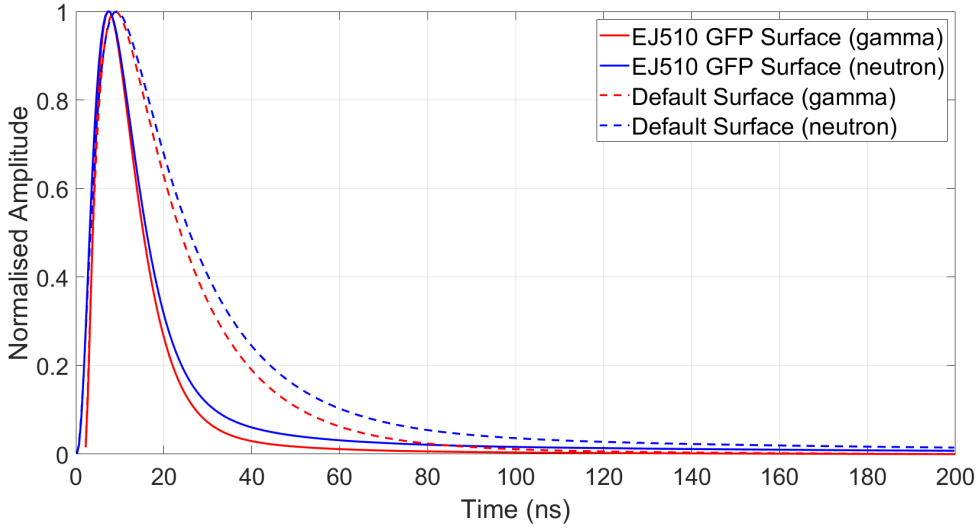

Figure 5.16: Comparison of summed light pulses generated using the simulated EJ-510 `groundfrontpainted` (GFP) optical surface and Geant4's Default Surface (without an explicitly defined surface), following normalisation and temporal alignment.

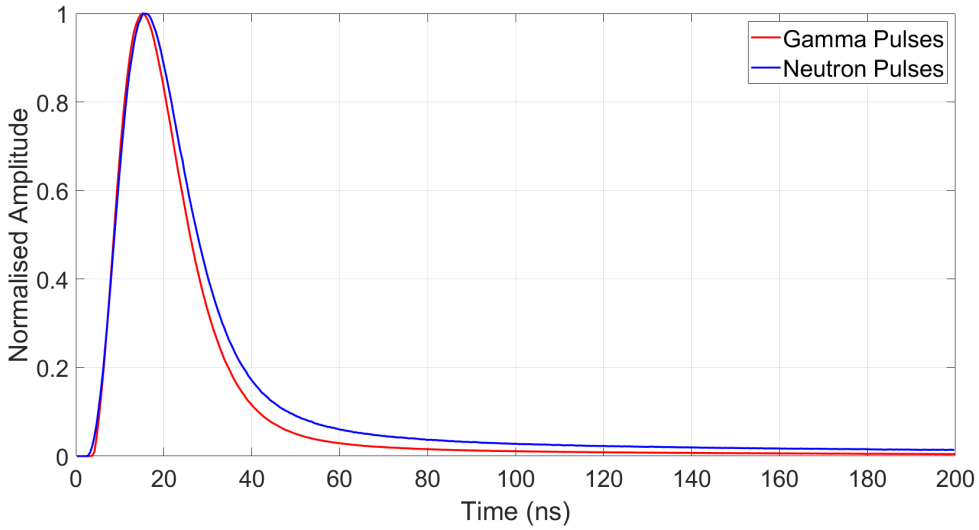

Figure 5.17: Summed simulated light pulses from neutron and gamma-ray interactions in a 50 mm × 50 mm × 1000 mm EJ-276 plastic scintillator with a simulated EJ-510 `groundfrontpainted` (GFP) optical surface. Each pulse shape represents the sum of 1000 individual pulses, following normalisation and temporal alignment.

the EJ-510 painted scintillator and the Default Surface. A substantial reduction in pulse width is observed for both gamma- and neutron-induced pulses in the EJ-510 configuration compared to the Default Surface, indicating improved timing characteristics.

Figure 5.17 presents normalised and temporally aligned simulated light pulses obtained from simulations of a cuboid scintillator (50 mm × 50 mm × 1000 mm) with an EJ-510 reflective paint surface. Similar to pulses shown in Figures 5.5 and 5.11, these neutron- and gamma-induced pulse shapes do not exhibit secondary peaks in the decay tail observed in Figure 4.18. Though broadened due to the longer scintillator length, they remain smooth, Gaussian-like, and free of distortions.

Figure 5.18 shows the pulse shape discrimination (PSD) performance of an EJ-276 plastic scintillation detector with a simulated EJ-510 reflective paint having a

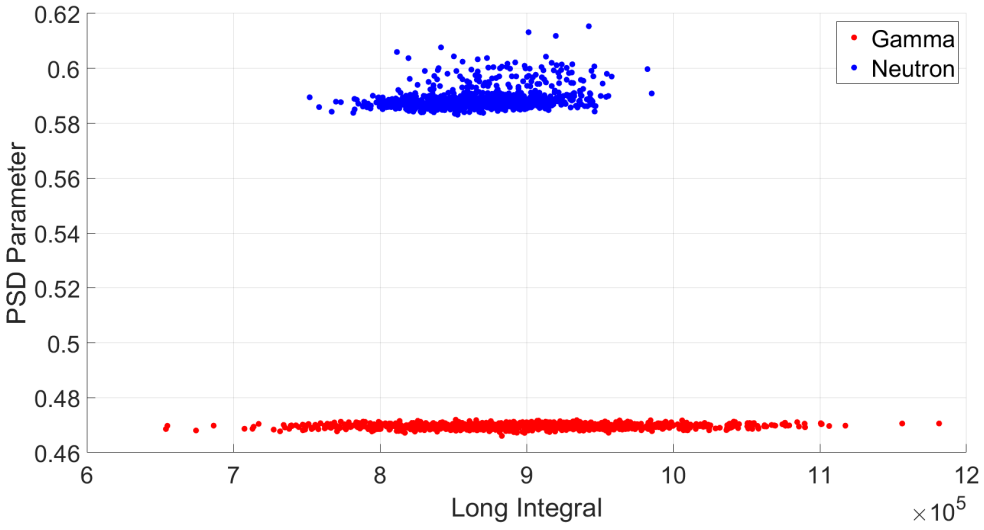

Figure 5.18: PSD parameter distributions for neutron and gamma-ray pulses in an EJ-276 cuboid scintillator with a simulated EJ-510 `groundfrontpainted` optical surface. The PSD parameter is defined as the ratio of long to short integrals

`groundbackpainted` (GBP) finish. Each subplot depicts the PSD parameter (long integral/short integral) plotted against the long integral for simulated neutron (blue) and gamma-ray (red) pulses, shown without any simulated noise.

For this idealised, noise-free case, the neutron and gamma plumes are distinctly well separated with limited variability in PSD parameter for both distributions. The gamma plume is centred around a PSD parameter of ≈ 0.45 and the neutron plume near ≈ 0.56.

5.3 Aluminium Foil

Figure 5.19 illustrates the summed light pulses obtained from simulations using an aluminium foil optical surface with a `polishedbackpainted` (PBP) finish. The surface reflectivity was set to 95%, with a dielectric-dielectric material type. Since this surface represents an idealised specular reflector, no surface roughness parameter

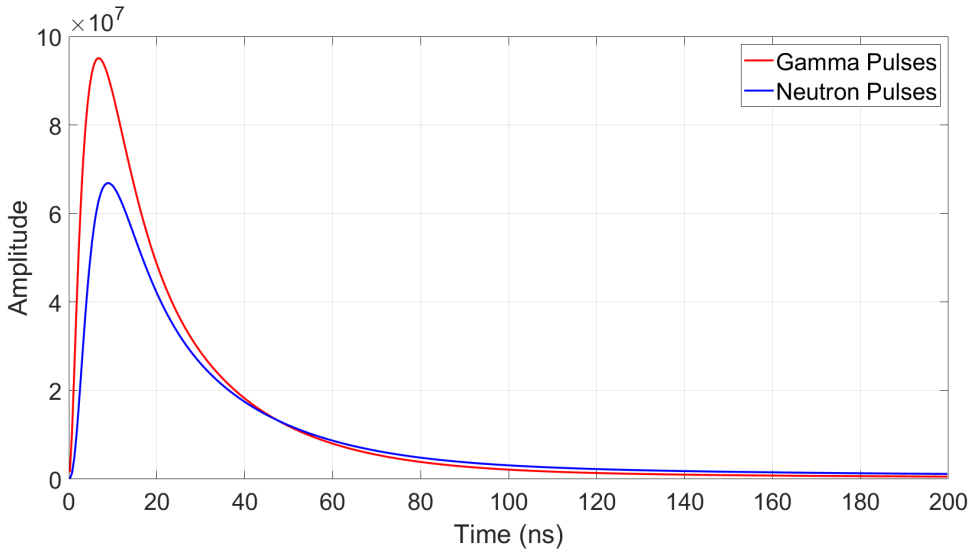

Figure 5.19: Summed simulated light pulses from neutron and gamma-ray interactions in an EJ-276 plastic scintillator with a simulated aluminium foil `polishedbackpainted` (PBP) optical surface. Each pulse shape represents the sum of 1000 individual pulses, prior to normalisation and temporal alignment.

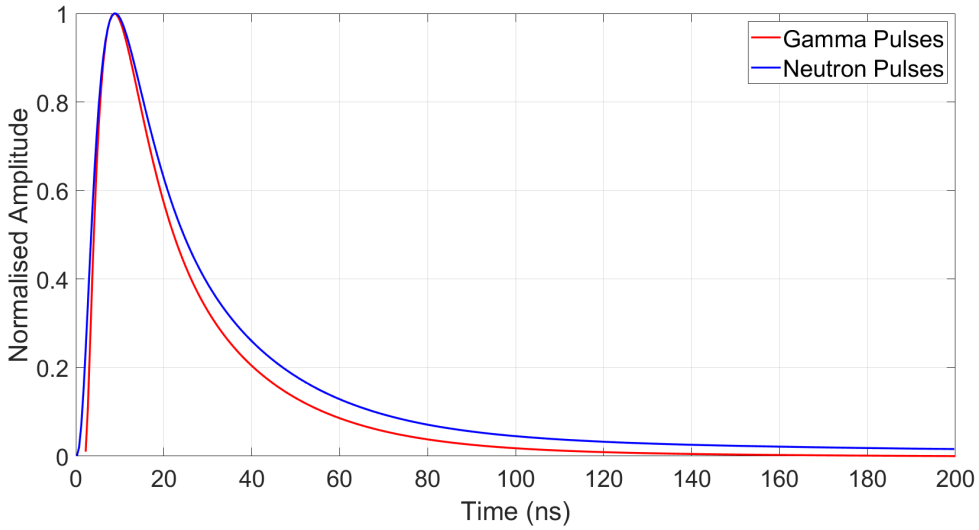

Figure 5.20: Summed simulated light pulses from neutron and gamma-ray interactions in an EJ-276 plastic scintillator with a simulated aluminium foil `polishedbackpainted` (PBP) optical surface. Each pulse shape represents the sum of 1000 individual pulses, following normalisation and temporal alignment.

was defined. The specular lobe and specular spike parameters were set to 0 and 1, respectively.

The gamma-induced pulse reaches a peak amplitude of 9.51×10^7 photons at 6.75 ns, while the neutron-induced pulse peaks at 6.69×10^7 photons at 8.75 ns. The total number of detected photons is 2.51×10^9 for gamma-ray events and 2.15×10^9 for neutron events.

Figure 5.20 presents the normalised and temporally aligned pulses, which exhibit smooth, approximately Gaussian-like shapes with no noticeable artefacts or distortions.

Figure 5.21 presents a comparison of summed light pulses generated using the aluminium foil `polishedbackpainted` (PBP) optical surface and those obtained with Geant4's Default Surface. The neutron- and gamma-induced pulse shapes for the aluminium foil surface exhibit higher peak amplitudes compared to those from

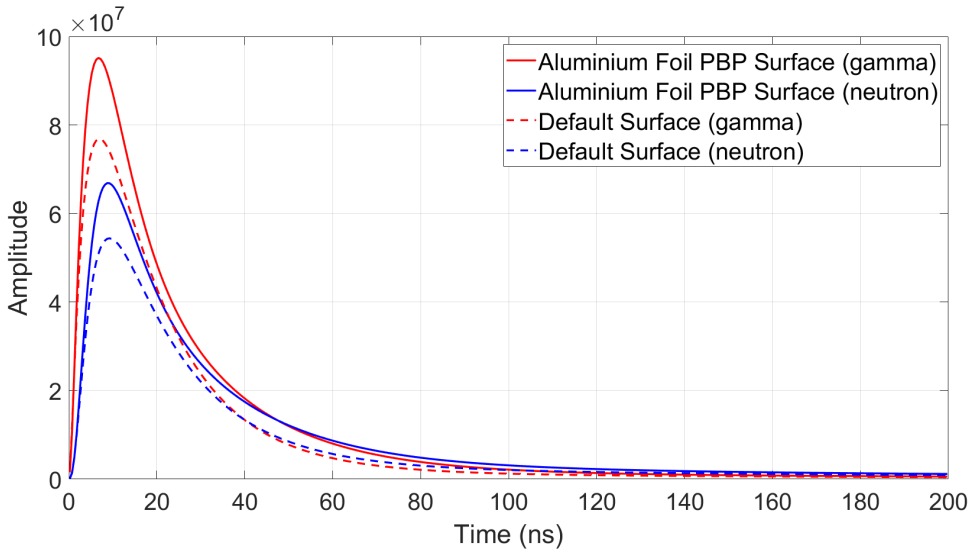

Figure 5.21: Comparison of summed light pulses generated using the simulated aluminium foil `polishedbackpainted` (PBP) optical surface and Geant4's Default Surface (without an explicitly defined surface), prior to normalisation and temporal alignment.

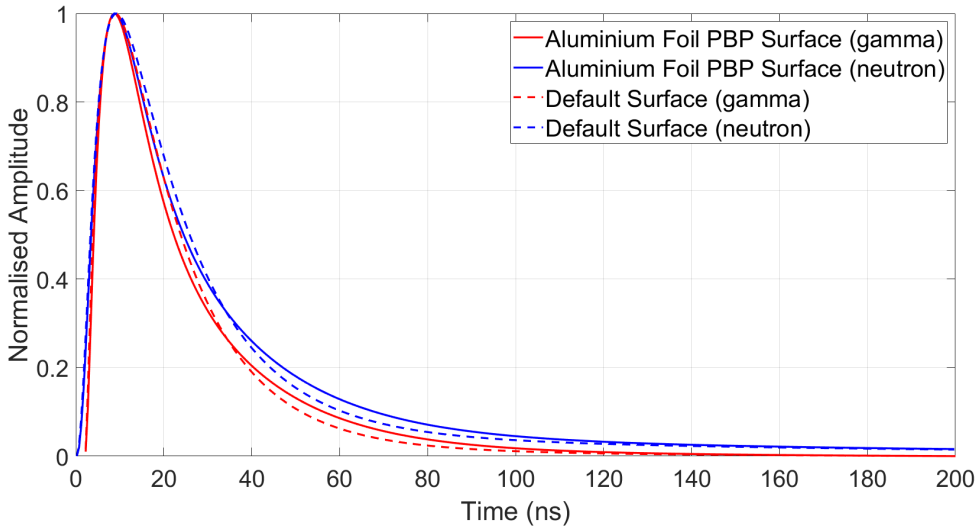

Figure 5.22: Comparison of summed light pulses generated using the Aluminium foil `polishedbackpainted` (PBP) optical surface and Geant4's Default Surface (without an explicitly defined surface), following normalisation and temporal alignment.

the Default Surface.

Figure 5.22 presents the same pulses following normalisation and temporal alignment. Notably, the Default Surface exhibits a faster pulse decay than the aluminium foil wrapped scintillator. Furthermore, the aluminium foil surface displays a higher peak amplitude.

Figure 5.23 presents normalised and temporally aligned simulated summed light pulses from a cuboid scintillator (50 mm × 50 mm × 1000 mm) with a simulated aluminium foil `polishedbackpainted` (PBP) surface. In contrast to the results for the simulated Teflon and EJ-510 surfaces, the light pulses for the aluminium surface exhibits artefacts at the pulse peaks, which are more pronounced in the gamma-induced pulse. There is also subtle distortion in the decay tail of the pulses; however, good separation between neutron- and gamma-induced pulses is maintained.

Figure 5.24 shows the pulse shape discrimination (PSD) performance of an EJ-276 plastic scintillation detector with a simulated aluminium foil having a

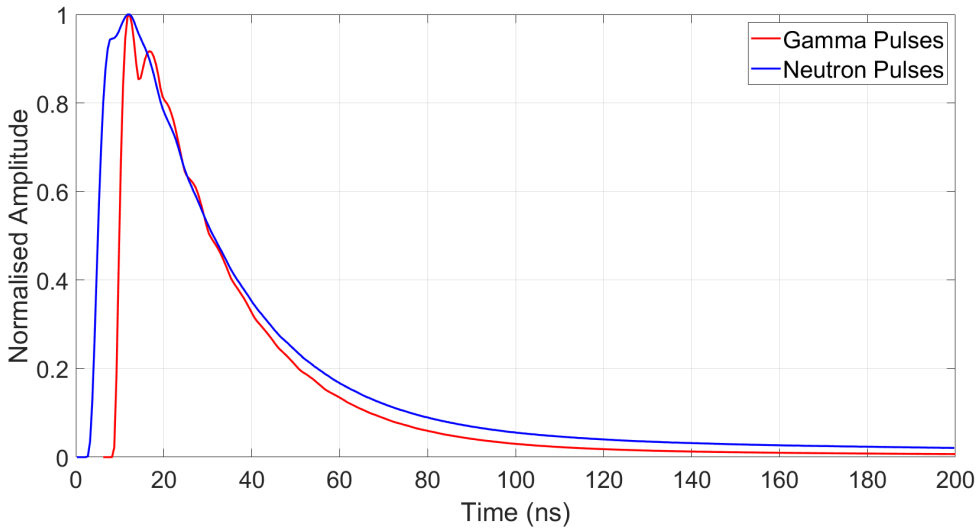

Figure 5.23: Summed simulated light pulses from neutron and gamma-ray interactions in a 50 mm × 50 mm × 1000 mm EJ-276 plastic scintillator with a simulated aluminium foil `polishedbackpainted` (PBP) optical surface. Each pulse shape represents the sum of 1000 individual pulses, following normalisation and temporal alignment.

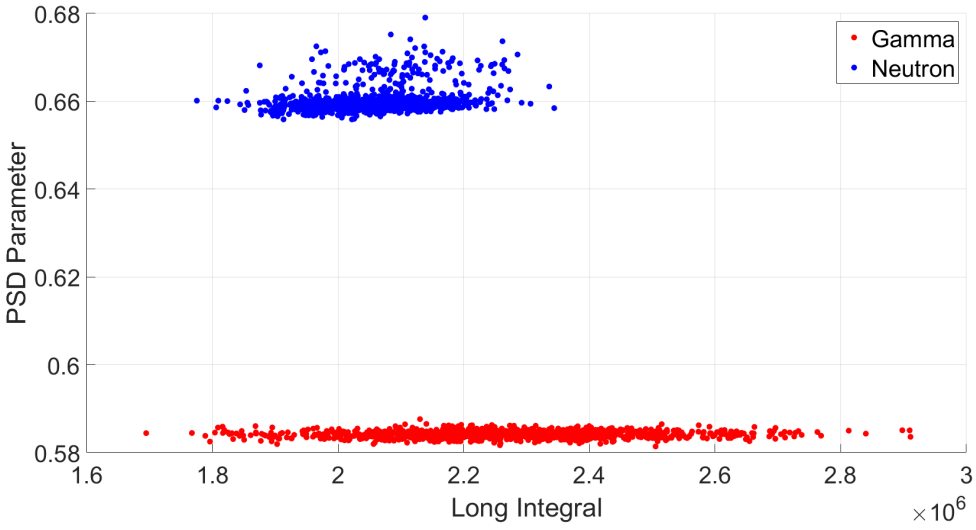

Figure 5.24: PSD parameter distributions for neutron and gamma-ray pulses in an EJ-276 cuboid scintillator with an aluminium foil `polishedbackpainted` (PBP) optical surface. The PSD parameter is defined as the ratio of long to short integrals.

`polishedbackpainted` (PBP) finish. Each subplot depicts the PSD parameter (long integral/short integral) plotted against the long integral for simulated neutron (blue) and gamma-ray (red) pulses, shown in the absence of simulated noise.

For this idealised, noise-free case, the neutron and gamma plumes are distinctly well separated with limited variability in PSD parameter for both distributions. The gamma plume is centred around a PSD parameter of ≈ 0.57 and the neutron plume near ≈ 0.66.

5.4 Enhanced Specular Reflector (ESR) Film

Figure 5.25 shows the summed simulated light pulses obtained using an optical surface modelled to replicate the optical properties of an Enhanced Specular Reflector (ESR) film. The surface was assigned a reflectivity of 98% and a material type of dielectric-dielectric. No surface roughness parameter was defined for this

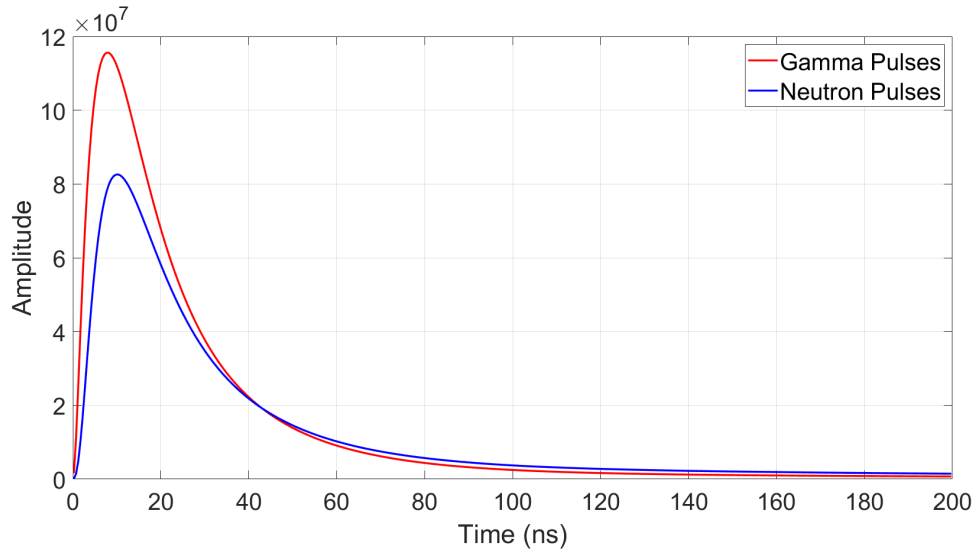

Figure 5.25: Summed simulated light pulses from neutron and gamma-ray interactions in an EJ-276 plastic scintillator with a simulated ESR film `polishedfrontpainted` (PBP) optical surface. Each pulse shape represents the sum of 1000 individual pulses, prior to normalisation and temporal alignment.

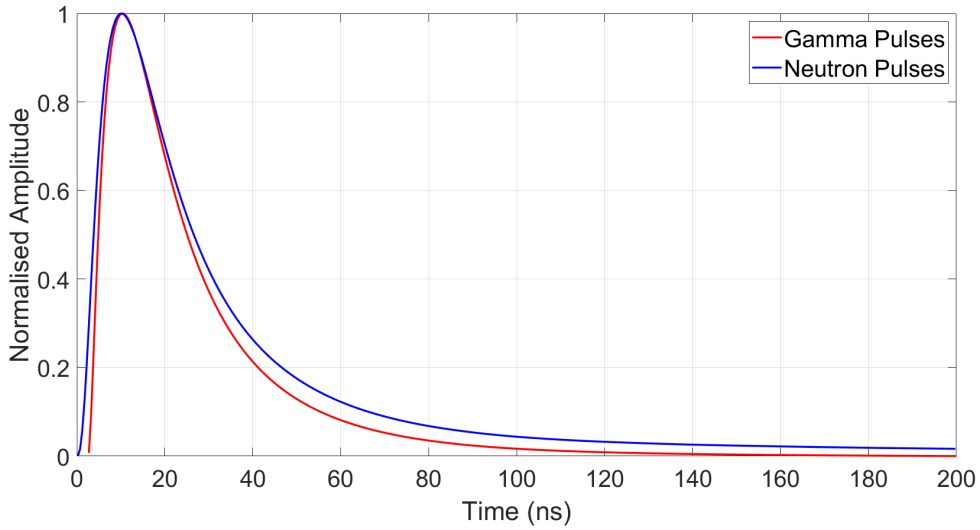

Figure 5.26: Summed simulated light pulses from neutron and gamma-ray interactions in an EJ-276 plastic scintillator with a simulated ESR film `polishedfrontpainted` (PBP) optical surface. Each pulse shape represents the sum of 1000 individual pulses, following normalisation and temporal alignment.

configuration. To represent a highly specular, polished film wrapped around the scintillator, the specular lobe and specular spike components were set to 1 and 0, respectively. The optical finish applied was `polishedbackpainted` (PBP).

For this configuration, the gamma-induced pulse reaches a peak amplitude of 1.16×10^8 photons at 7.75 ns, while the neutron-induced pulse peaks at 8.26×10^7 photons at 10.25 ns.

The total number of detected photons is 3.16×10^9 for gamma-ray events and 2.72×10^9 for neutron events.

Figure 5.26 shows the same pulses after normalisation and temporal alignment. Clear separation is observed between neutron- and gamma-induced pulses, with both pulses exhibiting smooth, Gaussian-like shapes which are free from distortions and artefacts.

Figure 5.27 presents a comparison between the simulated light pulses generated

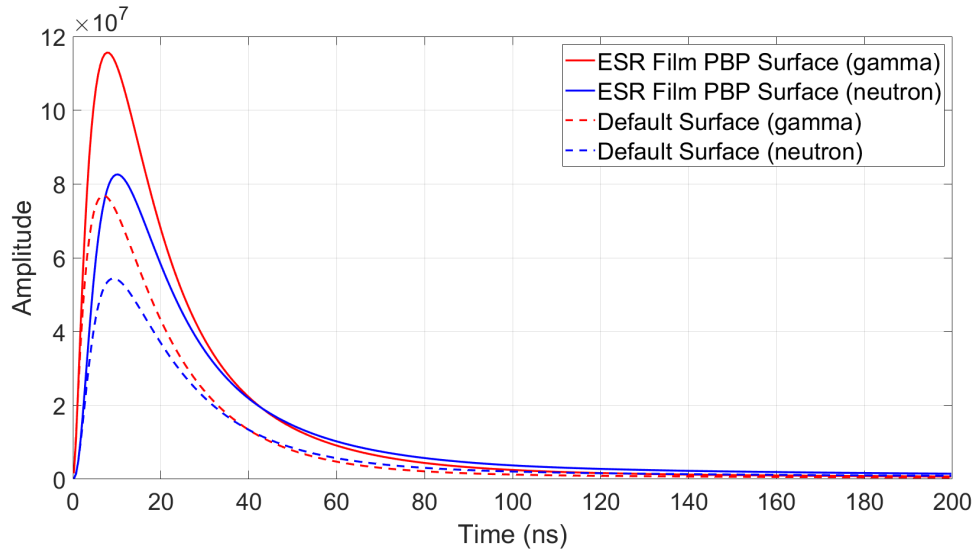

Figure 5.27: Comparison of summed light pulses generated using the simulated Enhanced Specular Reflector (ESR) film `polishedbackpainted` (PBP) optical surface and Geant4's Default Surface (without an explicitly defined surface), prior to normalisation and temporal alignment.

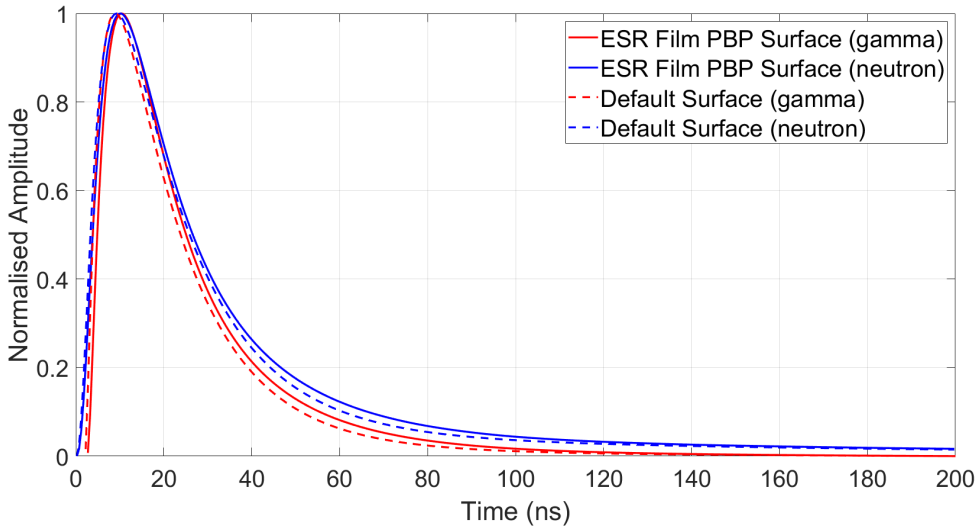

Figure 5.28: Comparison of summed light pulses generated using the simulated ESR film `polishedbackpainted` (PBP) optical surface and Geant4's Default Surface (without an explicitly defined surface), following normalisation and temporal alignment.

using the Enhanced Specular Reflector (ESR) optical surface and those obtained with Geant4's Default Surface. The ESR pulses display higher amplitudes than the Default Surface pulses, demonstrating an improved light collection efficiency with the ESR surface.

Figure 5.28 shows the same pulses following normalisation and temporal alignment. When compared to the Default Surface, the pulse shapes exhibit limited differences; notably, the pulses corresponding to the ESR surface appear slightly broader.

Figure 5.29 presents normalised and temporally aligned simulated summed light pulses from a cuboid scintillator (50 mm × 50 mm × 1000 mm) with a simulated Enhanced Specular Reflector (ESR) film `polishedbackpainted` (PBP) surface. The ESR surface pulses closely resemble those obtained for aluminium foil, as shown in Figure 5.23 for the same scintillator geometry and length. This similarity

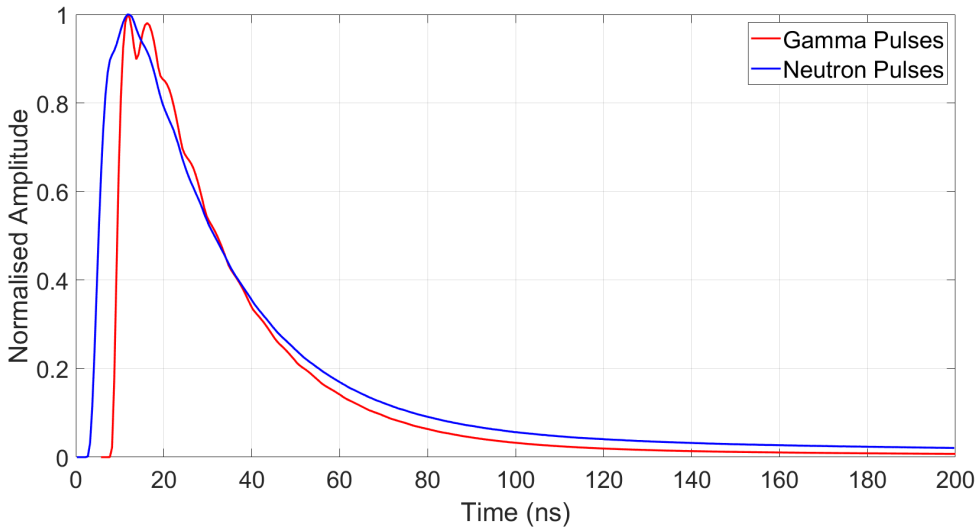

Figure 5.29: Summed simulated light pulses from neutron and gamma-ray interactions in a 50 mm × 50 mm × 1000 mm EJ-276 plastic scintillator with a simulated Enhanced Specular Reflector (ESR) `polishedbackpainted` (PBP) optical surface. Each pulse shape represents the sum of 1000 individual pulses, following normalisation and temporal alignment.

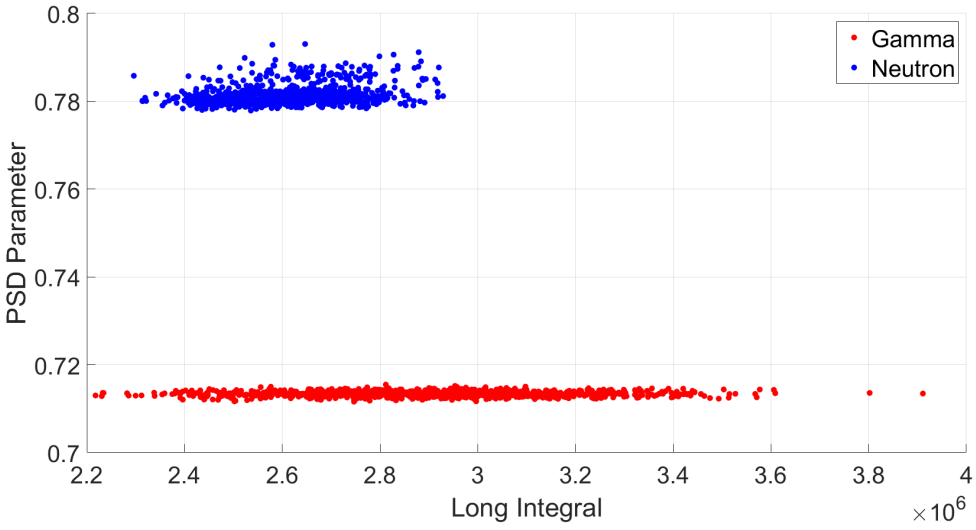

Figure 5.30: PSD parameter distributions for neutron and gamma-ray pulses in an EJ-276 cuboid scintillator with an ESR film `polishedbackpainted` optical surface. The PSD parameter is defined as the ratio of long to short integrals.

likely results from both ESR and aluminium foil being purely specular reflectors and sharing identical values for both the specular lobe and specular spike surface parameters, as shown in Table 3.3. The primary distinction is the slightly higher reflectivity for ESR (98%), compared to aluminium foil (95%).

Figure 5.30 shows the pulse shape discrimination (PSD) performance of an EJ-276 plastic scintillation detector with a simulated aluminium foil having a `polishedbackpainted` (PBP) finish. Each subplot depicts the PSD parameter (long integral/short integral) plotted against the long integral for simulated neutron (blue) and gamma-ray (red) pulses, shown in the absence of simulated noise.

For this idealised, noise-free case, the neutron and gamma plumes are distinctly well separated with limited variability in PSD parameter for both distributions. The gamma plume is centred around a PSD parameter of ≈ 0.50 and the neutron plume near ≈ 0.66.

The pulse integrals for gamma- and neutron-induced pulses across all simulated

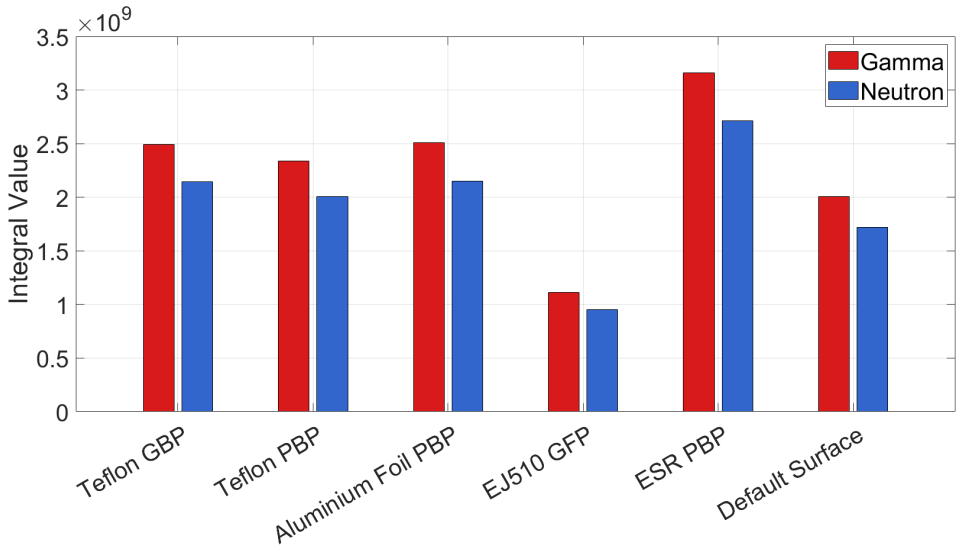

Figure 5.31: Integral values (total area under the pulse) for scintillators with different surface treatments, including the Default Surface (no surface explicitly specified).

surface types are shown in Figure 5.31. The simulated Enhanced Specular Reflector (ESR) surface yields the highest integrals, while the lowest are observed for the EJ-510 reflective paint surface. This behaviour is consistent for both gamma and neutron pulses.

Figure 5.32 depicts the peak amplitudes of gamma- and neutron-induced pulses for each simulated surface type. The highest peak amplitudes occur with the Enhanced Specular Reflector (ESR) surface, while the lowest are observed for the EJ-510 reflective paint surface, consistent across both pulse types.

Table 5.1 summarises the integrals, peak amplitudes, and neutron-to-gamma ratios obtained for each simulated surface configuration.

Table 5.1: Peak amplitudes, integrated photon counts, and neutron-to-gamma integral ratios for gamma- and neutron-induced pulses for each simulated optical surface.

Surface	**Peak Amplitude (gamma)**	**Peak Amplitude (neutron)**	**Integral (gamma)**	**Integral (neutron)**	**Ratio (neutron/gamma)**
Teflon GBP	1.05×10^8	7.52×10^7	2.494×10^9	2.147×10^9	0.86095
Teflon PBP	1.067×10^8	7.54×10^7	2.339×10^9	2.006×10^9	0.85765
Aluminium Foil PBP	9.51×10^7	6.69×10^7	2.511×10^9	2.152×10^9	0.85702
EJ510 GFP	7.61×10^7	5.18×10^7	1.110×10^9	9.52×10^8	0.85768
ESR PBP	1.156×10^8	8.26×10^7	3.162×10^9	2.715×10^9	0.85870
Default Surface	7.69×10^7	5.44×10^7	2.008×10^9	1.717×10^9	0.85525

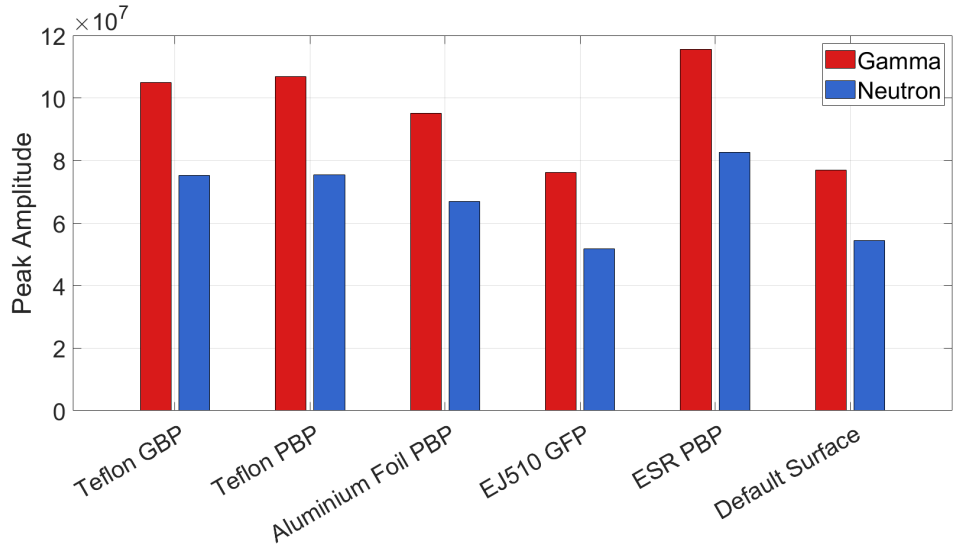

Figure 5.32: Peak amplitudes for scintillators with different surface treatments, including the Default Surface (no surface explicitly specified) used in Chapter 4.

Chapter 6

Simulating Photodetector Noise

This chapter presents results demonstrating the effect of various types and levels of simulated photodetector noise on the pulse shape discrimination (PSD) performance across the scintillator geometries described in Chapter 4. Shot noise — which scales with pulse amplitude — and Gaussian noise of fixed level were added to the previously simulated light pulses corresponding to the slab, cylinder, and cuboid geometries in Geant4. The impact of this noise on pulse shape discrimination (PSD) was then evaluated for each geometry. Both types of noise are common in photodetectors, including photomultiplier tubes (PMTs) and silicon photomultipliers (SiPMs), and thus introduce additional complexity into the simulations to better approximate experimental observations.

6.1 Slab Geometry

Figure 6.1 presents the PSD performance of slab scintillator geometries with lengths ranging from 50 mm to 2000 mm, with simulated shot noise applied to the light pulses. Clear separation between neutron and gamma PSD distributions is observed across all slab lengths.

It can be seen that the addition of shot noise to the simulated pulses has minimal impact on discrimination performance compared with the ideal, no-noise case shown

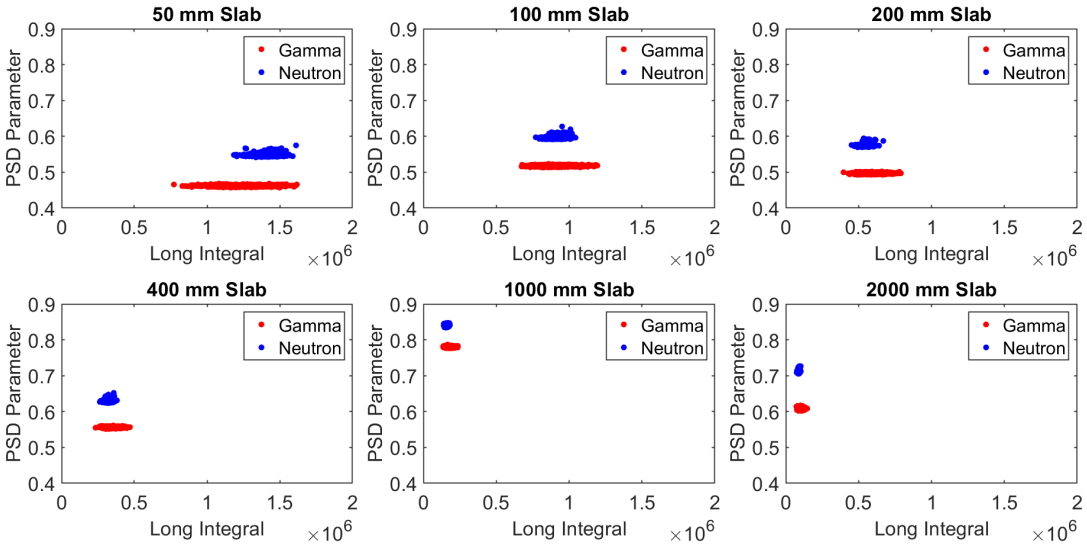

Figure 6.1: Pulse shape discrimination (PSD) for slab scintillator geometries with lengths ranging from 50 mm to 2000 mm, with simulated shot noise applied. The plot illustrates the effect of shot noise on neutron-gamma pulse separation across different slab lengths.

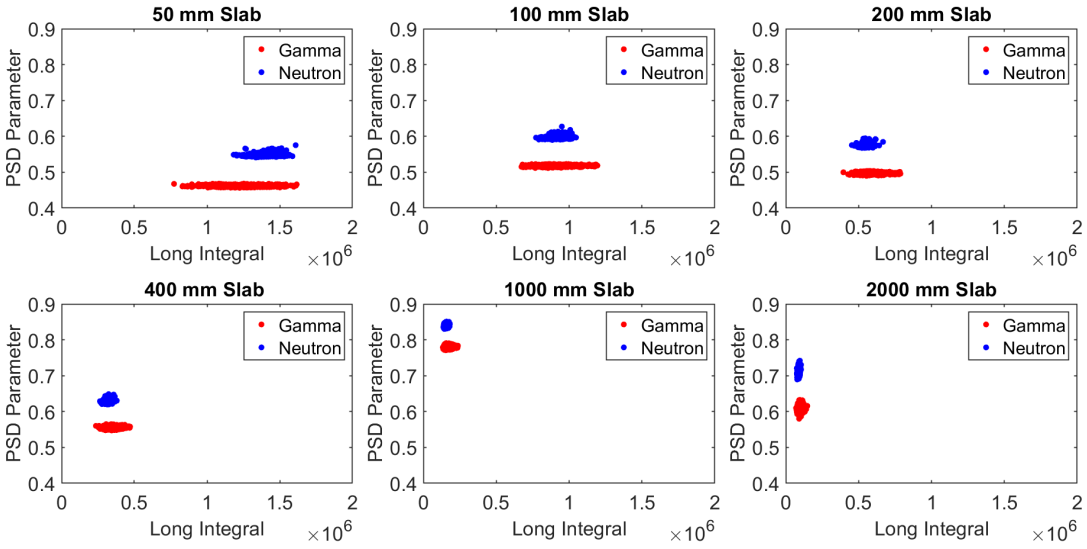

Figure 6.2: Pulse shape discrimination (PSD) for slab scintillator geometries with lengths ranging from 50 mm to 2000 mm, with simulated shot noise and a fixed Gaussian noise level of 2×10^2 applied. The plot illustrates the effect of combined noise on neutron-gamma pulse separation across different slab lengths.

in Figure 4.7.

Figure 6.2 presents the PSD performance of slab scintillators with lengths ranging from 50 mm to 2000 mm, incorporating both simulated shot noise and a fixed Gaussian noise level of 2×10^2.

At this noise level, the simulated noise has a greater impact on the PSD distributions, particularly for slab lengths of 400 mm and above. From this length onwards, increased variability is observed in both neutron and gamma PSD distributions. Although the mean PSD value at 1000 mm remains unchanged compared to Figure 6.1, the variability in the PSD parameter increases for both distributions. This increased spread causes the neutron and gamma plumes to widen and move closer together, indicating degraded PSD performance due to the added noise.

Figure 6.3 presents the pulse shape discrimination (PSD) performance of slab

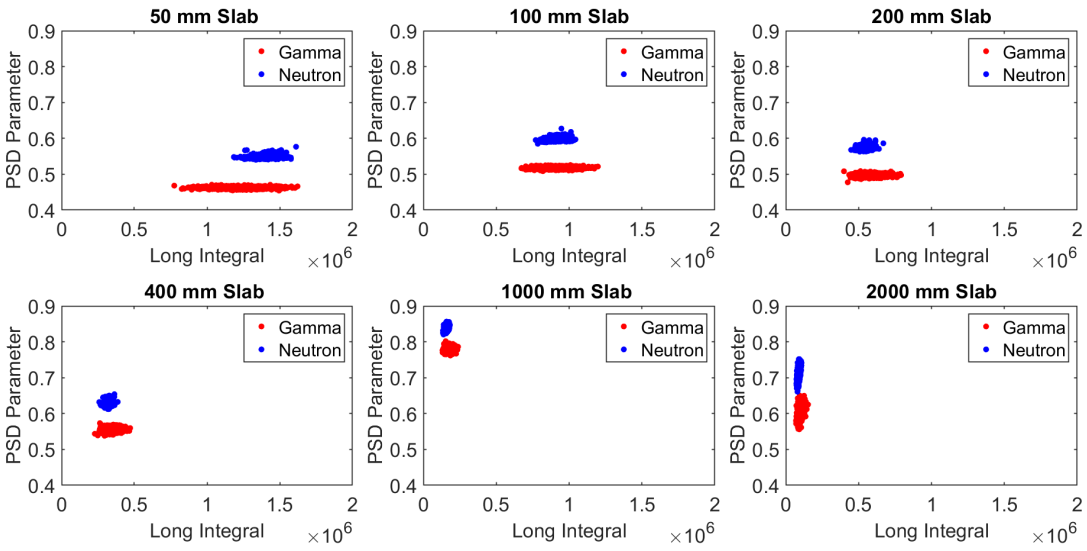

Figure 6.3: Pulse shape discrimination (PSD) for slab scintillator geometries with lengths ranging from 50 mm to 2000 mm, with simulated shot noise and a fixed Gaussian noise level of 4×10^2 applied. The plot illustrates the effect of combined noise on neutron-gamma pulse separation across different slab lengths.

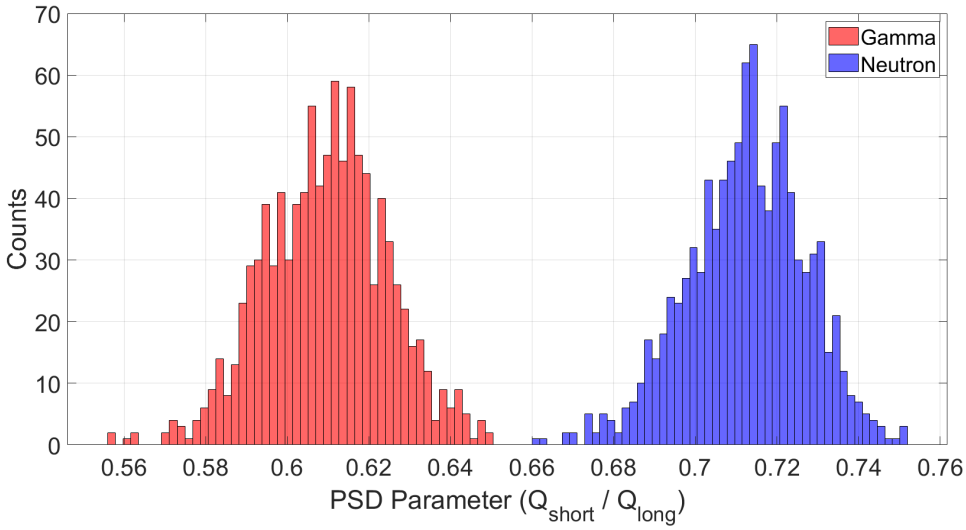

Figure 6.4: PSD histogram showing the number of counts versus the PSD parameter for the slab geometry with combined shot noise and Gaussian noise at a Gaussian noise level of 4×10^2. The Figure of Merit (FoM) value is 1.38.

scintillators with lengths ranging from 50 mm to 2000 mm, incorporating both simulated shot noise and a fixed Gaussian noise level of 4×10^2. At this noise level, increased variability in the PSD parameter is observed for both neutron and gamma distributions as the scintillator length increases. Notably, for the largest scintillator (2000 mm), the plumes have moved very close together but do not overlap, as illustrated in Figure 6.4, where the FoM is ≈ 1.48.

Figure 6.5 presents the pulse shape discrimination (PSD) performance of slab scintillators with lengths ranging from 50 mm to 2000 mm, incorporating both simulated shot noise and a fixed Gaussian noise level of 8×10^2. At this noise level, there is increased variability in the PSD parameter for both distributions, for all slab lengths; however, this variability is most noticeable for slab lengths of 400 mm and above, with 1000 mm and 2000 mm lengths showing an overlap between the two plumes.

The overlap between the PSD distributions for the 2000 mm slab length with

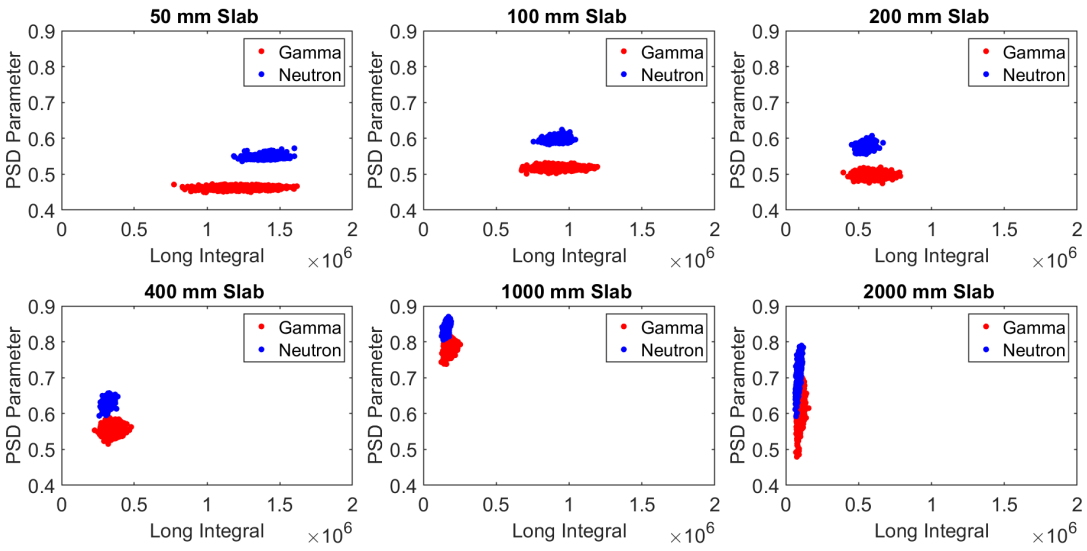

Figure 6.5: Pulse shape discrimination (PSD) for slab scintillator geometries with lengths ranging from 50 mm to 2000 mm, with simulated shot noise and a fixed Gaussian noise level of 8×10^2 applied. The plot illustrates the effect of combined noise on neutron-gamma pulse separation across different slab lengths.

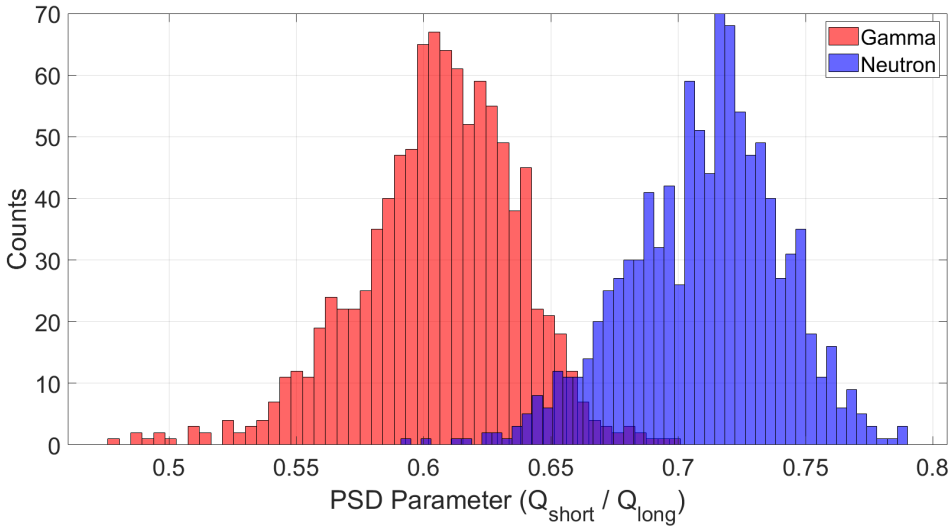

Figure 6.6: PSD histogram showing the number of counts versus the PSD parameter for the slab geometry with combined shot noise and Gaussian noise at a Gaussian noise level of 8×10^2. The Figure of Merit (FoM) value is 0.723.

this noise level applied is shown in Figure 6.6.

Figure 6.7 presents the pulse shape discrimination (PSD) performance of slab scintillators with lengths ranging from 50 mm to 2000 mm, incorporating both simulated shot noise and a fixed Gaussian noise level of 1×10^3. At this noise level, there is overlap between the plumes for the 1000 mm and 2000 mm slab lengths; however, the plumes for both the 100 mm length and 200 mm length have increased their proximity, showing the increasing effect of noise on the PSD performance. However, the 100 mm slab length still has FoM values above 1, with a FoM of $\approx$ 1.26 and for 200 mm this is $\approx$ 1.86, indicating reasonable separation.

Figure 6.8 presents the pulse shape discrimination (PSD) performance of slab scintillators with varying lengths ranging from 50 mm to 2000 mm, incorporating both simulated shot noise and a fixed Gaussian noise level of 2×10^3. At this noise level, separation is maintained at 50 mm and 100 mm, but there is overlap between the plumes at and above 200 mm. This is shown in Figure 6.9.

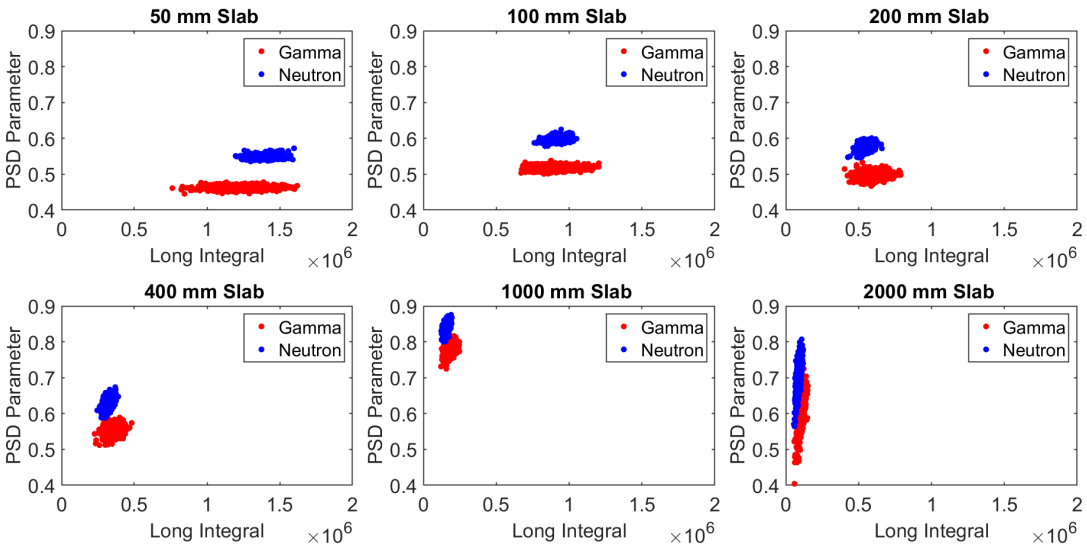

Figure 6.7: Pulse shape discrimination (PSD) for slab scintillator geometries with lengths ranging from 50 mm to 2000 mm, with simulated shot noise and a fixed Gaussian noise level of 1×10^3 applied. The plot illustrates the effect of combined noise on neutron-gamma pulse separation across different slab lengths.

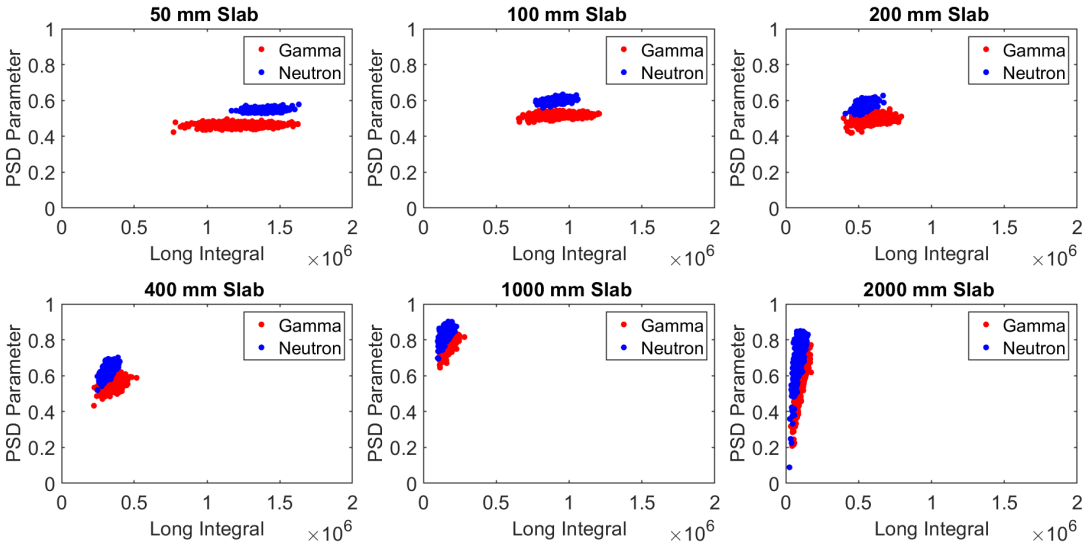

Figure 6.8: Pulse shape discrimination (PSD) for slab scintillator geometries with lengths ranging from 50 mm to 2000 mm, with simulated shot noise and a fixed Gaussian noise level of 2×10^3 applied. The plot illustrates the effect of combined noise on neutron-gamma pulse separation across different slab lengths.

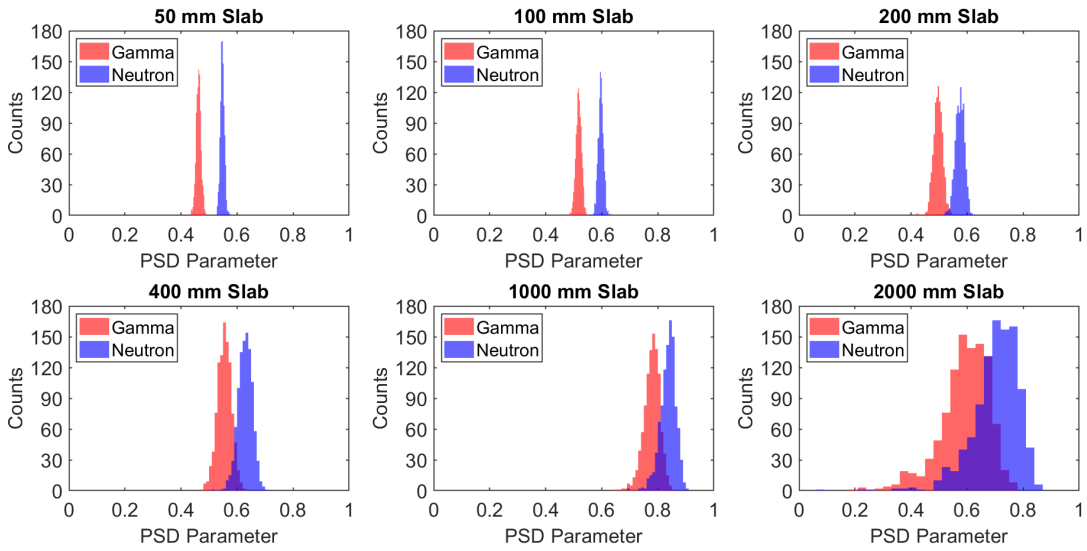

Figure 6.9: Pulse shape discrimination (PSD) histograms for a slab scintillator at the highest simulated noise level, showing increasing overlap between gamma and neutron distributions with scintillator length. Overlap begins at 200 mm and becomes significant at 1000 and 2000 mm lengths.

For the slab geometry, the Figure of Merit (FoM) was calculated and the PSD histograms for the largest and smallest slab scintillators are shown, for 50 mm and 2000 mm, at the largest noise values. This shows how noise impacts the longer scintillators more than the smaller ones.

For each noise level and slab length investigated, the Figure of Merit (FoM) value was calculated and this is shown in Table 6.1.

Table 6.1: Figure of Merit (FoM) values for slab geometry scintillator detectors at varying lengths under increasing levels of simulated noise.

Length	**No Noise**	**Shot Noise**	**200**	**400**	**800**	**1000**	**2000**
50 mm	7.352	7.278	6.916	6.142	4.696	3.941	2.249
100 mm	7.415	7.327	6.648	5.486	3.631	3.050	1.720
200 mm	7.044	6.882	5.640	4.040	2.366	1.861	1.647
400 mm	7.262	6.949	4.561	2.893	1.516	1.258	0.632
1000 mm	7.924	7.349	3.956	2.214	1.147	0.943	0.439
2000 mm	8.582	7.923	2.820	1.480	0.723	0.573	0.275

The calculated Figure of Merit (FoM) values for all slab scintillator lengths at each simulated noise level are shown in Figure 6.10.

6.2 Cylinder Geometry

Figure 6.11 presents the PSD performance of cylindrical scintillator geometries with lengths ranging from 50 mm to 2000 mm, with simulated shot noise applied to the light pulses. Clear separation between neutron and gamma PSD distributions is observed across all cylinder lengths.

The addition of shot noise to the simulated pulses has minimal impact on discrimination performance compared with the ideal, no-noise case shown in Figure 4.14. This follows the trend observed in Figure 6.1.

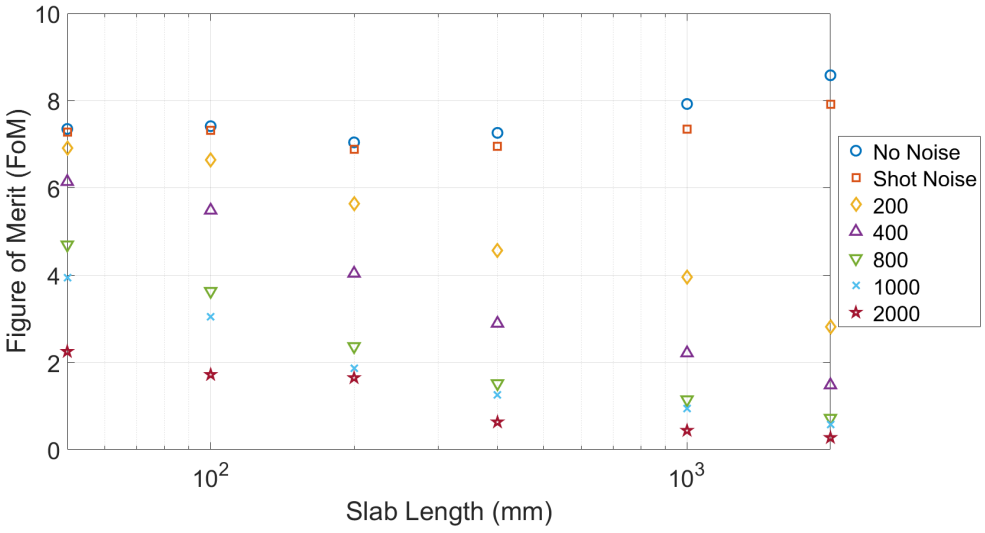

Figure 6.10: Figure of Merit (FoM) as a function of simulated photodetector noise for slab scintillator geometries, demonstrating the impact of increasing noise on pulse shape discrimination (PSD) performance.

Figure 6.12 presents the pulse shape discrimination (PSD) performance of cylindrical scintillators of the same length range, incorporating both simulated shot noise and a fixed Gaussian noise level of 2×10^2.

At this noise level, the neutron and gamma plumes remain well separated for all scintillator lengths, although increased variability in the PSD parameter is evident for the 1000 mm and 2000 mm scintillators.

Figure 6.13 shows the pulse shape discrimination (PSD) performance under increased noise conditions, with simulated shot noise and a fixed Gaussian noise level of 4×10^2 applied. At this level, the neutron and gamma plumes move closer together, most notably for the 2000 mm scintillator length.

Figure 6.14 presents the PSD performance for the same scintillator geometries with simulated shot noise and a fixed Gaussian noise level of 8×10^2. The trend of the neutron and gamma plumes moving closer together continues at this increased noise level, with the poorest separation observed for the 2000 mm length.

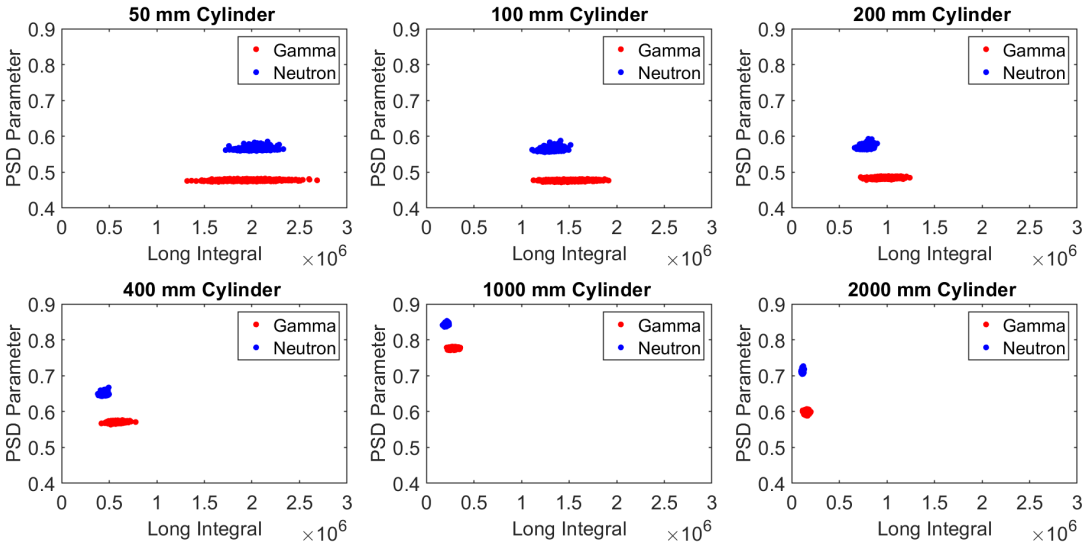

Figure 6.11: Pulse shape discrimination (PSD) for cylindrical scintillator geometries with lengths ranging from 50 mm to 2000 mm, with simulated shot noise applied. The plot illustrates the effect of shot noise on neutron-gamma pulse separation across different cylinder lengths.

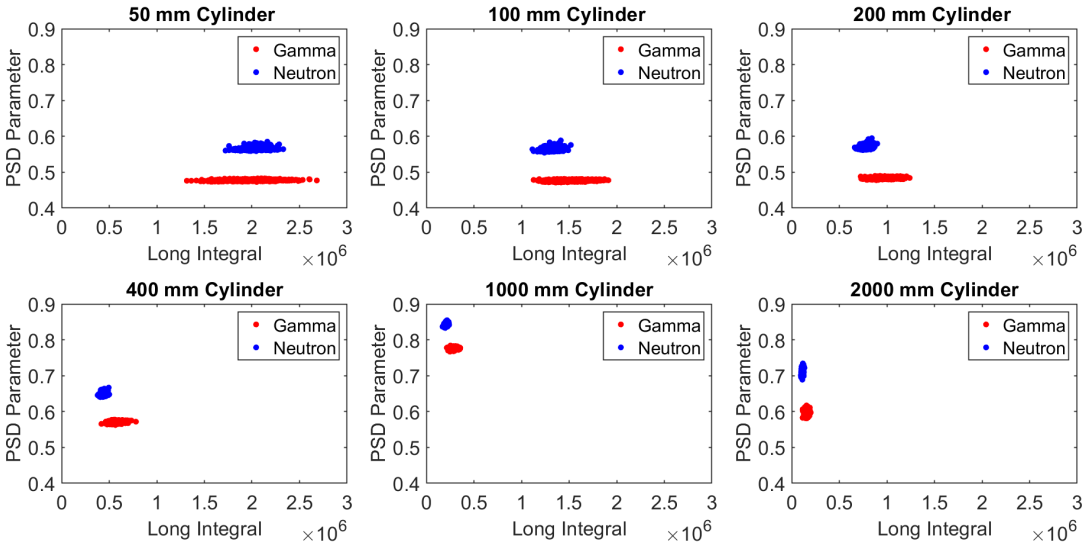

Figure 6.12: Pulse shape discrimination (PSD) for cylindrical scintillator geometries with lengths ranging from 50 mm to 2000 mm, with simulated shot noise and a fixed Gaussian noise level of 2×10^2 applied. The plot illustrates the effect of combined noise on neutron-gamma pulse separation across different cylinder lengths.

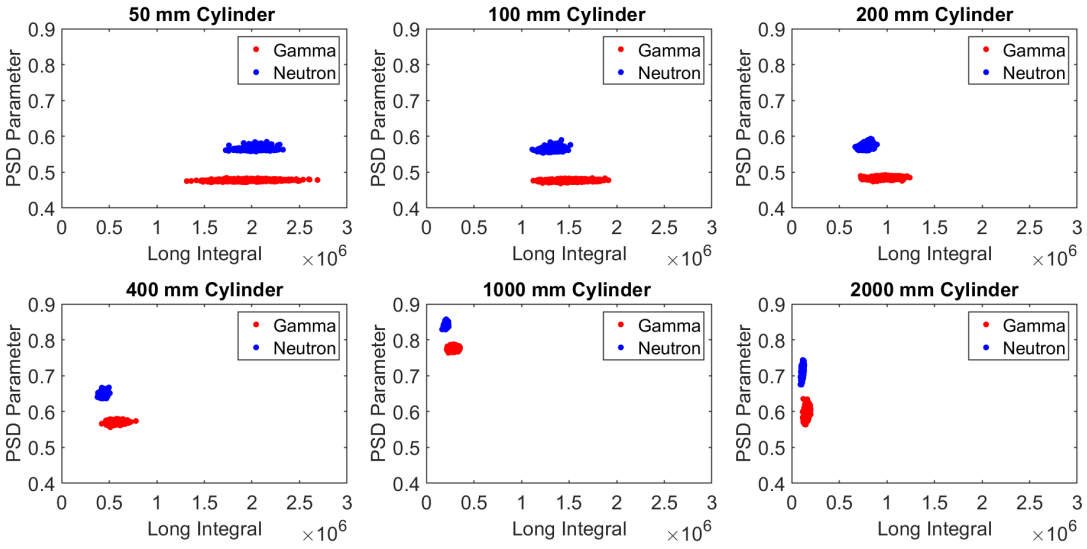

Figure 6.13: Pulse shape discrimination (PSD) for cylindrical scintillator geometries with lengths ranging from 50 mm to 2000 mm, with simulated shot noise and a fixed Gaussian noise level of 4×10^2 applied. The plot illustrates the effect of combined noise on neutron-gamma pulse separation across different cylinder lengths.

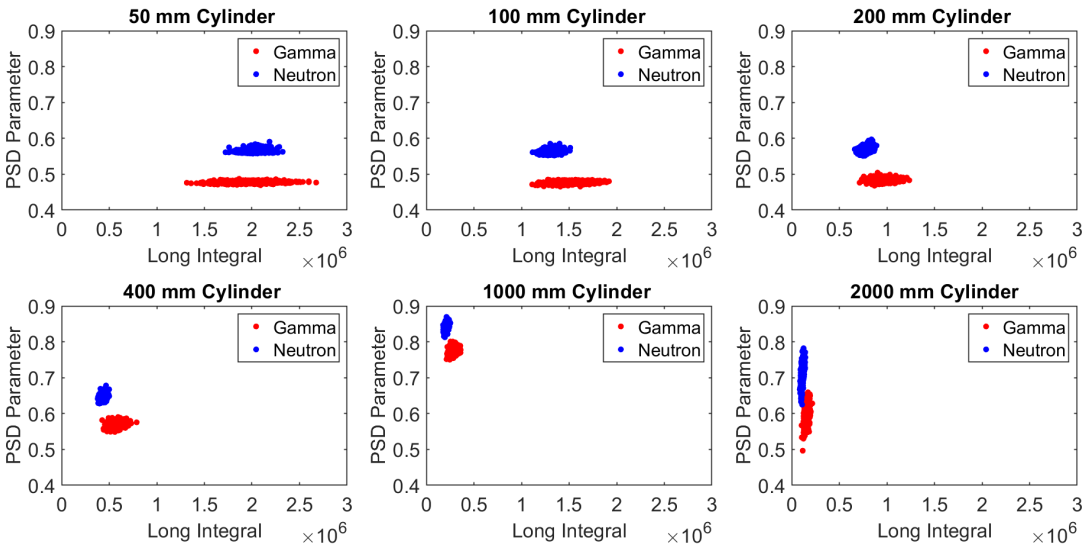

Figure 6.14: Pulse shape discrimination (PSD) for cylindrical scintillator geometries with lengths ranging from 50 mm to 2000 mm, with simulated shot noise and a fixed Gaussian noise level of 8×10^2 applied. The plot illustrates the effect of combined noise on neutron-gamma pulse separation across different cylinder lengths.

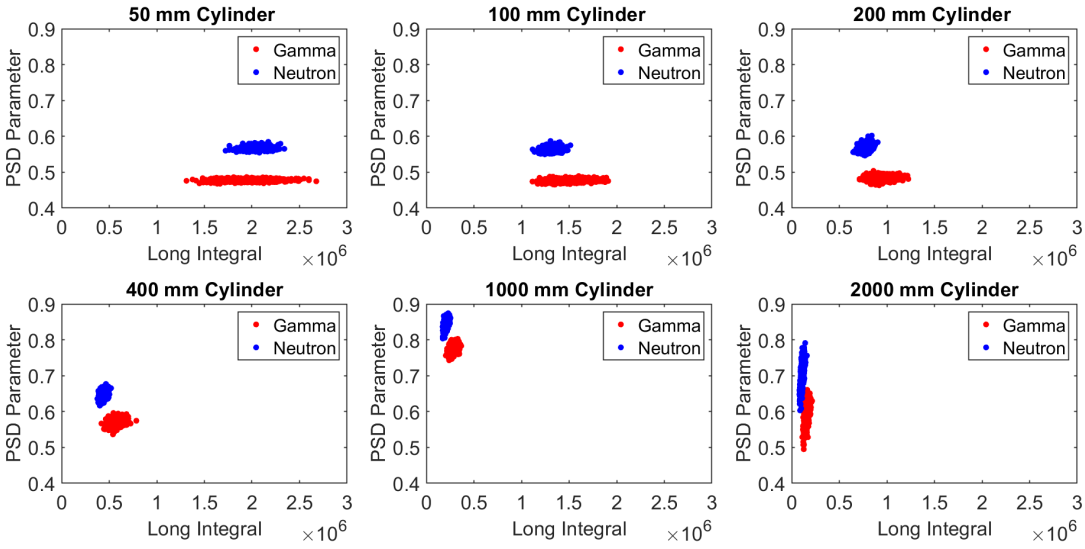

Figure 6.15: Pulse shape discrimination (PSD) for cylindrical scintillator geometries with lengths ranging from 50 mm to 2000 mm, with simulated shot noise and a fixed Gaussian noise level of 1×10^3 applied. The plot illustrates the effect of combined noise on neutron-gamma pulse separation across different cylinder lengths.

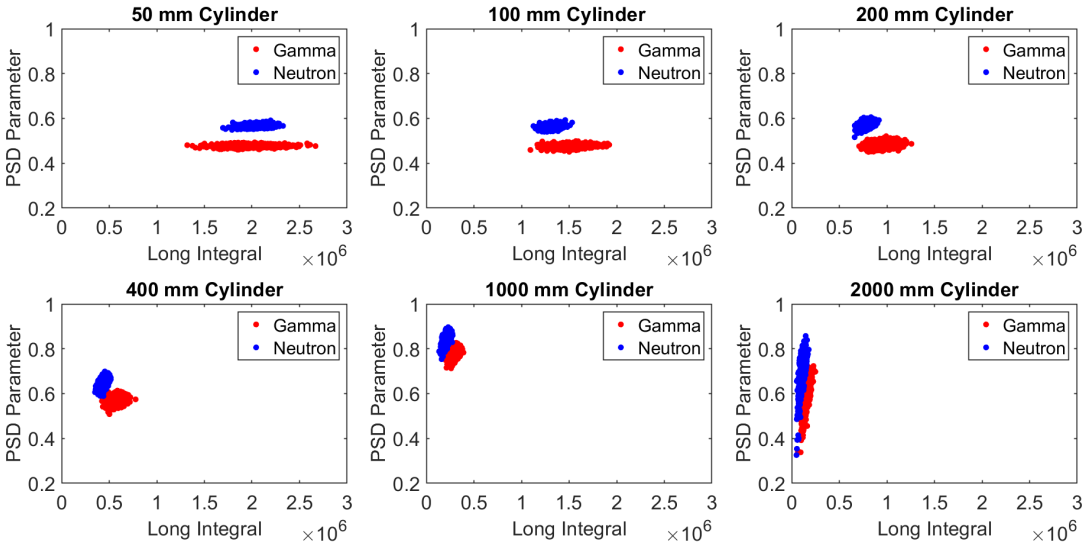

Figure 6.16: Pulse shape discrimination (PSD) for cylindrical scintillator geometries with lengths ranging from 50 mm to 2000 mm, with simulated shot noise and a fixed Gaussian noise level of 2×10^3 applied. The plot illustrates the effect of combined noise on neutron-gamma pulse separation across different cylinder lengths.

Figure 6.15 presents the PSD performance with simulated shot noise and a Gaussian noise level of 1×10^3. At this level, further degradation in separation is evident, although the neutron and gamma plumes retain partial separation across all scintillator lengths.

Finally, Figure 6.16 presents the PSD performance at the highest investigated noise level, with a Gaussian noise level of 2×10^3 applied in addition to the simulated shot noise. At this level, the neutron and gamma plumes are overlapping for the 2000 mm length and for the 1000 mm length, with some overlap observed for the 400 mm length. Increased variability in the PSD parameters is observed for lengths of 200 mm and below, with the best separation retained at 50 mm. This is shown in Figure 6.17.

For each noise level and cylinder length investigated, the Figure of Merit value was calculated and this is shown in Table 6.2.

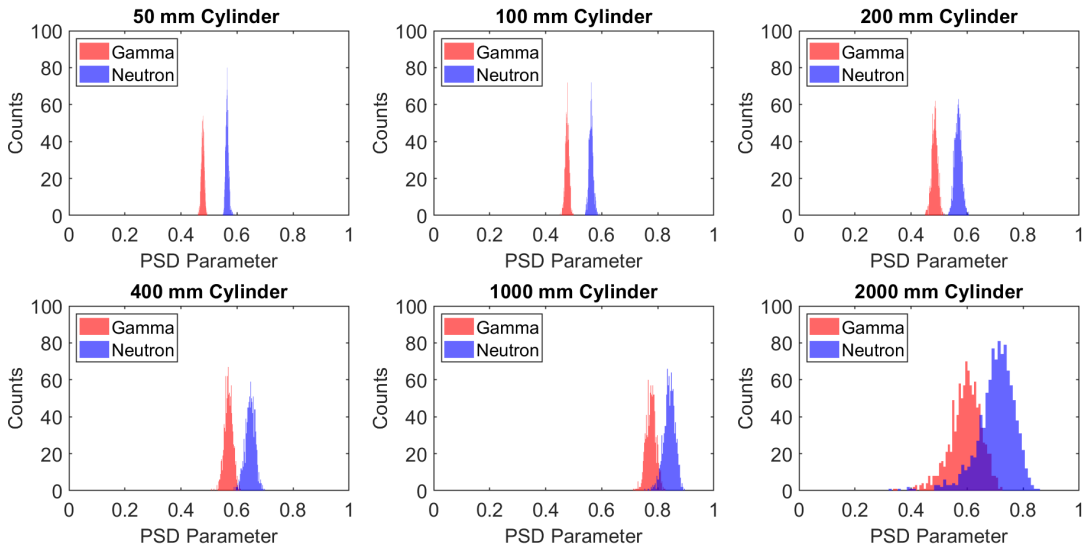

Figure 6.17: Pulse shape discrimination (PSD) histograms for a cylindrical scintillator at the highest simulated noise level, showing increasing overlap between gamma and neutron distributions with scintillator length. Overlap begins at 500 mm and becomes significant at 1000 and 2000 mm lengths.

Table 6.2: Figure of Merit (FoM) values for cylindrical scintillator detectors at varying lengths under increasing levels of simulated noise.

Length	**No Noise**	**Shot Noise**	**200**	**400**	**800**	**1000**	**2000**
50 mm	7.962	7.900	7.712	7.110	6.015	5.490	3.378
100 mm	7.363	7.304	6.947	6.295	4.853	4.246	2.457
200 mm	7.025	6.998	6.326	5.177	3.501	2.797	1.538
400 mm	7.152	6.987	5.743	4.127	2.421	1.938	1.017
1000 mm	8.140	7.720	5.328	3.370	1.761	1.453	0.742
2000 mm	7.607	7.661	3.884	2.107	1.106	0.862	0.385

The calculated Figure of Merit (FoM) values for all cylinder scintillator lengths at each simulated noise level are shown in Figure 6.18.

6.3 Cuboid Geometry

Figure 6.19 presents the pulse shape discrimination (PSD) performance of cuboid scintillators with lengths ranging from 50 mm to 2000 mm, incorporating simulated shot noise only, with no additional Gaussian noise applied.

At this noise level — as observed with the slab and cylindrical geometries — there is limited variability in the PSD parameter for both neutron and gamma distributions.

Figure 6.20 presents the PSD performance with simulated shot noise and a fixed Gaussian noise level of 2×10^2. Despite increased variability in the PSD parameter at the largest scintillator lengths, good separation between neutron and gamma distributions is still observed across all scintillator lengths.

Figure 6.21 presents the PSD performance with simulated shot noise and a fixed Gaussian noise level of 4×10^2. Although the neutron and gamma plumes move closer together — especially for the largest scintillator lengths — good separation is

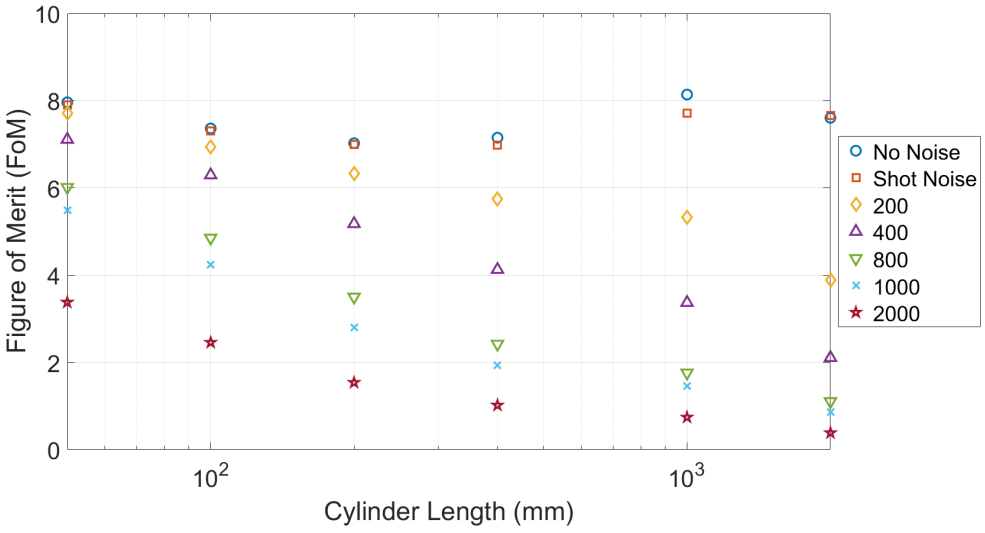

Figure 6.18: Figure of Merit (FoM) as a function of simulated photodetector noise for cylindrical scintillator geometries, illustrating the impact of noise on PSD performance.

still maintained across all lengths.

Figure 6.22 presents the PSD performance with simulated shot noise and a fixed Gaussian noise level of 8×10^2. At this noise level, the neutron and gamma plumes remain separated across all scintillator lengths; however, there is increased variability in the PSD parameter values, especially for the largest scintillator lengths.

Figure 6.23 presents the PSD performance with simulated shot noise and a fixed Gaussian noise level of 1×10^3. At this noise level, the variability in the PSD parameter increases for both neutron and gamma plumes, with the plumes nearly overlapping for the 2000 mm scintillator length.

Lastly, Figure 6.24 presents the PSD performance at the highest investigated noise level, with a Gaussian noise level of 2×10^3 applied in addition to the simulated shot noise. As with the cylindrical geometry, at this noise level, the neutron and gamma plumes are overlapping for the 1000 mm and 2000 mm lengths, with some overlap also observed for the 400 mm length. Similarly, increased variability in

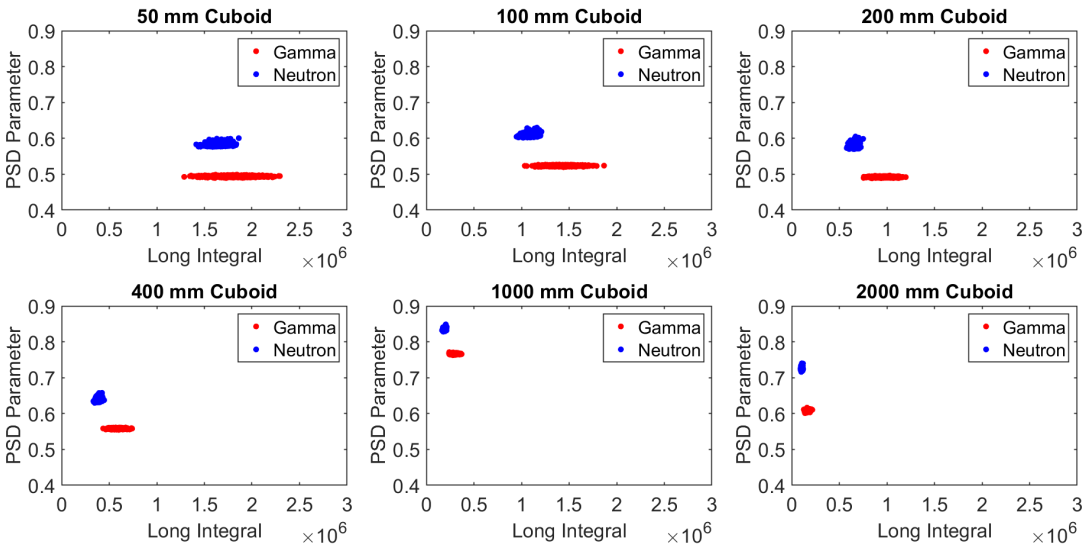

Figure 6.19: Pulse shape discrimination (PSD) for cuboid scintillator geometries with lengths ranging from 50 mm to 2000 mm, with simulated shot noise applied. The plot illustrates the effect of shot noise on neutron-gamma pulse separation across different cuboid lengths.

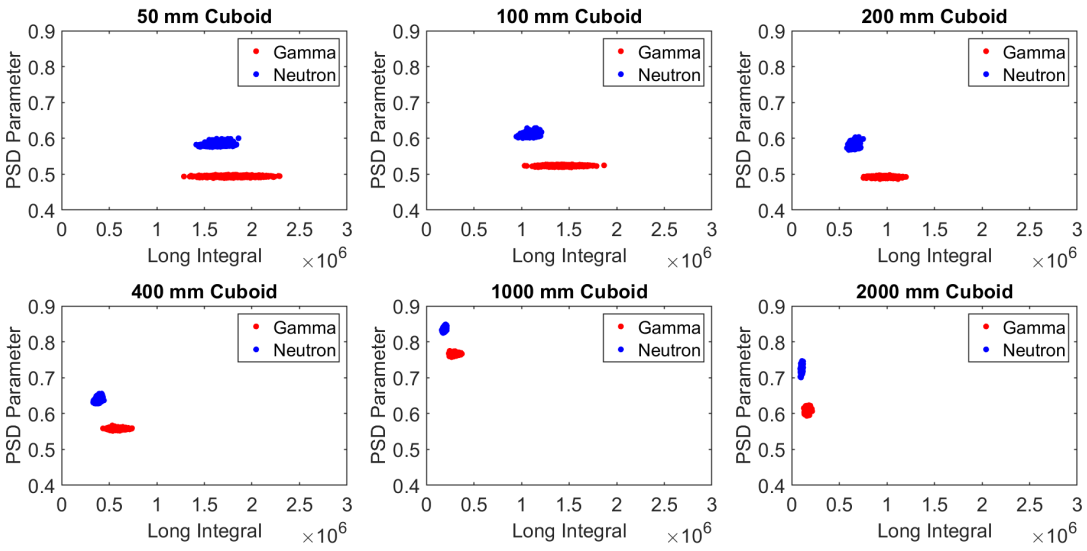

Figure 6.20: Pulse shape discrimination (PSD) for cuboid scintillator geometries with lengths ranging from 50 mm to 2000 mm, with simulated shot noise and a fixed Gaussian noise level of 2×10^2 applied. The plot illustrates the effect of combined noise on neutron-gamma pulse separation across different cuboid lengths.

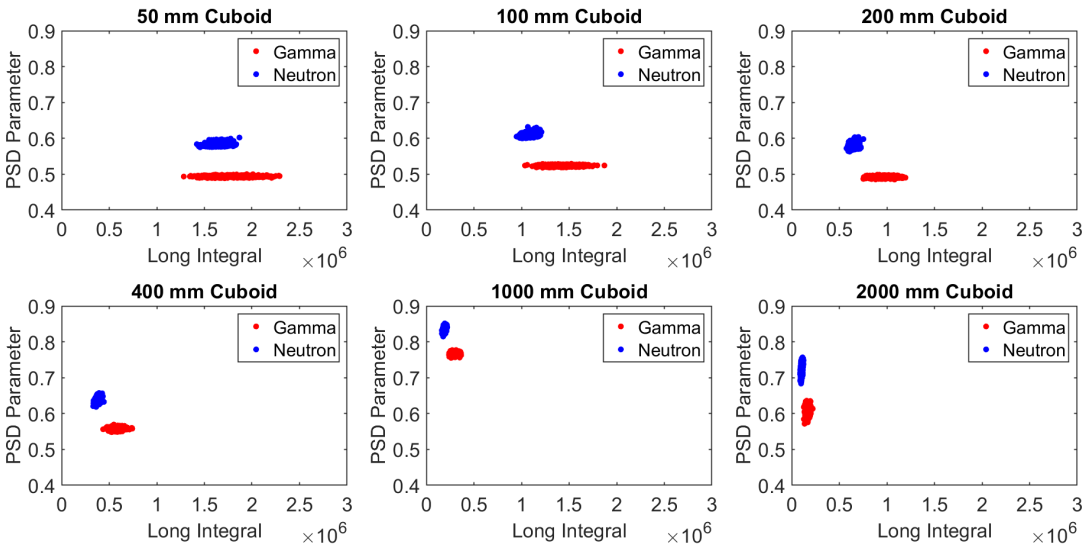

Figure 6.21: Pulse shape discrimination (PSD) for cuboid scintillator geometries with lengths ranging from 50 mm to 2000 mm, with simulated shot noise and a fixed Gaussian noise level of 4×10^2 applied. The plot illustrates the effect of combined noise on neutron-gamma pulse separation across different cuboid lengths.

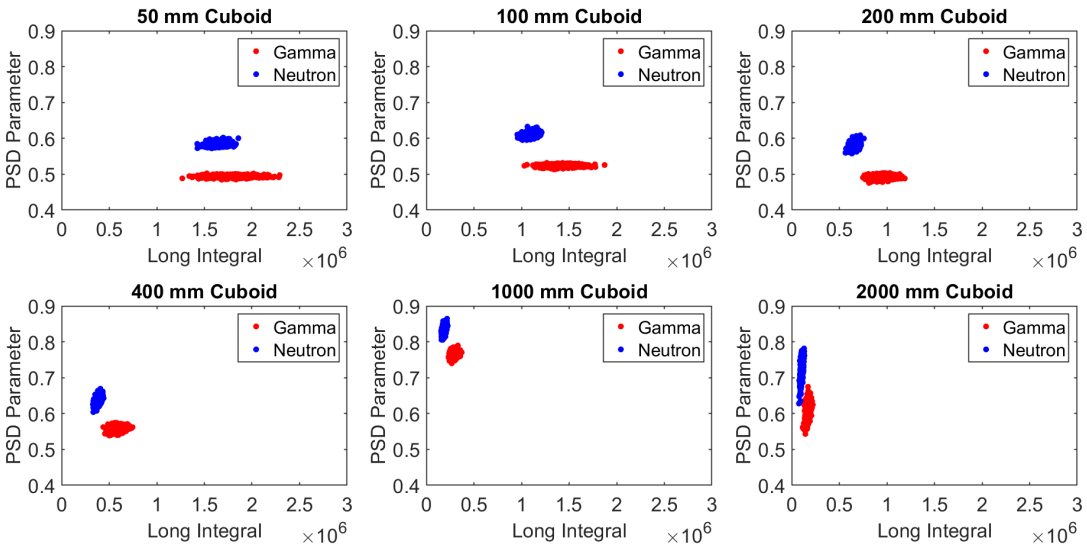

Figure 6.22: Pulse shape discrimination (PSD) for cuboid scintillator geometries with lengths ranging from 50 mm to 2000 mm, with simulated shot noise and a fixed Gaussian noise level of 8×10^2 applied. The plot illustrates the effect of combined noise on neutron-gamma pulse separation across different cuboid lengths.

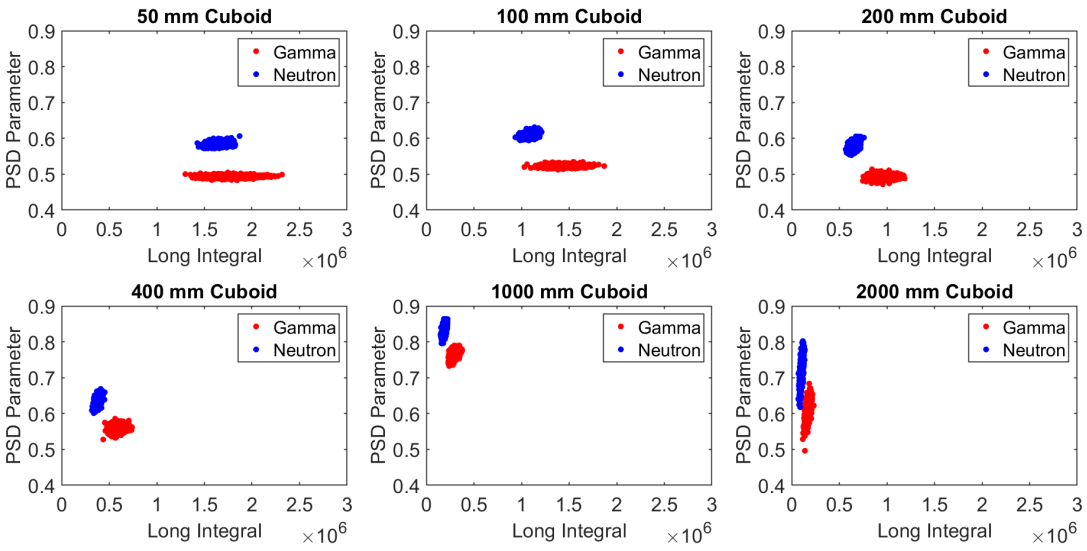

Figure 6.23: Pulse shape discrimination (PSD) for cuboid scintillator geometries with lengths ranging from 50 mm to 2000 mm, with simulated shot noise and a fixed Gaussian noise level of 1×10^3 applied. The plot illustrates the effect of combined noise on neutron-gamma pulse separation across different cuboid lengths.

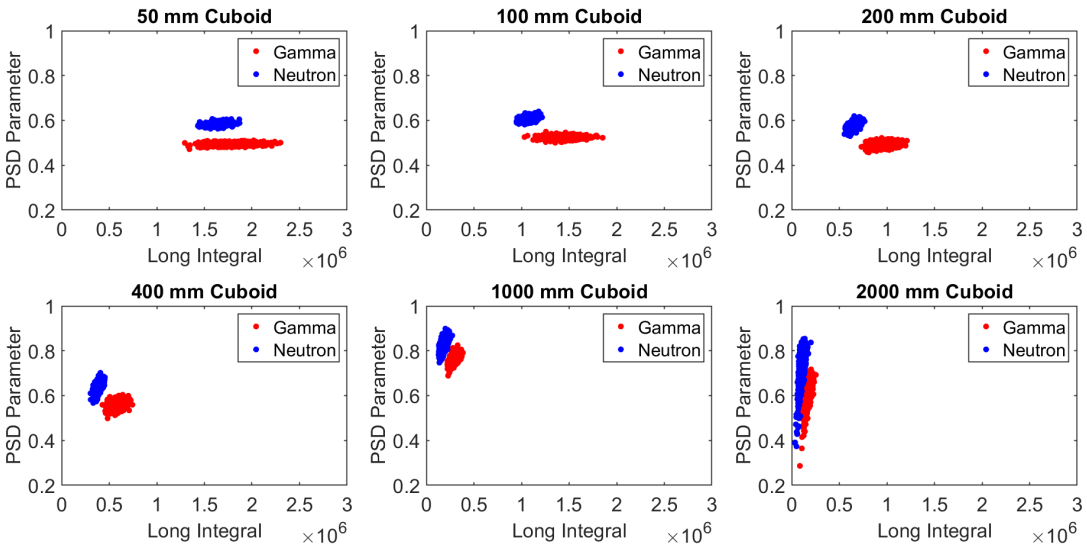

Figure 6.24: Pulse shape discrimination (PSD) for cuboid scintillator geometries with lengths ranging from 50 mm to 2000 mm, with simulated shot noise and a fixed Gaussian noise level of 2×10^3 applied. The plot illustrates the effect of combined noise on neutron-gamma pulse separation across different cuboid lengths.

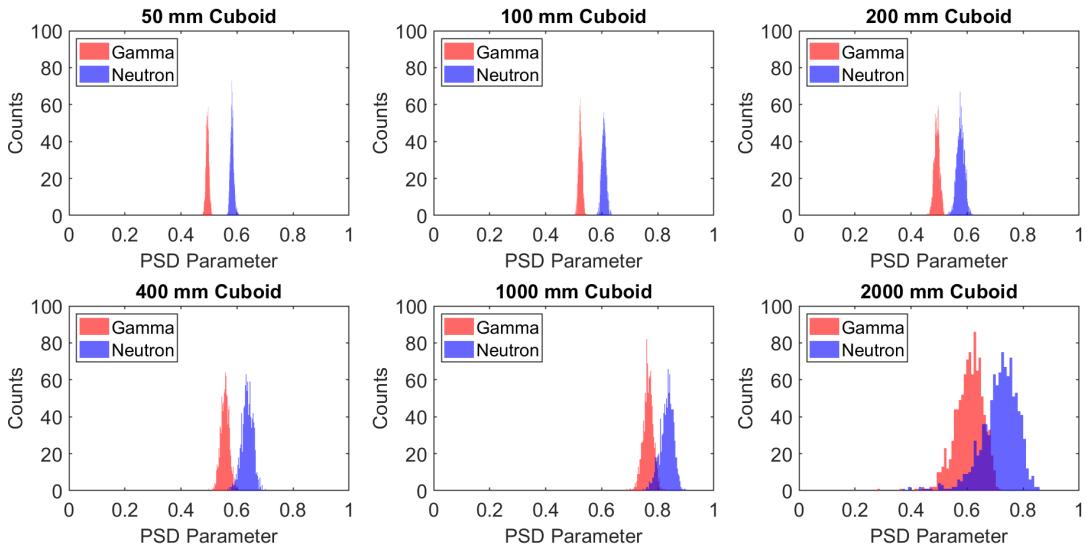

Figure 6.25: Pulse shape discrimination (PSD) histograms for a cuboid scintillator at the highest simulated noise level, showing increasing overlap between gamma and neutron distributions with scintillator length. Overlap begins at 400 mm and becomes significant at 1000 and 2000 mm lengths.

the PSD parameters is observed for lengths of 200 mm and below, with the best separation retained at 50 mm. This is shown in Figure 6.25.

For each noise level and cuboid length investigated, the Figure of Merit (FoM) value was calculated and this is shown in Table 6.3.

Table 6.3: Figure of Merit (FoM) values for cuboid scintillator detectors at varying lengths under increasing levels of simulated noise.

Length	**No Noise**	**Shot Noise**	**200**	**400**	**800**	**1000**	**2000**
50 mm	7.030	6.990	6.804	6.400	5.312	4.739	3.125
100 mm	7.327	7.223	6.955	6.137	4.693	4.093	2.361
200 mm	6.319	6.233	5.645	4.774	3.131	2.674	1.506
400 mm	6.979	6.805	5.461	3.792	2.173	1.848	0.966
1000 mm	8.738	8.220	5.265	3.170	1.735	1.417	0.684
2000 mm	9.436	8.868	4.076	2.269	1.174	0.907	0.402

The calculated Figure of Merit (FoM) values for all cuboid scintillator lengths at each simulated noise level are shown in Figure 6.26.

6.4 Optical Surfaces

The impact of noise on the summed simulated light pulses obtained for the `G4OpticalSurfaces` simulated in Chapter 4.

For each noise level and surface type investigated, the Figure of Merit (FoM) value was calculated and this is shown in Table 6.4.

The calculated Figure of Merit (FoM) values for all optical surface types at each simulated noise level are shown in Figure 6.27.

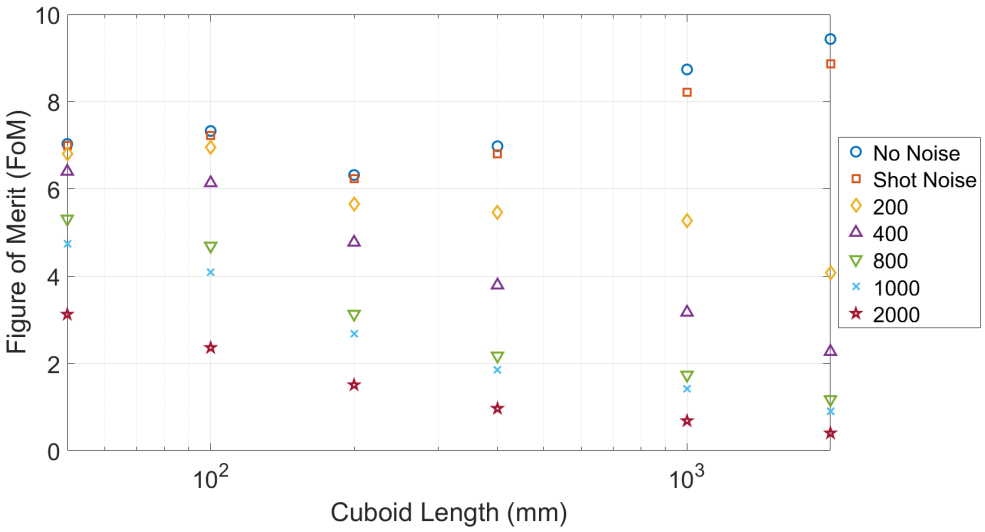

Figure 6.26: Figure of Merit (FoM) as a function of simulated photodetector noise for cuboid scintillator geometries, illustrating the impact of noise on PSD performance.

Table 6.4: Figure of Merit (FoM) values for different surfaces under varying noise levels.

Surface	**No Noise**	**Shot Noise**	**200**	**400**	**800**	**1000**	**2000**
Teflon GBP	9.48	9.40	8.994	8.448	6.868	6.376	4.028
Teflon PBP	9.196	9.118	8.885	8.045	6.562	5.917	3.849
Al-foil PBP	8.423	8.300	8.136	7.628	6.401	5.754	3.822
EJ510 GFP	11.007	10.839	9.423	7.376	4.982	4.265	2.253
ESR PBP	8.217	8.154	8.020	7.633	6.585	6.221	4.481
Default Surface	7.03	6.99	6.804	6.400	5.312	4.739	3.125

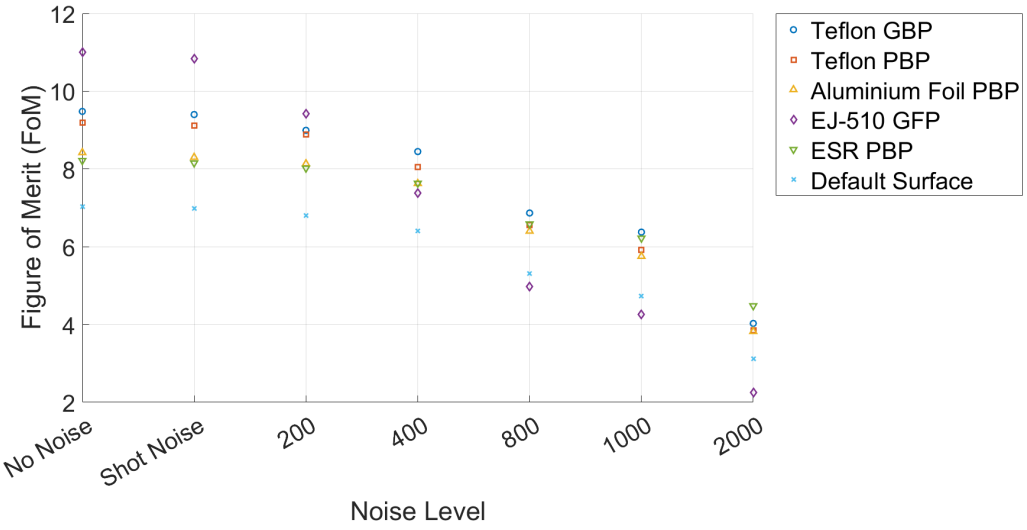

Figure 6.27: Figure of Merit (FoM) as a function of simulated photodetector noise for different surface types investigated, illustrating the impact of noise on PSD performance.

Chapter 7

Discussion

Several key trends emerged from the simulation results presented in this thesis. Most notably, distortions — hereafter referred to as artefacts — were consistently observed in the simulated light pulse shapes produced by the simulated EJ-276 plastic scintillation detector across all three scintillator geometries studied (slab, cylinder, and cuboid) as the scintillator length was increased along the Z-axis. These artefacts became apparent at lengths $\geq$ 400 mm, initially affecting the rising edge and peak of the pulse. At larger lengths (1000 mm and 2000 mm), the artefacts developed into distinct secondary peaks.

These effects were observed while all other detector parameters were held constant and represent distortions relative to the Gaussian-like pulse shapes obtained for shorter scintillator lengths (50 mm to 200 mm). The simulated light pulses correspond to the arrival time distribution of scintillation photons at the photodetector, and therefore represent the pulse shapes prior to signal amplification by the photodetector and any additional effects introduced by the readout electronics, both of which are known to modify the shapes of the pulses in experimental measurements (Taggart and P. J. Sellin, 2018; Hellesen et al., 2013; Flaska et al., 2013).

Similar artefacts, described by Hubbard as 'bumps', were reported in (Hubbard, Paul J Sellin, and Lotay, 2020) using Geant4 simulations at scintillator lengths of

300 mm and above, providing independent confirmation of the results presented here. These features were attributed to the directionality of scintillation photon emission combined with the scintillator geometry. Photons emitted toward the photodetector contributed to the initial pulse peak, whereas photons emitted in the opposite direction followed longer paths with multiple reflections, producing the delayed bump. These effects were observed for both PSD-capable EJ-276 and non-PSD EJ-200 scintillators and were present in optical-photon-only simulations without incident radiation, indicating that these artefacts are likely due to light transport effects in the scintillator.

However, whereas Hubbard (Hubbard, Paul J Sellin, and Lotay, 2020) observed such artefacts only for cuboid geometries with reflective surface treatments — implemented via a `G4OpticalSurface` applied to the scintillator — this work identifies these features across slab, cylindrical, and cuboid geometries. Simulations conducted without a defined `G4OpticalSurface` and scintillator housing confirmed that these artefacts persist regardless of the simulation setup.

The heatmaps of photon emission directions, shown in Figures 4.22 and 4.24 for 50 mm and 2000 mm cuboids, respectively, provide direct evidence that these artefacts are intrinsic to light transport within the scintillator, confirming a geometry-dependent mechanism primarily driven by extended photon path lengths along the elongated axis.

The artefacts appear robust against scintillator type, surface treatment, simulation parameters, or incident particle type, strongly supporting a geometrical origin intrinsic to light transport dynamics within elongated scintillators. Simulations conducted without reflective surfaces or housing, combined with these heatmap observations, indicate that the artefacts are not computational artefacts, but rather a physical consequence of the scintillator geometry and photon transport.

In order to exclude the possibility that the observed pulse shape artefacts were due to insufficient statistics, additional simulations were carried out with up to 5000 simulated pulses collected per particle type, and across a range of incident energies.

In all cases, the artefacts persisted, confirming that they arise from the underlying light transport physics rather than computational effects.

While these artefacts are observed in the simulated light pulses shapes with 0.5 ns binning, they are unlikely to be resolved in typical experimental measurements. This is because the finite timing resolution of standard photodetectors smears out fine timing structures in the photon arrival distribution. Additionally, electronic bandwidth limitations, sampling rates, and the various types of noise described in Section 2.4.2 can further obscure these features. Detecting such fine structure would require ultra-fast photodetectors, high-bandwidth, high-sampling rate sub-nanosecond oscilloscopes, and sufficient photon statistics — particularly since these features are observed in elongated scintillators, which have lower light collection efficiencies. Advances in timing resolution and high-speed electronics may, in the future, enable the experimental observation of these artefacts.

Pulse shape changes were observed across all geometries as length increased, indicating that longitudinal extension, rather than overall shape or cross-sectional area, is the principal factor influencing the formation of the artefacts.

Across all geometries explored, pulses exhibited Gaussian-like shapes when the scintillator length was $\leq$ 200 mm. However, as length increased from 50 mm to 200 mm, noticeable broadening of the pulse width was observed. This broadening arises from the longer photon path lengths in larger volumes: photons generated farther from the photodetector take more time to arrive and undergo a greater number of internal reflections. Under Geant4's default surface model (perfectly polished dielectric-dielectric interfaces), only specular internal reflection is present, with no surface roughness, wrapping, or absorption at the medium boundaries. Photon absorption still occurs within the bulk scintillator material according to its defined absorption length, contributing to the reduction in collected light.

Another important observation was a reduction in light collection efficiency (LCE) as the scintillator length increased along the Z-axis, a trend consistently observed across all geometries. At the longest length considered (2000 mm), under

the default surface configuration (i.e., no explicitly defined `G4OpticalSurface`), the slab geometry exhibited the lowest LCE, while the cylindrical geometry demonstrated the highest. LCE was evaluated using the integrated pulse area, which reflects the total photon collection at the photodetector.

The lowest LCE observed for the slab geometry is likely due to its smaller photodetector surface area compared to the cylindrical and cuboid geometries. Photons emitted away from the photodetector must travel longer distances before detection, resulting in greater variability in path lengths. These extended paths increase the likelihood of bulk absorption within the scintillator — whose absorption length is 3.8 m — as well as photon escape from the scintillator.

The asymmetry of the slab geometry can also contribute to photon losses. Photons undergo multiple reflections, including reflections that occur due to total internal reflection (TIR), which can keep photons travelling within the scintillator for longer times. The increase in this time spent in the scintillator raises the probability of bulk absorption or escape and can delay photon arrival time, contributing to the artefacts, such as secondary peaks, observed in the simulated light pulse shapes. At the scintillator-air interface TIR occurs for photons incident at angles greater than the critical angle (approximately 39.2° for the scintillator-air boundary), while photons below this threshold can escape, further reducing LCE, particularly in elongated volumes. For elongated slab geometries, it is advisable to add a photodetector at both ends of the scintillator.

In contrast, cylindrical scintillators behave like light guides due to their curved surfaces and axial symmetry, which allows photons to be guided efficiently toward the photodetector. Cuboid geometries, which demonstrated the second highest LCE among those studied, also benefit from their symmetry, which facilitates effective photon transport towards the photodetector.

The reduction in LCE observed with increasing scintillator length is attributable primarily to optical losses caused by photon escape at the scintillator–air interface and increased bulk absorption due to longer photon path lengths. In the absence of

an explicitly defined `G4OpticalSurface`, photon behaviour at material boundaries is governed by Snell's Law and the Fresnel Equations, corresponding to a perfectly polished interface. Under these conditions, photons incident at angles smaller than the critical angle can escape the scintillator, while those above the critical angle undergo total internal reflection (TIR). As scintillator length increases, photons typically travel longer and more variable paths, increasing the probability of both escape and absorption, thereby reducing overall LCE.

As scintillator length increased along the Z-axis, pulse shapes broadened (up to 400 mm), peak arrival times were delayed, and both peak amplitude and LCE decreased. Pulse shape distortions became noticeable at 400 mm, initially affecting the rising edge and extending into the decay tail. At 1000 mm, secondary features became more apparent, and by 2000 mm, these were clearly defined and accompanied by further reductions in peak amplitude and LCE. Interestingly, at the largest lengths, the initial peak sharpened and the overall pulse width decreased. These changes are likely to degrade PSD performance, as the artefacts distort the pulse from its expected Gaussian-like shape, potentially compromising techniques that rely on smooth, consistent pulses for accurate selection of integration windows.

Modifications to the scintillator's optical were found to have a significant impact on pulse shapes. Enhanced Specular Reflector (ESR) film provided the highest LCE among all surfaces investigated. The EJ-510 reflective paint surface exhibited the lowest LCE, even lower than the case with no explicitly defined `G4OpticalSurface`.

Certain optical surfaces can eliminate the 'bump' artefact observed in elongated scintillators. For example, in a 1000 mm cuboid, the artefact disappears when using Teflon GBP, Teflon PBP, or EJ-510 surfaces. These are primarily diffuse reflectors, except for Teflon PBP, which combines specular and diffuse components. Specular reflectors behave like mirrors, preserving the angle of incidence and reflection, causing photons to undergo multiple bounces before reaching the photodetector, which can produce artefacts due to delayed photon arrival. In contrast, diffuse reflectors scatter photons in multiple directions, randomising arrival times and

smoothing pulse shapes, thereby reducing the appearance of secondary peaks and artefacts.

The simulated ESR surface provided the best LCE, owing to its high reflectivity and specular nature. However, like the Default Surface (also specular) and the aluminium foil surface, ESR introduced artefacts into the pulse peaks, distorting the pulses from their ideal Gaussian-like shape. These distortions can artificially increase the short integral, particularly when they appear as secondary peaks. This effect was evident in the pulse shape discrimination (PSD) plots for scintillator lengths of 1000 mm and 2000 mm across all geometries in the absence of noise. In this ideal, noise-free scenario, the Figure of Merit (FoM) did not decrease with increasing scintillator length; instead, it increased. This idealised condition, lacking realistic noise influences, likely caused the short integral to be artificially enhanced, resulting in an exaggerated separation between neutron and gamma distributions in the no-noise PSD plots for these lengths.

Simulated photodetector noise was also found to strongly influence the PSD performance in EJ-276. Shot noise had negligible effect across all geometries, whereas fixed Gaussian noise — particularly at higher magnitudes — substantially degraded PSD performance. This degradation was most pronounced for the longer scintillators (1000 mm and 2000 mm), as evidenced by a decrease in Figure of Merit (FoM) with increasing Gaussian noise levels for all geometries. It was also found that FoM decreases with increasing scintillator length for all geometries. A similar trend of decreasing FoM with increasing scintillator length was reported by Grodzicka-Kobylka for EJ-276 for cylindrical geometries with lengths between 2 and 8 inches (Grodzicka-Kobylka et al., 2020).

In contrast, shorter scintillators maintain higher LCE and preserve more Gaussian-like pulse shapes, exhibiting greater resilience to noise-induced PSD degradation. This highlights the importance of minimising noise in elongated scintillators, which have larger surface areas and reduced LCE. Since Gaussian noise predominantly affects the decay tail — essential for CCM PSD — alternative

approaches that emphasise the rising edge or pulse peak may offer improved resilience against this type of noise (Jones and Malcolm J. Joyce, 2013).

Consequently, in longer scintillators where the intrinsic signal is already weakened, the relative impact of added noise becomes more pronounced. In contrast, shorter scintillators maintain higher light collection efficiency and also maintain their Gaussian-like appearance with no distortions, maintaining the overall integrity of the pulse shape, thereby exhibiting a greater resilience to noise-induced PSD degradation. This highlights the important role of minimising noise, particularly in elongated scintillators which have a large surface area and already have a reduced LCE due to longer and more variable path lengths and escape from the scintillator. Gaussian noise impacts the decay tail of the pulse initially and particularly, which is the critical component for PSD using the charge comparison method. Alternative approaches possibly based on the rising edge of the pulse could provide some resilience against the effects of noise.

This degradation is primarily due to the diminishing signal-to-noise ratio (SNR) in elongated scintillators. Longer scintillators produce fewer detected photons and lower peak amplitudes as a result of increased optical path lengths, bulk absorption, and multiple internal reflections. Consequently, noise has a relatively larger impact on the weakened intrinsic signal in long scintillators, leading to distortion and greater overlap between features critical for the Charge Comparison Method (CCM), particularly in the decay tail, which is the first region affected by Gaussian noise.

As observed in earlier analysis of geometrical variations, increasing the length of the scintillator leads to a reduction in the total number of detected photons, as quantified by the pulse integrals, as well as a corresponding decrease in peak amplitudes. These effects arise due to increased optical path lengths, bulk absorption in the scintillator, and multiple internal reflectors prior to reaching the detector.

In all cases, gamma-induced pulses arrived earlier than neutron-induced pulses, reflecting fundamental differences in their interactions within plastic scintillators. Gamma-rays primarily interact via Compton scattering, producing fast recoil elec-

trons that deposit energy almost instantaneously and generate prompt scintillation photons. In contrast, neutrons at the energies considered in this work, primarily interact via elastic scattering with hydrogen nuclei, producing slower recoil protons. The energy deposition from these protons occurs over a longer timescale, leading to a delayed onset of scintillation compared to gamma interactions. This distinction demonstrates the capability of Geant4 to accurately model both the light transport dynamics and timing differences arising from particle-specific interactions within plastic scintillators.

Chapter 8

Conclusions and Future Work

This thesis presents Geant4-based Monte Carlo simulations to investigate neutron- and gamma-induced pulse shapes in EJ-276, a commercially available plastic scintillator with pulse shape discrimination (PSD) capabilities. A systematic methodology was developed to isolate and analyse the key detector parameters influencing pulse shape formation in PSD-capable plastic scintillators. Pulse shapes were evaluated under a range of conditions, including variations in scintillator geometry and length, modifications to optical surface properties, and differing types and levels of simulated photodetector noise. The Charge Comparison Method (CCM), a widely used PSD technique, was employed to quantify the effects of these variations on the PSD performance of EJ-276.

A notable challenge with PSD-capable plastic scintillators is the degradation in PSD performance as scintillator length increases. This research examined three elongated geometries — a slab, cylinder, and cuboid — to study how increasing length along a single dimension affects pulse shapes and subsequent PSD performance. These findings are particularly relevant for applications in homeland security, such as radiation portal monitors, where plastic scintillators are appealing due to their affordability, ability to be scaled up to larger sizes, and robustness in harsh environments.

The simulations revealed that light collection efficiency (LCE) decreases as the

scintillator length increases along a single dimension, a trend that was consistent across all three geometries studied. This work corroborates earlier observations by (Hubbard, Paul J Sellin, and Lotay, 2020) regarding the appearance of so-called 'bumps' — or artefacts — in the simulated pulse shapes of large scintillators (greater than 300 mm in length) across different geometries. These distortions were attributed primarily to the increased length in one dimension, indicating that they are a geometrical effect. This study further supports the conclusion that these features arise from the initial emission direction of scintillation photons, and were observed both for explicitly defined specular surfaces and for the cases where no explicit surface properties were defined.

These simulations represent pulse shapes at a specific stage in their development: after scintillation emission and light transport through the scintillator, but prior to the influence of photodetector and readout electronics. The final observed pulse shape is ultimately a convolution of all these effects. A key limitation of this work is the lack of experimental validation. While the simulations provide valuable insight into pulse shapes following scintillation and light transport, they do not currently capture the full signal chain — from scintillation emission through the response of the photodetector (e.g.: PMTs or silicon photomultipliers (SiPMs)) to subsequent data processing electronics.

Future work should involve experimental studies to capture realistic pulse shapes and compare them with the Geant4 simulated results to help determine whether observed artefacts are preserved or smeared out by the detector response. A promising direction is to incorporate photodetector response models into the simulations and convolve these with the simulated light pulses, potentially using an integrated approach within Geant4. While similar convolutions have been performed in other scintillator simulation studies, they are typically applied outside of Geant4.

One practical approach would be to develop a comprehensive database or 'Look-Up Table (LUT)' of photodetector responses. This resource would enhance simulation accuracy and enable easier direct comparison with experimental data.

It would be invaluable for the wider community and could significantly improve reproducibility and benchmarking efforts. Creating such a LUT would involve experimentally capturing the single-photoelectron response of a variety of commonly used photomultiplier tubes (PMTs) and silicon photomultipliers (SiPMs) and incorporating this into the Geant4 framework in the same manner as the LUTs for optical surface data.

A challenge identified when using Geant4 for scintillator simulation studies is the variability in simulation setups among users. Differences in material properties, optical surface models, and geometry definitions can lead to inconsistencies, making comparison across studies difficult. This issue could be alleviated through greater adoption of standardised material and optical surface libraries, such as those developed by the SSLG4 project (Kandemir et al., 2025). Facilitating code sharing and reuse — with clear documentation of material properties, and their sources — would further reduce the learning curve for new users and improve simulation reliability, thereby enabling meaningful comparisons between studies to be made.

An additional important improvement would be the acquisition of experimental data for the parameter values used in simulations, as this would improve their overall accuracy. In this work, this approach was applied to the EJ-276 decay time constants and relative intensities, which were obtained from experimental measurements reported in Iwanowska-Hanke et al., 2014.

The optical surface models used in this research rely on the UNIFIED model, which was originally developed for inorganic scintillators. The more recent LUT-Davis model, which which enables the inclusion of experimentally measured reflectance data, was not explored here but represents a promising avenue for improving model accuracy (Trigila, Moghe, and Roncali, 2021). However, generating these LUTs is non-trivial and currently requires electron microscopy for the scanning of scintillator surfaces. Additional limitations exist in Geant4's treatment of wavelength-dependent reflectivity and quantum efficiency. In this study, photon detection was assumed to have 100% efficiency at all wavelengths

— an approximation that future work should address by incorporating realistic, wavelength-dependent quantum efficiency values.

Another practical constraint is the computational cost associated with simulating large numbers of optical photons for PSD analysis. Despite leveraging a high-performance computing cluster, simulations remained time-intensive due to the inherent complexity of photon transport modelling. This limited both the range of parameters that could be explored and the number of simulated neutron/gamma pulses that could be generated. Future work could focus on optimising the simulation code for parallel execution and ensuring thread safety to exploit multi-core or distributed computing, enabling more pulses to be simulated. This would improve comparison with experimental data, enhance statistical reliability, and allow a comprehensive uncertainty analysis, which was beyond the scope of the current work due to the aforementioned computational constraints.

While tools such as GODDeSS (E. Dietz-Laursonn et al., 2017) and (Niggemann et al., 2015) G4SiPM extend Geant4's capabilities, many of these tools are no longer actively maintained. Continued development and community support of such tools could facilitate broader adoption and smoother integration into new research. Moreover with the increasing interest in the use of artificial intelligence (AI) for pulse shape discrimination (PSD) (Fu et al., 2018; Griffiths et al., 2020), pulse shape simulations could serve as valuable training data, potentially enabling faster and more accurate PSD.

Geant4 has recently introduced features allowing for particle-dependent yields and decay time constants, enabling more accurate simulations of mixed radiation fields. Although this study simulated neutron and gamma-ray interactions separately, future work can now explore mixed-field environments with physically correct decay dynamics for each particle type.

Several additional areas for future work are also apparent:

- **Position-sensitive detection**: Investigating how interaction position within the scintillator effects pulse shape could inform the development of position-

sensitive neutron detectors based on PSD-capable plastics.

- **Energy dependence**: Only 1 MeV particles were considered in this study. Future work should explore a broader energy range to assess PSD behaviour under different incident radiation energies since it is known that PSD is highly energy dependent.
- **Surface model comparison**: A detailed comparison between the GLISUR, UNIFIED, and LUT models could clarify their impacts on pulse shape modelling.
- **Alternative PSD metrics**: The Figure of Merit (FoM), while widely used, is often not comparable across studies due to differences in detector configuration and analysis methods. Developing or adopting more standardised or robust metrics could improve comparability across studies.
- **Optical coupling**: Introducing optical coupling agents (e.g., optical grease) and systematically increasing simulation complexity may yield further insights into their influence on pulse shape and pulse shape discrimination (PSD) capability.

In summary, this thesis has demonstrated that Geant4 is a valuable tool for modelling PSD-capable plastic scintillators. While the current simulations provide a solid foundation, the identified limitations highlight several opportunities to improve accuracy and expand capability — particularly through experimental validation, improved photodetector modelling, and the sharing of code for material and optical surface definitions.

Chapter 9

Appendix

9.1 EJ-276 Data Sheet

PSD PLASTIC SCINTILATOR
EJ-276 & EJ-276G

EJ-276 pulse-shape discriminating (PSD) plastic scintillator enables the separation of gamma and fast neutron signals on the basis of their timing characteristics. This scintillator replaces all versions of EJ-299-33 and EJ-299-34 PSD scintillators and embodies the following improvements:

- Excellent physical hardness, equal to or superior to that of standard plastic scintillators
- Long-term stability of scintillation and optical characteristics
- Basic PSD properties increased to being comparable to the best liquid scintillators

EJ-276G with green fluorescence is also available for use with solid state sensors.

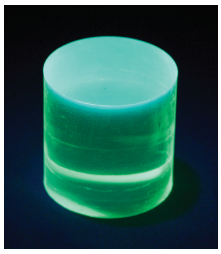

PROPERTIES		EJ-276	EJ-276G
Light Output (% Anthracene)		56	52
Scintillation Efficiency (photons/1 MeV e$^-$)		8,600	8,000
Wavelength of Maximum Emission (nm)		425	490
H Atoms per cm^3 ($\times 10^{22}$)		4.53	4.53
C Atoms per cm^3 ($\times 10^{22}$)		4.89	4.89
Electrons per cm^3 ($\times 10^{23}$)		3.52	3.52
Density (g/cm^3)		1.096	1.096
Approx. Mean Decay Times of First 3 Components (ns)	**Gamma Excitation**	13, 35, 270	—
	Neutron Excitation	13, 59, 460	—

CHEMICAL COMPATIBILITY

Attacked By: Aromatic solvents, Chlorinated solvents, Ketones, Solvent bonding cements, etc.
Stable In: Water, Dilute acids and alkalis, Lower alcohols, Silicone greases.
It is safe to use most epoxies with this scintillator.

Available Sizes

Cylinders up to 127 mm diameter x 200 mm long and plates up to 25 mm thick x 250 mm x 250 mm can be supplied. Precision imaging arrays with square pixels with cross sections as small as 0.75 mm can also be supplied.

PSD SCATTER CHART, AmBe

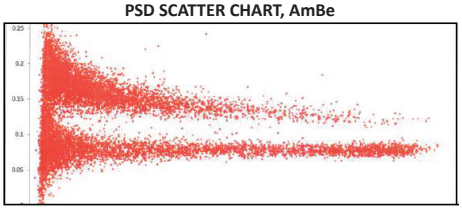

SCINTILLATOR SIZE: 127 mm DIA × 51 mm THICK

EJ-276 & EJ-276G EMISSION SPECTRUM

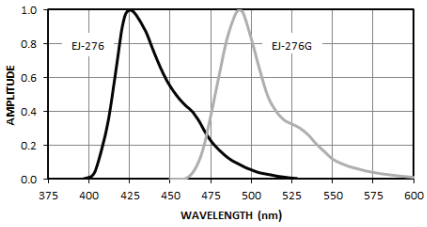

Revision Date: October 2017

ELJEN TECHNOLOGY
1300 W. Broadway, Sweetwater, TX 79556
www.eljentechnology.com • eljen@eljentechnology.com
Toll Free (USA): (888)-800-8771 • Tel: (325)-235-4276 • Fax: (325) 235-0701

Figure 9.1: EJ-276 data sheet. Obtained from Eljen-Technology, 2017

9.2 Geant4 EJ-276 Optical Properties Definition

```
1
2  void Materials::SetOpticalPropertiesEJ276()
3
4  {
5      /// Refractive Index
6      const G4int nRINDEX = 2;
7      //G4double photonEnergyRindex[nRINDEX] = {8.5506*eV,0.7973*eV};
8      G4double photonEnergyRindex[nRINDEX] = {0.7973*eV, 8.5506*eV};
9          G4double refractiveIndexEJ276[nRINDEX]= {1.58, 1.58};
10
11         /// Bulk Absorption length
12         /// Taken as Light Attenuation Length from datasheet -
               EJ200
13         const G4int nABS = 2;
14         G4double photonEnergyAbsLength[nABS] = {0.7973*eV,
               8.5506*eV};
15         G4double absLengthEJ276[nABS]= {3.8*m, 3.8*m};
16
17         /// Emission spectra
18         const G4int nEM = 25;
19
20     /// EJ-276 emission spectrum
21
22     G4double photonEnergyEM[nEM] =
23            {2.259*eV, 2.288*eV, 2.318*eV, 2.349*eV, 2.381*eV,
                  2.413*eV, 2.447*eV,
24             2.481*eV, 2.517*eV, 2.554*eV, 2.591*eV, 2.630*eV,
                  2.670*eV, 2.710*eV,
25             2.753*eV, 2.797*eV, 2.842*eV, 2.888*eV, 2.937*eV,
                  2.987*eV, 3.038*eV,
26             3.091*eV, 3.146*eV, 3.204*eV, 3.263*eV};
27
```

```
28      G4double emEJ276[nEM] =
29              {0.009, 0.031, 0.047, 0.064, 0.07, 0.099, 0.133, 0.168,
                    0.223, 0.276, 0.336,
30               0.411, 0.544, 0.667, 0.729, 0.763, 0.885,
31               0.988, 0.793, 0.373, 0.156, 0.08, 0.025, 0.02,
                    0.003};
32
33      /// Creating the materials property table and adding entries
            into
34      /// properties table
35      G4MaterialPropertiesTable* EJ276_mpt = new
            G4MaterialPropertiesTable();
36
37      EJ276_mpt->AddProperty("SCINTILLATIONCOMPONENT1",
            photonEnergyEM,emEJ276,nEM);
38      EJ276_mpt->AddProperty("SCINTILLATIONCOMPONENT2",
            photonEnergyEM, emEJ276, nEM);
39      EJ276_mpt->AddProperty("SCINTILLATIONCOMPONENT3",
            photonEnergyEM, emEJ276, nEM);
40      EJ276_mpt->AddProperty("RINDEX",
            photonEnergyRindex,refractiveIndexEJ276,nRINDEX);
41
42
43      EJ276_mpt->AddProperty("ABSLENGTH",
            photonEnergyAbsLength,absLengthEJ276,nABS);
44      EJ276_mpt->AddConstProperty("SCINTILLATIONYIELD",
            8600/MeV);    //8600
45      EJ276_mpt->AddConstProperty("RESOLUTIONSCALE", 1.0);
46
47
48      EJ276_mpt->AddConstProperty("SCINTILLATIONTIMECONSTANT1",
            4.3*ns);
49      EJ276_mpt->AddConstProperty("SCINTILLATIONTIMECONSTANT2",
            18.*ns);
```

```
50      EJ276_mpt->AddConstProperty("SCINTILLATIONTIMECONSTANT3",
            140.*ns);
51      EJ276_mpt->AddConstProperty("SCINTILLATIONYIELD1", 0.740);

52      EJ276_mpt->AddConstProperty("SCINTILLATIONYIELD2", 0.140);

53      EJ276_mpt->AddConstProperty("SCINTILLATIONYIELD3", 0.120);


54
55      EJ276_mpt->AddConstProperty("SCINTILLATIONRISETIME1",
            0.9*ns);
56      EJ276_mpt->AddConstProperty("SCINTILLATIONRISETIME2", 0*ns);
57      EJ276_mpt->AddConstProperty("SCINTILLATIONRISETIME3", 0*ns);
58
59  /*
60      EJ276_mpt->AddConstProperty("SCINTILLATIONTIMECONSTANT1",
            4.5*ns);
61      EJ276_mpt->AddConstProperty("SCINTILLATIONTIMECONSTANT2",
            20.*ns);
62      EJ276_mpt->AddConstProperty("SCINTILLATIONTIMECONSTANT3",
            170.*ns);
63      EJ276_mpt->AddConstProperty("SCINTILLATIONYIELD1", 0.580);

64      EJ276_mpt->AddConstProperty("SCINTILLATIONYIELD2", 0.180);
65      EJ276_mpt->AddConstProperty("SCINTILLATIONYIELD3", 0.240);
66  */
67
68      EJ276->GetIonisation()->SetBirksConstant(0.126*mm/MeV);


69
70      EJ276->SetMaterialPropertiesTable(EJ276_mpt);
71
72      EJ276_mpt->DumpTable();
73
74  }
```

Listing 9.1: Geant4 code for EJ276 material properties

9.3 Geant4 Photocathode Surface Definition

```
1
2       /// PHOTOCATHODE SURFACE
3       /// The parameter 'efficiency' for optical surfaces refers to
            the probability that an optical photon will be absorbed by
            the surface. This represents the
4       /// fraction of incident photons that are absorbed by the
            surface. When a photon hits the surface, if it is not
            absorbed (based on the efficiency), it may be reflected,
            refracted, or transmitted depending on other properties of
            the surface.
5       /// Efficiencies should be between 0 and 1 to represent
            probability.
6
7       G4double photocath_EFF[] = {1.0, 1.0}; // Enables 'detection'
            of photons, perfect efficiency, not variable with
            wavelength, 1.0,1.0
8       assert(sizeof(photocath_EFF) / sizeof(G4double) == num);
                /// Ensures 100% absorption.
9
10      /// For a photocathode, usually real part of refractive index
            is approx. 1.92 - 2.
11      G4double photocath_ReR[] = {1.92, 1.92}; // Real part of the
            refractive index. 1.92
12      assert(sizeof(photocath_ReR) / sizeof(G4double) == num);
13
14      G4double photocath_ImR[] = {1.69, 1.69}; // Imaginary part of
            the refractive index
15      assert(sizeof(photocath_ImR) / sizeof(G4double) == num);
16
17      G4double photocath_REF[] = {0.0, 0.0}; // Reflectivity
            /// at 0 this is full absorption.
18      assert(sizeof(photocath_REF) / sizeof(G4double) == num);
19
```

```
20      G4MaterialPropertiesTable* photocath_mt = new
            G4MaterialPropertiesTable();
21      photocath_mt->AddProperty("EFFICIENCY", ephoton,
            photocath_EFF, num);
22      photocath_mt->AddProperty("REALRINDEX", ephoton,
            photocath_ReR, num);
23      photocath_mt->AddProperty("IMAGINARYRINDEX", ephoton,
            photocath_ImR, num);
24      photocath_mt->AddProperty("REFLECTIVITY", ephoton,
            photocath_REF, num);
25
26      G4OpticalSurface* photocath_opsurf = new
            G4OpticalSurface("photocath_opsurf");
27      photocath_opsurf->SetType(dielectric_metal);
28      photocath_opsurf->SetFinish(polished);
29      photocath_opsurf->SetModel(glisur);
30
31      photocath_opsurf->SetMaterialPropertiesTable(photocath_mt);
32
33      /// Create logical skin surface
34      new G4LogicalSkinSurface("photocath_surf", logicPhotonDet,
            photocath_opsurf);
35
36  }
```

Listing 9.2: Geant4 code for photocathode surface definition

9.4 Charge Comparison Method MATLAB Script

```
%% Charge Comparison Method (CCM) MATLAB script
%% 01/11/2023

% Defining the number of pulses
num_pulses = 1000;
num_pulses2 = 1000;

% Determining the number of samples (binning) per pulse from
    the pulse data
num_samples = size(NeutronCube400mm1MeV(1).data, 1);
num_samples2 = size(NeutronCube400mm1MeV(1).data, 1);

% Initialize matrices to store pulse data
GammaPulsesX = zeros(num_samples, num_pulses);
GammaPulsesY = zeros(num_samples, num_pulses);

NeutronPulsesX = zeros(num_samples2, num_pulses2);
NeutronPulsesY = zeros(num_samples2, num_pulses2);

% Initialising noise arrays
noise_gamma = zeros(num_samples, num_pulses);
noise_neutron = zeros(num_samples, num_pulses);

% Define fixed noise level
% When this is set to a value, it's specifying that the
    noise has  standard
% deviation of (value) --> it's not adding those values.
    Generating random
```

```
% values from a Gaussian distribution with mean = 0 and
    standard deviation
% = (value). Random value drawn from a Gaussian
    distribution. +/- (value)
% random fluctuations in the photon count.
fixed_noise_amplitude = 0;

% Extract time and signal values for each pulse. Looping
    through each pulse
% and extracting the time and signal amplitude for neutron
    and gamma pulses
for i = 1:num_pulses

    % Extract gamma pulse data
    GammaPulsesX(:,i) = GammaSlab400mm1MeV(i).data(:,2);
    GammaPulsesY(:,i) = GammaSlab400mm1MeV(i).data(:,end);

    % Extract neutron pulse data
    NeutronPulsesX(:,i) = NeutronSlab400mm1MeV(i).data(:,2);
    NeutronPulsesY(:,i) =
        NeutronSlab400mm1MeV(i).data(:,end);

    %Each point in the signal gets a random "jitter" added
        to it.
    %For shot noise, that jitter depends on the signal%s
        amplitude.
    %For fixed noise, the jitter is constant in size,
        regardless of the signal.

    % Shot Noise: Proportional to the square root of the
        signal. Shot noise
```

```
48      %is signal dependent (Poisson nature)
49      shot_noise_gamma = sqrt(abs(GammaPulsesY(:,i))) .*
           randn(size(GammaPulsesY(:,i)));
50      shot_noise_neutron = sqrt(abs(NeutronPulsesY(:,i))) .*
           randn(size(NeutronPulsesY(:,i)));
51
52      % Fixed Noise: Constant Gaussian noise added - such as
           from dark current of PMT
53      fixed_noise_gamma = fixed_noise_amplitude *
           randn(size(GammaPulsesY(:,i)));  % Fixed noise for
           gamma pulses
54      fixed_noise_neutron = fixed_noise_amplitude *
           randn(size(NeutronPulsesY(:,i)));  % Fixed noise for
           neutron pulses
55
56      % Add noise to the pulses (Fixed + Shot noise)
57      noisy_data_gamma(:,i) = GammaPulsesY(:,i) +
           shot_noise_gamma + fixed_noise_gamma;
58      noisy_data_neutron(:,i) = NeutronPulsesY(:,i) +
           shot_noise_neutron + fixed_noise_neutron;
59
60      % Now we calculate the average pulse shapes for both
           gamma and neutron
61      averageGammaPulseY = mean(noisy_data_gamma, 2); %
           Average over the 1000 pulses
62      averageNeutronPulseY = mean(noisy_data_neutron, 2); %
           Average over the 1000 pulses
63
64      % Normalize the averaged pulse shapes
65      normalizedAverageGammaPulseY =
           normalize(averageGammaPulseY, 'range');
```

```
66      normalizedAverageNeutronPulseY =
            normalize(averageNeutronPulseY, 'range');
67
68      % For no noise case
69      % noisy_data_gamma(:,i) = GammaPulsesY(:,i);
70      % noisy_data_neutron(:,i) = NeutronPulsesY(:,i);
71
72  end
73
74  % Plot the averaged and normalized gamma and neutron pulses
75  figure;
76  plot(GammaPulsesX(:,1), normalizedAverageGammaPulseY, 'r-',
        'LineWidth', 2);
77  hold on;
78  plot(NeutronPulsesX(:,1), normalizedAverageNeutronPulseY,
        'b-', 'LineWidth', 2);
79  xlabel('Time (ns)', 'FontSize', 24);
80  ylabel('Normalised Amplitude', 'FontSize', 24);
81  xlim([0, 200]);  % Set x-axis limits
82  grid on;
83  legend('Average Gamma Pulse', 'Average Neutron Pulse',
        'FontSize', 24);
84  hold off;
85  set(gcf, 'Position', [100, 100, 800, 600]);  % Width x
        Height in pixels
86
87  % Parameters for integration gates
88  % Found from looking at differences in sum of pulses
89  short_gate_start = 37;
90  short_gate_end =  num_samples;
91  long_gate_start = 10;
```

```
92 long_gate_end = num_samples;          %% entire duration of
       pulse
93
94 % Preallocate arrays for charge comparison
95 short_gate_charge_gamma = zeros(num_pulses, 1);
96 long_gate_charge_gamma = zeros(num_pulses, 1);
97
98 short_gate_charge_neutron = zeros(num_pulses, 1);
99 long_gate_charge_neutron = zeros(num_pulses, 1);
100
101 % Calculate charges in the defined gates using trapz
102 for i = 1:num_pulses
103
104     %% Trapz function (Trapezoid Integration) is used for
           charge calculation.
105     % For gamma pulses
106     short_gate_charge_gamma(i) =
           trapz(GammaPulsesX(short_gate_start:short_gate_end,
           i), noisy_data_gamma(short_gate_start:short_gate_end,
           i));
107     long_gate_charge_gamma(i) =
           trapz(GammaPulsesX(long_gate_start:long_gate_end, i),
           noisy_data_gamma(long_gate_start:long_gate_end, i));
108
109     % For neutron pulses
110     short_gate_charge_neutron(i) =
           trapz(NeutronPulsesX(short_gate_start:short_gate_end,
           i),
           noisy_data_neutron(short_gate_start:short_gate_end,
           i));
```

```
111     long_gate_charge_neutron(i) =
            trapz(NeutronPulsesX(long_gate_start:long_gate_end,i),
            noisy_data_neutron(long_gate_start:long_gate_end, i));
112
113 end
114
115 % Calculate the PSD parameter (ratio of charges)
116 psd_ratio_gamma = short_gate_charge_gamma ./
        long_gate_charge_gamma;
117 psd_ratio_neutron = short_gate_charge_neutron ./
        long_gate_charge_neutron;
118
119 sumGammaPulsesY = sum(GammaPulsesY(:,1:1000),2);
120 sumNeutronPulsesY = sum(NeutronPulsesY(:,1:1000),2);
121
122 % Use the X time vector from the first column (assuming all
        are aligned)
123 xGamma = GammaPulsesX(:,1);
124 xNeutron = NeutronPulsesX(:,1);
125
126 % % Normalise the gamma and neutron pulses
127 normalizedGammaPulsesY = (sumGammaPulsesY -
        min(sumGammaPulsesY)) / (max(sumGammaPulsesY) -
        min(sumGammaPulsesY));
128 normalizedNeutronPulsesY = (sumNeutronPulsesY -
        min(sumNeutronPulsesY)) / (max(sumNeutronPulsesY) -
        min(sumNeutronPulsesY));
129
130 % % Calculate the difference between normalized gamma and
        neutron pulses
```

```
131 difference = normalizedGammaPulsesY -
        normalizedNeutronPulsesY;
132
133 %% Plot the normalized difference
134 figure;
135 plot(xGamma, difference, 'LineWidth', 2);
136 xlabel('Time (ns)');
137 ylabel('Normalised Difference (Gamma - Neutron)');
138 title('Normalised Difference Plot (Gamma - Neutron)');
139 grid on;
140
141 % Find the index where the difference is minimal (valley) as
        this
142 % corresponds to where neutron pulse is largest, relative to
        gamma
143 min_diff_index = find(difference == min(difference))
144
145 % If there are multiple minimums, you can choose the first
        one:
146 min_diff_index = min_diff_index(1)  % This will ensure you
        get the first occurrence
147
148
149 %% Long gate vs PSD parameter
150 figure;
151 scatter(long_gate_charge_gamma,
        psd_ratio_gamma,'filled','r'); %short_gate_charge_gamma
152 hold on;
153 scatter(long_gate_charge_neutron,
        psd_ratio_neutron,'filled','b');
        %short_gate_charge_neutron
```

```
154 hold on;
155 xlabel('Long Integral');
156 ylabel('PSD Parameter');
157 hold on;
158 % Set font size for ticks and labels to 18
159 set(gca, 'FontSize', 24);  % This affects both the tick
    labels and axis labels
160 grid on;
161 legend('Gamma','Neutron', 'FontSize', 24);
162 xlim([0, 200]);  % Set x-axis limits
163 hold off;
164 % Set figure size
165 set(gcf, 'Position', [100, 100, 800, 600]);  % Width x
    Height in pixels
166
167 normalizedGammaPulsesY = normalize(sumGammaPulsesY,'range');
168 normalizedNeutronPulsesY =
    normalize(sumNeutronPulsesY,'range');
169
170 % figure;
171 % plot(xGamma, sumGammaPulsesY, 'r', 'LineWidth', 2);
172 % hold on;
173 % plot(xNeutron, sumNeutronPulsesY, 'b', 'LineWidth', 2);
174 % hold on;
175 % xlabel('Time (ns)', 'FontSize', 24);
176 % ylabel('Amplitude', 'FontSize', 24);
177 % xlim([0, 200]);  % Set x-axis limits
178 % % Set font size for ticks and labels to 24
179 % set(gca, 'FontSize', 24);  % This affects both the tick
    labels and axis labels
180 % grid on;
```

```
% legend('Gamma Pulses','Neutron Pulses', 'FontSize', 24);
% hold off;
% % Set figure size
% set(gcf, 'Position', [100, 100, 800, 600]);  % Width x Height in pixels

% figure;
% plot(2+xGamma, normalize(sumGammaPulsesY, 'range'), 'r', 'LineWidth', 2);
% hold on;
% plot(xNeutron, normalize(sumNeutronPulsesY, 'range'), 'b', 'LineWidth', 2);
% hold on;
% xlabel('Time (ns)', 'FontSize', 24);
% ylabel('Normalised Amplitude', 'FontSize', 24);
% xlim([0, 200]);  % Set x-axis limits
% % Set font size for ticks and labels to 24
% set(gca, 'FontSize', 24);  % This affects both the tick labels and axis labels
% grid on;
% legend('Gamma Pulses','Neutron Pulses', 'FontSize', 24);
% hold off;
% % Set figure size
% set(gcf, 'Position', [100, 100, 800, 600]);  % Width x Height in pixels

% Find the time of the maximum amplitude for gamma and neutron pulses
[~, maxIdxGamma] = max(normalize(sumGammaPulsesY, 'range'));
[~, maxIdxNeutron] = max(normalize(sumNeutronPulsesY, 'range'));
```

```
205
206 % Get the corresponding time values
207 maxTimeGamma = xGamma(maxIdxGamma);
208 maxTimeNeutron = xNeutron(maxIdxNeutron);
209
210 % Display the times
211 disp(['Max amplitude for Gamma occurs at time: ',
       num2str(maxTimeGamma), ' ns']);
212 disp(['Max amplitude for Neutron occurs at time: ',
       num2str(maxTimeNeutron), ' ns']);
```

Listing 9.3: MATLAB script for PSD using Charge Comparison Method

References

Adams, J. M. and G. White (Nov. 1978). "A versatile pulse shape discriminator for charged particle separation and its application to fast neutron time-of-flight spectroscopy". In: *Nuclear Instruments and Methods* 156.3, pp. 459–476. ISSN: 0029554X. DOI: 10.1016/0029-554X(78)90746-2.

Allison, J., K. Amako, J. Apostolakis, H. Araujo, et al. (2006). "Geant4 developments and applications". In: *IEEE Transactions on Nuclear Science* 53.1, pp. 270–278. ISSN: 00189499. DOI: 10.1109/TNS.2006.869826.

Allison, J., K. Amako, J. Apostolakis, P. Arce, et al. (Nov. 2016). "Recent developments in Geant4". In: *Nuclear Instruments and Methods in Physics Research Section A: Accelerators, Spectrometers, Detectors and Associated Equipment* 835, pp. 186–225. ISSN: 0168-9002. DOI: 10.1016/J.NIMA.2016.06.125.

Archambault, J. P. et al. (2003). "GEANT4 photon readout simulations of plastic scintillating strips with embedded WLS fibers". In: *IEEE Nuclear Science Symposium Conference Record* 3, pp. 1549–1551. ISSN: 10957863. DOI: 10.1109/NSSMIC.2003.1352172.

Aspinall, M. D., B. D'Mellow, R. O. Mackin, M. J. Joyce, N. P. Hawkes, et al. (2007). "Verification of the digital discrimination of neutrons and γ rays using pulse gradient analysis by digital measurement of time of flight". In: *Nuclear Instruments and Methods in Physics Research, Section A: Accelerators, Spectrometers, Detectors and Associated Equipment* 583.2-3, pp. 432–438. ISSN: 01689002. DOI: 10.1016/j.nima.2007.09.041.

Aspinall, M. D., B. D'Mellow, R. O. Mackin, M. J. Joyce, Z. Jarrah, et al. (2007). "The empirical characterization of organic liquid scintillation detectors by the normalized average of digitized pulse shapes". In: *Nuclear Instruments and Methods in Physics Research, Section A: Accelerators, Spectrometers, Detectors and Associated Equipment* 578.1, pp. 261–266. ISSN: 01689002. DOI: 10.1016/j.nima.2007.05.114.

Bell, Zane W. (Sept. 1981). "Tests on a digital neutron-gamma pulse shape discriminator with NE213". In: *Nuclear Instruments and Methods in Physics Research* 188.1, pp. 105–109. ISSN: 0167-5087. DOI: 10.1016/0029-554X(81)90327-X.

Bertrand, Guillaume H.V. et al. (2015). "Pulse shape discrimination between (fast or thermal) neutrons and gamma rays with plastic scintillators: State of the art". In: *Nuclear Instruments and Methods in Physics Research, Section A: Accelerators, Spectrometers, Detectors and Associated Equipment* 776, pp. 114–128. ISSN: 01689002. DOI: 10.1016/j.nima.2014.12.024.

Boxer, B. et al. (2023). "Studies in pulse shape discrimination for an optimized ASIC design". In: *Journal of Instrumentation* 18.1. ISSN: 17480221. DOI: 10.1088/1748-0221/18/01/P01020.

Brenizer, J. S. (Jan. 2013). "A Review of Significant Advances in Neutron Imaging from Conception to the Present". In: *Physics Procedia* 43, pp. 10–20. ISSN: 1875-3892. DOI: 10.1016/J.PHPRO.2013.03.002.

Brooks, F. D. (Apr. 1959). "A scintillation counter with neutron and gamma-ray discriminators". In: *Nuclear Instruments and Methods* 4.3, pp. 151–163. ISSN: 0029554X. DOI: 10.1016/0029-554X(59)90067-9.

— (June 1979). "Development of organic scintillators". In: *Nuclear Instruments and Methods* 162.1-3, pp. 477–505. ISSN: 0029-554X. DOI: 10.1016/0029-554X(79)90729-8.

Brooks, F. D., R. W. Pringle, and B. L. Funt (1960). "Pulse Shape Discrimination in a Plastic Scintillator". In: *IRE Transactions on Nuclear Science* NS-7.2-3, pp. 35–38. ISSN: 00962015. DOI: 10.1109/TNS2.1960.4315733.

Brun, Rene and Fons Rademakers (Apr. 1997). "ROOT - An object oriented data analysis framework". In: *Nuclear Instruments and Methods in Physics Research, Section A: Accelerators, Spectrometers, Detectors and Associated Equipment* 389.1-2, pp. 81–86. ISSN: 01689002. DOI: 10.1016/S0168-9002(97)00048-X.

Budakovsky, Sergey V. et al. (2006). "New effective organic scintillators for fast neutron and short-range radiation detection". In: *IEEE Nuclear Science Symposium Conference Record* 2.6, pp. 935–939. ISSN: 10957863. DOI: 10.1109/NSSMIC.2006.356000.

Cester, D. et al. (2014). "Experimental tests of the new plastic scintillator with pulse shape discrimination capabilities EJ-299-33". In: *Nuclear Instruments and Methods in Physics Research, Section A: Accelerators, Spectrometers, Detectors and Associated Equipment* 735.2014, pp. 202–206. ISSN: 01689002. DOI: 10.1016/j.nima.2013.09.031.

Chadwick, J. (Feb. 1932). *Possible existence of a neutron*. DOI: 10.1038/129312a0.

Choppin, Gregory et al. (2013). *Radiochemistry and Nuclear Chemistry: Fourth Edition*. Elsevier Inc., pp. 1–858. ISBN: 9780124058972. DOI: 10.1016/C2011-0-07260-5.

Comrie et al. (2014). "Tests of pulse shape discrimination with EJ299-33 plastic scintillator for use in portable spectroscopy". In: *Proceedings of Science*, pp. 2–6. ISSN: 18248039. DOI: 10.22323/1.213.0251.

— (2015). "Digital neutron/gamma discrimination with an organic scintillator at energies between 1 MeV and 100 MeV". In: *Nuclear Instruments and Methods in Physics Research, Section A: Accelerators, Spectrometers, Detectors and Associated Equipment* 772, pp. 43–49. ISSN: 01689002. DOI: 10.1016/j.nima.2014.10.058.

Corre, G. et al. (2015). "Neutron detection with large plastic scintillators for RPM applications". In: *2015 4th International Conference on Advancements in Nuclear Instrumentation Measurement Methods and their Applications, ANIMMA 2015* 33.0, pp. 1–4. DOI: 10.1109/ANIMMA.2015.7465625.

D'Mellow, B. et al. (2007). "Digital discrimination of neutrons and γ-rays in liquid scintillators using pulse gradient analysis". In: *Nuclear Instruments and Methods in Physics Research, Section A: Accelerators, Spectrometers, Detectors and Associated Equipment* 578.1, pp. 191–197. ISSN: 01689002. DOI: 10.1016/j.nima.2007.04.174.

Dietz-Laursonn, E. et al. (2017). "GODDeSS: A Geant4 extension for easy modelling of optical detector components". In: *Journal of Instrumentation* 12.4. ISSN: 17480221. DOI: 10.1088/1748-0221/12/04/P04026.

Dietz-Laursonn, Erik (2016). "Peculiarities in the Simulation of Optical Physics with Geant4". In: URL: http://arxiv.org/abs/1612.05162.

Eljen Technology (2023). "General Purpose Plastic Scintillator EJ-200, EJ-204, EJ-208, EJ-212". In: 888. URL: www.eljentechnology.com%E2%80%A2eljen@eljentechnology.comTollFree.

Eljen-Technology (2017). *PSD Plastic Scintillator EJ-276 & EJ-276G*. Tech. rep. October, p. 79556.

Ellis, Mark E., Kirk Duroe, and Paul A. Kendall (2016). "Pulse-shape discrimination scintillators for homeland security applications". In: *International Journal of Modern Physics: Conference Series* 44.2010, p. 1660214. DOI: 10.1142/s2010194516602143.

Flaska, Marek et al. (2013). "Influence of sampling properties of fast-waveform digitizers on neutron-gamma-ray, pulse-shape discrimination for organic scintillation detectors". In: *Nuclear Instruments and Methods in Physics Research, Section A: Accelerators, Spectrometers, Detectors and Associated Equipment* 729, pp. 456–462. ISSN: 01689002. DOI: 10.1016/j.nima.2013.07.008.

Ford, M J et al. (2021). *Optimization of Plastic Scintillators with Pulse-Shape Discrimination Capabilities*. Tech. rep. URL: https://www.osti.gov/servlets/purl/1818396.

Fu, C. et al. (2018). "Artificial neural network algorithms for pulse shape discrimination and recovery of piled-up pulses in organic scintillators". In: *Annals of Nuclear Energy* 120, pp. 410–421. ISSN: 18732100. DOI: 10.1016/j.anucene.2018.05.054.

Geant4 Collaboration (2023). "Book For Application Developers". In: *Rev.04 Release 10.6*, pp. 1–437. URL: https://indico.cern.ch/event/647154/contributions/2714212/attachments/1529029/2397032/BookForApplicationDevelopers.pdf.

— (n.d.). *Reference Physics Lists*. URL: http://geant4.web.cern.ch/geant4/support/physicsLists/referencePL/referencePL.shtml.

Geist, William H., Peter A. Santi, and Martyn T. Swinhoe, eds. (2024). *Nondestructive Assay of Nuclear Materials for Safeguards and Security*. Cham: Springer Nature Switzerland. ISBN: 978-3-031-58276-9. DOI: 10.1007/978-3-031-58277-6.

Ghadiri, Rasoul and Jamshid Khorsandi (2015). "Studying the response of a plastic scintillator to gamma rays using the Geant4 Monte Carlo code". In: *Applied Radiation and Isotopes* 99, pp. 63–68. ISSN: 18729800. DOI: 10.1016/j.apradiso.2015.02.017.

Ghorbani, P. et al. (2018). "Assessment of optical photon collection in a large plastic scintillator using Geant4-Gate code". In: *Optik* 158, pp. 305–311. ISSN: 00304026. DOI: 10.1016/j.ijleo.2017.12.111.

Griffiths, J. et al. (2020). "Pulse shape discrimination and exploration of scintillation signals using convolutional neural networks". In: *Machine Learning: Science and Technology* 1.4. ISSN: 26322153. DOI: 10.1088/2632-2153/abb781.

Grodzicka-Kobylka, M. et al. (2020). "Fast neutron and gamma ray pulse shape discrimination in EJ-276 and EJ-276G plastic scintillators". In: *Journal of Instrumentation* 15.3. ISSN: 17480221. DOI: 10.1088/1748-0221/15/03/P03030.

Hartwig, Zachary S. and Peter Gumplinger (2014). "Simulating response functions and pulse shape discrimination for organic scintillation detectors with Geant4". In: *Nuclear Instruments and Methods in Physics Research, Section A: Accelerators, Spectrometers, Detectors and Associated Equipment* 737, pp. 155–162. ISSN: 01689002. DOI: 10.1016/j.nima.2013.11.027.

Hawkes, N. P. and G. C. Taylor (2013). "Analysis of the pulse shape mechanism in a plastic scintillator with efficient neutron/gamma pulse shape discrimination". In: *Nuclear Instruments and Methods in Physics Research, Section A: Accelerators, Spectrometers, Detectors and Associated Equipment* 729, pp. 522–526. ISSN: 01689002. DOI: 10.1016/j.nima.2013.07.071.

Hellesen, C. et al. (2013). "Impact of digitization for timing and pulse shape analysis of scintillator detector signals". In: *Nuclear Instruments and Methods in Physics Research, Section A: Accelerators, Spectrometers, Detectors and Associated Equipment* 720, pp. 135–140. ISSN: 01689002. DOI: 10.1016/j.nima.2012.12.016.

Hubbard, Michael WJ, Paul J Sellin, and Gavin Lotay (Nov. 2020). "Light transport modelling of pulse shape discrimination within plastic scintillators". PhD thesis. DOI: 10.15126/THESIS.00857773.

Iwanowska-Hanke, J. et al. (2014). "Comparative study of large samples (2)". In: *Journal of Instrumentation* 9.6. ISSN: 17480221. DOI: 10.1088/1748-0221/9/06/P06014.

J.B. Birks (1964). *The Theory and Practice of Scintillation Counting*. London: Pergamon Press.

Janecek, Martin and William M. Moses (2010). "Simulating scintillator light collection using measured optical reflectance". In: *IEEE Transactions on Nuclear*

Science 57.3 PART 1, pp. 964–970. ISSN: 00189499. DOI: 10.1109/TNS.2010.2042731.

Jastaniah, S. D. and P. J. Sellin (2004). "Digital techniques for n/γ pulse shape discrimination and capture-gated neutron spectroscopy using liquid scintillators". In: *Nuclear Instruments and Methods in Physics Research, Section A: Accelerators, Spectrometers, Detectors and Associated Equipment* 517.1-3, pp. 202–210. ISSN: 01689002. DOI: 10.1016/j.nima.2003.08.178.

Jones, Ashley and Malcolm J. Joyce (2013). "Pulse-shape discrimination in organic scintillators using the rising edge". In: *2013 3rd International Conference on Advancements in Nuclear Instrumentation, Measurement Methods and Their Applications, ANIMMA 2013*, pp. 1–3. DOI: 10.1109/ANIMMA.2013.6727923.

Jönsson, Bo Anders (July 2021). "Henri Becquerel's discovery of radioactivity – 125 years later". In: *Physica Medica* 87, pp. 144–146. ISSN: 1120-1797. DOI: 10.1016/J.EJMP.2021.03.032.

Kandemir, Mustafa et al. (2025). "SSLG4: A novel scintillator simulation library for Geant4". In: *Computer Physics Communications* 306.May 2024. ISSN: 00104655. DOI: 10.1016/j.cpc.2024.109385.

Khodaei, A et al. (2023). "A review of the Geant4 simulation platform for applications involving optical-based sensing and dosimetry". In: *Radiation Physics and Chemistry* 212.March, p. 111062. ISSN: 0969-806X. DOI: 10.1016/j.radphyschem.2023.111062.

Knoll, Glenn F. (2000). *Radiation Detection and Measurement*. 3rd. John Wiley and Sons. ISBN: 0-471-07338-5.

Kouzes, Richard T., James H. Ely, et al. (2010). "Neutron detection alternatives to 3He for national security applications". In: *Nuclear Instruments and Methods in Physics Research, Section A: Accelerators, Spectrometers, Detectors and Associated Equipment* 623.3, pp. 1035–1045. ISSN: 01689002. DOI: 10.1016/j.nima.2010.08.021.

Kouzes, Richard T., Azaree T. Lintereur, and Edward R. Siciliano (2015). "Progress in alternative neutron detection to address the helium-3 shortage". In: *Nuclear Instruments and Methods in Physics Research, Section A: Accelerators, Spectrometers, Detectors and Associated Equipment* 784, pp. 172–175. ISSN: 01689002. DOI: 10.1016/j.nima.2014.10.046.

Langeveld, Willem G.J. et al. (2017). "Pulse Shape Discrimination Algorithms, Figures of Merit, and Gamma-Rejection for Liquid and Solid Scintillators". In: *IEEE Transactions on Nuclear Science* 64.7, pp. 1801–1809. ISSN: 00189499. DOI: 10.1109/TNS.2017.2681654.

Lavietes, Anthony et al. (2012). "Liquid scintillator-based neutron detector development". In: *IEEE Nuclear Science Symposium Conference Record*, pp. 230–244. ISSN: 10957863. DOI: 10.1109/NSSMIC.2012.6551100.

Lawrence, Chris C. et al. (2014). "Neutron response characterization for an EJ299-33 plastic scintillation detector". In: *Nuclear Instruments and Methods in Physics Research, Section A: Accelerators, Spectrometers, Detectors and Associated Equipment* 759, pp. 16–22. ISSN: 01689002. DOI: 10.1016/j.nima.2014.04.062.

Levin, A. and C. Moisan (1996). "More physical approach to model the surface treatment of scintillation counters and its implementation into DETECT". In: *IEEE Nuclear Science Symposium & Medical Imaging Conference* 2, pp. 702–706. DOI: 10.1109/nssmic.1996.591410.

Liao, Can and Haori Yang (2014). "N/γ Pulse shape discrimination comparison of EJ301 and EJ339A liquid scintillation detectors". In: *Annals of Nuclear Energy* 69, pp. 57–61. ISSN: 03064549. DOI: 10.1016/j.anucene.2014.01.039.

M. Ebrahimi Shohani et al. (2017). "Geant4 Comparative Study of Affecting Different Parameters on Optical Photons Related to the Plastic Scintillation Detector". In: *Journal of Physical Science and Application* 7.6. ISSN: 21595348. DOI: 10.17265/2159-5348/2017.06.007.

Marrone, S. et al. (2002). "Pulse shape analysis of liquid scintillators for neutron studies". In: *Nuclear Instruments and Methods in Physics Research, Section*

A: Accelerators, Spectrometers, Detectors and Associated Equipment 490.1-2, pp. 299–307. ISSN: 01689002. DOI: 10.1016/S0168-9002(02)01063-X.

Martin, R. C., J. B. Knauer, and P. A. Balo (Nov. 2000). "Production, distribution and applications of californium-252 neutron sources". In: *Applied Radiation and Isotopes* 53.4-5, pp. 785–792. ISSN: 0969-8043. DOI: 10.1016/S0969-8043(00)00214-1.

Michael F. L'Annunziata (2016). *Radioactivity: Introduction and History, from the Quantum to Quarks*. 2nd. Elsevier. ISBN: 9780444634962.

Mike Pacey (2023). *HEC 3.0 Documentation*. URL: https://lancaster-hec.readthedocs.io/en/latest/index.html#.

Li-Ming, Zhang et al. (June 2004). "Simulation study for a single TOF scintillator using GEANT4". In: *Measurement Science and Technology* 15.7, N54. ISSN: 0957-0233. DOI: 10.1088/0957-0233/15/7/N02.

Nagy, J. Kónya and N.M. (2018). *Nuclear and Radiochemistry - Chapter 4: Radioactive Decay*, pp. 49–84. ISBN: 9780128136430.

National Institute of Standard and Technology (NIST) (2017). *NIST Database*. DOI: https://doi.org/10.18434/T4D303.

NEA Nuclear Data Services (2022). *JEFF Nuclear Data Library*. URL: https://www.oecd-nea.org/dbdata/jeff/.

Ngo, Khai D. et al. (2023). "Fast neutron response characterization of an EJ-276 plastic scintillator for use as a neutron monitor". In: *Nuclear Instruments and Methods in Physics Research, Section A: Accelerators, Spectrometers, Detectors and Associated Equipment* 1051.March, p. 168216. ISSN: 01689002. DOI: 10.1016/j.nima.2023.168216.

Niggemann, Tim et al. (2015). "G4SiPM: A novel silicon photomultiplier simulation package for Geant4". In: *Nuclear Instruments and Methods in Physics Research, Section A: Accelerators, Spectrometers, Detectors and Associated Equipment* 787, pp. 344–347. ISSN: 01689002. DOI: 10.1016/j.nima.2015.01.067.

Nishada, Qadir (2014). *Characterisation of a new type of solid organic scintillator for neutron-gamma discrimination using PSD techniques*. Tech. rep. URL: https://www.diva-portal.org/smash/get/diva2:752586/FULLTEXT01.pdf.

Ogawara, R. and M. Ishikawa (2016). "Signal pulse emulation for scintillation detectors using Geant4 Monte Carlo with light tracking simulation". In: *Review of Scientific Instruments* 87.7. ISSN: 10897623. DOI: 10.1063/1.4959186.

Payne, Christopher et al. (2016). "Neutron/gamma pulse shape discrimination in EJ-299-34 at high flux". In: *2015 IEEE Nuclear Science Symposium and Medical Imaging Conference, NSS/MIC 2015*, pp. 1–5. DOI: 10.1109/NSSMIC.2015.7581994.

Photonis (2002). *Photomultiplier tubes: Principle & Applications*. Tech. rep. URL: https://psec.uchicago.edu/library/photomultipliers/Photonis_PMT_basics.pdf.

Polyakov, Sergey V. (2013). "Photomultiplier Tubes". In: *Experimental Methods in the Physical Sciences* 45, pp. 69–82. ISSN: 10794042. DOI: 10.1016/B978-0-12-387695-9.00003-2.

Pozzi, S. A., M. M. Bourne, and S. D. Clarke (2013). "Pulse shape discrimination in the plastic scintillator EJ-299-33". In: *Nuclear Instruments and Methods in Physics Research, Section A: Accelerators, Spectrometers, Detectors and Associated Equipment* 723, pp. 19–23. ISSN: 01689002. DOI: 10.1016/j.nima.2013.04.085.

Reddy, C. Malla, K. Anantha Padmanabhan, and Gautam R. Desiraju (Dec. 2006). "Structure-property correlations in bending and brittle organic crystals". In: *Crystal Growth and Design* 6.12, pp. 2720–2731. ISSN: 15287483. DOI: 10.1021/cg060398w.

Riggi, S. et al. (2010). "Geant4 simulation of plastic scintillator strips with embedded optical fibers for a prototype of tomographic system". In: *Nuclear Instruments and Methods in Physics Research, Section A: Accelerators, Spectrometers,*

Detectors and Associated Equipment 624.3, pp. 583–590. ISSN: 01689002. DOI: 10.1016/j.nima.2010.10.012.

Roncali, Emilie and Simon R Cherry (2013). "Simulation of light transport in scintillators based on 3D characterization of crystal surfaces". In: *Physics in Medicine and Biology* 58.7, pp. 2185–2198. ISSN: 00319155. DOI: 10.1088/0031-9155/58/7/2185.

Roncali, Emilie, Mariele Stockhoff, and Simon R. Cherry (2017). "An integrated model of scintillator-reflector properties for advanced simulations of optical transport". In: *Physics in Medicine and Biology* 62.12, pp. 4811–4830. ISSN: 13616560. DOI: 10.1088/1361-6560/aa6ca5.

Roy, Pratap et al. (2018). "Detailed investigation on the possibility of using EJ-299-33A plastic scintillator for fast neutron spectroscopy in large scale experiments". In: *Nuclear Instruments and Methods in Physics Research, Section A: Accelerators, Spectrometers, Detectors and Associated Equipment* 901.June, pp. 198–202. ISSN: 01689002. DOI: 10.1016/j.nima.2018.06.007.

Rutherford, E. (2012). "The scattering of α and β particles by matter and the structure of the atom". In: *Philosophical Magazine* 92.4, pp. 379–398. ISSN: 1478-6435. DOI: 10.1080/14786435.2011.617037.

Schorr, Marvin G. and Franklin L. Torney (Nov. 1950). "Solid Non-Crystalline Scintillation Phosphors". In: *Physical Review* 80.3, p. 474. ISSN: 0031899X. DOI: 10.1103/PhysRev.80.474.

Stockhoff, Mariele et al. (2017). "Advanced optical simulation of scintillation detectors in GATE V8.0: First implementation of a reflectance model based on measured data". In: *Physics in Medicine and Biology* 62.12, pp. L1–L8. ISSN: 13616560. DOI: 10.1088/1361-6560/aa7007.

Stromswold, D C et al. (1998). *Direct Fast-Neutron Detection: a Progress Report.* Tech. rep. Richmond, Washington: Pacific Northwest National Laboratory. URL: https://www.osti.gov/servlets/purl/750259-0eeyT3/webviewable/.

Taggart, M. P. and P. J. Sellin (2018). "Comparison of the pulse shape discrimination performance of plastic scintillators coupled to a SiPM". In: *Nuclear Instruments and Methods in Physics Research, Section A: Accelerators, Spectrometers, Detectors and Associated Equipment* 908.August, pp. 148–154. ISSN: 01689002. DOI: 10.1016/j.nima.2018.08.054.

Taheri, Ali and Reza Gholipour Peyvandi (2017). "The impact of wrapping method and reflector type on the performance of rod plastic scintillators". In: *Measurement: Journal of the International Measurement Confederation* 97, pp. 100–110. ISSN: 02632241. DOI: 10.1016/j.measurement.2016.10.051.

Tavernier, Stefaan (2010). *Experimental techniques in nuclear and particle physics*, pp. 1–306. ISBN: 9783642008283. DOI: 10.1007/978-3-642-00829-0.

Tobergte, David R. and Shirley Curtis (Mar. 1991). "Passive Nondestructive Assay of Nuclear Materials". In: *Journal of Chemical Information and Modeling* 53.9, pp. 1689–1699. ISSN: 1098-6596. DOI: 10.2172/5428834.

Tomanin, Alice, Paolo Peerani, and Greet Janssens-Maenhout (2013). "On the optimisation of the use of 3He in radiation portal monitors". In: *Nuclear Instruments and Methods in Physics Research, Section A: Accelerators, Spectrometers, Detectors and Associated Equipment* 700, pp. 81–85. ISSN: 01689002. DOI: 10.1016/j.nima.2012.10.002.

Torrisi, L. (2000). "Plastic scintillator investigations for relative dosimetry in proton-therapy". In: *Nuclear Instruments and Methods in Physics Research, Section B: Beam Interactions with Materials and Atoms* 170.3, pp. 523–530. ISSN: 0168583X. DOI: 10.1016/S0168-583X(00)00237-8.

Trigila, Carlotta, Eshani Moghe, and Emilie Roncali (June 2021). "Technical Note: Standalone application to generate custom reflectance Look-Up Table for advanced optical Monte Carlo simulation in GATE/Geant4". In: *Medical Physics* 48.6, pp. 2800–2808. ISSN: 0094-2405. DOI: 10.1002/mp.14863.

UNODA (2023). *UNODA Treaties Database*. URL: https://treaties.unoda.org/t/npt%20https://treaties.unoda.org/t/tpnw/participants.

Vance, Andrew L et al. (2010). "Final LDRD Report : Advanced Plastic Scintillators for Neutron Detection". In: *Sandia National Laboratories* September, p. 16. URL: http://www.osti.gov/servlets/purl/990072-QSVY6g/.

Waxler, Roy M. and G. W. Cleek (1973). "The Effect of Temperature and Pressure on the Refractive Index of Some Oxide Glasses". In: *Journal of Research of the National Bureau of Standards. Section A, Physics and Chemistry* 77A.6, p. 755. ISSN: 0022-4332. DOI: 10.6028/JRES.077A.046.

Weldon, R. A. et al. (May 2019). "High-precision characterization of the neutron light output of stilbene along the directions of maximum and minimum response". In: *Nuclear Instruments and Methods in Physics Research Section A: Accelerators, Spectrometers, Detectors and Associated Equipment* 927, pp. 313–319. ISSN: 0168-9002. DOI: 10.1016/J.NIMA.2018.10.075.

Winyard, R. A., J. E. Lutkin, and G. W. McBeth (1971). "Pulse shape discrimination in inorganic and organic scintillators. I". In: *Nuclear Instruments and Methods* 95.1, pp. 141–153. ISSN: 0029554X. DOI: 10.1016/0029-554X(71)90054-1.

Zaitseva, N. P., A. M. Glenn, M. L. Carman, et al. (2020). "Multiple dye interactions in plastic scintillators: Effects on pulse shape discrimination". In: *Nuclear Instruments and Methods in Physics Research, Section A: Accelerators, Spectrometers, Detectors and Associated Equipment* 978.April, p. 164455. ISSN: 01689002. DOI: 10.1016/j.nima.2020.164455.

Zaitseva, N. P., A. M. Glenn, A. N. Mabe, et al. (2018). "Recent developments in plastic scintillators with pulse shape discrimination". In: *Nuclear Instruments and Methods in Physics Research, Section A: Accelerators, Spectrometers, Detectors and Associated Equipment* 889.February, pp. 97–104. ISSN: 01689002. DOI: 10.1016/j.nima.2018.01.093.

Zaitseva, Natalia, Andrew Glenn, et al. (2015). "Scintillation properties of solution-grown trans-stilbene single crystals". In: *Nuclear Instruments and Methods in Physics Research, Section A: Accelerators, Spectrometers, Detectors and*

Associated Equipment 789, pp. 8–15. ISSN: 01689002. DOI: 10.1016/j.nima.2015.03.090.

Zaitseva, Natalia, Benjamin L. Rupert, et al. (2012). "Plastic scintillators with efficient neutron/gamma pulse shape discrimination". In: *Nuclear Instruments and Methods in Physics Research, Section A: Accelerators, Spectrometers, Detectors and Associated Equipment* 668, pp. 88–93. ISSN: 01689002. DOI: 10.1016/j.nima.2011.11.071.

Zecher, Philip D. et al. (Aug. 2003). "Neutron/γ-ray pulse-shape discriminator". In: *Nuclear Instruments and Methods in Physics Research, Section A: Accelerators, Spectrometers, Detectors and Associated Equipment* 508.3, pp. 434–439. ISSN: 01689002. DOI: 10.1016/S0168-9002(03)01474-8.